

A METHOD FOR THE DESIGN OF A CLASS OF OPTIMUM MARINE PROPULSORS

by

William Bowles Coney

B. S., (1984), Massachusetts Institute of Technology

S. M., (1985), Massachusetts Institute of Technology

SUBMITTED IN PARTIAL FULFILLMENT OF
THE REQUIREMENTS FOR THE DEGREE OF

DOCTOR OF PHILOSOPHY

at the

MASSACHUSETTS INSTITUTE OF TECHNOLOGY

September 1989

©Massachusetts Institute of Technology, 1989

Signature of Author —

Certified by —

Accepted by —

Justin E. Kerwin
Thesis Supervisor

A. Douglas Carmichael
Chairman, Department Committee on Graduate Studies

MASSACHUSETTS INSTITUTE
OF TECHNOLOGY

NOV 17 1989

LIBRARIES

ARCHIVES

A METHOD FOR THE DESIGN OF A CLASS OF OPTIMUM MARINE PROPULSORS

by

William Bowles Coney

Submitted to the Department of Ocean Engineering in
September of 1989 in partial fulfillment of the requirements
for the degree of Doctor of Philosophy in Naval Architecture

Abstract

A systematic procedure for the design of a class of marine propulsors is presented. This class of propulsors includes traditional propellers, ducted propellers, contrarotating propellers, vane-wheel propulsors and propellers operating with pre or post-swirl stators.

The topic of optimum propulsor load distributions is discussed at some length. An algorithm for the determination of optimum radial distributions of circulation for these devices is presented. This algorithm is incorporated into a vortex-lattice, lifting-line model for lightly to moderately loaded marine propulsors. This computer model also incorporates algorithms for the determination of minimum propeller chord lengths and thicknesses as well as to determine optimum values of propeller RPM and diameter. Parametric studies and comparisons of various propulsor configurations can be carried out with this lifting-line model.

Once a propulsor configuration and radial distributions of circulation, chord, thickness, etc. have been arrived at, existing propeller design and analysis procedures can be used to determine the blade pitch and camber in order to produce the desired circulation. A discussion of how these procedures can be used, or modified, for the design of ducted and multiple stage propulsors is provided.

Several propulsor designs are presented. They include the design of a traditional propeller, a propeller operating behind a nonaxisymmetric stator, and ducted propellers. In each case the design process is described in some detail in order to illustrate the procedures.

Committee:

Professor Justin E. Kerwin (Chairman)

Dr. David V. Burke

Professor Mark Drela

Contents

1	Introduction	12
2	Optimum Circulation Distributions	16
2.1	Introduction	16
2.2	The Wing Problem	18
2.3	The Propeller Problem	22
2.3.1	Propeller Lifting Line Theory	22
2.3.2	The Vortex Lattice Model	24
2.3.3	Variational Optimization	25
2.3.4	Some General Results for the Propeller	28
2.3.5	Torque Limited Propellers	34
2.4	Multiple Stage Propulsors	35
2.4.1	Velocities and Forces	35
2.4.2	The Discretized Model	37
2.4.3	Two Component Optimization	39
2.4.4	Contrarotating Propellers	44
2.4.5	The Vane-Wheel Propulsor	48
2.4.6	Pre and Post Swirl Stators	49
3	Hubs and Ducts	54
3.1	Hub Effects	54
3.1.1	Hub Loaded Optimum Circulation Distributions	54
3.1.2	Hub Drag	59
3.1.3	Hub Vortex Cancellation	60
3.1.4	The Equivalent Propeller	63
3.2	Ducted Propellers	67
3.2.1	Lightly Loaded Ducted Propellers	68
3.2.2	Duct Forces	75
3.2.3	Multiple Stage Ducted Propellers	80

4	Other Considerations	82
4.1	Minimum Chord Lengths	82
4.1.1	Cavitation Constraint	83
4.1.2	Additional Constraints	84
4.1.3	Chord Length Optimization Procedure	84
4.2	Blade Strength and Thickness	85
4.2.1	ABS Rule Calculation	86
4.2.2	Selection of the Thickness Distribution	86
4.2.3	Approximate Stress Calculation	86
4.3	Hub and Tip Unloading	86
4.3.1	Series Representations of Circulation	87
4.4	Effective Wake Calculation	89
4.5	Optimum Operating Conditions	91
4.5.1	Determination of Ship Speed	93
4.6	Non-Axisymmetric Pre-Swirl Stators	93
4.6.1	The Nonaxisymmetric Lifting Line Model	93
4.6.2	Nonaxisymmetric Circulation Distributions	94
4.6.3	Experimental Verification	95
5	Determination of Blade Geometry	97
5.1	Propeller Blade Design	97
5.1.1	Consideration of the Hub	100
5.2	Blade Design for Multiple Stage Propulsors	105
5.2.1	Propeller/Stator Design	106
5.3	Ducted Propeller Design	108
5.3.1	The Ducted Propeller Design Procedure	109
5.3.2	The Neutral Duct	110
5.3.3	The Thrusting Duct	110
6	Illustrative Examples	113
6.1	The Design of a Propeller for a Human Powered Submarine	114
6.1.1	The Submarine Hull and Power Train	114
6.1.2	Preliminary Propeller Design	116
6.1.3	Detailed Propeller Design and Fabrication	119
6.1.4	Postscript	122
6.2	A Comparative Study of Marine Propulsors	125
6.3	Design of a Nonaxisymmetric Pre-swirl Stator	133
6.3.1	A Propeller Design	134
6.3.2	Propeller/Stator Design	134
6.4	Ducted Propeller Designs	145

6.4.1	Zero Gap Case	145
6.4.2	Finite Gap Case	150
7	Concluding Remarks	154
7.1	Future Considerations	154
7.2	Some Final Remarks on Propulsor Design	155
A	Velocity Calculation Algorithms	167
A.1	Self-Induced Velocities	167
A.2	Circumferential Mean Velocities	169
A.3	Asymmetric Stator Velocities	171
A.4	Vortex Ring Velocities	172
B	On the Tip Loaded Optimum	174
C	The Effective Wake Calculation	180
D	Reciprocity for Cosine Spacing	184

CONTENTS

5

6.4.1	Zero Gap Case	145
6.4.2	Finite Gap Case	150
7	Concluding Remarks	154
7.1	Future Considerations	154
7.2	Some Final Remarks on Propulsor Design	155
A	Velocity Calculation Algorithms	167
A.1	Self-Induced Velocities	167
A.2	Circumferential Mean Velocities	169
A.3	Asymmetric Stator Velocities	171
A.4	Vortex Ring Velocities	172
B	On the Tip Loaded Optimum	174
C	The Effective Wake Calculation	180
D	Reciprocity for Cosine Spacing	184

List of Figures

1.1	The propeller design procedure.	13
2.1	Notation for a Vortex Lattice Lifting Line	19
2.2	Propeller lifting line notation.	22
2.3	Combined velocity and force diagram on an expanded cylindrical section of radius r	23
2.4	Optimum circulation distributions at various advance coefficients	29
2.5	Propeller efficiency as a function of advance coefficient	31
2.6	Optimum circulation distributions for free-running and wake adapted pro- pellers	32
2.7	Axial inflow velocities for the wake adapted propeller of the previous figure.	33
2.8	Optimum circulation distributions from torque and thrust limited opti- mization procedures.	35
2.9	Combined velocity and force diagram for one component of a two stage propulsor.	36
2.10	Optimum circulation distributions for a pair of contrarotating propellers.	44
2.11	Tangential velocities induced far downstream by the contrarotating pro- pellers	46
2.12	Axial velocities induced far downstream by the contrarotating propellers.	47
2.13	Optimum circulation distributions for a vane-wheel propulsor.	48
2.14	Optimum circulation distributions for a propeller and pre-swirl stator.	51
2.15	Tangential velocities induced far downstream by propeller/stator combi- nations.	52
3.1	Schematic showing a vortex and its image.	55
3.2	Optimum hub loaded circulation distributions.	56
3.3	Panel method representation of a single vortex horseshoe set on a cylin- drical hub.	57
3.4	Optimum circulation distributions from the image and panel hub repre- sentations.	58
3.5	The Rankine vortex model used to determine the hub drag.	59

3.6	Propeller operating with and without a preswirl stator. The tunnel pressure is lowered in these pictures in order to visualize the hub vortex. . .	62
3.7	Optimum circulation distributions for a pair of hub loaded contrarotating propellers.	63
3.8	Optimum hub loaded circulation distributions for a propeller stator. . . .	64
3.9	Hub loaded circulation distribution and a circulation distribution unloaded through use of an equivalent propeller.	65
3.10	A sketch of a two stage propulsor whose components have different hub diameters.	66
3.11	Optimum circulation distributions for propellers operating inside of cylindrical, "image" ducts.	70
3.12	Panel method representation of the duct and lifting line.	72
3.13	Optimum circulation distributions for a zero gap ducted propeller as determined from image and panel representations of the duct.	73
3.14	Duct interaction velocities at the lifting line.	74
3.15	Schematic of the propeller/duct vortex system.	76
3.16	Efficiency vs. thrust ratio for optimum ducted propellers as determined by the current procedure.	78
3.17	Optimum circulation distributions for a ducted propeller/preswirl stator. .	81
4.1	Illustration of a cavitation "bucket" with the optimum operation point indicated.	83
4.2	Typical chord length distributions.	85
4.3	Sine series terms used for hub and tip unloading.	88
4.4	Hub and tip unloading functions used when the hub is modelled as a solid boundary.	88
4.5	Hub and tip unloading functions used when there is a solid boundary at the blade tip.	89
4.6	A nominal inflow wake and an effective wake from the algorithm implemented in PLL.	90
4.7	Efficiency vs advance coefficient for "optimum" propellers as determined by PLL	92
4.8	Tangential velocities at the plane of the propeller.	95
4.9	Nonaxisymmetric stator operating in the MIT Water Tunnel. Note the flow inclination.	96
5.1	Propeller blade geometry.	98
5.2	Vortex lattice representation of a propeller.	99
5.3	Propeller blade geometry as determined by PBD-10.	100
5.4	PBD-11 hub and blade geometry.	102

5.5	Circulation distributions used for the PBD-10/PBD-11 comparisons. . .	102
5.6	Blade geometries determined by PBD-10 and PBD-11 for the "hubless" circulation distribution.	103
5.7	Blade geometries determined by PBD-10 and PBD-11 for the hub loaded circulation distribution.	104
5.8	Blade geometries determined by PBD-10 and PBD-11 for the hub unloaded circulation distribution.	105
5.9	A vortex lattice representation of a nonaxisymmetric stator.	106
5.10	Ducted propeller with five percent gap between blade tip and duct. . . .	108
5.11	Flowchart presenting an overview of the ducted propeller design procedure	112
6.1	Exterior view of <i>HPS Icarus</i>	114
6.2	The propulsion drive train.	115
6.3	Articulated tail section (top view).	116
6.4	Inflow velocities used for the human powered submarine design.	117
6.5	Circulation distributions for the human powered submarine propeller. . .	121
6.6	Pitch and camber distributions for the human powered submarine. . . .	121
6.7	One-third scale plan view of propeller blade designed for the human powered submarine.	123
6.8	Computer depiction of human powered submarine propeller.	124
6.9	Computer depiction of a vane-wheel propulsor.	125
6.10	Circulation distributions for the baseline propeller.	126
6.11	Vane-wheel circulation distributions.	127
6.12	Circulation distributions for the contrarotating propellers.	129
6.13	Circulation distributions for a propeller/stator.	130
6.14	Computer generated depiction of a propeller operating behind a nonaxisymmetric, pre-swirl stator.	133
6.15	Plan view of the 3-bladed propeller geometry as determined by PLL and PBD-10.	136
6.16	A depiction of the PBD-10 vortex lattice for the 3-bladed propeller. . . .	136
6.17	Optimum circulation distributions as predicted by PLL for propeller/stator.	138
6.18	Plan view of the propeller designed for operation with the pre-swirl stator.	139
6.19	Angular variation in tangential velocity at the plane of the propeller presented at a number of radii.	141
6.20	Radial distribution of maximum variation in propeller advance angle. . .	142
6.21	Depiction of the nonaxisymmetric stator design.	144
6.22	Ducted propeller with zero gap between blade tip and duct.	146
6.23	Circulation distributions at the plane of the propeller with zero gap between duct and propeller.	147
6.24	Propeller blade geometry for the zero-gap design.	148

LIST OF FIGURES

9

6.25	Pressure coefficients on the inner surface of the zero-gap duct.	149
6.26	Chordwise circulation distributions on the propeller blade for the zero gap design.	150
6.27	Propeller circulation for the five percent gap design.	152
6.28	Geometry of five-percent gap propeller inside of the neutral duct.	152
6.29	Geometry of five-percent gap propeller inside of the thrusting duct.	153
B.1	Efficiency as a function of circulation distribution derived from a linear combination of the present results and those of Brockett and Korpus. The wake is aligned using moderately loaded theory.	176
B.2	Efficiency as a function of the circulation distribution as in the previous figure, except that the wake is here constrained to follow the undisturbed inflow.	177

List of Tables

2.1	Forces acting on a pair of contrarotating propellers.	45
2.2	Forces acting on the vane-wheel propulsor.	49
2.3	Forces acting on the propeller/pre-swirl stator.	52
3.1	Forces with and without hub drag.	60
3.2	Forces acting on optimum propellers operating inside of cylindrical "image" ducts.	71
3.3	Total forces acting on two optimum ducted propellers.	80
6.1	Characteristics of the human powered submarine hull.	115
6.2	Preliminary powering estimates.	116
6.3	Preliminary single propeller performance estimates.	118
6.4	Estimated single propeller performance.	120
6.5	Baseline propeller forces.	126
6.6	Vane-wheel propulsor forces.	128
6.7	Performance summary for various propulsor alternatives.	131
6.8	Geometry of propeller designed for 1250 RPM at 23 knots.	135
6.9	Optimum propeller diameter, SHP and efficiency as determined by PLL for propellers with varying number of blades.	135
6.10	Stator blade chord, rake, skew and thickness at radii for input to the computer codes.	137
6.11	Nondimensional rake, skew, chord, camber and thickness as a function of radius for propeller of the propeller/stator pair.	137
6.12	Pitch and camber distributions as determined by the version of PBD-10 modified to include an image representation of the hub.	139
6.13	Pitch and camber distributions for the nonaxisymmetric stator blades as determined by SSF-1	143
6.14	Radial chord and thickness distributions for the zero-gap propeller. . . .	146
6.15	Radial pitch and camber distributions zero-gap propeller.	148
6.16	Total forces acting on the zero-gap propeller/duct.	148
6.17	Radial chord and thickness distributions for the five percent gap propeller. .	151

LIST OF TABLES

11

6.18 Total forces acting on the five percent gap propeller/duct.	153
B.1 Convergence test	175

Chapter 1

Introduction

Typically screw propellers are used to supply the thrust needed to overcome the resistance experienced by a moving ship. Such propellers produce thrust through the production of lift on their rotating blades. In this thesis procedures for the design of a class of propulsion devices, typified by the screw propeller, are described.

The design of marine propellers has traditionally been performed on the basis of systematic series of model experiments. Such procedures have served, and continue to serve [27], propeller designers well for the design of typical ship's screws, but do not readily allow for the investigation of less traditional propulsor alternatives, such as contrarotating or ducted propellers. The use of series data also does not allow the designer to properly tailor the propulsor to the wake and physical arrangement of a particular ship.

Over the past several decades analytical procedures for the design of marine propellers have become well established. These procedures rely on computer models of the propeller. Typically the hydrodynamic design of a propeller is carried out in two steps. First, a lifting line model is used to establish the basic propeller geometry and operating conditions as well as to determine a radial distribution of circulation over the blades that will produce the desired total thrust, subject to considerations of efficiency and cavitation. In the second step the shape of the blade that will produce this desired distribution of circulation is determined.

Figure 1.1 illustrates the propeller design process. The lifting line model of the propeller, in which the blades are considered to be concentrated lines of bound vorticity, is used to estimate propeller forces and determine the radial distribution of circulation. Lifting line theory can also be used to carry out parametric studies in order to determine an optimum propeller design from the point of view of efficiency, cavitation, strength, cost, etc. Much of the propeller geometry can be estimated on the basis of lifting line results.

Lifting line theory alone cannot, however, provide the actual blade geometry which

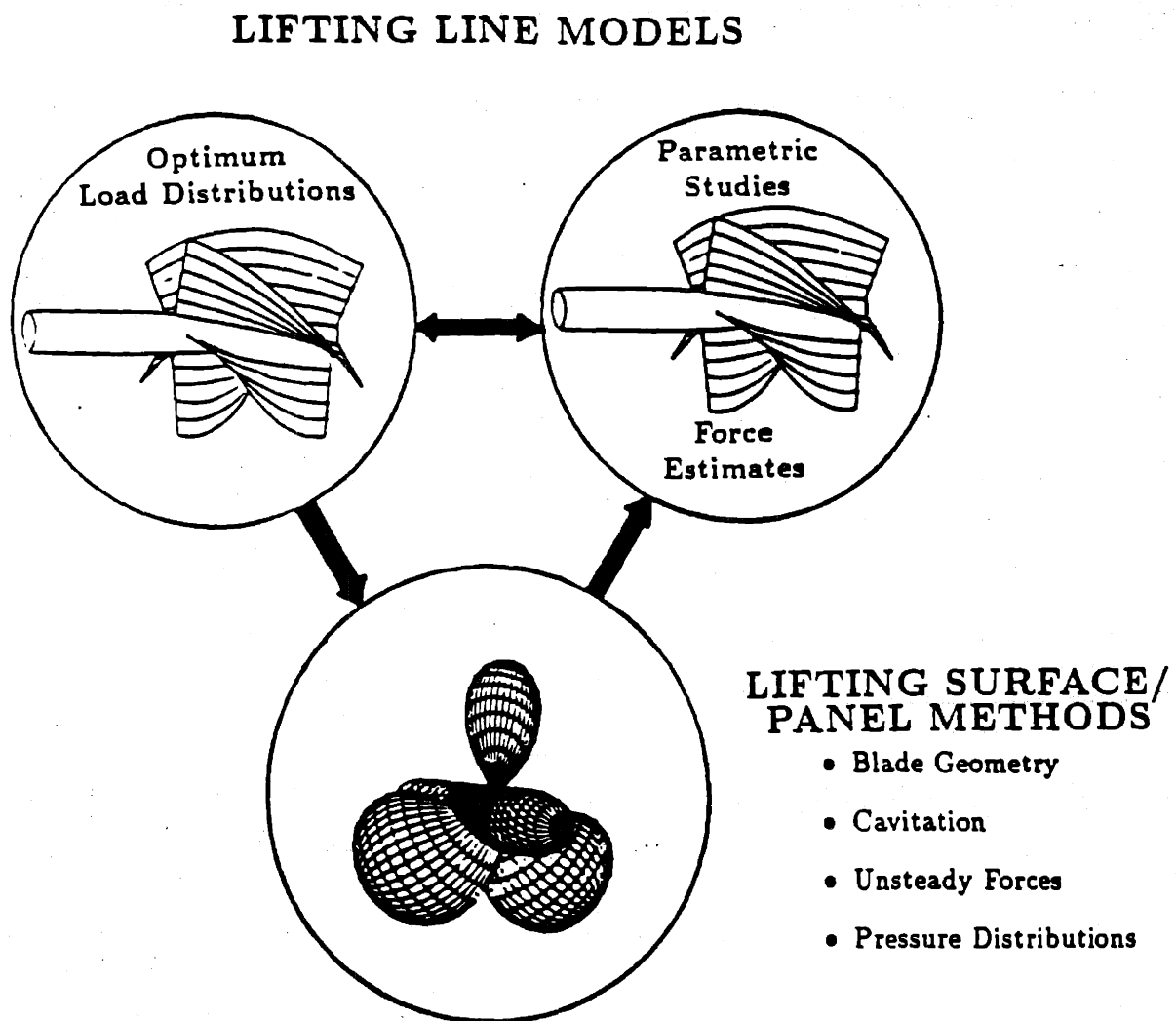


Figure 1.1: The propeller design procedure.

produces the desired circulation distribution. For this purpose more elaborate representations of the propeller are employed. Lifting surface methods, in which the blades are modelled as sheets of singularities, are usually used for this purpose. More sophisticated lifting surface or surface panel representations of the propeller can then be used to analyze the performance of the resulting blade geometry. Consideration of the unsteady forces or cavitation predicted by these methods might then lead back to new design constraints at the lifting line level.

Multiple stage propulsors have been proposed as an alternative to traditional propellers. Much as a wing experiences a drag force as well as lift, not all of the energy input to the propeller is recovered as thrust. Some portion of the energy goes to viscous losses, another is lost to an undesired rotation of the downstream flowfield. The employment of multiple stage propulsors can be used to reduce these rotational losses. The induced losses can further be reduced through the use of ducts or tip fins.

Procedures for the design of these less traditional propulsor alternatives are not so well developed. Design of such propulsors have generally been performed on an ad hoc basis. Multiple stage propulsors have been considered by coupling single propeller codes together in an iterative manner. A number of procedures have been developed for ducted propellers, but few, if any, appear to capture all of the important duct effects. The presence of the propeller shaft or hub is also seldom considered in current design procedures.

It was therefore deemed worthwhile to develop a new lifting line procedure which could handle a wide variety of propulsor configurations in a consistent manner. A description of the theory behind, and the elements of, such a code makes up much of the work presented here. This code, referred to as PLL (*Propulsor Lifting Line*), can handle single propellers, contrarotating propellers, propellers with pre or post-swirl stators, propellers with vane wheels, ringed propellers, ducted propellers and ducted multiple stage propulsors.

Included in the code is an optimization procedure which enables one to determine both the division of loading between propulsor components and the corresponding radial distributions of circulation. PLL also includes a variety of procedures which can be used to assist in the determination of the optimum propeller geometry and operating conditions. In order to be useful for preliminary design purposes and for performance estimates all of the procedures included in the code were required to be computationally efficient. Further, it was required that inputs be kept flexible and outputs comprehensive. The theory employed in the PLL code makes use of a vortex lattice representation of the bound and trailing vortex distributions representing each lifting line. There is no fundamental limit to the complexity of the propulsor which can be analyzed and/or optimized under the framework developed here.

Existing lifting surface design codes can be used to determine the blade geometries of multiple stage propulsors. Interaction velocities between propulsor stages can be predicted through use of the lifting line model. A description of the design process for such propulsors is provided in this work. The importance of modelling the presence of the hub

is also investigated.

In order to illustrate the overall propulsor design process using the tools and procedures described here the design of a propeller for a rather unusual application, a human powered submarine, is presented. The design of this propeller is followed through to the construction of the actual propeller. This design illustrates the importance of a procedure based on hydrodynamic considerations as opposed to the use of series data. The final propeller design looked little like that of a traditional marine propeller, but was predicted to have a propulsive efficiency of over ninety percent.

A comparative study of various propulsor alternatives using the PLL algorithms is also presented. This study illustrates how PLL can be used to evaluate their potential performance. It also provides insight into when, for example, a ducted propeller might be more appropriate than a contrarotating pair of propellers, or a propeller/stator a better choice than a vane-wheel propulsor. The ability to perform such a study using a common set of algorithms to evaluate the various propulsor alternatives is of primary importance if nontraditional propulsors are to be realistically considered.

Nonaxisymmetric pre-swirl stators have been proposed in order to reduce unsteady propulsor forces due to asymmetries in the propeller inflow. PLL includes procedures for the design of such nonaxisymmetric stator/propeller systems. The stator blade geometries which develop prescribed blade circulation distributions can be determined through use of a recently developed lifting surface design procedure. A description of these procedures is provided along with an example of design process for a propeller operating behind a nonaxisymmetric stator.

The design of a ducted propeller provides an additional challenge. In addition to the propeller blade geometry the geometry of the duct must also be determined. In this work a procedure for determining propeller and duct geometries which provide a desired distribution of thrust between duct and propeller and have a specified circulation distribution on the propeller blades is developed. This procedure makes use of existing lifting surface and panel method analysis codes in an iterative manner. Sample ducted propeller designs are presented.

The primary goal of the research described in this thesis has been the development of tools for the propeller designer which make possible the design and, perhaps of equal importance, the realistic performance evaluation of a wide range of marine propulsors.

Chapter 2

Optimum Circulation Distributions

2.1 Introduction

In lifting line theory the propeller blade is replaced by a concentrated line of bound vorticity. The strength of this vorticity is given by the circulation, Γ , developed about the blade. It is assumed that this radial distribution of circulation is related to the actual blade geometry in some predictable manner. It is further assumed that forces developed on this bound vortex system approximate those of the actual propeller.

In this chapter methods for determining optimum circulation distributions for both single and multiple stage propulsors are developed. Optimum distributions discussed here are those for which the energy not expended in the creation of thrust is minimized. Before beginning this development, a brief, historical review of some of the work done on this problem is appropriate.

Betz [4] extended the lifting line theory developed by Prandtl [92] [91] to the case of the propeller. Betz determined a condition for minimum energy loss on the flow downstream of the propeller. The Betz condition considers the geometrical surfaces passed through by the blades of the propeller. Infinitely far downstream of the propeller, these surfaces must, for the optimum propeller, translate as rigid surfaces in the downstream direction. This translation velocity is related to the thrust developed by the propeller.

The Betz condition is the correct, inviscid, linear result for the case of a propeller operating in uniform inflow. Davidson [26] and Sparenberg [99] used the calculus of variations to show that the Betz condition is a general result for this class of lightly loaded propulsors which deliver thrust by means of lift on their blades. Sparenberg [100] also showed that, under linear theory, an upper bound on the efficiency of such a propulsor is given by that of the actuator disc.

The vorticity needed to realize the flow required by Betz condition is the free vorticity of the optimum propeller. The free vorticity uniquely determines the circulation about the lifting lines. Goldstein [40] developed expressions for the potential field of an

infinite helical surface translating with uniform axial velocity. This potential field was in turn used to determine optimum propeller circulation distributions. Goldstein presented laboriously calculated numerical results for the optimum circulation of the two bladed propeller.

Lerbs [73] presented efficient algorithms for the calculation of velocities induced on the propeller lifting lines. Lerbs' algorithms were based on an analytical expression for the velocity potential due to Kawada [54]. Lerbs also derived criteria on the induced velocities for the optimum propeller operating in nonuniform inflow. These criteria were in turn used to numerically determine the optimum propeller circulation distribution for the wake adapted case. Lerbs also originated moderately loaded propeller theory, in which the pitch of the helical trailing vorticity is aligned with the induced velocities.

Yim [123] and Achkinadzhe [2] have extended Lerbs' results to include the effects of viscous and cavity drag through an application of variational calculus. Alternate conditions on the optimum propeller circulation distribution have been proposed by Burrill [11] and van Manen [112].

Brockett and Korpus [9] [8] apply a nonlinear, numerical, constrained optimization approach to various propeller lifting line models in order to find optimum circulation distributions. They also apply this method to the case of a propeller operating behind a set of nonrotating vanes. Similar techniques have been implemented by Chang [16] [17] to determine optimum twist distributions for aircraft propellers. Chang's approach has also been extended to the case of contrarotating propellers [74].

Theodorsen [105] [106] developed a theory for the optimum circulation distribution for contrarotating propellers based on the assumption that an electrical field of uniform resistance obeys the same field equations as an ideal fluid flow. Theodorsen tabulated actual measurements of the electrical field around "helical wakes" constructed of insulating material inserted into a conductive liquid and subjected to an electrical field in the direction of the axis of the helix. These measurements were then used to determine optimum circulation distributions for single and contrarotating propellers.

Van Manen and Sentic [116] designed contrarotating propellers as two independent propellers with corrections on the inflow velocities and the speed of rotation of the aft propeller. These corrections were determined from mutually induced velocities derived from the results of model tests. Van Gunsteren [108] and Honkanen [48] developed analytic and numerical expressions for these correction. A similar technique has been employed by Glover [38]. These approaches ignore the nonlinear dependence of the circulation distribution on the induced velocity, but they only require slight modifications to design methods for single propellers.

Lerbs [72] outlined a lifting line method for predicting the optimum circulation distributions of contrarotating propellers. Lerbs' method for contrarotating propellers was an extension of his method for single propellers [73] with the inclusion of the effects of the mutual interaction velocities. Lerbs' approach treats the interacting propellers in an

iterative manner. Morgan [79], Morgan and Wrench [83] and Caster and LaFone [14] have extended and improved the approach adopted by Lerbs. Reed and Cox [24] described their own advances and provided a review of lifting line theory for contrarotating propellers.

The possibility of using a stage of nonrotating blades to increase propulsive efficiency has long been recognized. Both Glauert [37] and Betz [5] have considered such a possibility. Betz described a procedure for determining circulation distributions for the stator blades under the assumption of light loading and uniform inflow.

In the approach presented here the lifting line model for the propeller is discretized with a vortex lattice. Variational calculus is then applied to the discretized problem. This results in a general procedure for determining optimum circulation distributions. This procedure can be readily extended to increasingly complex combinations of interacting lifting lines.

Equations for optimum load distributions for the wing problem are first presented. This is done in order to illustrate the vortex lattice and optimization procedures for a problem without the added complexity of the propeller's helical vortex system. Optimization equations for a traditional propeller are then derived. The vortex lattice model for multiple stage propulsors is described. Finally optimization equations for two component propulsors are presented.

2.2 The Wing Problem

In this section the optimum circulation distribution will be determined for a straight lifting line, as modelled by a vortex lattice. The solution to this problem will be seen to be identical to that from classical lifting line theory. This discretized representation also provides a general procedure which can be readily expanded to complex combinations of lifting lines. The development given here closely follows that presented by Kerwin [56].

As illustrated in figure 2.1 the span of the lifting line is divided into M equally spaced panels of length Δy . The continuous distribution of circulation over the span is replaced by a stepped distribution which is constant within each panel. The value of the circulation in each panel is set equal to the value of the continuous distribution at the panel midpoints. The location of these control points is denoted by $y_c(n)$ and the corresponding circulation by $\Gamma(n) \equiv \Gamma_n$.

Since the circulation is piecewise constant, the free vortex sheet is replaced by a set of concentrated vortex lines shed from each panel boundary, with strength equal to the difference in bound vortex strength across the boundary. This is equivalent to replacing the continuous vortex distribution with a set of discrete horseshoe vortices, each consisting of a bound vortex segment, and two concentrated tip vortices. The y coordinate of the panel boundaries, which are the coordinates of the free vortices, will

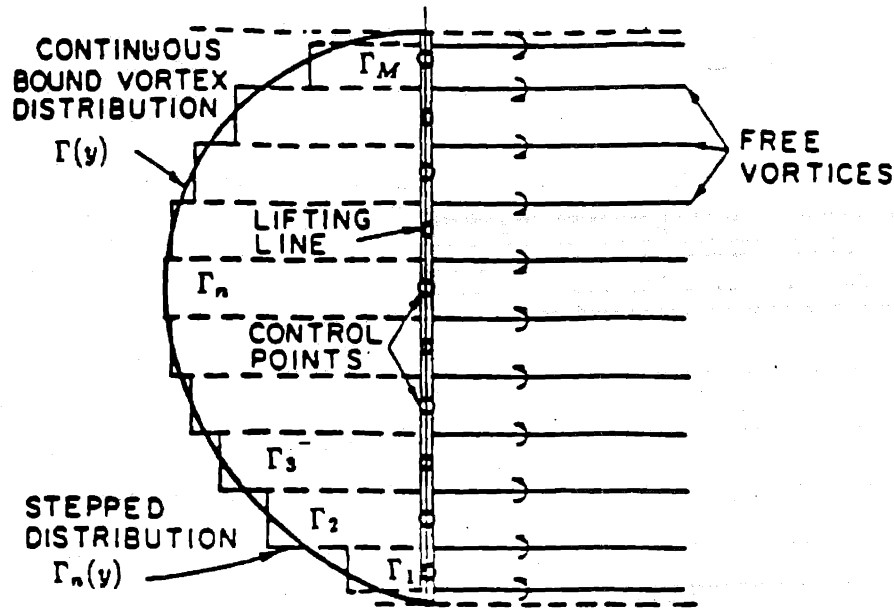


Figure 2.1: Notation for a Vortex Lattice Lifting Line

be denoted by $y_c(n)$. If there are M panels there will be $M + 1$ free vortices.

The velocity field of this discrete set of concentrated vortices can be readily computed at points on the lifting line by an application of the law of Biot and Savart. The velocity induced at a given point is a summation of the velocities induced by the individual vortex horseshoes.

$$w^*(y_c(n)) \equiv w_n^* = \sum_{m=1}^M \Gamma(m) w_{n,m} \quad (2.1)$$

where $w_{n,m}$ is the velocity induced at the control point $y_c(n)$ by a unit horseshoe vortex surrounding the point $y_c(m)$. Since the bound vortex segment of the horseshoe does not induce any velocity on the lifting line itself, the influence function, $w_{n,m}$, consists of the contribution of two semi infinite trailing vortices of opposite sign,

$$w_{n,m} = \frac{1}{4\pi [y_v(m) - y_c(n)]} - \frac{1}{4\pi [y_v(m+1) - y_c(n)]}. \quad (2.2)$$

The lift and induced drag on the lifting line can now be written as sums of the elementary lift and drag forces on each panel, found from a local application of the Kutta-Joukowski law.

$$\vec{F}_z = \rho U \sum_{n=1}^M \Gamma(n) \Delta y. \quad (2.3)$$

$$\vec{F}_x = \rho \sum_{n=1}^M w^*(n) \Gamma(n) \Delta y. \quad (2.4)$$

The goal of the optimization procedure is to find a set of discrete circulation values, $\Gamma_1, \dots, \Gamma_M$, such that the induced drag, \vec{F}_x , is minimized, subject to the constraint that the total lift, \vec{F}_z , has a prescribed value, L_r .

This problem can be solved using the method of the calculus of variations, as described, for example, in Hildebrand [47]. We begin by forming the auxiliary function, H , where

$$H = \vec{F}_x + \lambda(\vec{F}_z - L_r), \quad (2.5)$$

and then find Γ_i and λ such that

$$\frac{\partial H}{\partial \Gamma_i} = 0 \quad \text{for } i = 1, \dots, M; \quad (2.6)$$

$$\frac{\partial H}{\partial \lambda} = 0. \quad (2.7)$$

Equation 2.7 recovers the lift constraint. The Lagrange multiplier, λ , introduces an additional unknown which must be solved for along with the discrete circulation strengths.

Introducing equation 2.1 for w^* and combining equations 2.3, 2.4, 2.6 and 2.7 yield the expressions

$$\frac{\partial H}{\partial \Gamma_i} = 0 = \frac{\partial}{\partial \Gamma_i} \left\{ \rho \sum_{n=1}^M \left[\sum_{m=1}^M \Gamma_m w_{n,m} \right] \Gamma_n \Delta y + \lambda \rho U \sum_{n=1}^M \Gamma_n \Delta y \right\}, \quad (2.8)$$

$$\frac{\partial H}{\partial \lambda} = 0 = \frac{\partial}{\partial \lambda} \{ \dots \}. \quad (2.9)$$

If these differentiations are carried out, bearing in mind that the index of either or both of the sums in equation 2.8 can take on the value i , the following is obtained.

$$\sum_{n=1}^M [w_{i,n} \Delta y + w_{n,i} \Delta y] + \lambda U \Delta y = 0; \quad \text{for } i = 1, \dots, M. \quad (2.10)$$

$$\rho U \sum_{n=1}^M \Gamma_n \Delta y = L_r. \quad (2.11)$$

Equations 2.10 and 2.11 together form a system of $M + 1$ simultaneous equations which can be solved for the discrete values of circulation on each panel. For the constant panel spacing employed in this presentation, equation 2.10 can be considerably simplified if a reciprocity relationship is noted. In the case of constant spacing this relation is

$w_{i,n} = w_{n,i}$. Equation 2.10 then becomes

$$\begin{aligned}\frac{\partial H}{\partial \Gamma_i} &= 2 \sum_{n=1}^M w_{i,n} \Gamma_n + \lambda U = 0 & \text{for } i = 1, \dots, M \\ &= 2w^*(i) + \lambda U = 0 & \text{for } i = 1, \dots, M \\ \Rightarrow w^*(i) &= -\frac{\lambda U}{2}.\end{aligned}\tag{2.12}$$

Thus the downwash, w^* , must be constant over the span for the optimum circulation distribution. The value of the constant is proportional to the Lagrange multiplier, λ , which is set by the required lift. This result of constant downwash can be recovered from classical lifting line theory [92] [91] and corresponds to an elliptical distribution of circulation.

Equation 2.12 is also valid if the inflow velocity, U , is a function of span. This could happen, for example, if the lifting line represented a control surface immersed in the boundary layer of the hull, or a sail operating in a wind gradient. Equation 2.12 then tells us that the induced angle, w^*/U , should be constant. The circulation distribution will not be elliptical, but will be whatever is necessary to generate a downwash proportional to $U(y)$.

Equations 2.10 and 2.11 can readily be made more general. The restriction of constant spacing can be relaxed if suitable locations for control points are determined. For example, cosine spacing may be employed. In this case the vortices and control points are spaced equally in the angular coordinate \tilde{y} .

$$\tilde{y} = \cos^{-1} \left(\frac{-2y}{s} \right), \tag{2.13}$$

where s is the span of the lifting line. For other than constant spacing Δy also becomes a function of radius, $\Delta y = \Delta y(n)$.

For the case of cosine spacing, Kinnas [65] has given a proof for the following reciprocity relationship.

$$w_{i,n} \Delta y(n) = w_{n,i} \Delta y(i). \tag{2.14}$$

A different proof of this relations is presented in appendix D. If this reciprocity relationship is applied to equation 2.10 the result of constant downwash, equation 2.12, is recovered for the cosine spaced vortex lattice. It is expected that this will be the case for any consistent spacing algorithm.

The arrangement of the lifting line can also be made more complicated. Greeley and Cross [42] have presented optimum circulation distributions for lifting line representations of winged sailboat keels and for various arrangements of keels and rudders.

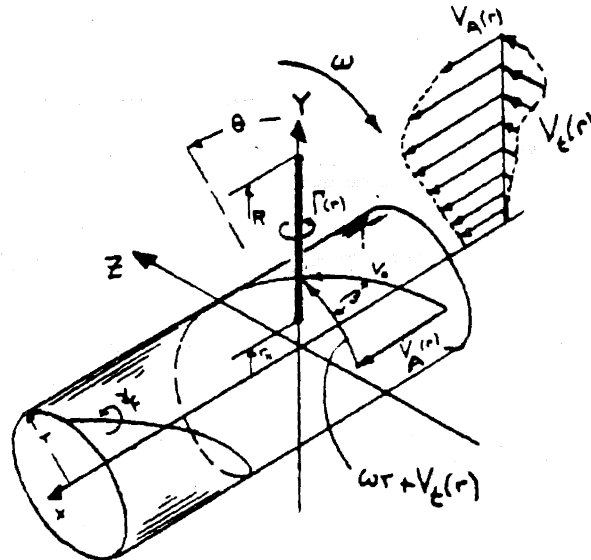


Figure 2.2: Propeller lifting line notation.

2.3 The Propeller Problem

2.3.1 Propeller Lifting Line Theory

The lifting line theory employed here represents the propeller as a set of Z , straight, radial, lifting lines, one for each blade of the propeller. The blades are assumed to have equal angular spacing and identical loading. The geometry (pitch, camber, chord, thickness, etc.) of the physical propeller blade is replaced by a radial distribution of circulation. This circulation, $\Gamma(r)$, is the total strength of the bound vorticity. The lifting lines rotate with angular velocity ω about the x -axis. The lifting lines start at a hub radius, r_h , and extend to the maximum propeller radius, R . The presence of the hub is, for the time being, ignored.

A coordinate system rotating with the propeller is employed, since the flow is unsteady relative to a ship fixed coordinate system. The chosen coordinate system is cylindrical (x, r, θ) , with θ measured clockwise as seen by a viewer facing downstream, the positive x direction. This coordinate system, as well as other notation is illustrated in figure 2.2. The inflow to the propeller is assumed to consist of an effective axial inflow, $V_A(r)$, and an effective tangential inflow, $V_t(r)$. Since we are presently concerned with steady, or time-averaged, propeller forces, these inflows are assumed to vary radially, but not circumferentially.

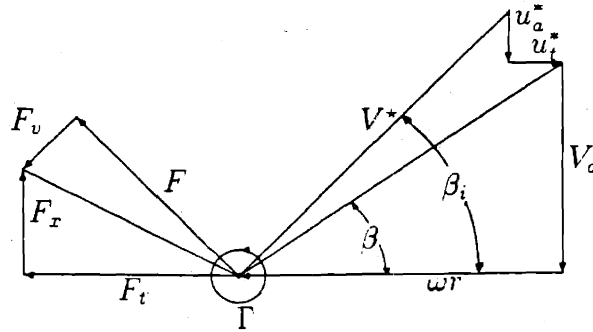


Figure 2.3: Combined velocity and force diagram on an expanded cylindrical section of radius r .

The geometry of the free vortex wake is assumed to be purely helical. Under linear lifting line theory the pitch, $\beta(r)$, of the helices is determined by the propeller's rotation and the undisturbed inflow.

$$\beta(r) = \tan^{-1} \left[\frac{V_a(r)}{\omega r + V_t(r)} \right]. \quad (2.15)$$

Under moderately loaded theory the geometry of the helices is additionally aligned with the induced velocities at the lifting line.

Expressions for the forces acting at radius r on the lifting line can be developed from a local application of Kutta-Joukowski's law. Figure 2.3 shows a combined velocity and force diagram. The axial and tangential induced velocities due to the free vortex system, $u_a^*(r)$ and $u_t^*(r)$, combine with the effective inflow components, $V_a(r)$ and $V_t(r)$, and the propeller rotational speed, ωr , to produce a total velocity V^* oriented at an angle β_i with respect to the plane of rotation.

$$V^*(r) = \sqrt{[V_a(r) + u_a^*(r)]^2 + [\omega r + V_t(r) + u_t^*(r)]^2}; \quad (2.16)$$

$$\beta_i(r) = \tan^{-1} \left[\frac{V_a(r) + u_a^*(r)}{\omega r + V_t(r) + u_t^*(r)} \right]. \quad (2.17)$$

The force per unit radius on the vortex, $F(r)$, is therefore given by

$$F(r) = \rho V^*(r) \Gamma(r), \quad (2.18)$$

and is directed at right angles to V^* .

The effect of viscous drag can be included by adding a force $F_v(r)$ acting in a direction parallel to V^* . This force may be estimated on the basis of an experimentally determined, or theoretically calculated, two-dimensional, sectional, drag coefficient $C_{Dv}(r)$. This means, of course, that the section chord lengths, $c(r)$, must be specified. The viscous drag force will then be

$$F_v(r) = \frac{1}{2} \rho [V^*(r)]^2 c(r) C_{Dv}(r). \quad (2.19)$$

These forces can be resolved into components in the axial and tangential direction, integrated over the radius and summed over the number of blades to produce the total propeller thrust, T , and torque, Q .

$$T = \rho \mathcal{Z} \int_{r_h}^R \left[V^* \Gamma \cos \beta_i - \frac{1}{2} (V^*)^2 c C_{Dv} \sin \beta_i \right] dr; \quad (2.20)$$

$$Q = \rho \mathcal{Z} \int_{r_h}^R \left[V^* \Gamma \sin \beta_i + \frac{1}{2} (V^*)^2 c C_{Dv} \cos \beta_i \right] r dr. \quad (2.21)$$

Note that $V^* \cos \beta_i$ is simply the total tangential velocity acting at the lifting line, $(V_t + \omega r + u_i^*)$, and that $V^* \sin \beta_i$ is the axial velocity, $(V_a + u_a^*)$.

2.3.2 The Vortex Lattice Model

The continuous distribution of vorticity along the lifting line is discretized by a lattice of vortex elements of constant strength. The element arrangement in the present work employs constant spacing. This is done in order to facilitate the alignment of the discretized vortex sheets when more complicated propulsor geometries are examined. As shown by Kerwin and Lee [63], this is not quite as accurate as "cosine" spacing, but the difference is extremely small. As shown by James [53], the panels at the endpoints must be inset one-quarter interval in order to properly represent the square root singularity in trailing vortex strength. The induced velocity is calculated at control points located at the mid-radius of each panel. The location of these control points is denoted by $r(n)$.

Thus the radius of each of the \mathcal{Z} lifting lines is divided up into M panels of length Δr . As was the case for the wing, the continuous distribution of circulation over the radius is replaced by a stepped distribution. The value of the circulation in each panel, $\Gamma(n)$, is set equal to the value of the continuous distribution at the control points. Since the circulation is piecewise constant, the helical free vortex sheet is replaced by a set of concentrated, helical, vortex lines shed from each panel boundary. The strength of these trailing vortices is equal to the difference in bound vortex strength across the boundary. Therefore we can again consider the continuous vortex distribution to be replaced by a set of vortex horseshoes. Each of these horseshoes consists of a bound vortex segment and two helical trailing vortices.

The velocity induced at the lifting line by this system of vorticity is computed using the very efficient asymptotic formulas developed by Wrench [122]. These formulas are reproduced in appendix A. The velocity induced at a given point is a summation of the velocities induced by the individual vortex horseshoes.

$$u_a^*(r(n)) \equiv u_a^*(n) = \sum_{m=1}^M \Gamma(m) \bar{u}_a^*(n, m). \quad (2.22)$$

$$u_t^*(r(n)) \equiv u_t^*(n) = \sum_{m=1}^M \Gamma(m) \bar{u}_t^*(n, m). \quad (2.23)$$

u_a^* and u_t^* are the axial and tangential components of induced velocity. $\bar{u}_a^*(n, m)$ and $\bar{u}_t^*(n, m)$ are the axial and tangential components of velocity induced at the control point at radius $r(n)$ by a unit, helical, horseshoe vortex surrounding the control point at $r(m)$.

Under this discrete model the integrations of equation 2.20 and 2.21 for the forces are replaced by summations over the number of panels. The total forces acting on the propeller can therefore be expressed as

$$T = \rho Z \sum_{m=1}^M \left\{ [V_t(m) + \omega r(m) + u_t^*(m)] \Gamma(m) \Delta r - \frac{1}{2} V^*(m) [V_a(m) + u_a^*(m)] c(m) C_{Dv}(m) \Delta r \right\}; \quad (2.24)$$

$$Q = \rho Z \sum_{m=1}^M \left\{ [V_a(m) + u_a^*(m)] \Gamma(m) r(m) \Delta r + \frac{1}{2} V^*(m) [V_t(m) + \omega r(m) + u_t^*(m)] c(m) C_{Dv}(m) r(m) \Delta r \right\}. \quad (2.25)$$

Here $V^*(m)$ is the magnitude of the total velocity at the control point located at radius $r(m)$. $c(m)$ is the chord at this control point and $C_{Dv}(m)$ is the value of the two-dimensional sectional drag coefficient there.

2.3.3 Variational Optimization

In section 2.2 we used a variational approach to determine the optimum circulation distribution for a simple lifting line. In a similar manner an optimum propeller circulation distribution can be determined. As was the case for the planar hydrofoil, the problem can be formulated for the discretized vortex lattice representation of the propeller. This will provide a general procedure which can then be extended to more complicated problems, such as contrarotating propellers.

For the time being the wake geometry is assumed to be frozen and the viscous force is ignored. The goal of the optimization procedure is to find a set of discrete circulation values, $\Gamma(1), \dots, \Gamma(M)$, such that the torque,

$$Q = \rho \mathcal{Z} \sum_{m=1}^M [V_a(m) + u_a^*(m)] r(m) \Gamma(m) \Delta r, \quad (2.26)$$

is minimized, subject to the constraint that the thrust,

$$T = \rho \mathcal{Z} \sum_{m=1}^M [V_t(m) + \omega r(m) + u_t^*(m)] \Gamma(m) \Delta r, \quad (2.27)$$

has a prescribed value, T_r .

As in the simple lifting line case, we form an auxiliary function, H , and set its partial derivatives with respect to the unknowns equal to zero. Here $H = Q + \lambda(T - T_r)$. The Lagrange multiplier, λ , introduces an additional unknown and must be solved for along with the discrete circulation strengths, the $\Gamma(i)$'s.

$$\frac{\partial H}{\partial \Gamma(i)} = 0 \quad \text{for } i = 1, \dots, M \quad (2.28)$$

$$\frac{\partial H}{\partial \lambda} = 0. \quad (2.29)$$

Combining equations 2.28 and 2.29, with expansions for the thrust and torque, 2.26, and 2.27, and the velocity expansions, 2.22 and 2.23, and after carefully carrying out the partial differentiations, the following system of equations is obtained:

$$\begin{aligned} \frac{\partial H}{\partial \Gamma(i)} = 0 &= V_a(i) r(i) \Delta r \\ &+ \sum_{m=1}^M [\Gamma(m) \bar{u}_a^*(i, m) r(m) \Delta r + \Gamma(m) \bar{u}_a^*(m, i) r(i) \Delta r] \\ &+ \lambda [V_t(i) + \omega r(i)] \Delta r \\ &+ \lambda \sum_{m=1}^M [\Gamma(m) \bar{u}_t^*(i, m) \Delta r + \Gamma(m) \bar{u}_t^*(m, i) \Delta r], \\ &\text{for } i = 1, \dots, M; \end{aligned} \quad (2.30)$$

$$T_r = \rho \mathcal{Z} \sum_{m=1}^M \left[V_t(m) + \omega r(m) + \sum_{n=1}^M \Gamma_n \bar{u}_t^*(m, n) \right] \Gamma(m) \Delta r. \quad (2.31)$$

Equations 2.30 and 2.31 form a nonlinear system of $M + 1$ equations with M unknown values of circulation, and an unknown Lagrange multiplier, λ . This system can

be replaced with a linear system of equations, if the Lagrange multiplier is assumed to be known in equation 2.30 where it forms quadratic terms with the circulations, and the tangential induced velocity in equation 2.31 is also assumed to be known.

$$\begin{aligned}
 \frac{\partial H}{\partial \Gamma(i)} = 0 = & V_a(i)r(i)\Delta r \\
 & + \sum_{m=1}^M [\Gamma(m)\bar{u}_a^*(i,m)r(m)\Delta r + \Gamma(m)\bar{u}_a^*(m,i)r(i)\Delta r] \\
 & + \lambda [V_t(i) + \omega r(i)] \Delta r \\
 & + \tilde{\lambda} \sum_{m=1}^M [\Gamma(m)\bar{u}_t^*(i,m)\Delta r + \Gamma(m)\bar{u}_t^*(m,i)\Delta r], \\
 \text{for } i = 1, \dots, M; & \quad (2.32)
 \end{aligned}$$

$$T_r = \rho \mathcal{Z} \sum_{m=1}^M [V_t(m) + \omega r(m) + u_t^*(m)] \Gamma(m) \Delta r. \quad (2.33)$$

The solution to the nonlinear system of equations 2.30 and 2.31 can be found by iteratively solving the linear system of equations 2.32 and 2.33. On each iteration the frozen Lagrange multiplier, $\tilde{\lambda}$, in equation 2.32 and the tangential induced velocity, $u_t^*(m)$, in equation 2.33 take on values from the previous iteration. In most instances this procedure was found to converge quite rapidly (5 or 6 iterations) to a solution of the nonlinear system. Initially setting the induced velocities equal to zero and the Lagrange multiplier equal to -1 proved to be a suitable initial estimate of these quantities.

This iterative process can also be used to partially account for the effect of viscous drag. On each iteration, the required thrust in equation 2.33 can have an additional thrust equal to the viscous term of equation 2.24 added to it.

$$\begin{aligned}
 T_r = & \rho \mathcal{Z} \sum_{m=1}^M [V_t(m) + \omega r(m) + u_t^*(m)] - T_{\text{viscous}} \\
 = & \rho \mathcal{Z} \sum_{m=1}^M [V_t(m) + \omega r(m) + u_t^*(m)] \\
 & + \frac{1}{2} \rho \mathcal{Z} \sum_{m=1}^M V^*(m) [V_a(m) + u_a^*(m)] c(m) C_{Dv}(m) \Delta r. \quad (2.34)
 \end{aligned}$$

Equation 2.34 ignores the partial derivatives of the viscous terms with respect to the unknown circulations, but does recover the desired total thrust.

Under moderately loaded lifting line theory, the induced velocities are used in the determination of the wake geometry. However, during the circulation optimization procedure the wake is frozen. Since the velocity influence functions, $\bar{u}_a^*(m,n)$ and $\bar{u}_t^*(m,n)$,

are themselves functions only of geometry, they are fixed throughout the procedure. Therefore, the nonlinear variations of these quantities with respect to changes in the wake geometry are neglected. This avoids the tip-loaded optimum solutions presented by Brockett and Korpus [9] [8] and Loukakis [75]. This matter was discussed at some length by Kerwin, Coney and Hsin [60]. Their arguments are reproduced in appendix B.

Velocities and forces consistent with moderately loaded lifting line theory can be obtained, however, by an iterative approach. An optimum circulation distribution is obtained with a frozen wake geometry. The wake is then aligned with the velocities induced by this circulation distribution. A new optimum circulation distribution is determined, ..., and so on, until convergence. This approach still neglects variations with respect to changes in the wake geometry inside of the circulation optimization, but does provide wake aligned velocities and forces. This is especially important when the propeller is required to produce relatively large amounts of thrust or is operating at small advance ratios.

The convergence of the solution with the number of vortex panels is also addressed in appendix B. Converged values for both forces and circulation distributions are generally obtained with a relatively small number of panels. For most purposes a 10 panel solution is sufficient. Unless otherwise noted, numerical results presented in this thesis are for 10 panel solutions, $M = 10$.

The optimization equations 2.30 and 2.31 are not dependent on the assumption of constant spacing. Any spacing algorithm which produces correct values of the induced velocities may be employed. Both constant and cosine spacing have been implemented with satisfactory results. If the spacing is not constant the length of the vortex panels, Δr , is also a function of radius, $\Delta r = \Delta r(n)$.

Equations 2.30 and 2.31 are also somewhat more general than previously indicated. Any algorithm for determining the velocity influence functions, $\bar{u}_a^*(m, n)$ and $\bar{u}_t^*(m, n)$, may be employed. The assumption that the trailing vortices follow helices of constant radius allows for very fast computation of these induction factors. The wake geometry can be allowed to contract and roll up if such a calculation is desired. The wake geometry must, however, be frozen during the solution of the nonlinear system in order to avoid the tip loaded solutions discussed in appendix B.

2.3.4 Some General Results for the Propeller

Figure 2.4 shows some typical optimum circulation distributions for a free-running ($V_a(r) = V_\infty = \text{constant}$), hubless propeller. In this case viscous effects are ignored and the lightly loaded model is employed (the wake is aligned to the undisturbed inflow). Note that the circulation falls off to zero at both the hub and tip radius. In this respect the optimum propeller circulation distribution is similar to the elliptical optimum distribution of the planar hydrofoil.

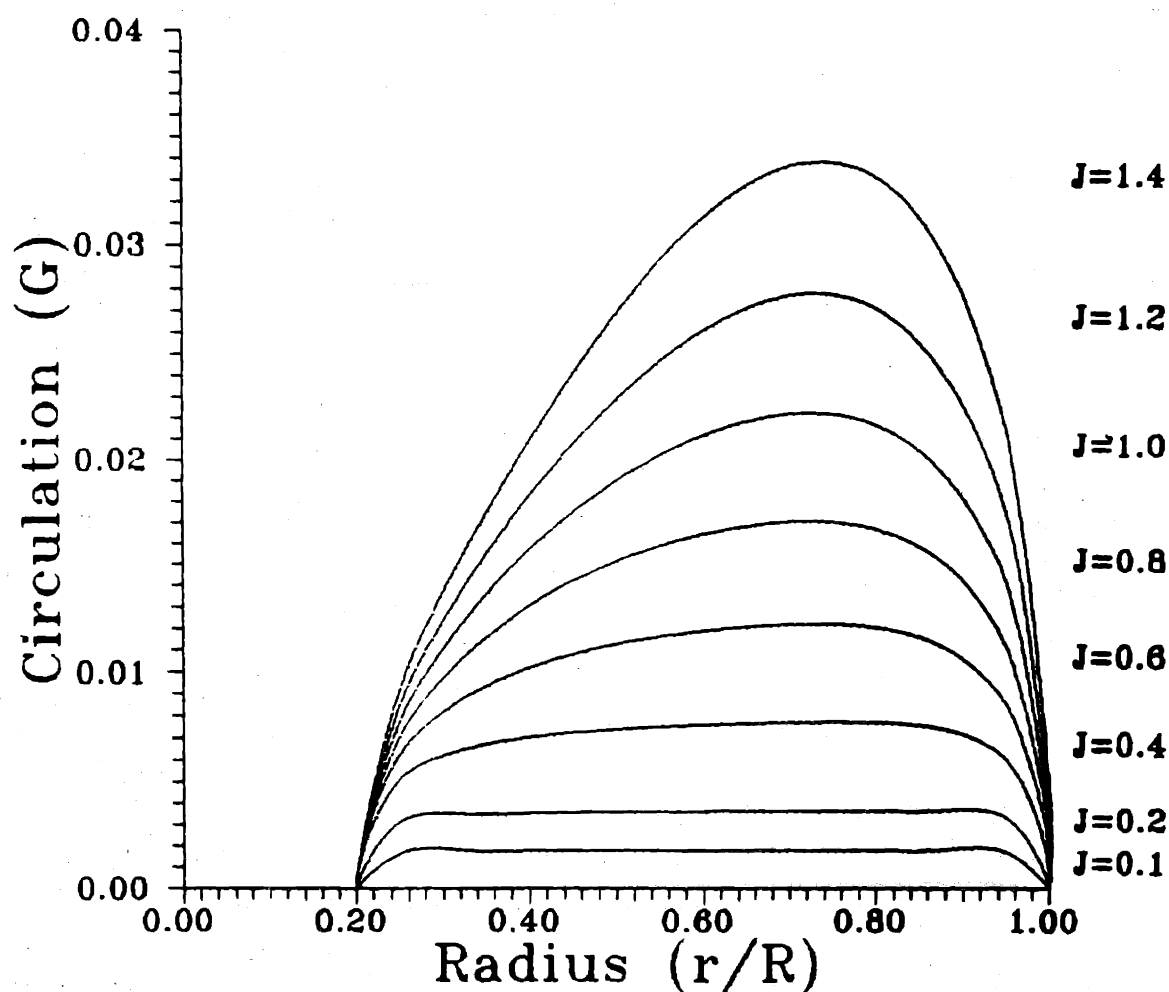


Figure 2.4: Optimum radial circulation distributions for a free-running, hubless propeller for varying values of $J_S = V_S/nD$. Each circulation distribution was required to generate the same value of $C_T = 2T/(\rho V_S^2 A_0) = 0.512$. Viscous effects are ignored. The propeller is 5 bladed with a hub diameter 20% that of the propeller diameter.

Some physical insight into optimum load distributions can be obtained by noting how the distributions vary with the advance coefficient,

$$J_S = \frac{V_S}{nD}, \quad (2.35)$$

where n is the propeller rotation rate in revolutions per second. Each of the curves of figure 2.4 are optimum distributions for propellers operating at various advance coefficients, but each is required to generate the same thrust.

For a fixed ship speed, V_S , and propeller diameter, D , the rotational velocity increases with decreasing advance coefficient. The thrust developed by the propeller is related to the product of the total tangential velocity and the circulation as can be seen in equation 2.27. Thus, the innermost curve of figure 2.4, the one with the smallest values of circulation, corresponds to the lowest value of J_S and, therefore, the largest tangential inflow velocities. As J_S increases the loading must increase in order to produce the same thrust.

As J_S increases the load also moves out toward the propeller's tip. It can be seen in equation 2.26 that the torque is a function of circulation and the axial velocity, with a weighting from the moment arm, r . For larger J_S the relative magnitude of the axial velocity is increased. Thus, a larger "penalty" is paid for added circulation. Since more thrust is available to an increment of circulation placed at the outer radii, where the tangential velocity is high, the distribution becomes more tip loaded. For each propeller operating condition a balance between the prescribed thrust and minimum torque results in the optimum load distribution.

Figure 2.5 gives propeller efficiency as a function of advance coefficient for a free-running propeller. Here the propeller's efficiency, η , is defined as

$$\eta = \frac{TV_A}{\omega Q}, \quad (2.36)$$

where V_A is the volumetric mean effective inflow,

$$V_A = \frac{2}{(R^2 - r_h^2)} \int_{r_h}^R r V_a(r) dr. \quad (2.37)$$

One curve of figure 2.5 gives inviscid results that correspond to the circulation distributions of figure 2.4. The lower curve gives results for a propeller generating the same total thrust with typical drag coefficients and chord distributions assumed. Note that in the inviscid case the efficiency increases as J_S is lowered.

At zero J_S the propeller has infinite rotational velocity and the identity of the individual blades is lost. In this limit the propeller has become an *actuator disc*. A brief description of actuator disc theory can be found in *Principles of Naval Architecture* [21].

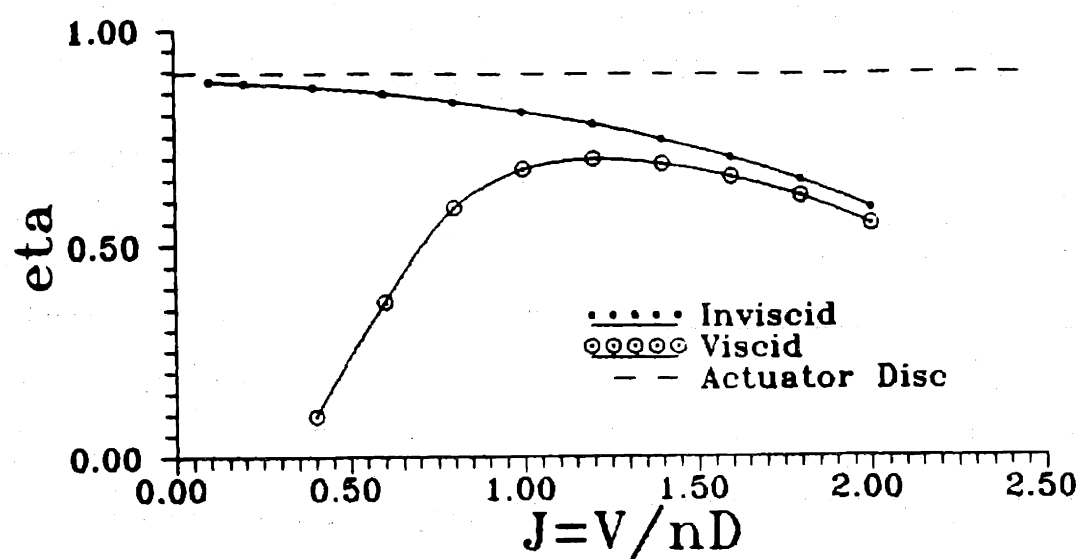


Figure 2.5: Propeller efficiency as a function of advance coefficient for a 5 bladed, free-running propeller. The thrust coefficient is held to a constant value of $C_T = 0.512$. Curves are given for an inviscid case and for a case with typical values of chord and drag coefficient.

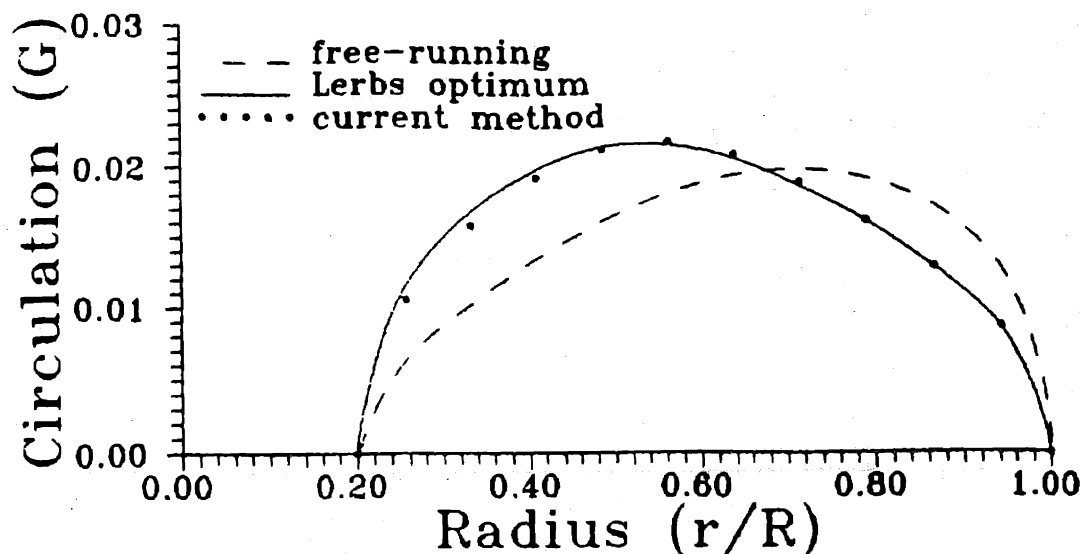


Figure 2.6: Optimum circulation distributions for a free-running and a wake adapted propeller. In both cases $C_T = 0.307$ and $J_S = 1.377$. The propellers are 5 bladed. Moderately loaded lifting line theory was used for these predictions.

For an actuator disc the optimum load distribution is a constant across the span, and the efficiency is given by

$$\eta_i = \frac{2}{1 + \sqrt{C_T + 1}}. \quad (2.38)$$

In figure 2.5 the inviscid efficiency appears to be headed to the actuator disc efficiency of $\eta_i = 0.9$ as the advance coefficient is decreased. Referring back to figure 2.4, the optimum circulation distribution becomes more nearly constant and, thus, more like that of the actuator disc, as J_S is reduced.

However, it is clear from figure 2.5 that viscous drag takes its largest toll at low J_S . This is because the relatively large rotational velocities, ωr , lead to large total velocities, V^* , and thus to larger values for drag. Note that the viscous losses can easily account for 50% or more of the total losses. Finally, note in figure 2.5 that when viscous losses are included in the efficiency, there is some optimum value of the advance coefficient where the efficiency is highest, even though the efficiency curve is relatively flat.

The effect of the axial inflow on the optimum circulation distribution can be seen in figure 2.6. Results for a free-running propeller and a propeller operating in a radially varying wake are presented. Both propellers have the same number of blades, are operating at identical J_S , and are required to develop the same thrust. In the case of the "wake adapted" propeller, the axial inflow velocities are lower at the inner propeller

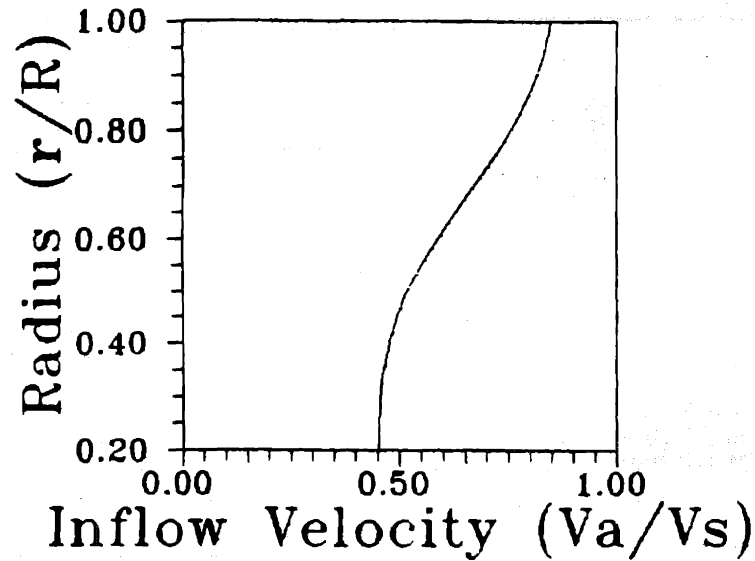


Figure 2.7: Axial inflow velocities for the wake adapted propeller of the previous figure.

radii than at the propeller's tip. The effective inflow is shown in figure 2.7. The reduced axial velocities at the inner propeller radii result in an inward shift of the optimum load distribution. More circulation is placed where the axial velocities are lower, and thus a smaller torque penalty is paid.

The circulation distributions of figure 2.6 were determined under moderately loaded lifting line theory. This was done using the previously described iterative procedure. An optimum circulation distribution was found from equations 2.30 and 2.31 with a frozen wake geometry. The wake geometry was then aligned with the velocities induced by this circulation distribution. A new optimum distribution was determined, and so on, until a converged circulation distribution is obtained.

A similar process was carried out using Lerbs' method [73] for the wake adapted case. The circulation distribution so obtained is also shown in figure 2.6. The Lerbs optimum distribution is very nearly the same as that from the variational procedure. As the propeller's load is decreased the two distributions become more nearly the same. The difference in the optimum distribution determined from the two procedures may be attributed to a linearizing assumption made in the derivation of the Lerbs optimum criteria, as well as to differences in the numerical implementation of the two procedures. In the limit of light loading both methods recover the classic Betz condition [4] in the case of a free-running propeller.

2.3.5 Torque Limited Propellers

The optimization equations 2.30 and 2.31 solve for minimum torque and a prescribed thrust. This is the appropriate problem if the ship's operating condition has been determined, but the powering has not yet been fixed. If the torque is known, and the thrust is to be maximized, it is a simple matter to reformulate the optimization equations.

In this case the auxiliary function to be minimized is $H = T + \lambda(Q - Q_r)$. Expanding H with equations 2.27, 2.26, 2.22, 2.23, taking partial derivatives with respect to the unknowns, and setting these derivatives equal to zero, results in the following system of equations.

$$\begin{aligned} \frac{\partial H}{\partial \Gamma(i)} = 0 &= \lambda V_a(i) r(i) \Delta r \\ &+ \lambda \sum_{m=1}^M [\Gamma(m) \bar{u}_a^*(i, m) r(m) \Delta r + \Gamma(m) \bar{u}_a^*(m, i) r(i) \Delta r] \\ &+ [V_t(i) + \omega r(i)] \Delta r \\ &+ \sum_{m=1}^M [\Gamma(m) \bar{u}_t^*(i, m) \Delta r + \Gamma(m) \bar{u}_t^*(m, i) \Delta r], \\ \text{for } i &= 1, \dots, M; \end{aligned} \quad (2.39)$$

$$Q_r = \rho \mathcal{Z} \sum_{m=1}^M \left[V_a(m) + \sum_{n=1}^M \Gamma(n) \bar{u}_a^*(m, n) \right] \Gamma(m) \Delta r. \quad (2.40)$$

Equations 2.39 and 2.40 form a nonlinear system of $M+1$ equations with M unknown values of circulation and an unknown Lagrange multiplier, λ . These equations can be linearized in the same manner that equations 2.30 and 2.31 were linearized. The nonlinear system of equations 2.39 and 2.40 can be solved by iteratively solving the linearized equations and updating the frozen variables, the Lagrange multiplier where it forms a product with unknown circulations in equation 2.39 and the axial induced velocities in equation 2.40.

A sample result from this procedure is shown in figure 2.8. Also shown is an optimum distribution determined from equations 2.30 and 2.31, in which the thrust was required to be the same as that produced by the torque limited procedure. For propellers at identical operating conditions, providing the same thrust and torque, the optimum circulation distributions from the two optimization procedures are, as expected, identical.

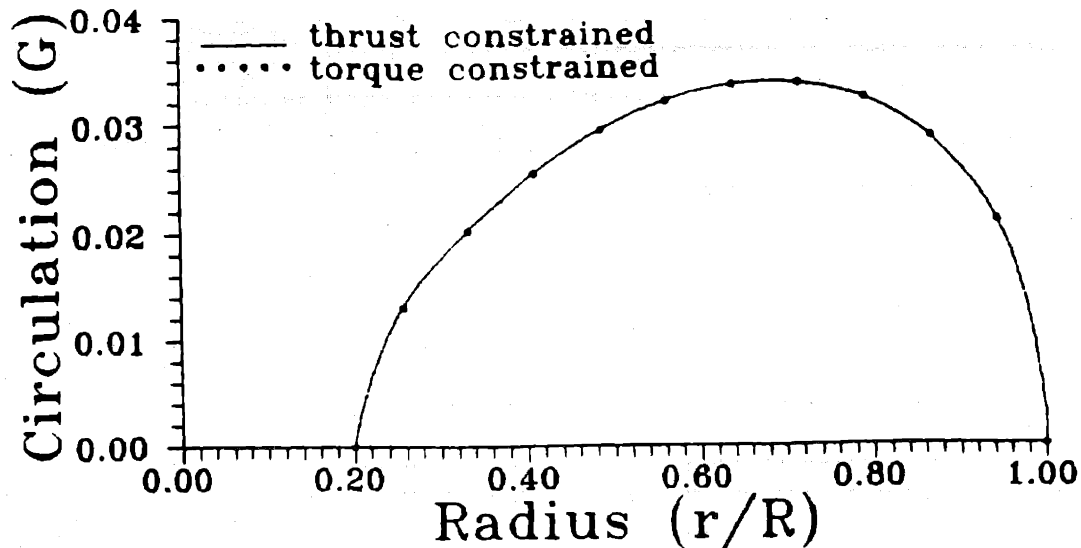


Figure 2.8: Optimum circulation distributions from torque and thrust limited optimization procedures.

2.4 Multiple Stage Propulsors

2.4.1 Velocities and Forces

For a multiple stage propulsor, not only must the self-induced velocity be calculated, but also the interaction velocities between components. Here the self-induced velocity is defined as the velocity induced by a set of lifting lines, lying in a plane at one axial location, on these same lifting lines. Calculation methods appropriate for a single propeller can be used to determine this velocity. For straight, radial, lifting lines, that have equal angular spacing and identical loading, the self-induced velocity will come only from the trailing vortex sheet. For a purely helical wake geometry, the asymptotic formulas developed by Wrench [122] can be used for the computation of this velocity.

The interaction velocity is the velocity induced at the plane of one of the propulsor components by the lifting lines at the plane of another propulsor component. For the determination of steady propulsor forces the time-averaged interaction velocities are those of interest. If the components are rotating at different speeds, these time-averaged velocities are equivalent to the circumferential mean interaction velocities calculated in the rotating reference frame of the inducing component.

The interaction velocities come from both the bound and trailing vorticity. Using

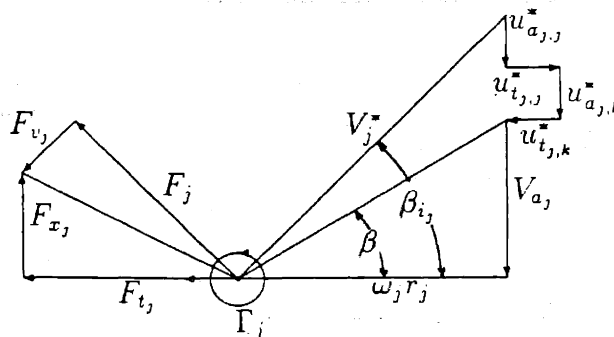


Figure 2.9: Combined velocity and force diagram for one component of a two stage propulsor.

either a simple geometrical relationship, or by a formal application of Biot-Savart's law, one can show that the circumferential mean interaction velocity induced by the bound vorticity has only a tangential component. Thus, the circumferential mean interaction velocity consists of axial, radial and tangential components induced by the trailing vorticity, and a tangential component induced by the bound vorticity.

Hsin [51] compared a number of methods for the computation of the circumferential mean interaction velocity. He found the formulas developed by Hough and Ordway [49] to be the most computationally efficient for the part due to the trailing vorticity. The circumferential mean velocity due to the bound vorticity can be found directly through an application of Kelvin's theorem. Formulas used for the calculation of these velocity components are presented in appendix A.

If the propulsor components are rotating in lockstep together, as is the case for tandem propellers, the time-averaged interaction velocity is no longer the circumferential mean. In this case the relative positions of the trailing vorticity and the field points do not change with time. Here, the velocity induced by the bound and trailing vortex lines can be found by numerical integration of the Biot-Savart velocity integral. This process is much less computationally efficient than that used for the self-induced and circumferential mean velocities. For approximate tandem propeller force calculations, it may be appropriate to replace the actual interaction velocity with the circumferential mean velocity induced at the same axial plane.

Forces acting on the lifting lines are again developed from a local application of the Kutta-Joukowski law. Now, however, the total velocity includes contributions from both the self-induced and interaction velocities. A combined velocity and force diagram for

one component of a two stage propulsor is given in figure 2.9. The axial and tangential components of induced velocity on propulsor component j are given by

$$u_{a_j}^*(r) = \sum_{k=1}^K u_{a_{j,k}}(r), \quad (2.41)$$

$$u_{t_j}^*(r) = \sum_{k=1}^K u_{t_{j,k}}(r). \quad (2.42)$$

Here there are K propulsor components. $u_{a_{j,k}}$ and $u_{t_{j,k}}$ are the axial and tangential components of the self-induced velocity whenever $j = k$, otherwise they are the interaction velocities. The thrust and torque acting on each component can again be found from the integrals of equations 2.20 and 2.21.

2.4.2 The Discretized Model

The lifting lines of each propulsor component are discretized by a lattice of constant strength vortex elements. One of the propulsor components, denoted by the subscript "1", is selected as the key component. The span of each of the \mathcal{Z}_1 lifting lines, which represent the blades of the key component, is divided up into M_1 panels of length Δr_1 . The lifting lines of each of the other components are then segmented into an integer number of panels, M_j , of length Δr_j . M_j is selected so that Δr_j is as nearly equal to Δr_1 as possible. In order to simplify this panel arrangement, the radius of the hub, r_h , is assumed to be the same for all components. As for the single propeller, converged results are obtained with a relatively small number of panels. Unless otherwise noted all numerical examples in this thesis are for $M_1 = 10$.

The continuous distribution of circulation on each component, $\Gamma_j(r)$, is replaced by a stepped distribution, $\Gamma_j(n)$. Thus, the continuous vortex distributions are replaced by sets of vortex horseshoes, each made up of a bound vortex segment and two helical trailing vortices. The radii of the helical trailing vortices are slightly adjusted whenever interaction velocities are needed. The helices are moved so that they correspond with the radii of the vortex lattice of the component on which the velocity is being induced. This results in a consistent vortex lattice system for the computation of the interaction velocity.

Moderately loaded lifting line theory gives reasonable results for velocities induced at, or upstream of, the plane of the lifting lines. However, the accuracy of velocity predictions downstream of the propeller is not as good. This is, to a great extent, due to the contraction of the slip stream, which is not modelled by a purely helical wake. This wake contraction is due both to considerations of mass flow conservation and to the rolling up of the tip vortices. Since the actual wake contraction occurs over a short distance,

compared to the propeller diameter, a better approximation to the wake geometry is to again model it as purely helical, but contracted to some new radius.

An empirical slipstream contraction ratio, the radius of the contracted wake divided by the radius of the propeller, can be employed. Water tunnel measurements of slipstream radii indicate that the contraction ratio is close to 0.83 for a wide variety of propeller types, over a reasonable range of advance coefficients [63]. If a wake contraction is employed, the radii of the trailing vortex helices, used for the computation of downstream interaction velocities, are moved to be as close as possible to the desired contracted radii. The self-induced velocity and the velocities induced on upstream components are computed from the uncontracted helices.

The velocity induced on a given control point is a summation of the velocities induced by the individual horseshoe vortices.

$$u_{a,j}^*(n) = \sum_{k=1}^K \sum_{m=1}^M \Gamma_k(m) \bar{u}_{a,j,k}^*(n, m), \quad (2.43)$$

$$u_{t,j}^*(n) = \sum_{k=1}^K \sum_{m=1}^M \Gamma_k(m) \bar{u}_{t,j,k}^*(n, m). \quad (2.44)$$

$\bar{u}_{a,j,k}^*(n, m)$ is the axial velocity induced at control point n of component j by the horseshoe vortex of unit strength surrounding control point m of component k . $\bar{u}_{t,j,k}^*(n, m)$ is similarly the tangential velocity. $\Gamma_k(m)$ is the strength of the horseshoe surrounding control point m of component k .

The force acting on each propulsor component is the sum of the forces acting on the individual vortex elements. The inviscid thrust and torque acting on a propulsor component can be expressed as:

$$T_{I,j} = \rho Z_j \sum_{n=1}^{M_j} [V_{t,j}(n) + \omega_j r_j(n) + u_{t,j}^*(n)] \Gamma_j(n) \Delta r_j, \quad (2.45)$$

$$Q_{I,j} = \rho Z_j \sum_{n=1}^{M_j} [V_{a,j}(n) + u_{a,j}^*(n)] r_j(n) \Gamma_j(n) \Delta r_j. \quad (2.46)$$

The viscous thrust and torque is similarly found to be:

$$T_{V,j} = -\frac{1}{2} \rho Z_j \sum_{n=1}^{M_j} V_j^*(n) [V_{a,j}(n) + u_{a,j}^*(n)] c_j(n) C_{Dv,j}(n) \Delta r_j, \quad (2.47)$$

$$Q_{V,j} = \frac{1}{2} \rho Z_j \sum_{n=1}^{M_j} V_j^*(n) [V_{t,j}(n) + \omega_j r_j(n) + u_{t,j}^*(n)] r_j(n) c_j(n) C_{Dv,j}(n) \Delta r_j. \quad (2.48)$$

Here $c_j(n)$ and $C_{Dv,j}(n)$ give the chord and two-dimensional sectional drag coefficient at control point n of component j . The total thrust on a component is given by $T_j = T_{I,j} + T_{V,j}$, and the torque by $Q_j = Q_{I,j} + Q_{V,j}$.

2.4.3 Two Component Optimization

In the case of two propulsor components, the goal is to find the discrete circulation values, $\Gamma_1(1), \dots, \Gamma_1(M_1), \Gamma_2(1), \dots, \Gamma_2(M_2)$, such that the total power, $P = \omega_1 Q_1 + \omega_2 Q_2$, absorbed by the propulsor is minimized. The propulsor is additionally required to develop a prescribed thrust, T_r . In addition two component propulsors are often constrained to have a specific division of torque between the two components. Therefore, a torque ratio, $q = Q_2/Q_1$, is also specified.

These three conditions are used to form the auxiliary function, H .

$$H = (\omega_1 Q_1 + \omega_2 Q_2) + \lambda_T (T_1 + T_2 - T_r) + \lambda_Q (q Q_1 - Q_2). \quad (2.49)$$

Partial derivatives of H with respect to the unknowns are taken and set equal to zero. If variations of the viscous terms with respect to the unknown circulation strengths are neglected, the following system of equations is obtained.

$$\begin{aligned} \frac{\partial H}{\partial \Gamma_j(i)} = 0 &= \omega_1 \frac{\partial Q_1}{\partial \Gamma_j(i)} + \omega_2 \frac{\partial Q_2}{\partial \Gamma_j(i)} + \lambda_T \left[\frac{\partial T_1}{\partial \Gamma_j(i)} + \frac{\partial T_2}{\partial \Gamma_j(i)} \right] \\ &+ \lambda_Q \left[q \frac{\partial Q_1}{\partial \Gamma_j(i)} - \frac{\partial Q_2}{\partial \Gamma_j(i)} \right] \\ &= (\omega_1 + q \lambda_Q) \frac{\partial Q_1}{\partial \Gamma_j(i)} + (\omega_2 - \lambda_Q) \frac{\partial Q_2}{\partial \Gamma_j(i)} \\ &+ \lambda_T \left[\frac{\partial T_1}{\partial \Gamma_j(i)} + \frac{\partial T_2}{\partial \Gamma_j(i)} \right], \\ &\text{for } j = 1, 2 \quad \text{and } i = 1, \dots, M_j, \end{aligned} \quad (2.50)$$

$$\frac{\partial H}{\partial \lambda_T} = 0 = (T_{I1} + T_{V1}) + (T_{I2} + T_{V2}) - T_r, \quad (2.51)$$

$$\frac{\partial H}{\partial \lambda_Q} = 0 = q(Q_{I1} + Q_{V1}) + (Q_{I2} + Q_{V2}). \quad (2.52)$$

This is a nonlinear system of $M_1 + M_2 + 2$ equations for the M_1 unknown values of circulation on component 1, the M_2 circulation strengths of component 2, and the 2 Lagrange multipliers.

Upon expansion with equations 2.43 and 2.46, the partial derivatives of the torque with respect to the circulation are given by:

$$\frac{\partial Q_j}{\partial \Gamma_j(i)} = \rho Z_j \left[V_{a,j}(i) + \sum_{m=1}^{M_j} \Gamma_j(m) \bar{u}_{a,j}^*(i, m) + \sum_{m=1}^{M_k} \Gamma_k(m) \bar{u}_{a,j,k}^*(i, m) \right] r_j(i) \Delta r_j$$

$$+ \rho \mathcal{Z}_j \sum_{m=1}^{M_j} \bar{u}_{a_{j,j}}^*(m, i) \Gamma_j(m) r_j(m) \Delta r_j. \quad (2.53)$$

$$\frac{\partial Q_j}{\partial \Gamma_k(i)} = \rho \mathcal{Z}_j \sum_{m=1}^{M_j} \bar{u}_{a_{j,k}}^*(m, i) \Gamma_j(m) r_j(m) \Delta r_j. \quad (2.54)$$

Similarly, expanding the partial derivatives of the thrust with equations 2.44 and 2.45 results in:

$$\begin{aligned} \frac{\partial T_j}{\partial \Gamma_j(i)} &= \rho \mathcal{Z}_j \left[V_{t_j}(i) + \omega_j r_j(i) + \sum_{m=1}^{M_j} \Gamma_j(m) \bar{u}_{t_{j,j}}^*(i, m) + \sum_{m=1}^{M_k} \Gamma_k(m) \bar{u}_{t_{j,k}}^*(i, m) \right] \Delta r_j \\ &+ \rho \mathcal{Z}_j \sum_{m=1}^{M_j} \bar{u}_{t_{j,j}}^*(m, i) \Gamma_j(m) \Delta r_j, \end{aligned} \quad (2.55)$$

$$\frac{\partial Q_j}{\partial \Gamma_k(i)} = \rho \mathcal{Z}_j \sum_{m=1}^{M_j} \bar{u}_{t_{j,k}}^*(m, i) \Gamma_j(m) \Delta r_j. \quad (2.56)$$

Substituting these expressions for the partial derivatives into equation 2.50 and expanding equations 2.51 and 2.52 with the expansions for thrust 2.45, torque 2.46, and with the velocity expansions of equations 2.43 and 2.44. results in the following system of equations.

$$\begin{aligned} \frac{\partial H}{\partial \Gamma_1(i)} = 0 &= (\omega_1 + q \lambda_Q) \rho \mathcal{Z}_1 \left\{ \left[V_{a_1}(i) + \sum_{m=1}^{M_1} \Gamma_1(m) \bar{u}_{a_{1,1}}^*(i, m) \right. \right. \\ &\quad \left. \left. + \sum_{m=1}^{M_2} \Gamma_2(m) \bar{u}_{a_{1,2}}^*(i, m) \right] r_1(i) \Delta r_1 \right. \\ &\quad \left. + \sum_{m=1}^{M_1} \bar{u}_{a_{1,1}}^*(m, i) \Gamma_1(m) r_1(m) \Delta r_1 \right\} \\ &+ (\omega_2 - \lambda_Q) \rho \mathcal{Z}_2 \sum_{m=1}^{M_2} \bar{u}_{a_{2,1}}^*(m, i) \Gamma_2(m) r_2(m) \Delta r_2(m) \\ &+ \lambda_T \rho \mathcal{Z}_1 \left\{ \left[V_{t_1}(i) + \omega r_1(i) + \sum_{m=1}^{M_1} \Gamma_1(m) \bar{u}_{t_{1,1}}^*(i, m) \right. \right. \\ &\quad \left. \left. + \sum_{m=1}^{M_2} \Gamma_2(m) \bar{u}_{t_{1,2}}^*(i, m) \right] \Delta r_1 \right. \\ &\quad \left. + \sum_{m=1}^{M_1} \bar{u}_{t_{1,1}}^*(m, i) \Gamma_1(m) \Delta r_1 \right\} \end{aligned}$$

$$\begin{aligned}
& + \lambda_T \rho \mathcal{Z}_2 \sum_{m=1}^{M_2} \bar{u}_{t_{2,1}}^*(m, i) \Gamma_2(m) \Delta r_2. \\
& \text{for } i = 1, \dots, M_1.
\end{aligned} \tag{2.57}$$

$$\begin{aligned}
\frac{\partial H}{\partial \Gamma_2(i)} = 0 &= (\omega_1 + q \lambda_Q) \rho \mathcal{Z}_1 \sum_{m=1}^{M_1} \bar{u}_{a_{1,2}}^*(m, i) \Gamma_1(m) r_1(m) \Delta r_1 \\
& + (\omega_2 - \lambda_Q) \rho \mathcal{Z}_2 \left\{ \left[V_{a_2}(i) + \sum_{m=1}^{M_2} \Gamma_2(m) \bar{u}_{a_{2,2}}^*(i, m) \right. \right. \\
& \quad \left. \left. + \sum_{m=1}^{M_2} \Gamma_1(m) \bar{u}_{a_{2,1}}^*(i, m) \right] r_2(i) \Delta r_2 \right. \\
& \quad \left. + \sum_{m=1}^{M_2} \bar{u}_{a_{2,2}}^*(m, i) \Gamma_2(m) r_2(m) \Delta r_2 \right\} \\
& + \lambda_T \rho \mathcal{Z}_1 \sum_{m=1}^{M_1} \bar{u}_{t_{1,2}}^*(m, i) \Gamma_1(m) \Delta r_1 \\
& + \lambda_T \rho \mathcal{Z}_2 \left\{ \left[V_{t_2}(i) + \omega_2 r_2(i) + \sum_{m=1}^{M_2} \Gamma_2(m) \bar{u}_{t_{2,2}}^*(i, m) \right. \right. \\
& \quad \left. \left. + \sum_{m=1}^{M_1} \Gamma_1(m) \bar{u}_{t_{1,2}}^*(i, m) \right] \Delta r_2 \right. \\
& \quad \left. + \sum_{m=1}^{M_2} \bar{u}_{t_{2,2}}^*(m, i) \Gamma_2(m) \Delta r_2 \right\} \\
& \text{for } i = 1, \dots, M_2.
\end{aligned} \tag{2.58}$$

$$\begin{aligned}
\frac{\partial H}{\partial \lambda_T} = 0 &= \rho \mathcal{Z}_1 \sum_{n=1}^{M_1} \left[V_{t_1}(n) + \omega_1 r_1(n) + \sum_{m=1}^{M_1} \Gamma_1(m) \bar{u}_{t_{1,1}}^*(n, m) \right. \\
& \quad \left. + \sum_{m=1}^{M_2} \Gamma_2(m) \bar{u}_{t_{1,2}}^*(n, m) \right] \Gamma_1(n) \Delta r_1 + T_{V_1} \\
& + \rho \mathcal{Z}_2 \sum_{n=1}^{M_2} \left[V_{t_2}(n) + \omega_2 r_2(n) + \sum_{m=1}^{M_2} \Gamma_2(m) \bar{u}_{t_{2,2}}^*(n, m) \right. \\
& \quad \left. + \sum_{m=1}^{M_1} \Gamma_1(m) \bar{u}_{t_{2,1}}^*(n, m) \right] \Gamma_2(n) \Delta r_2 + T_{V_2} \\
& - T_r.
\end{aligned} \tag{2.59}$$

$$\begin{aligned}
\frac{\partial H}{\partial \lambda_Q} = 0 = q \left\{ \rho \mathcal{Z}_1 \sum_{n=1}^{M_1} \left[V_{a_1}(n) + \sum_{m=1}^{M_1} \Gamma_1(m) \bar{u}_{a_{1,1}}^*(n, m) \right. \right. \\
\left. \left. + \sum_{m=1}^{M_2} \Gamma_2(m) \bar{u}_{a_{1,2}}^*(n, m) \right] \Gamma_1(n) r_1(n) \Delta r_1 - Q v_1 \right\} \\
- \left\{ \rho \mathcal{Z}_2 \sum_{n=1}^{M_2} \left[V_{a_2}(n) + \sum_{m=1}^{M_2} \Gamma_2(m) \bar{u}_{a_{2,2}}^*(n, m) \right. \right. \\
\left. \left. + \sum_{m=1}^{M_1} \Gamma_1(m) \bar{u}_{a_{2,1}}^*(n, m) \right] \Gamma_2(n) r_2(n) \Delta r_2 + Q v_2 \right\}. \quad (2.60)
\end{aligned}$$

Equations 2.57-2.60 form a system of $M_1 + M_2 + 2$ nonlinear equations for the unknown values of circulation on each component, and the Lagrange multipliers. This system can be replaced by a linear system of equations, if the Lagrange multipliers are assumed to be known constants where they form quadratic terms with the unknown circulations, and if the induced velocities in the constraint equations are also assumed to be known. Equations 2.61-2.64 are the result of these assumptions and a rearrangement of equations 2.57-2.60.

$$\begin{aligned}
(\text{RHS})_1 &= -\rho \mathcal{Z}_1 \left\{ \omega_1 V_{a_1}(i) + \tilde{\lambda}_Q q V_{a_1}(i) + \tilde{\lambda}_T [V_{t_1}(i) + \omega_1 r_1(i)] \right\} \\
&= \sum_{m=1}^{M_1} \Gamma_1(m) \left\{ (\omega_1 + q \tilde{\lambda}_Q) \rho \mathcal{Z}_1 [\bar{u}_{a_{1,1}}^*(i, m) r_1(i) \Delta r_1 \right. \\
&\quad \left. + \bar{u}_{a_{1,1}}^*(m, i) r_1(m) \Delta r_1] \right. \\
&\quad \left. + \tilde{\lambda}_T \rho \mathcal{Z}_1 [\bar{u}_{t_{1,1}}^*(i, m) \Delta r_1 + \bar{u}_{t_{1,1}}^*(m, i) \Delta r_1] \right\} \\
&+ \sum_{m=1}^{M_2} \Gamma_2(m) \left\{ [\omega_1 + q \tilde{\lambda}_Q] \rho \mathcal{Z}_1 \bar{u}_{a_{1,2}}^*(i, m) r_1(i) \Delta r_1 \right. \\
&\quad \left. + [\omega_2 - \tilde{\lambda}_Q] \rho \mathcal{Z}_2 \bar{u}_{a_{2,1}}^*(m, i) r_2(m) \Delta r_2 \right. \\
&\quad \left. + \tilde{\lambda}_T \rho \mathcal{Z}_1 \bar{u}_{t_{1,2}}^*(i, m) \Delta r_1 + \tilde{\lambda}_T \rho \mathcal{Z}_2 \bar{u}_{t_{2,1}}^*(m, i) \Delta r_2 \right\}, \\
&\quad \text{for } i = 1, \dots, M_1, \quad (2.61)
\end{aligned}$$

$$\begin{aligned}
(\text{RHS})_2 &= -\rho \mathcal{Z}_2 \left\{ \omega_2 V_{a_2}(i) + \tilde{\lambda}_Q q V_{a_2}(i) + \tilde{\lambda}_T [V_{t_2}(i) + \omega_2 r_2(i)] \right\} \\
&= \sum_{m=1}^{M_1} \Gamma_1(m) \left\{ [\omega_1 + q \tilde{\lambda}_Q] \rho \mathcal{Z}_1 \bar{u}_{a_{1,2}}^*(m, i) r_1(m) \Delta r_1 \right.
\end{aligned}$$

$$\begin{aligned}
& + \left[\omega_2 + q\tilde{\lambda}_Q \right] \rho \mathcal{Z}_2 \bar{u}_{a_{2,1}}^*(i, m) r_2(i) \Delta r_2 \\
& + \tilde{\lambda}_T \rho \mathcal{Z}_1 \bar{u}_{t_{1,2}}^*(m, i) \Delta r_1 + \tilde{\lambda}_T \rho \mathcal{Z}_2 \bar{u}_{t_{2,1}}^*(i, m) \Delta r_2 \Big\} \\
& + \sum_{m=1}^{M_2} \Gamma_2(m) \left\{ \left(\omega_2 - \tilde{\lambda}_Q \right) \rho \mathcal{Z}_2 \left[\bar{u}_{a_{2,2}}^*(i, m) r_2(i) \Delta r_2 \right. \right. \\
& \quad \left. \left. + \bar{u}_{a_{2,2}}^*(m, i) r_2(m) \Delta r_2 \right] \right. \\
& \quad \left. + \tilde{\lambda}_T \rho \mathcal{Z}_2 \bar{u}_{t_{2,2}}^*(i, m) \Delta r_2 + \tilde{\lambda}_T \rho \mathcal{Z}_2 \bar{u}_{t_{2,2}}^*(m, i) \Delta r_2 \right\}, \\
& \text{for } i = 1, \dots, M_2,
\end{aligned} \tag{2.62}$$

$$\begin{aligned}
T_r + T_{V_1} + T_{V_2} &= \rho \mathcal{Z}_1 \sum_{m=1}^{M_1} \left[V_{t_1}(m) + \omega_1 r_1(m) + u_{t_1}^*(m) \right] \Gamma_1(m) \Delta r_1 \\
&+ \rho \mathcal{Z}_2 \sum_{m=1}^{M_2} \left[V_{t_2}(m) + \omega_2 r_2(m) + u_{t_2}^*(m) \right] \Gamma_2(m) \Delta r_2
\end{aligned} \tag{2.63}$$

$$\begin{aligned}
Q_{V_2} - qQ_{V_1} &= q\rho \mathcal{Z}_1 \sum_{m=1}^{M_1} \left[V_{a_1}(m) + u_{a_1}^*(m) \right] \Gamma_1(m) r_1(m) \Delta r_1 \\
&- \rho \mathcal{Z}_2 \sum_{m=1}^{M_2} \left[V_{a_2}(m) + u_{a_2}^*(m) \right] \Gamma_2(m) r_2(m) \Delta r_2
\end{aligned} \tag{2.64}$$

The solution of the nonlinear system of equations 2.57-2.60 can be found by iteratively solving the linear system of equations 2.61-2.64. On each iteration the frozen Lagrange multipliers, $\tilde{\lambda}_T$ and $\tilde{\lambda}_Q$, and the induced velocities, u_a^* and u_t^* , are updated with values from the previous iteration. The viscous thrust and torque, T_V and T_Q , can also be updated with equations 2.47 and 2.48 on each iteration. In most instances this procedure was found to converge rapidly (less than 10 iterations) to a solution of the nonlinear system. An initial estimate of zero for the induced velocities and $\tilde{\lambda}_Q$, and of -1 for $\tilde{\lambda}_T$ was found suitable.

The wake geometry is assumed to be frozen in equations 2.57-2.60. Velocities and forces consistent with moderately loaded theory can be obtained by iteratively solving these equations, aligning the wake, solving the equations again, ..., and so on. This approach neglects variations with respect to changes in the wake geometry, but does provide wake aligned velocities and forces.

As was the case for the single propeller equations 2.57-2.60 are not dependant on the details of the vortex lattice model or the algorithms for computing velocities. For components of equal diameter both constant and cosine spacing have been successfully

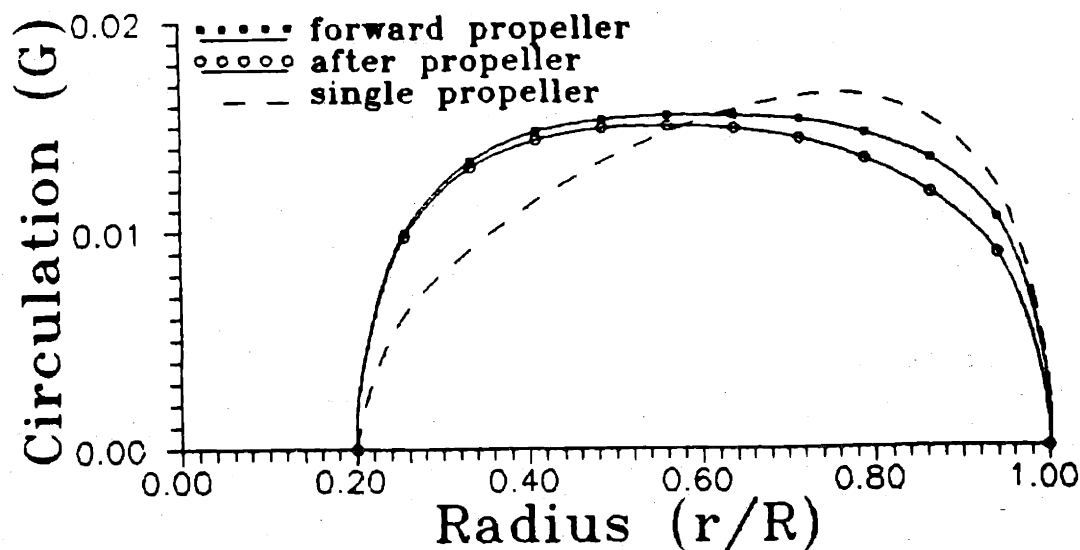


Figure 2.10: Optimum circulation distributions for a pair of contrarotating propellers.

implemented. For nonconstant spacing the length of the vortex panels, Δr_j , is also a function of radius, $\Delta r_j = \Delta r_j(n)$. Difficulties arose with the cosine spaced panel arrangement when the components were of different diameter. This led to the adoption of constant spacing.

It should be possible to extend the methods described here to address the case of three or more propulsor components. The present work is limited, however, to the case of one or two propulsor components.

2.4.4 Contrarotating Propellers

Equations 2.57-2.60 can be solved in order to provide optimum circulation distributions for contrarotating propellers. Figure 2.10 gives optimum distributions for a pair of free-running, contrarotating propellers. In this case the propellers have the same diameter and the contraction of the wake is ignored. The propellers are rotating at the same speed in opposite directions. Their advance coefficient is 0.89 and the contrarotating pair is required to develop a thrust corresponding to $C_T = 0.69$. Both propellers are four bladed and are required to develop equal torque, $q = 1.0$. The moderately loaded model is employed and viscous forces are neglected.

Also shown in figure 2.10 is an optimum circulation distribution for a single propeller operating at the same advance ratio and required to generate the same thrust. The single propeller is eight bladed, so that each blade generates approximately the same thrust as the blades of the contrarotating pair. Note that the circulation distribution of

	K_T	K_Q	η
forward propeller	0.1084	0.0181	
after propeller	0.1062	0.0181	
contrarotating pair	0.2146	0.0362	0.841
8-bladed propeller	0.2146	0.0376	0.809

Table 2.1: Forces acting on a pair of contrarotating propellers.

the contrarotating propellers is more uniform and less tip loaded than that of the single propeller.

Forces and efficiencies for each of the propellers is presented in table 2.1.¹ Note that, as anticipated, the contrarotating propellers are predicted to be more efficient than the single propeller. The efficiency of a two stage propulsor is defined here to be

$$\eta = \frac{T_1 V_{A1} + T_2 V_{A2}}{\omega_1 Q_1 + \omega_2 Q_2}. \quad (2.65)$$

V_{A_j} is the volumetric mean effective inflow as defined by equation 2.37 at the plane of component j . Note that while the contrarotating propellers develop equal torque, the thrust they produce differs by about 2%. This is due to differences in the induced velocities, and the resulting hydrodynamic pitch angles at each propeller.

Figure 2.11 presents circumferential mean tangential velocities induced far downstream by the contrarotating pair of propellers and by the single propeller. Note that the total tangential velocity induced by the contrarotating pair is very nearly zero, much less than that induced by the single propeller. This provides some insight into the increased efficiency of the contrarotating propellers, since these swirl velocities do not represent any thrust, only losses. Finite blade effects and the required torque balance prevent the tangential velocities from being identically zero for the contrarotating pair.

Figure 2.12 similarly presents the circumferential mean axial velocities induced far downstream. Note that the total axial velocity induced by the contrarotating pair is more uniform and less concentrated toward the tip than that of the single propeller. This effect is also connected with the increased efficiency. The axial velocities induced by the contrarotating pair are closer to those of the actuator disc. Sparenberg [100] showed that, in the limit of light loading and the absence of viscosity, the efficiency is bounded by that of the actuator disc. As the circumferential mean induced velocities approach those of the actuator disc, zero tangential velocity and uniform axial velocity, the efficiency should increase.

¹The forces presented here, and throughout this chapter, do not include any viscous forces and should not be used to determine the relative merits of various propulsor types.

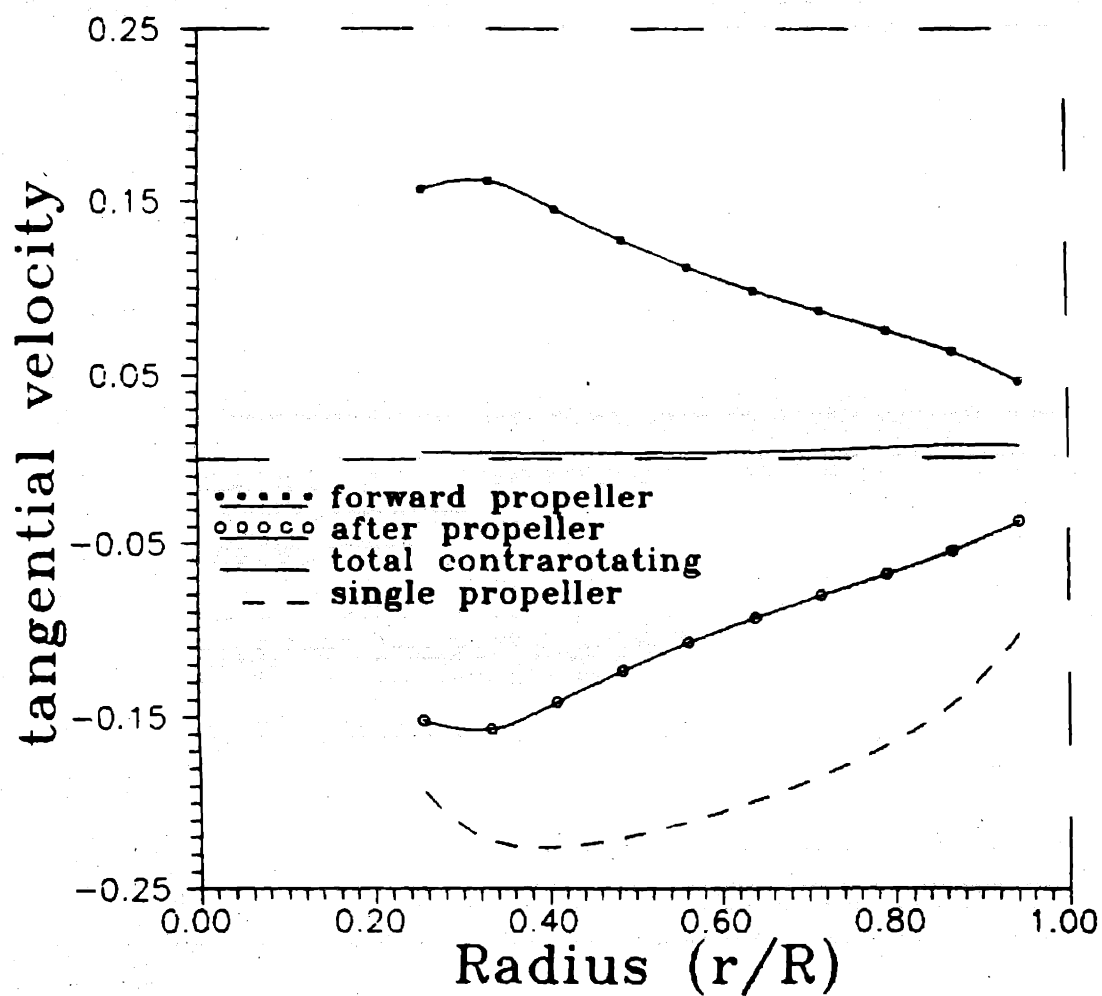


Figure 2.11: Tangential velocities induced far downstream by the contrarotating propellers. Velocities are given as fractions of ship speed, V_S .

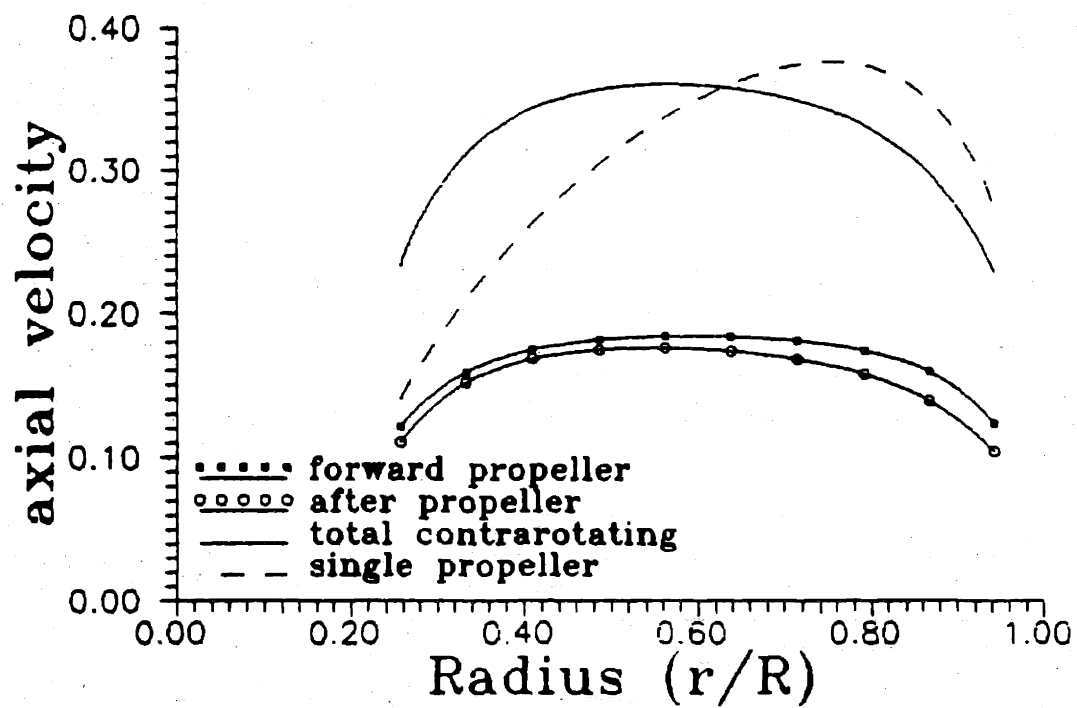


Figure 2.12: Axial velocities induced far downstream by the contrarotating propellers.

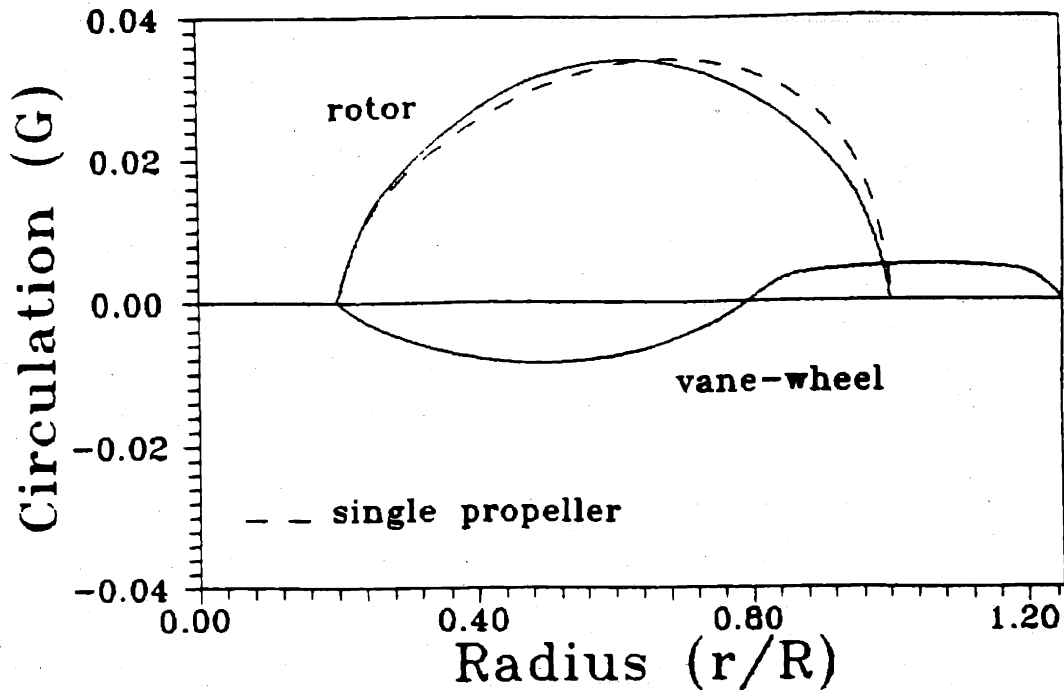


Figure 2.13: Optimum circulation distributions for a vane-wheel propulsor.

2.4.5 The Vane-Wheel Propulsor

The vane-wheel, as proposed by Grim [45] [44], is a freely rotating device placed behind a conventional propeller. The vane-wheel propulsor increases efficiency by reclaiming part of the energy lost in the propeller's slipstream and converting that energy into additional thrust. The rotor of the vane-wheel propulsor performs as a conventional propeller, whereas, the vane-wheel has an inner part which acts as a turbine, and an outer part which acts as a propeller, producing thrust.

Equations 2.57-2.60 can be used to find optimum circulation distributions for the vane-wheel propulsor. Since the vane-wheel is freely rotating, it can sustain no total torque. Thus, if the rotor is considered to be component #1 and the vane-wheel component #2, the torque ratio for the vane-wheel propulsor is $q = Q_2/Q_1 = 0$. The vane-wheel rotates in the same direction as the rotor, typically at about 40% of the propeller's rotation rate, and is somewhat larger in diameter than the rotor.

Figure 2.13 shows optimum circulation distributions for a vane-wheel propulsor. Note that, as expected, the inner part of the vane-wheel acts as a turbine with negative loading, while the outer part has positive circulation and acts as a propeller. In this example both

	K_T	K_Q	η
rotor	0.2030	0.0364	
vane-wheel	0.0116	0.0000	
vane-wheel propulsor	0.2146	0.0364	0.835
4-bladed propeller	0.2146	0.0389	0.781

Table 2.2: Forces acting on the vane-wheel propulsor.

the rotor and vane-wheel have four blades. The diameter of this vane wheel is 25% greater than the rotor's diameter. The lifting lines representing the components are separated by a distance of 20% of the rotor diameter. The vane-wheel is required to rotate at 40% of the rotor's rotation. Here the propeller's advance coefficient is 0.89 and the propulsor is required to produce a thrust corresponding to $C_T = 0.69$. Moderately loaded theory was employed and viscous forces neglected. A wake contraction of 0.83 was assumed. An optimum circulation distribution for a four bladed propeller with the same characteristics as the rotor is also presented.

Table 2.2 gives the forces acting on the vane-wheel propulsor² and the single propeller. Note that the torque on the vane-wheel is zero, as desired. Also note the increased efficiency of the vane-wheel propulsor over the propeller operating alone.

2.4.6 Pre and Post Swirl Stators

Propeller/stator combinations are a special case of the two component propulsor. There is no rotation of the stator blades and, therefore, no power applied to the stator. Also the ratio of torque between the propeller and stator is not typically constrained. The two component optimization equations 2.57-2.60 can be greatly simplified if all terms involving the stator's rotation and the torque ratio constraint are removed. If the propeller is assumed to be component #1 and the stator component #2 the equations become:

$$\frac{\partial H}{\partial \Gamma_1(i)} = 0 = \omega_1 \rho Z_1 \left\{ \left[V_{a1}(i) + \sum_{m=1}^{M_1} \Gamma_1(m) \bar{u}_{a1,1}^*(i, m) + \sum_{m=1}^{M_2} \Gamma_2(m) \bar{u}_{a1,2}^*(i, m) \right] r_1(i) \Delta r_1 + \sum_{m=1}^{M_1} \bar{u}_{a1,1}^*(m, i) \Gamma_1(m) r_1(m) \Delta r_1 \right\}$$

²Vane-wheel forces are nondimensionalized with the diameter and rotation of the rotor.

$$\begin{aligned}
& + \lambda_T \rho \mathcal{Z}_1 \left\{ \left[V_{t_1}(i) + \omega r_1(i) + \sum_{m=1}^{M_1} \Gamma_1(m) \bar{u}_{t_{1,1}}^*(i, m) \right. \right. \\
& \quad \left. \left. + \sum_{m=1}^{M_2} \Gamma_2(m) \bar{u}_{t_{1,2}}^*(i, m) \right] \Delta r_1 \right. \\
& \quad \left. + \sum_{m=1}^{M_1} \bar{u}_{t_{1,1}}^*(m, i) \Gamma_1(m) \Delta r_1 \right\} \\
& + \lambda_T \rho \mathcal{Z}_2 \sum_{m=1}^{M_2} \bar{u}_{t_{2,1}}^*(m, i) \Gamma_2(m) \Delta r_2, \\
& \quad \text{for } i = 1, \dots, M_1.
\end{aligned} \tag{2.66}$$

$$\begin{aligned}
\frac{\partial H}{\partial \Gamma_2(i)} = 0 &= \omega_1 \rho \mathcal{Z}_1 \sum_{m=1}^{M_1} \bar{u}_{t_{1,2}}^*(m, i) \Gamma_1(m) r_1(m) \Delta r_1 \\
& + \lambda_T \rho \mathcal{Z}_1 \sum_{m=1}^{M_1} \bar{u}_{t_{1,2}}^*(m, i) \Gamma_1(m) \Delta r_1 \\
& + \lambda_T \rho \mathcal{Z}_2 \left\{ \left[V_{t_2}(i) + \sum_{m=1}^{M_2} \Gamma_2(m) \bar{u}_{t_{2,2}}^*(i, m) \right. \right. \\
& \quad \left. \left. + \sum_{m=1}^{M_1} \Gamma_1(m) \bar{u}_{t_{1,2}}^*(i, m) \right] \Delta r_2 \right. \\
& \quad \left. + \sum_{m=1}^{M_2} \bar{u}_{t_{2,2}}^*(m, i) \Gamma_2(m) \Delta r_2 \right\} \\
& \quad \text{for } i = 1, \dots, M_2.
\end{aligned} \tag{2.67}$$

$$\begin{aligned}
\frac{\partial H}{\partial \lambda_T} = 0 &= \rho \mathcal{Z}_1 \sum_{n=1}^{M_1} \left[V_{t_1}(n) + \omega_1 r_1(n) + \sum_{m=1}^{M_1} \Gamma_1(m) \bar{u}_{t_{1,1}}^*(n, m) \right. \\
& \quad \left. + \sum_{m=1}^{M_2} \Gamma_2(m) \bar{u}_{t_{1,2}}^*(n, m) \right] \Gamma_1(n) \Delta r_1 + T_{V_1} \\
& + \rho \mathcal{Z}_2 \sum_{n=1}^{M_2} \left[V_{t_2}(n) + \sum_{m=1}^{M_2} \Gamma_2(m) \bar{u}_{t_{2,2}}^*(n, m) \right. \\
& \quad \left. + \sum_{m=1}^{M_1} \Gamma_1(m) \bar{u}_{t_{2,1}}^*(n, m) \right] \Gamma_2(n) \Delta r_2 + T_{V_2} \\
& - T_r.
\end{aligned} \tag{2.68}$$

Equations 2.66-2.68 form a nonlinear system of $M_1 + M_2 + 1$ equations for the unknown

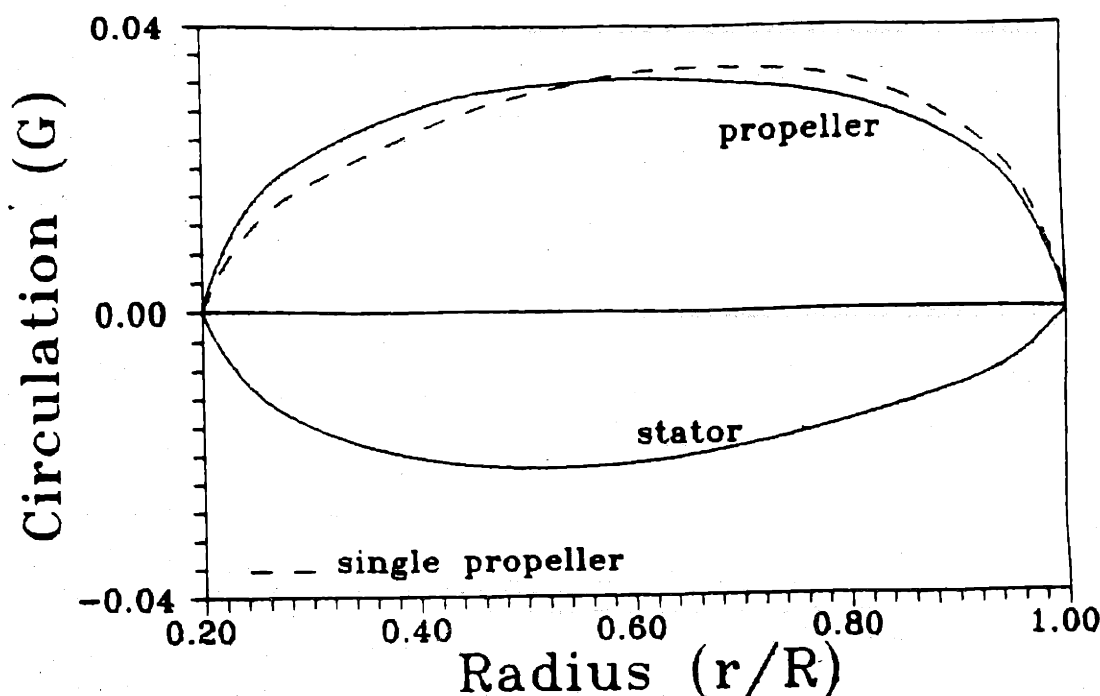


Figure 2.14: Optimum circulation distributions for a propeller and pre-swirl stator.

circulations and the Lagrange multiplier, λ_T . These equations can be linearized as before and the linear system iteratively solved for the solution to the nonlinear system.

Figure 2.14 gives optimum circulation distributions for a propeller operating downstream of a stator. The propeller and stator have the same diameter and are separated axially by 20% of this diameter. They both have four blades. The moderately loaded model was employed and viscous forces were neglected. The propulsor sees uniform inflow and the propeller is operating at an advance coefficient of $J_S = 0.69$. The propulsor is required to develop a thrust corresponding to $C_T = 0.69$. The optimum circulation distribution for a propeller operating alone under the same conditions is also presented.

Note in figure 2.14 that the stator's circulation has sign opposite that of the propeller. Further note that the propeller's loading is shifted inboard as compared to that of the propeller operating alone. Table 2.3 gives the forces for this propeller/stator. propeller/stator.³ Note that the total efficiency is increased even though the stator generates drag rather than thrust.

Some insight into this increased efficiency may be provided by figure 2.15. This figure gives the mean tangential velocity induced by the propeller/stator far downstream of the

³The stator forces are here nondimensionalized with the propeller's rotation.

	K_T	K_Q	η
rotor	0.2216	0.0375	
stator	-0.0070		
propeller/stator	0.2146	0.0375	0.811
4-bladed propeller	0.2146	0.0389	0.781

Table 2.3: Forces acting on the propeller/pre-swirl stator.

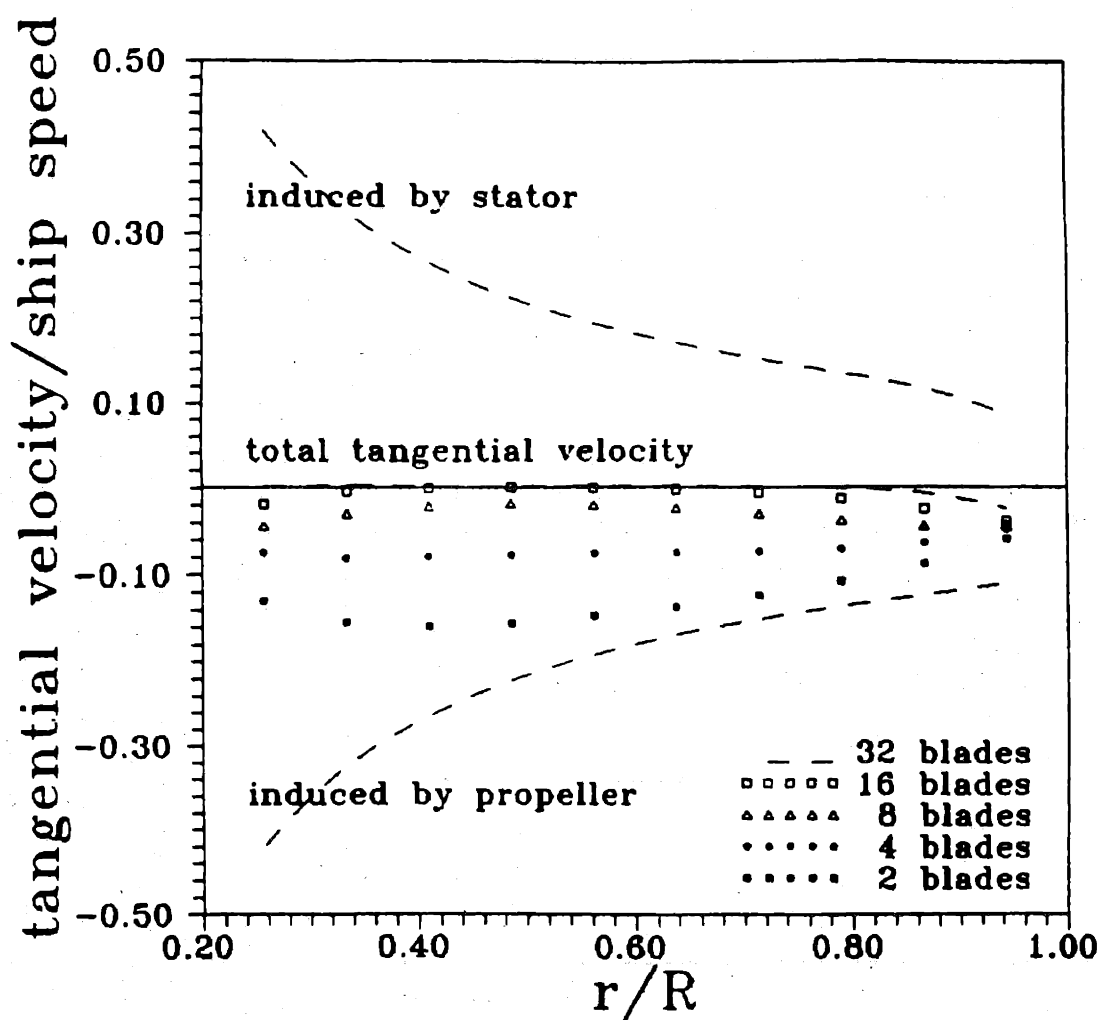


Figure 2.15: Tangential velocities induced far downstream by propeller/stator combinations.

propulsor. The propeller cancels the swirl induced by the stator, resulting in reduced downstream tangential velocities, and, therefore, decreased rotational losses.

Figure 2.15 gives the mean downstream tangential velocities for propeller/stators with varying number of blades. In each case the circulation distributions are required to be optimum. The propulsors are each required to generate the same thrust as the four bladed case, and the propellers all operate at the same advance coefficient. As the number of blades is increased in figure 2.15, the tangential velocity becomes more nearly equal to zero. Not surprisingly, the actuator disc result is approached with increasing number of blades. Note that for finite number of blades, the optimum circulation distribution does not generate zero mean tangential velocity far downstream.

Chapter 3

Hubs and Ducts

3.1 Hub Effects

3.1.1 Hub Loaded Optimum Circulation Distributions

Up to this point the lifting line theory employed here has not considered the presence of the hub as a solid boundary. The hub has been modeled in a number of ways within lifting line procedures. Lerbs [73] and Tachmindji [102] treated the hub as an infinitely long cylinder with two boundary conditions imposed on its surface. They required that both the circulation and the radial velocity component be zero at the hub. Tachmindji solved the potential problem for the Betz condition with the addition of these hub boundary conditions. Circulation distributions presented by Tachmindji are similar to optimum distributions from the Betz criteria in which the presence of the hub is neglected.

Lerbs and Tachmindji justify their boundary condition on circulation by arguing that, when approached from inside the hub, the circulation at the hub must vanish. They further argue that the circulation must vanish at the hub when approached from outside the hub in order to preserve a continuous circulation distribution. From a modern perspective it is clear that there is no such requirement on the interior flow. Therefore, this argument does not justify a requirement of zero circulation at the hub. Lerbs and Tachmindji also argued physically that pressures from the pressure side of one blade would equalize with those from the suction side of the next, resulting in vanishing circulation at the hub. However, this argument has not been borne out experimentally. Wang [118] measured propeller circulation distributions with substantial amounts of circulation maintained well within the hub's boundary layer.

McCormick [77] also modelled the hub as an infinite cylinder. He solved for the potential flow which satisfied the Betz condition and a condition of zero velocity normal to the hub cylinder. Circulation distributions presented by McCormick show finite circulation at the hub. These distributions also appear to tend toward zero slope at the hub.

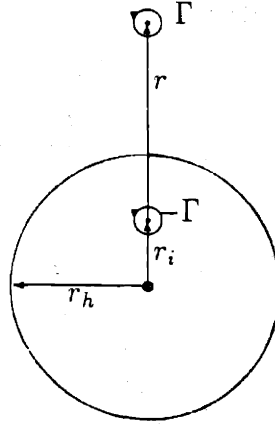


Figure 3.1: Schematic showing a vortex and its image.

Betz [5] considered a reflection inside of the hub of the flow outside of the hub when determining optimum load distributions for guide vanes placed downstream of a propeller. Similarly, Kerwin and Leopold [64] proposed the use of an image system of vorticity, located within the hub cylinder, to represent the hub. The image system they adopted was based on the known result that a pair of two dimensional vortices, of equal and opposite strength, located on the same line, induce no net radial velocity on a circle of radius r_h , providing

$$r_i = \frac{r_h^2}{r}. \quad (3.1)$$

Here r is the radius of the outer vortex, r_i the radius of its image and r_h the radius of the hub cylinder. This is shown schematically in figure 3.1.

It is assumed that the same result will hold approximately in the case of two helical vortices of equal and opposite strength, provided their pitch angle is sufficiently high. Kerwin and Leopold demonstrated numerically that the required cancellation of radial velocities at the hub radius, for such a pair of helical vortices, is excellent for vortices near the hub. The cancellation is not as good for distant elements. However, the velocity induced on the hub by these elements is small.

The vortex lattice model of the previous chapter is readily adapted to accommodate such an image system. this is done by adding to the velocity induced by each vortex lattice the velocity induced by a corresponding image horseshoe.

$$[\bar{u}_a^*(n, m)]_{\text{total}} = \bar{u}_a^*(n, m) + [\bar{u}_a^*(n, m)]_{\text{image}}, \quad (3.2)$$

$$[\bar{u}_i^*(n, m)]_{\text{total}} = \bar{u}_i^*(n, m) + [\bar{u}_i^*(n, m)]_{\text{image}}. \quad (3.3)$$

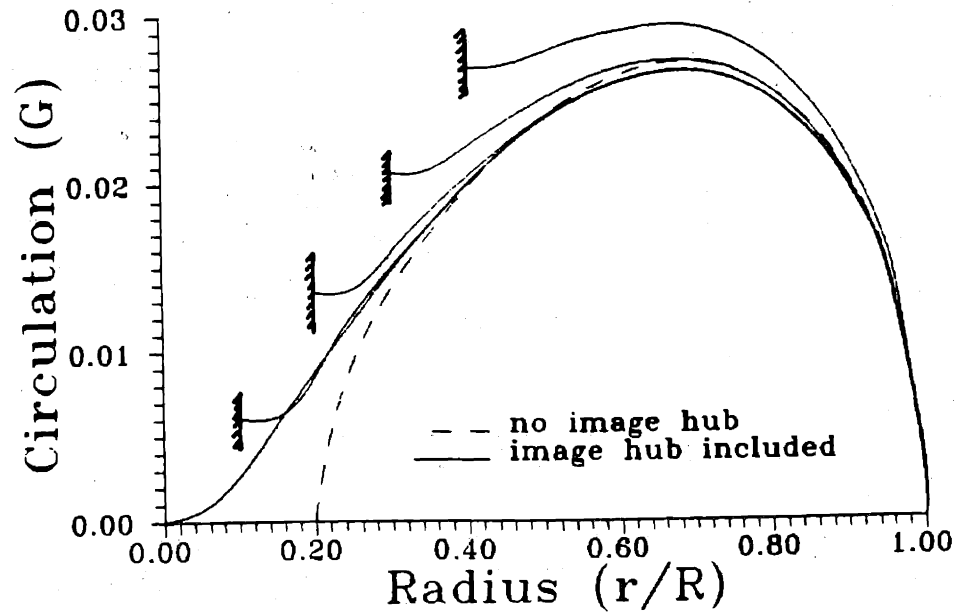


Figure 3.2: Optimum hub loaded circulation distributions.

If the influence functions in equations 2.30 and 2.31 are replaced by the total influence functions of equations 3.2 and 3.3 which include the velocities induced by the image system, optimum circulation distributions which include the effect of the image hub can be solved for.

Figure 3.2 shows such circulation distributions for hubs of various diameter. Note the finite values of circulation at the hub. Also note that the circulation distributions have zero slope at the hub. This must be the case in order for there to be a continuous circulation distribution at the junction of the lifting line and its image. Finally note that the hub circulation increases with the hub diameter. These results agree, at least qualitatively, with those presented by McCormick. The results presented here are for a 5 bladed propeller, operating at $J_S = 0.89$ in uniform inflow and required to develop a thrust corresponding to $C_T = 0.69$.

Caja [12] combined the previous chapter's vortex lattice, lifting line representation of the propeller with a panel method representation of the hub. Velocities induced by the hub panels, in the presence of unit strength helical vortex horseshoes, on the lifting line control points were determined. Figure 3.3 shows a single vortex horseshoe set on a panel representation of a cylindrical hub.¹ A similar problem is solved for each of the

¹The trailing vortex horseshoes are represented by quadrilateral panels, consisting of constant dipole sheets. The panels which make up each horseshoe are assigned identical strength. Mathematically, these

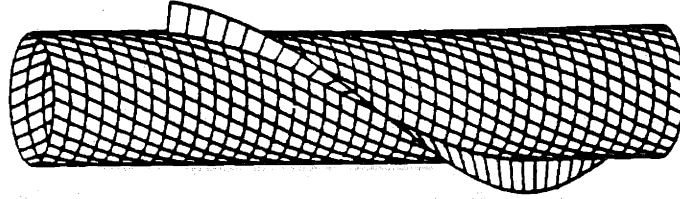


Figure 3.3: Panel method representation of a single vortex horseshoe set on a cylindrical hub. Here the pitch angle of the horseshoe is 80 degrees. For this figure 25 circumferential and 40 longitudinal panels were used on the cylinder.

M vortex horseshoes representing the propeller. The velocities induced at the control points by the unit strength horseshoe vortices, in the absence of the hub, are added to velocities induced by the hub in the presence of such vortices

$$[\bar{u}_a^*(n, m)]_{\text{total}} = \bar{u}_a^*(n, m) + [\bar{u}_a^*(n, m)]_{\text{panel method}}, \quad (3.4)$$

$$[\bar{u}_t^*(n, m)]_{\text{total}} = \bar{u}_t^*(n, m) + [\bar{u}_t^*(n, m)]_{\text{panel method}}. \quad (3.5)$$

Details of the panel method are supplied by Caja and in [62]. Caja solved equations 2.30 and 2.31 with the total influence functions of equations 3.4 and 3.5 to determine optimum circulation distributions in the presence of the hub.

While a procedure such as that employed by Caja is much too computationally intensive for most design purposes, it does allow for accurate computation of the velocities induced by the propeller/hub interaction. Caja found good agreement between velocities predicted by an image representation of the hub and those of the panel representation for panels near the hub, confirming the findings of Kerwin and Leopold [64]. Figure 3.4 gives optimum circulation distributions from velocity influence functions determined from the image representation of the hub and from Caja's panel method representation. The propeller is 5 bladed and is operating in uniform inflow. $J_S = 1.1$. $C_T = 0.48$. Viscous effects are neglected and the lightly loaded wake model is employed. Note the excellent agreement between the two hub models.

dipole sheets are equivalent to constant vortex segments along the panel boundaries. Thus, the vortices on the interior of each strip cancel, leaving horseshoes made up of straight line segments.

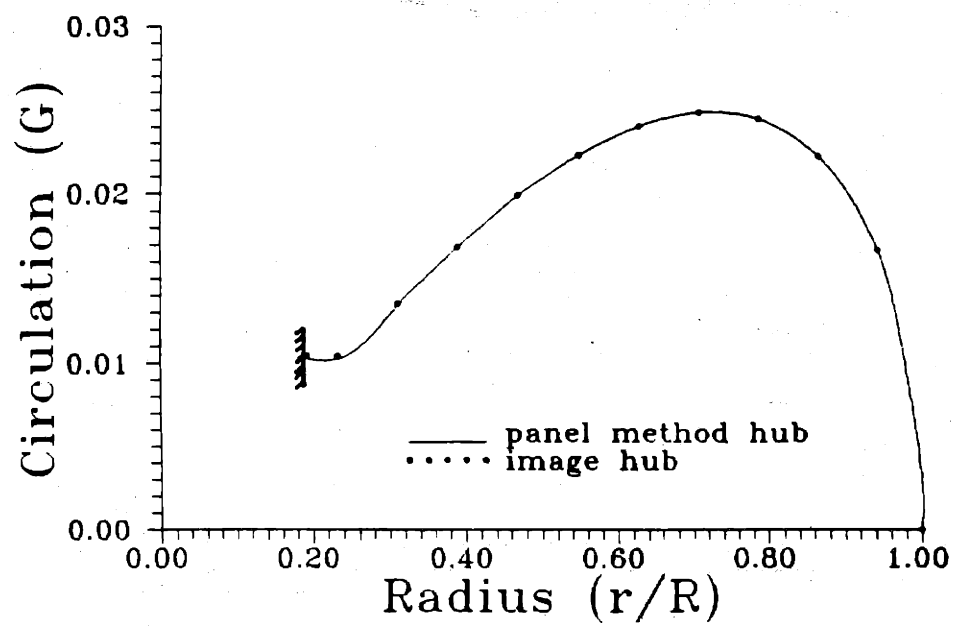


Figure 3.4: Optimum circulation distributions from the image and panel hub representations. 80 axial and 60 circumferential panels were used for the panel method representation.

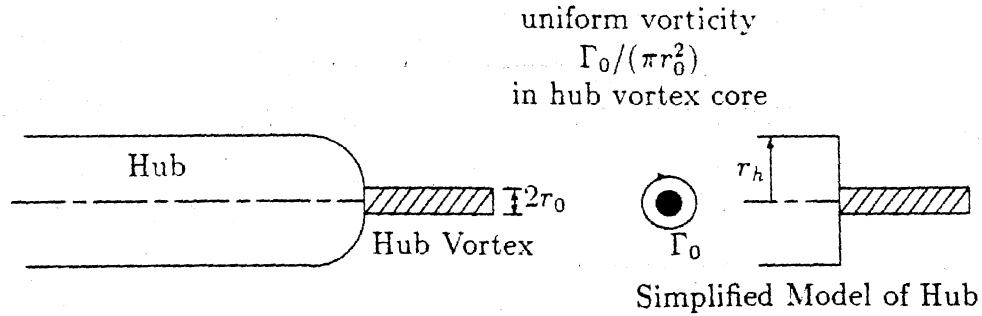


Figure 3.5: The Rankine vortex model used to determine the hub drag.

3.1.2 Hub Drag

In actuality the hub does not extend infinitely far downstream. A force can, therefore, act on the end of the hub. On actual propellers a vortex associated with the circulation on the propeller blades is shed from the downstream end of the hub. The hub experiences a force in the drag direction due to the decreased pressure associated with this concentrated hub vortex. Wang [118] experimentally determined that a Rankine vortex structure was an appropriate model for this hub vortex.

In Wang's simplified model for the hub drag, the hub is considered to be an abruptly truncated cylinder of radius r_h . The hub vortex is considered to be a vortex core of strength Γ_0 and radius r_0 , extending infinitely far downstream from the end of the hub cylinder. A sketch of this model is given in figure 3.5.

The circulation distribution of an infinitely long Rankine vortex is given by

$$\Gamma_{RV} = \begin{cases} \frac{\Gamma_0}{r_0^2} r^2 & \text{for } r \leq r_0; \\ \Gamma_0 & \text{otherwise.} \end{cases} \quad (3.6)$$

The corresponding velocity distribution is

$$u_{tRV} = \begin{cases} \frac{\Gamma_0}{2\pi r_0^2} r & \text{for } r \leq r_0; \\ \frac{\Gamma_0}{2\pi r} & \text{otherwise.} \end{cases} \quad (3.7)$$

The velocity induced at the end of a semi-infinite Rankine vortex is simply one-half that of the infinite vortex. The pressure corresponding to this velocity distribution is

$$p = \begin{cases} p_\infty + \frac{\rho \Gamma_0^2 r^2}{8\pi^2 r_0^4} - \frac{\rho \Gamma_0^2}{4\pi^2 r_0^2} & \text{for } r \leq r_0; \\ p_\infty + \frac{\rho \Gamma_0^2}{32\pi^2 r^2} & \text{otherwise.} \end{cases} \quad (3.8)$$

	r_0/r_h	K_T	K_Q	η
<i>hub drag not included</i>				
hubless propeller		0.215	0.0384	0.791
hub loaded propeller		0.218	0.0389	0.792
<i>hub drag included</i>				
hub loaded propeller	1.000	0.215	0.0387	0.785
	0.500	0.215	0.0388	0.782
	0.250	0.215	0.0389	0.780
	0.167	0.215	0.0403	0.752
	0.125	0.215	0.0426	0.709

Table 3.1: Forces with and without hub drag.

If this pressure is integrated over the hub disk, the following force in the drag direction is obtained.

$$F_h = \frac{\rho}{16\pi} \left(\ln \frac{r_h}{r_0} + 3 \right) \Gamma_0^2. \quad (3.9)$$

Note that this force is proportional to the strength of the Rankine vortex squared. Γ_0 is assumed to be equal to the total blade circulation at the hub. In this case there is a drag penalty associated with the presence of finite circulation at the hub. The radius of the hub vortex core must be empirically estimated or determined experimentally.

Table 3.1 gives forces on 5 bladed propellers in uniform inflow operating at $J_S = 0.89$. Forces are given for an optimum circulation distribution with the presence of the hub neglected, for a distribution determined by use of the image hub model and for this same circulation distribution with the hub drag included. Forces are given for several hub vortex core diameters. The diameter of the hub is 20% of the propeller diameter. The circulation distributions for this case are shown in figure 3.2.

If the hub drag is neglected, the hub loaded circulation distribution shows slightly increased efficiency over the hubless propeller. This efficiency gain is not realized when the hub drag is included, in fact the efficiency is reduced by an amount which depends on the hub vortex core diameter. For small hub vortex diameters the reduction in efficiency can be substantial. An investigation into what parameters determine the size of the hub vortex would be of considerable interest.

3.1.3 Hub Vortex Cancellation

The hub drag of equation 3.9 can be reduced, or eliminated entirely, in the case of multiple stage propulsors. If the circulation shed onto the hub from each propulsor component is

of opposite sign, a cancellation of hub vorticity results. Since, under the model employed here, the hub drag is a function of the strength of the concentrated hub vortex, a reduction in the strength of this vortex results in a decrease in the predicted hub drag.

An indication of the effectiveness of a stator in reducing the strength, and hence the associated losses, of the hub vortex can be seen from a comparison of the photographs shown in figure 3.6. These photographs are of the propeller tested by Bowling [6] operating with and without a preswirl stator. Both photographs were taken at the design operating condition, with the tunnel set at the same cavitation number.

The hub drag can be included in the optimization equations for multiple stage propulsors. In the case of two propulsor components, the hub drag is given by

$$F_h = \frac{\rho}{16\pi} \left(\ln \frac{r_h}{r_0} + 3 \right) [\Gamma_{01} + \Gamma_{02}]^2, \quad (3.10)$$

where Γ_{01} and Γ_{02} are the circulation shed onto the hub by component #1 and component #2, respectively. If the circulation shed onto the hub is assumed under the discrete vortex lattice model to be that of the innermost control point of each component, the hub drag can be rewritten as

$$F_h = \frac{\rho}{16\pi} \left(\ln \frac{r_h}{r_0} + 3 \right) [\Gamma_1^2(1) + \Gamma_1(1)\Gamma_2(1) + \Gamma_2^2(1)]. \quad (3.11)$$

If this hub drag term is included, the auxiliary function for the two component optimization becomes

$$H = (\omega_1 Q_1 + \omega_2 Q_2) + \lambda_T (T_1 + T_2 - F_h - T_r) + \lambda_Q (Q_2 - q Q_1). \quad (3.12)$$

When derivatives with respect to the unknown circulation strengths are taken two additional terms arise from the hub drag.

$$\frac{\partial H}{\partial \Gamma_1(1)} = 0 = \dots - \frac{\rho}{16\pi} \left(\ln \frac{r_h}{r_0} + 3 \right) [2\Gamma_1(1) + \Gamma_2(1)] + \dots, \quad (3.13)$$

$$\frac{\partial H}{\partial \Gamma_2(1)} = 0 = \dots - \frac{\rho}{16\pi} \left(\ln \frac{r_h}{r_0} + 3 \right) [\Gamma_1(1) + 2\Gamma_2(1)] + \dots \quad (3.14)$$

The hub drag must also be added to the thrust constraint. The resulting system of equations is identical to that of equations 2.57-2.60 with the addition of terms involving the hub drag.

This system of nonlinear equations can be solved for optimum circulation distributions as in chapter 2. Figure 3.7 gives optimum circulation distributions so determined for a pair of contrarotating propellers. The propellers are rotating at the same speed in opposite directions. their advance coefficient is 0.89 and the total thrust corresponds to

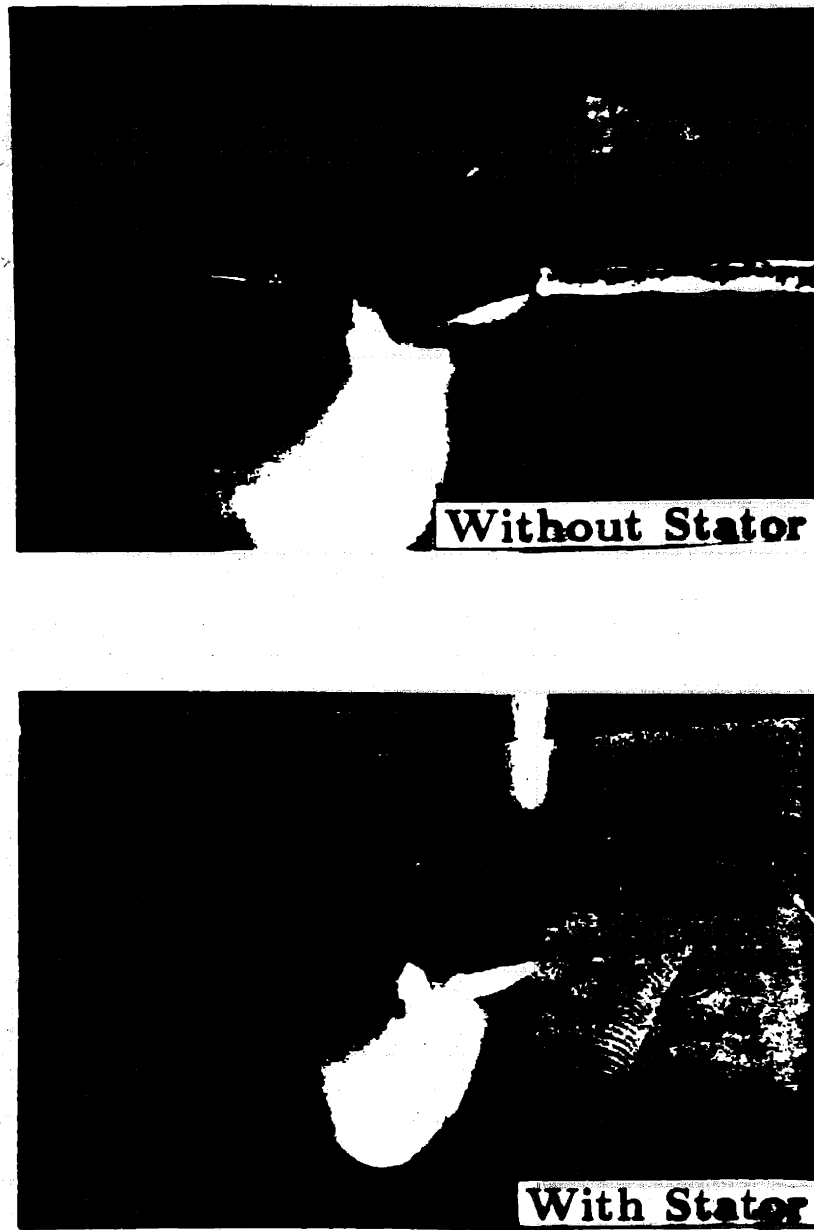


Figure 3.6: Propeller operating with and without a preswirl stator. The tunnel pressure is lowered in these pictures in order to visualize the hub vortex.

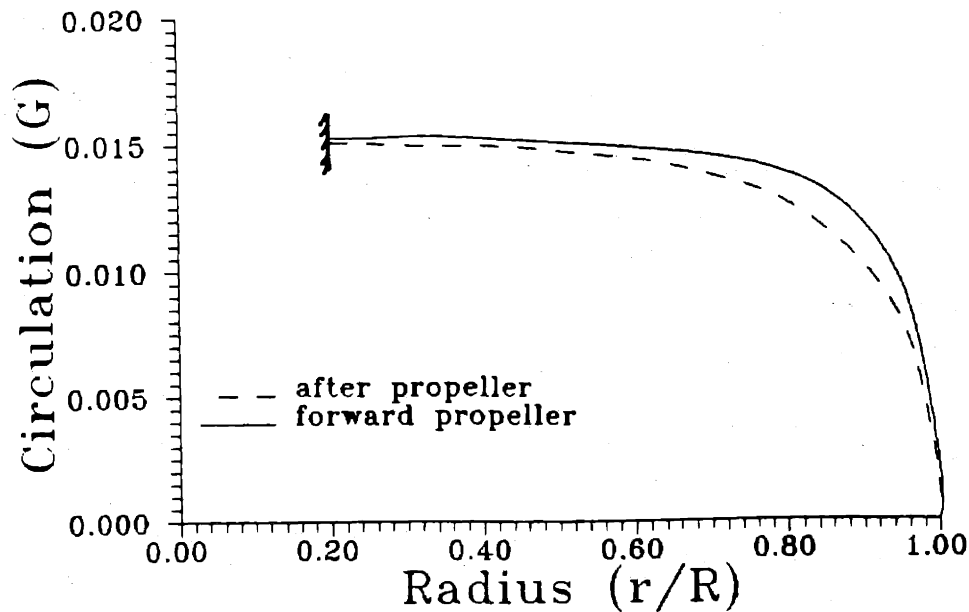


Figure 3.7: Optimum circulation distributions for a pair of hub loaded contrarotating propellers.

$C_T = 0.69$. Both propellers are 4 bladed and are required to develop equal torque. The moderately loaded model is employed and viscous forces neglected.

Note that the circulation distributions reach their maximum values at the hub. Further note that the circulation developed at the hub by the two propellers is equal. This results in a nearly complete cancellation of the hub drag term. The hub loaded circulation distributions presented here are predicted to yield an efficiency of 0.847 vs. 0.841 for a hubless propeller from the model used in chapter 2.

In a similar manner hub drag terms can be added to the optimization equations 2.66-2.68 for the propeller/stator. Figure 3.8 gives circulation distributions from this procedure. Again note the large hub loading. As for the contrarotating pair, there is a nearly complete cancellation of the hub drag term. The particulars for this propeller stator are the same as those for the propeller/stator of chapter 2. The hub loaded circulation distributions give an efficiency of 0.829 vs. 0.811 for the hubless model.

3.1.4 The Equivalent Propeller

For the single propeller there is no possibility of such circulation cancellation. Therefore, in order to reduce the hub drag, the circulation at the inner radii is usually arbitrarily reduced from the optimum distribution predicted under the hub loaded model. This

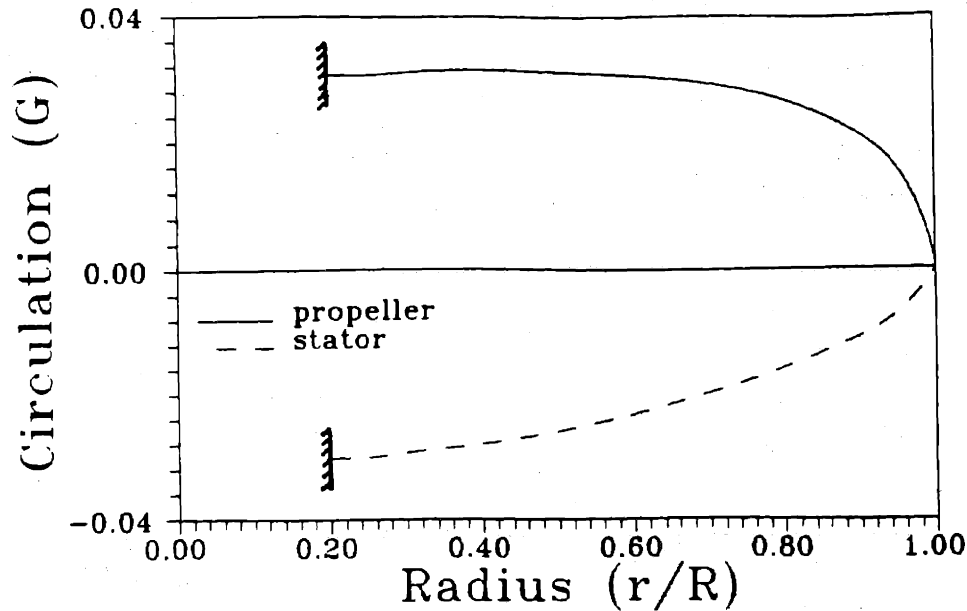


Figure 3.8: Optimum hub loaded circulation distributions for a propeller stator.

is often accomplished by simply neglecting the presence of the hub altogether when determining the desired circulation distribution. The requirement of zero circulation at the hub imposed by Lerbs [73] and Tachmindji [102] seems more attractive in the light of a consideration of hub drag.

The addition of hub drag terms to the optimization equations proved unsuccessful for the single propeller. In the formulation employed here, the hub drag is linked to the circulation at the innermost control point. The optimization process consistently found the circulation at this control point to be zero, while not significantly altering the circulation of the other control points from that of the hub loaded optimum. This resulted in a procedure which was not convergent with increased numbers of vortex horseshoes.

Wald [117] pointed out that the treatment of the optimum propeller with a hub as an infinitely long cylinder, was not correct, since this did not correspond to the geometry of the ultimate wake where the Betz condition must be imposed. Wald assumed that the Betz condition for optimum propeller loading must apply in the ultimate slipstream where the inner boundary has shrunk to zero radius. Wald presented a solution for the infinite bladed propeller, as well as approximate solutions for finite numbers of blades. In Wald's solutions the circulation at the hub of the optimum propeller was zero.

Andrews and Cummings [3] proposed the use of an equivalent propeller, of zero hub diameter, located far downstream. Optimum circulation distributions were determined

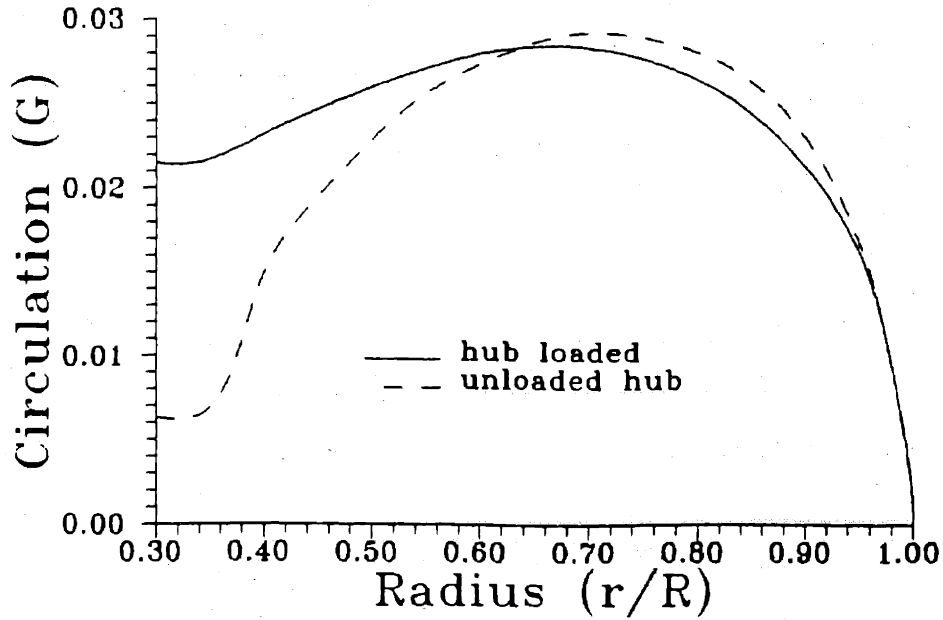


Figure 3.9: Hub loaded circulation distribution and a circulation distribution unloaded through use of an equivalent propeller.

for this equivalent propeller and the streamlines were traced back to the desired hub diameter to find circulation distributions of the actual propeller. This procedure had the advantage of allowing the use of existing lifting line tools for the determination of optimum circulation distributions.

A similar idea is proposed here. Rather than zero hub diameter, the hub diameter of the equivalent propeller is taken to be that of the concentrated hub vortex. This will result in small, but finite, circulation at the hub. Since vorticity is convected downstream with the flow, an application of continuity can be used to relate the circulation distribution of the equivalent propeller to that of the actual propeller. If velocities induced by the propeller are neglected, and the inflow is assumed to be circumferentially uniform,

$$\int_{r_{he}}^{r_e} \pi r V_{a_e}(r) dr = \int_{r_h}^{r_p} \pi r V_{a_p}(r) dr. \quad (3.15)$$

The subscript e here is used to refer to the equivalent propeller, p to the actual propeller. In the case of uniform axial inflow, this is simply reduced to a conservation of area

$$r_e^2 - r_{e_h}^2 = r_p^2 - r_h^2. \quad (3.16)$$

Figure 3.9 shows an optimum, hub loaded circulation distribution and a circulation distribution unloaded by finding an optimum distribution for an equivalent propeller

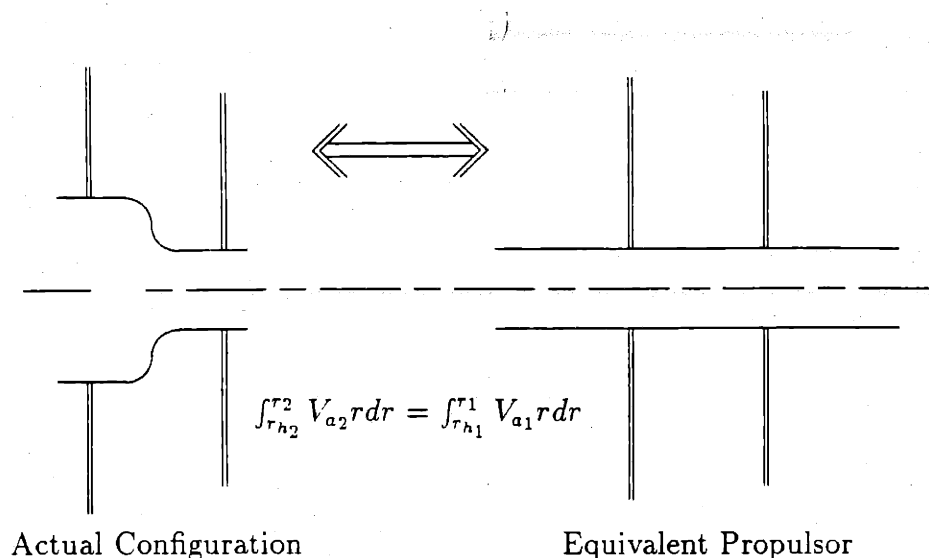


Figure 3.10: A sketch of a two stage propulsor whose components have different hub diameters.

and then relating that distribution back to the diameter of the actual propeller. The propellers are 4 bladed, operate in uniform inflow at $J_S = 0.69$, have a hub diameter of 30% of the propeller diameter and are required to develop a thrust of corresponding to $C_T = 0.69$. The diameter of the concentrated hub vortex was assumed here to be 5% of the propeller diameter. Viscous forces were neglected and the moderately loaded wake model was employed. The diameter of the hub vortex was also used as the hub diameter of the equivalent propeller. Note that the equivalent propeller procedure did result in the desired unloading of the hub, as well as preserving the condition of zero slope of the circulation distribution as the hub is approached. In this case the efficiency of the hub loaded propeller is predicted to be 0.752 when the hub drag is included, while that of the hub unloaded propeller is 0.777. This is an increase in efficiency of over 3 percent associated with unloading the hub.

It should be pointed out here that similar results can be obtained simply by ignoring the presence of the hub when determining the optimum circulation distribution, and then forcing a zero slope condition at the hub of the resulting circulation distribution. Of course, deciding how much of the circulation distribution to modify and what the loading at the hub should be, can prove problematic with such an ad hoc procedure. In chapter 4 a procedure is presented whereby the propeller designer can unload a circulation distribution to suit whatever requirements are imposed.

The idea of an equivalent propeller can also be used to address the problem of multiple stage propulsor components which do not have a common hub diameter. Such a propulsor is sketched in figure 3.10. This situation is not uncommon. However, in the present lifting

line model, components are assumed to share a common hub. It is appropriate to change the diameter of one of the propulsor components so that an equivalent propulsor with a single hub diameter is obtained. The optimum circulation distribution of the modified component can then be related back to the diameter of the actual component by a application of equations 3.15 or 3.16.

3.2 Ducted Propellers

The idea of surrounding a propeller by a duct or nozzle is quite old. Ducted propellers came into practical use after Stipa [101] and Kort [67] showed experimentally that propulsive efficiency could be increased by use of a duct in the case of heavy propeller loading. The use of ducted propellers on ships which require such propeller loadings, tugs, push-boats, trawlers, etc., has become common practice. These ducted propellers are often referred to as "Kort" nozzles.

Some insight into the increased efficiency of heavily loaded ducted propellers over propellers operating alone, may be obtained from the actuator disc arguments put forth by Küchemann and Weber [69]. In this theory the propeller is modelled by a constant pressure jump at the actuator disc, and the propulsive system of duct and propeller imparts a uniform acceleration to all the fluid passing through it. The fluid is assumed to be inviscid and incompressible and there is an unlimited, uniform, steady inflow of fluid to the propulsor. The thrust developed by the propeller is allowed to be different from the net thrust of the system. Therefore, a thrust ratio, τ , is defined as

$$\tau = \frac{T_p}{T} = \frac{\text{Propeller Thrust}}{\text{Total Thrust}}. \quad (3.17)$$

Küchemann and Weber show that the efficiency of such an actuator disc system is given by

$$\eta_I = \frac{2}{1 + \sqrt{1 + \tau C_T}}. \quad (3.18)$$

The thrust coefficient is determined from the total thrust.

$$C_T = \frac{2T}{\rho A_0 V_S^2}. \quad (3.19)$$

The velocity at the actuator disc is given by

$$\frac{V_S + u_a}{V_S} = \frac{C_T}{2\sqrt{1 + \tau C_T} - 2}. \quad (3.20)$$

When $\tau = 1$, equation 3.18 and 3.20 recover the actuator disc results for a traditional propeller. Note that an increased efficiency is predicted when τ is reduced. As the thrust

ratio is lowered, the portion of the total thrust carried by the duct is increased. This corresponds to an acceleration of the flow at the actuator disc over that from actuator disc theory for a traditional propeller. Such a duct is known as an accelerating duct.

Decelerating ducts, $\tau > 1$, have also been proposed. While the efficiency from equation 3.18 is reduced for such a ducted propeller, the lower velocities at the propeller plane may prove advantageous for reasons of cavitation reduction. A ducted propeller system of this type is sometimes referred to as a pumpjet. In this case the duct experiences a negative thrust, or drag, force.

Equation 3.18 also shows why ducted propellers have most often been applied in the case of heavy loading. Since the term which describes the effect of the duct, τ , is multiplied by the thrust coefficient, the duct effect is largest for large values of C_T . If the actual duct must develop enough thrust to provide an efficiency gain once duct viscous losses are accounted for, such gains can be readily realized only in the case of heavy loading.

Numerous practical and experimental investigations of ducted propellers have been performed. Those of van Manen [113] [115], Oosterveld [88] and Dyne [29] serve as examples. As methods for the design and analysis of traditional propellers have become more sophisticated so have those for ducted propellers. This trend can be seen in the reviews by Sacks and Burnell [95] and by Weissinger and Maas [120], and by way of example in the increasingly sophisticated procedures of Dyne [28], Morgan [81] [82], Glover and Ryan [39], Tsakonas and Jacobs [107], Falcão de Campos [31], van Houten [109] and Kerwin et al [62].

3.2.1 Lightly Loaded Ducted Propellers

Several researchers have proposed procedures for determining optimum circulation distributions for ducted propellers in the limit of light propeller loading. Tachmindji [103] solved the potential problem for the circulation distribution which satisfied the Betz condition on the vortex sheets, and the condition of zero normal velocity on an infinite cylinder representing the duct. He presented load distributions which showed increased tip loading as the gap between duct and propeller tip was decreased. In the case of zero gap between duct and propeller, Tachmindji presented a circulation distribution which fell off rapidly from its maximum value to zero in the vicinity of the propeller tip.

Sparenberg [97] [98] solved the potential problem for the circulation distribution which satisfied the Betz condition on the vortex sheets shed from both the propeller and duct. In this case the duct vorticity was assumed to rotate with the propeller. Sparenberg presented optimum bound circulation distributions for the duct and propeller for the zero gap case. This result had finite loading at the propeller tip, with the maximum circulation achieved there. Sparenberg demonstrated that in the limit of light loading any acceleration or deceleration of the flow due to the duct is of second order and, thus,

does not change the efficiency of the optimum propeller under linear theory. Sparenberg [100] also showed that, in this limit, the propulsor efficiency is bounded by that of the traditional actuator disc.

George [35] made use of the Lerbs criteria to determine optimum circulation distributions for a zero gap ducted propeller. In George's model the duct was represented by ring vortices which varied in strength both axially and circumferentially. The circumferential variation in strength of these ring vortices necessitated the use of vortices shed from the duct cylinder to model the trailing duct vorticity. For this purpose George employed axially oriented, semi-infinite, line vortices. He presented circulation distributions which had finite loading at the tip, but did not reach their maximum value there. George made no mention of forces experienced by the bound ring vortices used to represent the duct.

In the present theory the duct will also, for the time being, be modeled as an infinite cylinder. As for the hub, an image system of vorticity is used to represent the duct. In this case the radius of the image vortices is chosen such that

$$r_i = \frac{r_d^2}{r}. \quad (3.21)$$

Here r is the radius of the helical trailing vortex shed from the lifting line, r_i is the radius of its image, and r_d is the radius of the duct cylinder. It is assumed that such a system will approximately satisfy the condition of zero radial velocity on the duct cylinder.

As was the case for the hub, the velocity influence functions must be modified to account for the presence of the duct. This is accomplished by adding to the velocity induced by a unit strength horseshoe vortex, that induced by its image.

$$[\bar{u}_a^*(n, m)]_{\text{total}} = \bar{u}_a^*(n, m) + [\bar{u}_a^*(n, m)]_{\text{image}}, \quad (3.22)$$

$$[\bar{u}_t^*(n, m)]_{\text{total}} = \bar{u}_t^*(n, m) + [\bar{u}_t^*(n, m)]_{\text{image}}. \quad (3.23)$$

These influence functions which include the effect of the image vortex system can then be used in the optimization equations of chapter 2.

The vortex lattice itself must also be modified. When there is no duct, the outermost panel is inset one-quarter panel length in order to correctly capture the singular behavior of the circulation distribution. This is clearly not the correct tip inset when there is zero gap between duct and propeller. In this case there should be no inset. In the case of a propeller operating inside of a duct with small, but finite, gap, there should be some "optimum" tip inset between zero and one-quarter panel length, as the gap varies from zero to infinity.

Van Houten [109] performed numerical experiments with a lifting line approaching a wall in order to determine this "optimum" inset. His experiments were performed on a lifting line foil with optimum loading, in the sense that the induced drag was a minimum for given lift. The "exact" circulation distribution was found for this case by using a

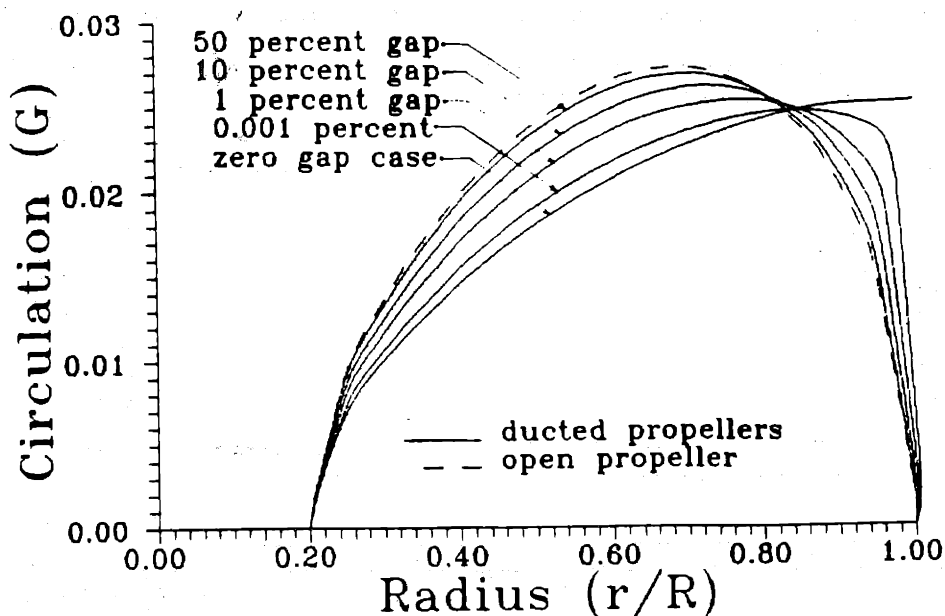


Figure 3.11: Optimum circulation distributions for propellers operating inside of cylindrical, "image" ducts.

large number of vortex segments (400) and requiring the downwash to be a constant at all control points. The solution was then repeated with a small number of vortices, and the inset was varied until a solution was obtained with the smallest mean squared error between the calculated vortex strengths and the "exact" solution at the corresponding control points. Fitting a curve to his results van Houten obtained the following formula for the tip inset.

$$\frac{\Delta r_i}{\Delta r} = \begin{cases} 0.30(g/\Delta r)^{0.178} & \text{for } g/\Delta r < 0.359, \\ 0.25 & \text{otherwise.} \end{cases} \quad (3.24)$$

Δr_i is the tip inset, Δr is the length of the panel and g is the gap length. This is the spacing algorithm employed with the present theory in the case of ducted propellers.

Figure 3.11 shows optimum circulation distributions for propellers represented by such a lifting line/image system. In this case the inflow is taken to be uniform. $J_S = 0.89$. $C_T = 0.69$. The propellers are 5 bladed. Viscous forces are ignored and the wake is aligned under the moderately loaded model. The individual curves are for different gaps between the propeller tip and the duct cylinder. Note that for large gaps the circulation approaches that of a propeller operating without a duct. As the gap is decreased, the circulation distribution becomes more tip loaded. In the limit of zero gap the circulation at the tip is finite, reaching its maximum value there. These results agree qualitatively

	K_T	K_Q	η
no duct	0.2147	0.0384	0.791
50% gap	0.2147	0.0384	0.792
10% gap	0.2147	0.0381	0.799
1% gap	0.2147	0.0377	0.807
0.1% gap	0.2147	0.0376	0.809
0.01% gap	0.2146	0.0373	0.815
0.001% gap	0.2146	0.0372	0.818
no gap	0.2148	0.0369	0.825

Table 3.2: Forces acting on optimum propellers operating inside of cylindrical “image” ducts. The gap between propeller tip and the duct surface is given as a percentage of the propeller diameter.

with those presented by Tachmindji [103] in the case of finite gap, and Sparenberg [97] in the zero gap case.

Table 3.2 gives the forces generated by the circulation distributions of figure 3.11. Note that as the gap is decreased the propeller efficiency is increased. This efficiency gain is due the increased tip loading brought about by the presence of the duct images. This tip loading is made possible by a cancellation by the image system of the axial induced velocities near the propeller tip. In the case of zero gap, the tip vortex is cancelled altogether by its image. Thus, the finite value of circulation at the tip. Similar results are found for a wing approaching a wall [62].

The lifting line representation of the propeller can also be combined with a more sophisticated representation of the duct. Kinnas and Coney [66] do so by using a potential based panel method to represent the duct. Figure 3.12 shows such a panel method representation of the duct and propeller lifting lines. Velocities induced on the lifting line control points, by the duct panels, in the presence of unit strength, helical, vortex horseshoes, are determined. These velocities are added to those induced by the vortex horseshoes in the absence of the duct as determined by the present lifting line model.

$$[\bar{u}_a^*(n, m)]_{\text{total}} = \bar{u}_a^*(n, m) + [\bar{u}_a^*(n, m)]_{\text{panel method}}, \quad (3.25)$$

$$[\bar{u}_t^*(n, m)]_{\text{total}} = \bar{u}_t^*(n, m) + [\bar{u}_t^*(n, m)]_{\text{panel method}}. \quad (3.26)$$

The inflow to the propeller lifting lines is further modified to account for the velocities induced by the duct in the absence of any horseshoe vortices, as predicted by the panel method. This modified inflow and influence functions can be used inside of the optimization equations of the previous chapter.

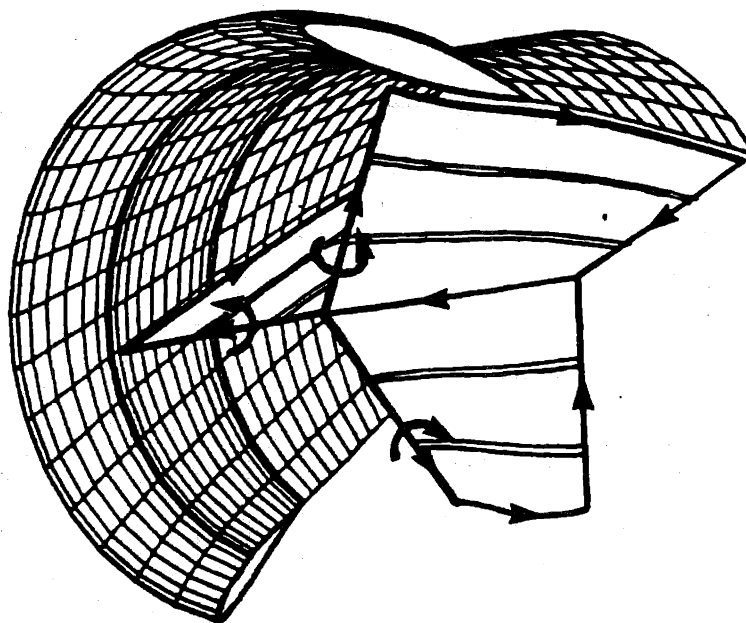


Figure 3.12: Panel method representation of the duct and lifting line.

The described procedure finds the optimum radial circulation distribution on a propeller operating inside of a given axisymmetric duct. The panel method provides the thrust or drag generated on the duct, however, variations of the duct force with the propeller circulation distribution are neglected in the optimization procedure.

Figure 3.13 gives a comparison of optimum circulation distributions for a zero gap ducted propeller with induced velocities from the panel method and from an image vortex system. $J_S = 1.143$. $C_T = 0.45$. The inflow to the duct is uniform. The wake is aligned under linear theory. Viscous effects are neglected. The duct geometry used in the panel method is described in [66]. The inflow velocities to the propeller in the image model are those induced by the duct operating in the absence of the propeller. Note the excellent agreement between the two models. This agreement is reassuring, since the panel method procedure is much too computationally intensive to be of great utility when performing parametric studies of various propulsor configurations.

Further confidence in the image model can be gained by comparing the velocities induced by the image system with those from a more complete representation of the propeller and duct. It is hoped that the image system correctly captures the local interaction velocities between the duct and propeller at the lifting lines. Figure 3.14 shows velocities at the plane of the propeller operating with zero gap between the propeller tip and the duct surface. The geometry and operating conditions for this case are described in chap-

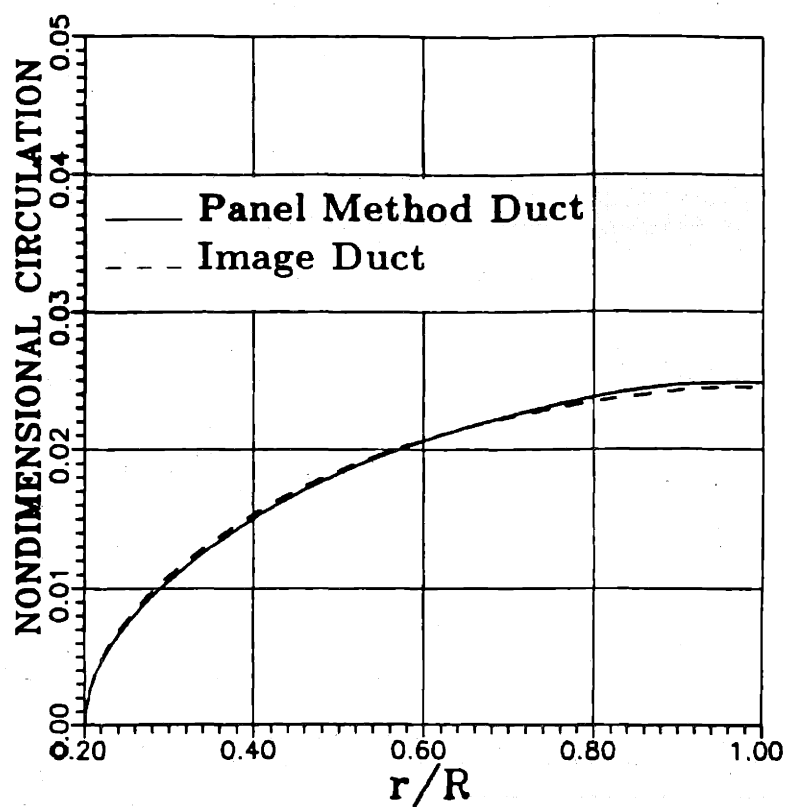


Figure 3.13: Optimum circulation distributions for a zero gap ducted propeller as determined from image and panel representations of the duct.

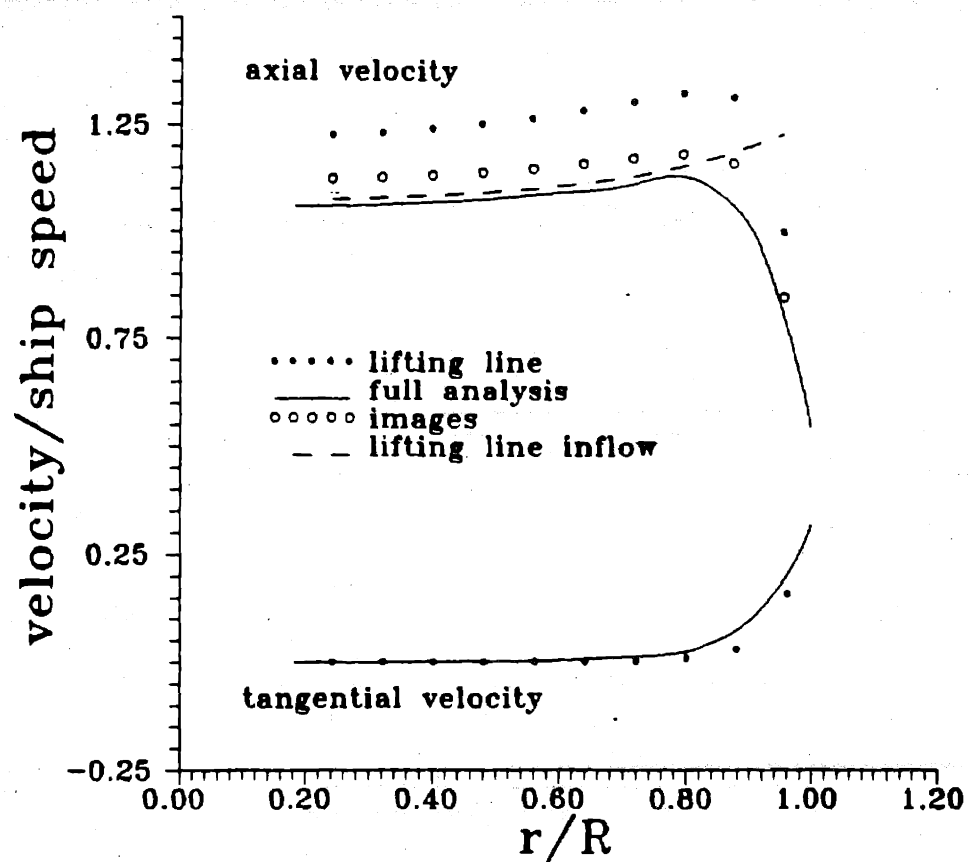


Figure 3.14: Duct interaction velocities at the lifting line.

ter 6. The velocities shown in this figure do not include the propeller's self induction, but do include the inflow and all duct effects. Velocities calculated by the analysis method described in [62] are shown, as are velocities calculated with the system of image vortices. The inflow to the image system is taken to be the flow at the plane of the propeller in a duct subject only to the uniform incoming flow, without the presence of the propeller. Note that while the fully analyzed flow differs quantitatively from that predicted by the image system of lifting lines, the images capture the local tip effect reasonably well. The differences in the overall flow can be attributed to details of duct geometry.

3.2.2 Duct Forces

Under the linear, lightly loaded model of the ducted propeller the acceleration or deceleration of the flow due to the duct does not change the efficiency of the propeller/duct system. This result was obtained by Sparenberg [97] and can be readily deduced from a Trefftz plane analysis. Lightly loaded theory relies on forces acting on elements of circulation placed in the flow infinitely far downstream of the propeller, the Trefftz plane. The addition of a rotationally symmetric flow at the plane of the propeller does not create any disturbance velocities far downstream. Thus the optimum circulation distribution and the propulsor efficiency determined by an analysis carried out there is not effected by the accelerating or decelerating nature of the duct.

This result stands in sharp contrast to the duct model of actuator disc theory, in which any efficiency gains associated with the duct are linked to the thrust developed on the duct. In the combined lifting line/panel method representation of the duct, duct forces are predicted [66]. This method is of limited practical usefulness, however, due to its computational expense. Some other, more computationally efficient, approach which combines lifting line theory with a simple representation of the duct is, therefore, necessary.

In order to provide an estimate of the total duct forces, and to predict any acceleration or deceleration of the flow at the propeller, a system of ring vortices at the radius of the duct cylinder is added to the lifting line/image duct model. The continuous axial distribution of duct vorticity is modelled by a system of discrete ring vortices. The location of these ring vortices is selected so that the distance between them is nearly the same as the lengths of the bound vortex segments used to represent the propeller. the location of these duct rings is further chosen so that the lifting lines representing each propulsor component fall at the center of the interval between a pair of vortex rings representing the duct bound vorticity. A schematic of this vortex system is given in figure 3.15. The strengths of these ring vortices are selected such that they are a discrete representation of either a NACA $a = 0.8$ meanline [1] or a sinusoidal distribution of vorticity over the length of the duct.

The duct ring vortices model the axisymmetric mean modification of the inflow to the

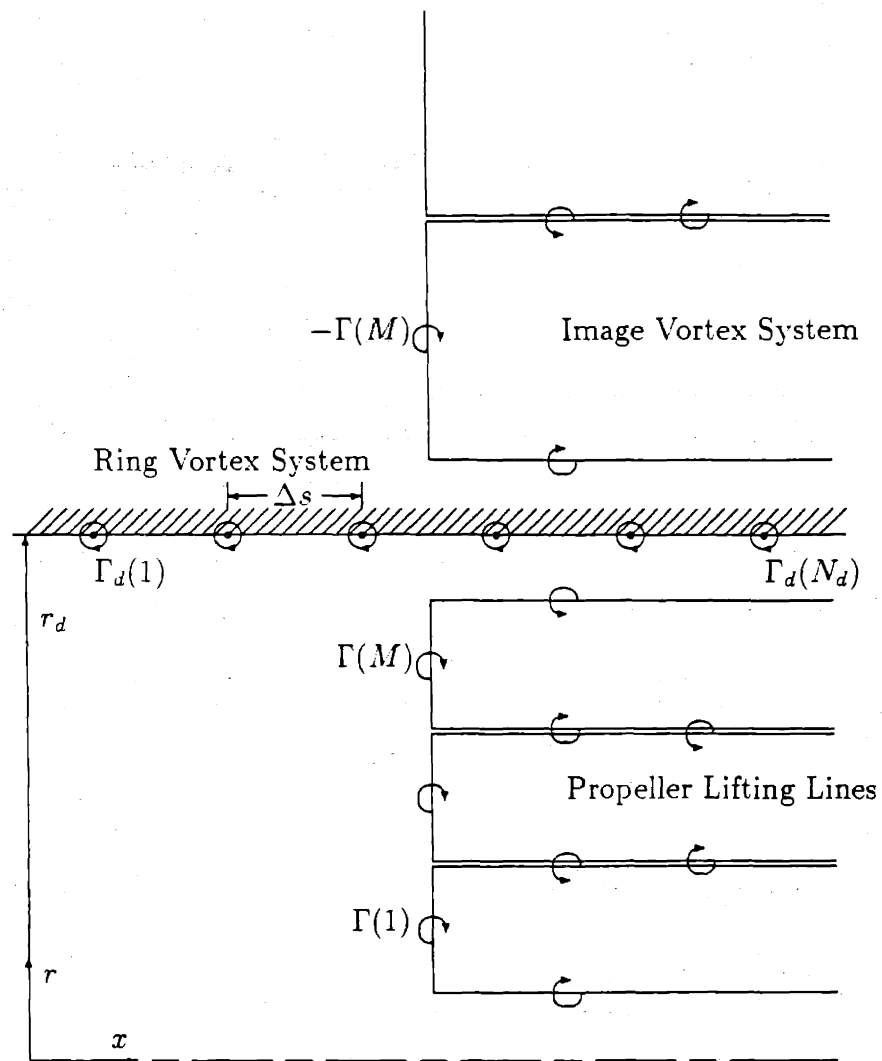


Figure 3.15: Schematic of the propeller/duct vortex system.

propeller due to the duct's vorticity, as well as providing duct forces. The image system models the nonaxisymmetric effect of the duct on the velocity influence functions. A similar representation of the duct bound vorticity was employed by Oosterveld [88] with a much simpler representation of the propeller. George [35] also modelled the bound vorticity in a similar manner, but made no mention of duct forces.

The velocity induced at the propeller by each of the ring vortices is calculated in terms of elliptic integrals as described by Küchemann and Weber [69]. Under the discrete model employed here, the axial component of velocity at the propeller lifting line control point i is given by a summation of the velocities induced by the individual ring vortices.

$$u_{a_{pd}}(i) = \sum_{n=1}^{N_d} \bar{u}_{a_{pd}}^*(i, n) \Gamma_d(n). \quad (3.27)$$

N_d is the number of ring vortices used to represent the duct. $\Gamma_d(n)$ is the strength of the n th ring vortex. $\bar{u}_{a_{pd}}^*(i, n)$ is the velocity induced by the n th vortex ring, of unit strength, on the i th propeller lifting line control point. The ring vortices induce no tangential velocity component and the radial velocities do not create any force on the propeller lifting lines.

The force acting on the rings is found from an application of the Kutta-Joukowski law with the viscous drag estimated through use of a two-dimensional airfoil sectional drag coefficient. The total thrust force acting on the duct is simply a summation of the axial forces acting on the individual rings.

$$T_d = -2\rho\pi r_d \sum_{n=1}^{N_d} \left\{ [V_r(r_d) + u_r(n, r_d)] \Gamma_d(n) + [V_a(r_d) + u_a(n, r_d)] c_d C_{D_d} \right\} \Delta s. \quad (3.28)$$

The axial and radial component of velocity, $u_a(n, r_d)$ and $u_r(n, r_d)$, induced by the propeller on the n th ring vortex is considered to be the circumferential mean induced velocity. This velocity is efficiently computed from the formulas of Hough and Ordway [49]. Δs is the spacing between the rings, c_d is the duct chord length and C_{D_d} is the duct sectional drag coefficient.

Optimum circulation distributions for such a duct/propeller system are determined by use of the previous chapters optimization equations. The inflow velocities are modified to include the velocity induced by the duct rings, and the influence functions include the effects of the image horseshoes. The thrust developed on the duct is subtracted from the required thrust in the same manner that the propeller's viscous drag is added to the required thrust. An iterative procedure is employed such that a specified ratio of propeller thrust to total thrust, τ , is achieved. On each iteration of the solution of the circulation optimization equations, a new estimate of the total duct circulation needed to provide the desired duct thrust is employed. While the optimum circulation distribution determined in this manner arrives at the desired thrust distribution it does not take

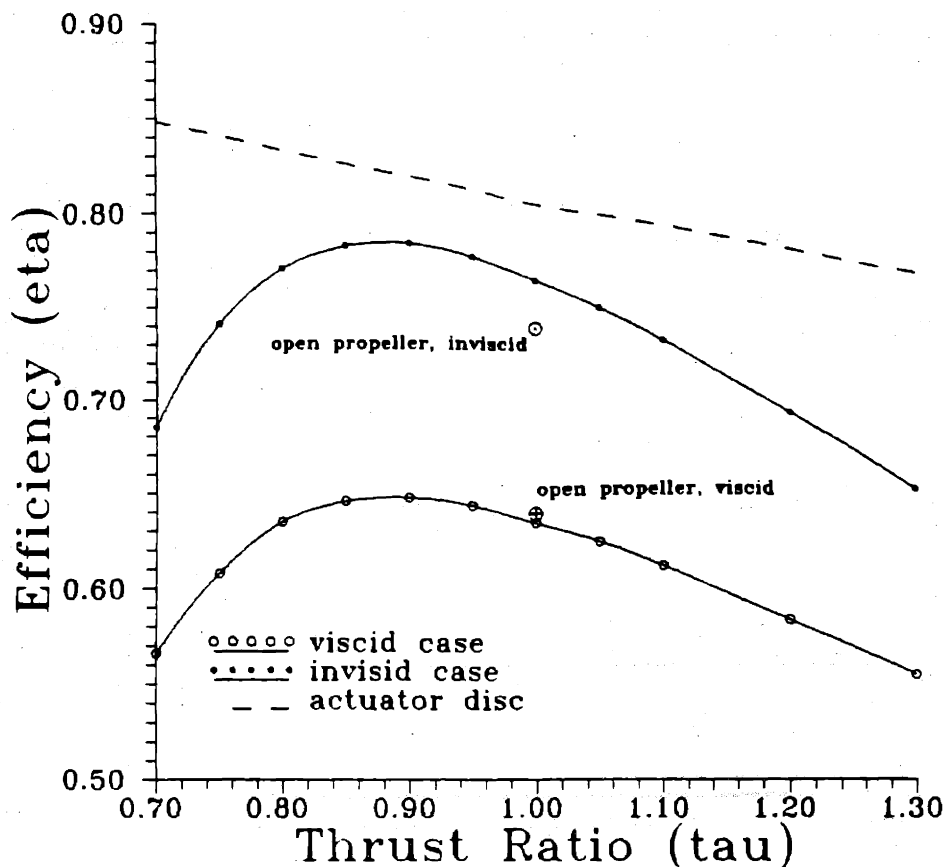


Figure 3.16: Efficiency vs. thrust ratio for optimum ducted propellers as determined by the current procedure.

account of the variation of duct thrust with respect to the unknown propeller circulation distribution.

This model for the ducted propeller is in some respects analogous to the moderately loaded and wake adapted theories for a propeller operating in the absence of a duct. The pitch of the trailing vortices shed from the propeller is here aligned with the inflow and the velocities induced by the system of ring vortices. The wake can be further aligned with the lifting line's self induced velocity field. Since the pitch of the helices changes with the velocity induced by the ring system, we expect the propeller forces and the overall propulsor efficiency to change as the duct circulation is varied.

Figure 3.16 gives the overall propulsor efficiency vs. thrust ratio, as determined by the present model for ducted propellers with optimum circulation distributions. $J_S = 0.60$. $C_T = 1.20$. The inflow to the propeller is assumed to be uniform and moderately loaded wake alignment is employed. There is zero gap between the duct cylinder and the

propeller blade tip. The duct length is one-half the propeller diameter and the propeller is located at the midchord axial location of the duct. The chordwise distribution of duct vorticity is assumed to be that of a NACA $a = 0.8$ meanline [1]. Results with the viscous forces neglected and with viscous forces included are presented. When viscous drag is considered typical propeller chord lengths and drag coefficients are assumed. The duct drag corresponds to a two-dimensional sectional drag coefficient of 0.0085.

Note in figure 3.16 that the efficiency for both the viscid and inviscid cases is reduced as the thrust ratio is increased, for $\tau > 1$. This trend agrees qualitatively with the actuator disc result also presented in figure 3.16. As the thrust ratio is lowered from $\tau = 1$ the efficiency increases until a maximum value is reached and then falls. This is not in agreement with the actuator disc model, in which the efficiency continues to rise. As the thrust ratio is decreased, the thrust generated by the duct must increase, and, thus, the duct loading and the velocity induced by the duct at the propeller plane are increased. The actuator disc model and the ring vortex model both predict increased axial velocities at the propeller plane as the thrust ratio is lowered. In the actuator disc model no penalty is paid for this increased axial velocity. This is not the case, however, when finite blade effects are considered in the lifting line model. As the axial velocities at the lifting lines increase the "effective" advance ratio increases. As seen in the previous chapter propeller efficiency is reduced as the advance ratio, and, thus, the finite blade effects, is increased.

The tradeoff between this finite blade effect, and reduced propeller loading as it is taken up by the duct, results in the efficiency maximum. This yields an optimum value of duct loading of approximately $\tau = 0.9$ in the presented case. Previous investigators [115] [88], who relied on actuator disc models of the propeller, have used arguments involving separation from the duct surface to explain experimental results which show this same trend.

The efficiency of unducted propellers under both the viscid and inviscid models is also given in figure 3.16. When viscous forces are neglected, a clear gain in efficiency is predicted for the ducted propulsor over the open propeller for most thrust ratios. At $\tau = 1$ this efficiency gain is due entirely to the increased loading at the propeller tip made possible by the tip vortex cancellation. Efficiency gains are nowhere near as dramatic when the viscous drag is considered. This is because a relatively large drag force is experienced by the duct. Larger gains over the open propeller are anticipated for lower J_S and larger C_T .

It should be noted that in the present procedure the effect of duct thickness has so far been neglected. Since ducts are often quite thick relative to their chord, 15% or more, thickness effects on the velocity field can be significant. A simple method for including this thickness effect is to modify the inflow velocity field at the propeller plane, so that it is the same as that produced by a duct with the desired thickness distribution and zero angle of attack and camber. This propeller inflow velocity field can come from

	K_T	K_Q	C_T duct	C_T total	τ
<i>zero gap case</i>					
lifting line	0.283	0.0514	0.1051	2.105	0.950
full analysis	0.286	0.0509	0.1027	2.126	0.952
<i>five percent gap case</i>					
lifting line	0.193	0.0515	0.0690	0.690	0.900
full analysis	0.191	0.0515	0.0743	0.690	0.892

Table 3.3: Total forces acting on two optimum ducted propellers.

experiment or be calculated by a procedure such as a panel method. Since a single panel method run can be used for all duct and propeller geometries which share a duct thickness distribution, the computational expense of such a procedure should not be prohibitive.

Table 3.3 presents forces acting on two ducted propellers with optimum circulation distributions determined through the described procedure. In one case there is no gap between the blade tip and the inner surface of the duct, in the other there is a gap of five percent of the propeller diameter. Details of the operating conditions and the propeller and duct geometries are provided in chapter 6. In both cases the axisymmetric inflow due to the duct thickness alone was found by use of the panel method described in [62]. Forces are presented for optimum lifting line circulation distributions, and from the analysis method of [62] with blade and duct geometries chosen to, as near as possible, have the lifting line circulation distributions. Again, more details can be found in chapter 6. Note that the lifting line results compare favorably with those of the full analysis.

3.2.3 Multiple Stage Ducted Propellers

Multiple stage ducted propellers are also of interest. Ducted propeller/stator combinations are perhaps the most natural, since the stator blades can also serve as the struts which support the duct. Such combinations have been proposed for the purpose of increasing propulsive efficiency [104] and to protect the propeller from ice damage [121].

The image/ring representation of the duct can be combined with the vortex lattice model of chapter 2 for multiple stage propulsors. In the present work this has been done for the case of two propulsor stages. It is also a relatively simple matter to include an image representation of the hub in addition to that of the duct. Since hub loading resulted in efficiency increases under the lifting line model for the case of two stage propulsors, the image hub model is incorporated in the present work.

Figure 3.17 presents optimum circulation distributions for a propeller/preswirl stator operating inside of a duct. There is no gap between the tip of the stator blades and the

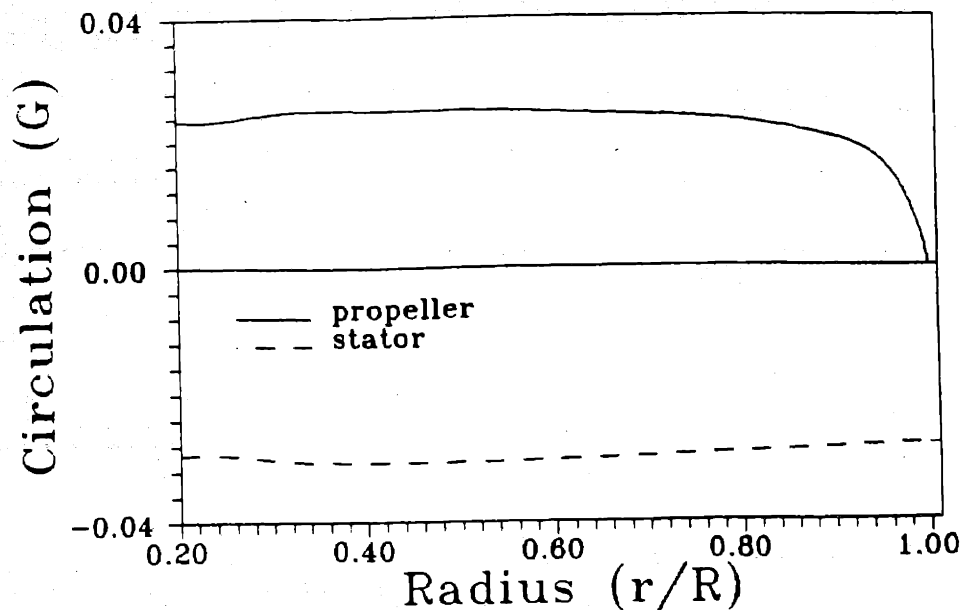


Figure 3.17: Optimum circulation distributions for a ducted propeller/preswirl stator.

duct while there is a gap of one percent of its diameter for the propeller. Note that, as anticipated, the stator circulation is nonzero at the tip, while that of the propeller vanishes. Since the image hub is included here, the circulation at the hub of both the propeller and stator is nonzero, but the circulation distributions have zero slope there.

The circulation distributions of figure 3.17 are for a 5 bladed propeller and a 4 bladed stator. The inflow to the system is uniform with $J_S = 0.6$ and $C_T = 1.2$. The wake was aligned under the moderately loaded model. Viscous forces were considered with typical values of c and C_D assumed for the propeller. The chord length of the duct is one-half the diameter of the propeller. $C_{D_a} = 0.0085$. The stator is located at the one-quarter chord location of the duct, the propeller at the three-quarter chord location. The chordwise duct distribution of vorticity is assumed to be that of a NACA $a = 0.8$ meanline [1]. Ten percent of the total thrust is generated on the duct, $\tau = 0.9$. The efficiency of this ducted propeller/stator is predicted to be 0.671 vs. 0.641 for an open propeller at the same operating condition.

Chapter 4

Other Considerations

In this chapter algorithms which have been added to the previously described lifting line model are described. These algorithms allow the propeller designer to estimate such quantities as chord lengths and thickness distributions. These algorithms, and the lifting line model and optimization procedures of chapters 2 and 3, are together implemented in a computer program [23] called MIT-PLL, referred to here as PLL. PLL can be used to evaluate forces produced by a given circulation distribution, as well as to determine optimum circulation distributions with the methods of chapter 2.

PLL was conceived as a tool for the preliminary design and evaluation of marine propulsors. As such, much effort was expended in making this code both fast and simple to use. The procedures described here were required to be both computationally efficient and to need a minimum of additional data.

4.1 Minimum Chord Lengths

The radial distribution of chord length is a necessary input to the viscous force calculations of the circulation optimization procedure, as well as to any final propeller design. In order to minimize viscous drag forces it is desirable to keep propeller chord lengths as short as possible. However, strength and cavitation considerations place limits on how short these chord lengths may become. PLL can compute a radial distribution of chord length which minimizes viscous drag and ensures a fair blade shape, while meeting some simple constraints on cavitation and strength.

Smooth chord distributions are obtained by defining the chord shape with a third order b-spline [93]. The b-spline is described by either four or five vertices which, in the case of an unducted propeller or nonzero gap between duct and propeller, define a chord distribution varying from a root chord length at the hub to zero at the tip. The location of the b-spline vertices are adjusted until the chord lengths are everywhere greater than

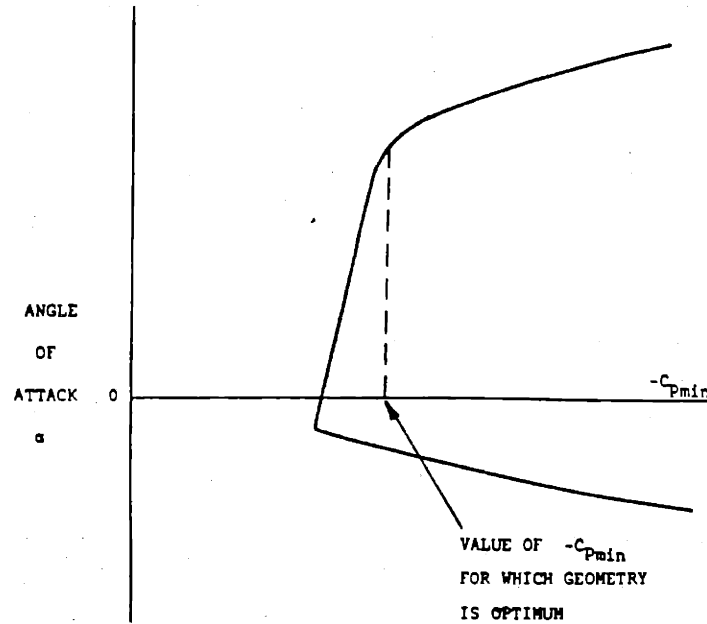


Figure 4.1: Illustration of a cavitation “bucket” with the optimum operation point indicated.

the minimum values obtained from the strength and cavitation considerations described below. For a ringed or zero gap ducted propeller, the chord is no longer zero at the propeller tip.

4.1.1 Cavitation Constraint

For the purpose of determining minimum chord lengths, the propeller foil section is assumed to be a NACA 66 (TMB modified nose and tail) thickness form [7] with a NACA $a = 0.8$ meanline [1]. Brockett [7] presents figures showing minimum pressure coefficient versus angular variation in angle of attack for these sections. These figures are known as “bucket” diagrams. Optimum values of the minimum pressure coefficient which allow for the largest variation in angle of attack, for the smallest value of the minimum pressure coefficient can be read from these bucket diagrams.

Brockett generated a figure giving the thickness to chord ratio and camber to chord ratio as functions of the minimum pressure coefficient, such that the optimum location in the bucket diagram is achieved. Kroeger [68] mapped this figure to the following equation, setting the local cavitation number, $\sigma(r)$, equal to the minimum pressure coefficient.

$$\sigma(r) = 26.67 \left(\frac{f(r)}{c(r)} \right)^2 + 8.09 \left(\frac{f(r)}{c(r)} \right) + 10.0 \left(\frac{f(r)}{c(r)} \right) \left(\frac{t(r)}{c(r)} \right) + 3.033 \left(\frac{t(r)}{c(r)} \right). \quad (4.1)$$

$c(r)$ gives the chord distribution as a function of the radius, r , $f(r)$ gives the camber,

and $t(r)$ the thickness. Solving for the chord distribution we have:

$$c(r) = \frac{[8.09f(r) + 3.033t(r)]}{2\sigma(r)} + \frac{\sqrt{[8.09f(r) + 3.033t(r)]^2 + 4\sigma(r)[26.67f^2(r) + 10f(r)t(r)]}}{2\sigma(r)}. \quad (4.2)$$

If the camber is approximated with a linearized, ideal, two-dimensional camber then

$$\kappa \frac{f(r)}{c(r)} = C_L(r) = \frac{L(r)}{\frac{1}{2}\rho V^{*2}(r)c(r)}, \quad (4.3)$$

with $\kappa = 15.035$ for this section [1]. $C_L(r)$ is the local lift coefficient, $L(r)$ the lift force and $V^*(r)$ the local velocity. Under the lifting line model used by PLL, $L(r) = \rho V^*(r)\Gamma(r)$, thus $f(r) = 2\Gamma(r)/[\kappa V^*(r)]$. With this approximation for the camber and equation 4.2, a minimum chord length at each radius can be found given the section thickness, circulation, local velocity and cavitation number. The local cavitation number is itself simply a function of these quantities and the shaft centerline depth.

4.1.2 Additional Constraints

The thickness to chord ratio is additionally constrained to be less than some value, typically 0.2. In other words, the section thickness is required to be less than twenty percent of the chord. This is done in order to ensure the validity of typical propeller design and analysis methods to be used after the lifting line design is complete. This also allows for the use of approximate methods when computing the stresses acting on the propeller blade.

A further constraint on the chord length is supplied by placing a limit on the local lift coefficient, C_L . This has the effect of constraining the camber to chord ratio to be less than some value. This constraint is intended to model local strength and flow considerations. The maximum value of the local lift coefficient is usually chosen to be about 0.6.

A minimum chord length at the propeller root must also be specified. This is intended to reflect propeller strength considerations since stresses are usually greatest at the hub. It is suggested that either approximate stress calculations be carried out in order to determine this root chord length, or that previous propeller designs be used as a guide.

4.1.3 Chord Length Optimization Procedure

Since two of the described constraints on chord length are functions of circulation and induced velocity, and since these quantities are to some extent themselves functions of

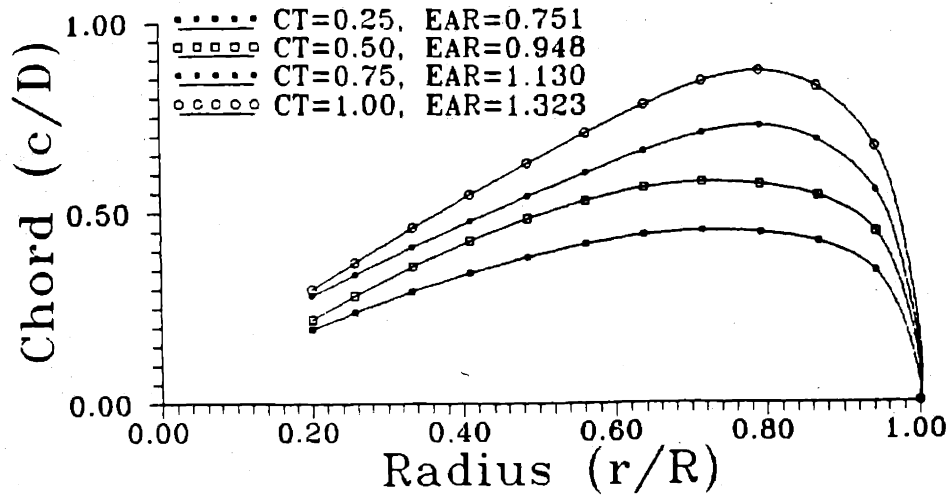


Figure 4.2: Typical chord length distributions.

the chord length, it is a natural step to make the selection of chord lengths part of the circulation optimization procedure. This is done by using the procedure described above to determine chord lengths after each circulation optimization iteration. If chord lengths are optimized, they are also updated after each iteration of the wake alignment procedure. This means that the chord lengths may be optimized even if the circulation optimization is not employed.

Figure 4.2 presents some typical radial distributions of chord length from the described procedure. Curves are presented for a range of required thrust. Note that as the propeller loading is increased the chord is increased.

4.2 Blade Strength and Thickness

A radial distribution of thickness is needed for any final propeller design. It is also necessary for the chord length optimization procedure described in the previous section. For this reason a simple procedure for the estimation of a minimum root thickness has been added to PLL. The ability to modify an input thickness distribution or have one supplied by PLL has also been included.

4.2.1 ABS Rule Calculation

The minimum root thickness is provided from an application of the American Bureau of Shipping rule on propeller strength [20]. This rule uses quantities which describe the propeller geometry, material and loading to determine a minimum root thickness. The needed quantities are either estimated by PLL or supplied by the user. Two rules are implemented, one for controllable pitch propellers the other for “normal” propellers. This is because of the large hub diameters associated with controllable pitch propellers.

4.2.2 Selection of the Thickness Distribution

Once a minimum root thickness has been determined the input thickness distribution may be scaled so that the root thickness becomes the minimum required by the ABS rule, or some other value desired by the user. PLL can also supply a thickness distribution. The PLL thickness distribution varies linearly from the root thickness to a specified thickness at the propeller’s tip. If optimum chord lengths are being determined with PLL, it is suggested that they be reoptimized after modifying the thickness distribution, since the optimum chord lengths may change with the thickness distribution.

4.2.3 Approximate Stress Calculation

An approximate calculation of stresses acting on the foil has been included in PLL. The method used is that of Morgan [30] as implemented by Kroeger [68]. Stresses acting on the blade section at the leading edge, trailing edge and point of maximum thickness are computed. The section is assumed to be a modified NACA 66 thickness form [7] with an $\alpha = 0.8$ meanline [1]. This method assumes that centrifugal stresses are small enough to be neglected and uses a simple correction to change the local lift coefficient to a three-dimensional camber.

4.3 Hub and Tip Unloading

For a variety of reasons including cavitation, strength and efficiency it is sometimes desirable to reduce the loading near the hub or tip of the propeller. For this reason a means to redistribute propeller circulation has been built into PLL. This process is carried out by subtracting a hub/tip unloading function, $\tilde{\Gamma}$, from the given circulation distribution. $\Gamma_{\text{unloaded}}(r) = \Gamma(r) - \tilde{\Gamma}(r)$. The wake is then aligned, and the circulation scaled, until the desired forces are obtained.

4.3.1 Series Representations of Circulation

We have found that under the vortex lattice model used by PLL the circulation distribution must be fair and have the proper square root singular behavior at the ends of the lifting lines. If this is not the case, large discontinuities in velocity may result. A small discontinuity in circulation was found to produce a large one in velocity. We were pleased to find that the PLL optimization procedures always produce circulation distributions which behave properly.

In order to modify circulation distributions in a manner which maintains fairness while also maintaining the proper singular behavior at the root and tip a set of series expansions for circulation have been employed. By adding or subtracting proper amounts of terms in these series the desired hub or tip unloading can be achieved.

In the case of a propeller whose blades are modelled by lifting lines with two free ends, the circulation distribution has a square root singularity at both the hub and tip. In this case a sine, or Glauert, series is used to represent the load distribution. Individual terms in this series can be written as

$$\tilde{\Gamma} = A \sin(n\pi\tilde{r}) ; \quad \tilde{r} = \frac{r - r_h}{1 - r_h} . \quad (4.4)$$

r_h is the radius of the hub, A gives the size of the unloading term and the integer n gives its "order". If $n = 2$ then $\tilde{\Gamma}(r)$ can be used to shift load from the hub to the tip or vice-versa depending on the sign of A . $n = 3$ unloads both the hub and the tip simultaneously. These sine series unloading functions are shown in figure 4.3

If the hub is modelled as a solid boundary and the tip is free the circulation has zero slope at the hub and is square root singular at the tip. In this case the following function is used to unload the hub.

$$\tilde{\Gamma} = A\sqrt{1 - \tilde{r}^2}(1 - \tilde{r}^2)^{2n-2} . \quad (4.5)$$

A again gives the size to the unloading term. n now determines how globally the effect of the unloading is felt. The larger n the more the unloading is localized to the region near the hub. A similar function is used to unload the tip.

$$\tilde{\Gamma} = A\sqrt{1 - \tilde{r}^2}\tilde{r}^{2n-2} . \quad (4.6)$$

In this case the unloading is increasingly localized to the tip with increasing n . The unloading functions used when the hub is modelled as a solid boundary are shown in figure 4.3.

If a solid boundary is present at the tip, but not the hub, the circulation distribution is now square root singular at the hub and has zero slope at the tip. In this case the hub unloading term is given by

$$\tilde{\Gamma} = A\sqrt{1 - p^2}p^{2n-2} , \quad (4.7)$$

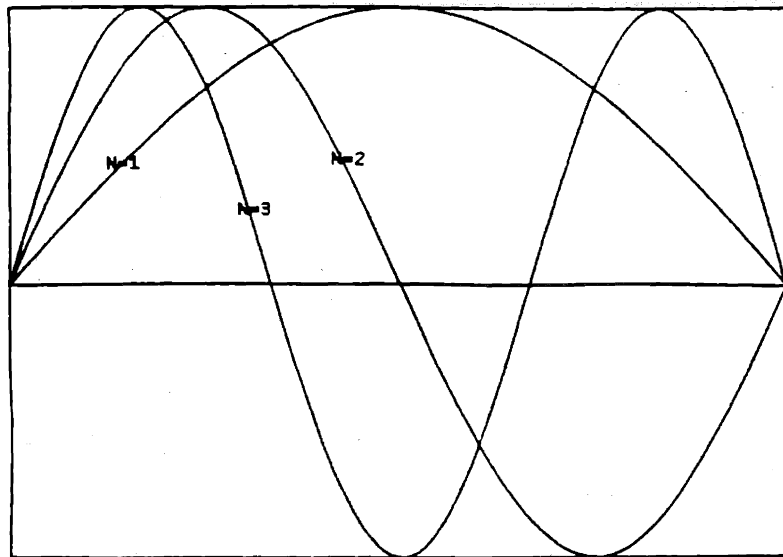


Figure 4.3: Sine series terms used for hub and tip unloading.

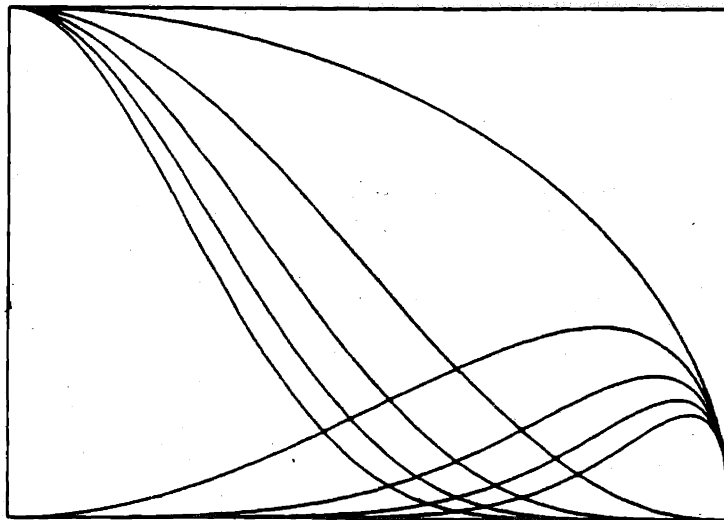


Figure 4.4: Hub and tip unloading functions used when the hub is modelled as a solid boundary.

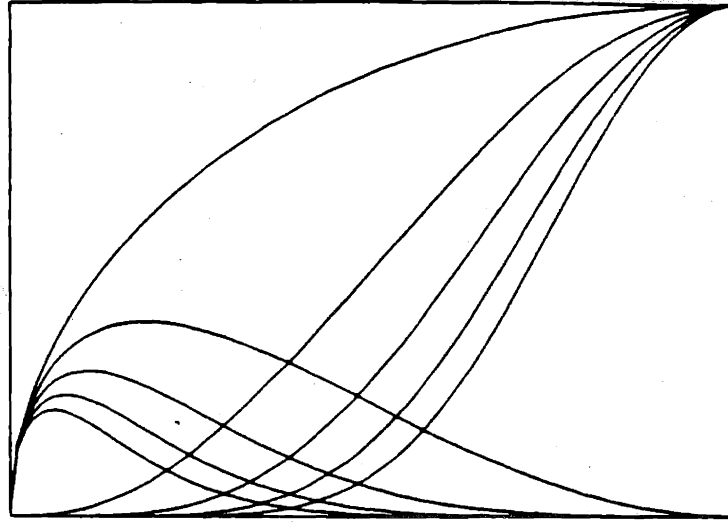


Figure 4.5: Hub and tip unloading functions used when there is a solid boundary at the blade tip.

and the tip unloading term by

$$\tilde{\Gamma} = A\sqrt{1-p^2}(1-p^2)^{2n-2}, \quad (4.8)$$

where $p = 1 - \tilde{r}$. The unloading functions used when there is a solid boundary at the tip are shown in figure 4.5.

No unloading has been implemented in the case where the circulation distribution at both the hub and tip have zero slope.

4.4 Effective Wake Calculation

The velocity field that describes the ship's wake in the absence of the propeller is defined as the nominal inflow. With the propeller present, the flow through the propeller plane is contracted and accelerated through the interaction of the propeller induced velocities and the ship's wake. If the nominal inflow is not a potential flow, then superposition of the nominal inflow and the induced velocities does not accurately model this flow. The effective wake is a modified nominal inflow which can be added to the induced velocities to give the correct total velocity field. This effective inflow is defined as the total velocity in the presence of the propeller, minus the potential flow velocity field induced by the propeller itself. If there is no vorticity in the inflow field, this definition reduces to the usual result that the total velocity is the linear superposition of the inflow in the absence of the propeller, and the velocity induced by the propeller

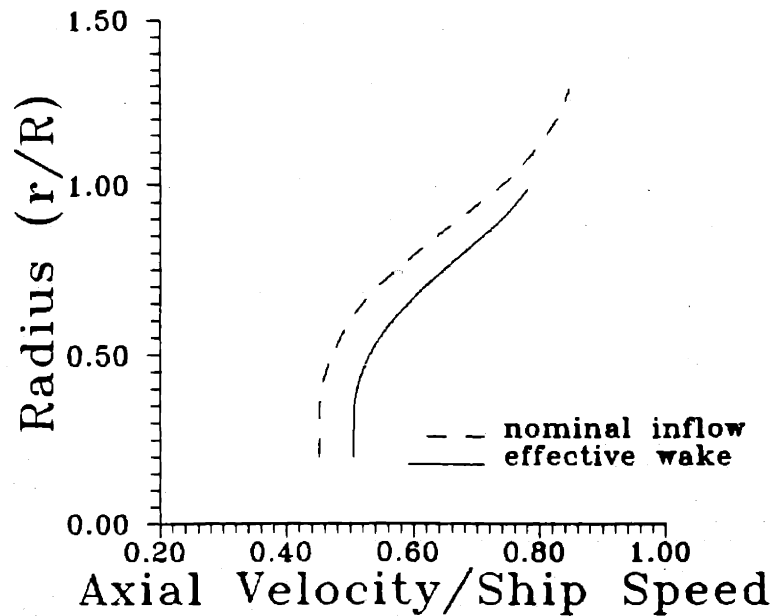


Figure 4.6: A nominal inflow wake and an effective wake from the algorithm implemented in PLL.

The effective wake calculation implemented in PLL is a modified version of that developed by Van Houten and used in WKPROC [110], which was in turn based on a method developed by Huang and Groves [52].

To analyze the mean flow, the assumptions of steady, inviscid, incompressible flow about an axisymmetric body leads to an equation of motion that is further modified by some assumptions about the flow upstream of the propeller:

- the induced velocities are irrotational,
- the axial velocity gradient is small compared to the radial velocity gradient as in a boundary layer,
- the energy in a stream tube is constant.

Under these assumptions the governing equations for the flow can be written in a finite difference form. In WKPROC and PLL the axial induced velocities needed for this finite difference effective wake calculation are approximated with actuator disk theory. The finite difference effective wake calculation as implemented by Van Houten is described in an appendix. Van Houten also added the ability to handle tunnel wall effects and higher wake harmonics to the method of Huang and Groves.

Figure 4.6 gives results from the effective wake calculation implemented in PLL. The nominal inflow and its effective wake corresponding to a C_T of 0.69 are shown. Note that velocity from the outer radii is redistributed inward as the streamlines are contracted by the actuator disc. For typical inflow wake profiles this procedure results in increased velocities “seen” by the lifting lines.

4.5 Optimum Operating Conditions

The previously described procedures for determining the propeller load distribution and chord lengths require the input of the propeller diameter and its rate of rotation. Often one or both of these quantities is not known at the outset of the propeller design process. For this reason a procedure for determining the propeller diameter or rpm which provides a given thrust for the highest propulsive efficiency at a given ship speed is included in PLL.

Figure 4.7 gives efficiency vs advance coefficient for optimum, 5 bladed propellers as determined by the optimization procedure. In one case the advance coefficient is varied by changing the rpm and holding the propeller diameter fixed. In the other J is varied by changing the diameter for a fixed rpm. In the results presented here both the circulation and chord distributions are determined by the optimization procedures. For the fixed diameter case $C_T = 2T/(\rho V_S^2 A_0) = 0.69$. When the rpm is held constant, it is fixed to the value which corresponds to $J = V_S/(nD) = 0.89$. In each case the propeller is required to generate identical thrust.

The procedure implemented in PLL allows for either the rpm or the diameter of a propeller to be optimized while the other quantity is held fixed. It is assumed that the variation of rpm for a fixed diameter will produce a unimodal (single maximum) curve of efficiency vs rpm. Such a curve is generated by a balance of high induced drag at low propeller rotation rates and large viscous drag at high rpm's. A similar assumption is made concerning efficiency and propeller diameter. In this case the induced drag is large for small diameters and the viscous drag is high for large diameter propellers.

The optimum rpm or ship speed can be determined by iteratively applying the circulation and chord optimization procedures. Kroeger [68] determined the Fibonacci method to be the fastest procedure available for determining the optimum propeller rpm for a fixed diameter. This method determines the optimum diameter or rpm to within some specified range of uncertainty. Upper and lower bounds on the quantity to be varied are determined, and then a Fibonacci series is used to provide new estimates of the optimum value. A detailed description of this process is given in [68].

In the case of multiple stage propulsors, the optimum rpm or diameter of one component can be determined, while the diameter and rpm of the other is held fixed. PLL does not currently allow for the determination of an optimum diameter for a ducted propeller,

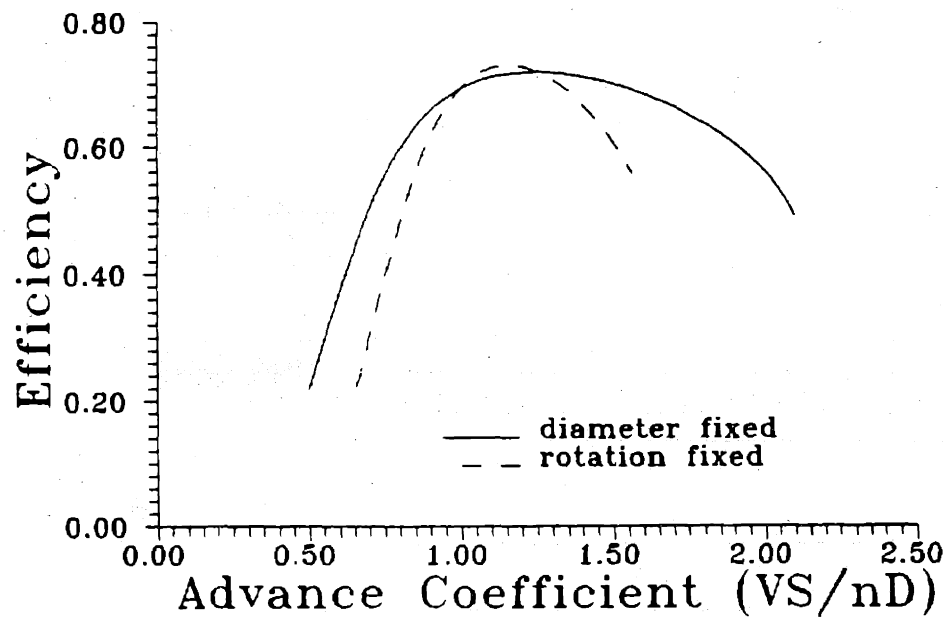


Figure 4.7: Efficiency vs advance coefficient for “optimum” propellers as determined by PLL. Results are given for fixed propeller diameter and for fixed rpm. The propellers were required to generate identical thrust and were free-running.

and, naturally, the rpm of a stator cannot be optimized.

4.5.1 Determination of Ship Speed

Another typical problem is that of finding the maximum ship speed for a specified powering. Here the designer is given the available horsepower, the propeller's rotation rate and a relationship between the required thrust and the ship's speed.

The fixed torque procedure of chapter 2 can be used to determine a propeller circulation distribution producing the largest possible thrust for a fixed propeller torque and rotation. Given an initial estimate of the ship speed, a maximum thrust may be obtained. A new ship speed corresponding to this thrust can then be found from the relationship between thrust and ship speed. This process can be carried out iteratively until the ship speed has been determined to within some specified value.

Such a procedure has been implemented in PLL for the case of a single propeller. The relationship between thrust and velocity is provided by assuming that the thrust coefficient, $C_T = 2T/(\rho V_S^2 A_0)$, is a specified constant. This is approximately true over small velocity ranges. This procedure could be easily extended so that the designer provides a more exact relationship as well as to the case of multiple stage propulsors.

4.6 Non-Axisymmetric Pre-Swirl Stators

It is well known that the placement of stators upstream or downstream of a propeller can result in a reduction of rotational energy losses, and therefore higher propulsive efficiency. In addition a nonaxisymmetric arrangement of stator blades can alter the inflow to a downstream propeller in such a way that unsteady forces and cavitation are reduced. Both of these concepts are well established. Papers by Larimer, et al [71] and Gearhart and Marboe [33] review patent literature on pre-swirl guide vanes extending back to the first decade of this century. They also describe their experience with a nonaxisymmetric pre-swirl stator arrangement on a United States Coast Guard boat.

While the methods of previous sections can be used to determine optimum circulation distributions and performance estimates for a propeller operating downstream of a stator, they do not account for nonaxisymmetries of the inflow or the stator blades. The lifting line model can be readily adapted, however, to handle such nonaxisymmetric stators.

4.6.1 The Nonaxisymmetric Lifting Line Model

The inflow velocities to the nonaxisymmetric stator are not required to be circumferentially uniform, rather they are allowed to vary both radially and circumferentially. The lifting lines are also allowed to differ in loading and angular spacing. If the interaction

between the propeller and stator is ignored, the velocities induced by this system of lifting lines are steady since the inflow velocity seen by the stator blades does not vary with time.

The lifting lines representing the stator can be discretized with a vortex lattice. The trailing vortices are considered to be straight, semi-infinite, line vortices aligned in the axial direction. An application of the law of Biot and Savart provides formulas for the velocities induced by both the bound and trailing vorticity. These formulas are provided in appendix A. The velocities induced by this vortex system on control points on the stator lifting lines is computed. These velocities are added to the inflow velocity and the velocity induced on the stator by the propeller. The velocity induced by the propeller is assumed to be that of the axisymmetric model. Forces and moments acting on each of the stator blades is calculated from a local application of the Kutta-Joukowski law and the usual viscous drag relations.

Velocities induced by the stator are also calculated at a number of circumferential locations at the axial plane of the propeller. The calculation of these velocities is substantially more time consuming than that of the axisymmetric case, since the velocities must be found at a large number of circumferential locations, and the velocities induced by each blade must be calculated independently. The resulting velocity field can be added to the nonuniform inflow to give the total nonuniform velocity seen by the propeller.

4.6.2 Nonaxisymmetric Circulation Distributions

A nonaxisymmetric pre-swirl stator can be used to modify the circumferential distribution of tangential and radial velocities seen by the propeller. If the undisturbed inflow velocity field varies about the propeller disk, a properly chosen set of pre-swirl stator blades can be used to reduce this variation. Reduced velocity fluctuations at the propeller can result in a reduction of cavitation and unsteady forces. The location of stator blades and their radial distributions of circulation must somehow be chosen in order to provide both a high propulsive efficiency and obtain a reduction in the velocity fluctuation.

While methods for automatically determining such a circulation distribution have not yet been developed, tools for assisting the designer in selecting circulation distributions have been implemented. If the foremost design consideration is one of propulsive efficiency, the stator circulation distribution averaged over the blades should be the optimum distribution of the axisymmetric stator. The PLL code allows the designer to scale the optimum axisymmetric stator circulation distribution for each blade of the nonaxisymmetric stator. If the goal is a reduction in the variation of tangential velocity the load distribution might be scaled by a factor proportional to the tangential component of inflow at each blade's angular position.

Examples of how this lifting line procedure can be used for the design of a nonaxisymmetric stator are provided in [22] and [59], as well as in chapter 6 of this thesis.

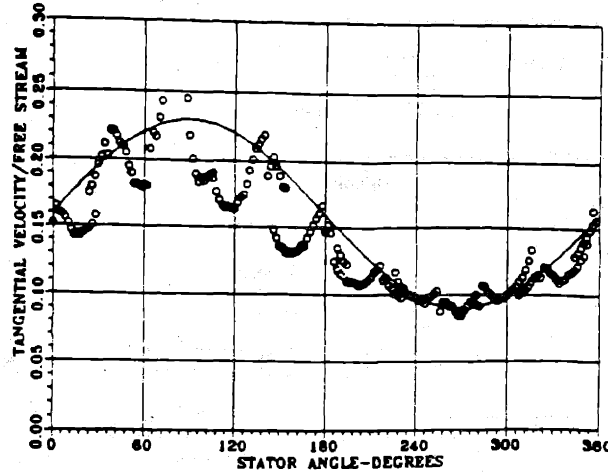


Figure 4.8: Tangential velocities at the plane of the propeller.

4.6.3 Experimental Verification

An experiment was performed by Bowling [6] in the MIT Water Tunnel in order to provide data for correlation with the theory. The goal of Bowling's nonaxisymmetric stator test was to generate a flow inclination by a circumferential variation in the loading of the stator blades. The lifting line code was used to determine the required circulation for each of nine stator blades. The actual stator model was designed with nine adjustable pitch blades with symmetrical sections. The pitch angle of the blades was set so as to best approximate the desired circulation distribution as predicted by the MIT-SSF1 stator lifting surface code [50].

The model was placed in the tunnel and the circulation at several radii was determined for the most heavily and most lightly loaded blades. This was accomplished by measuring the velocity at a large number of points along closed contours surrounding the stator blades. The circulation was then calculated by numerical evaluation of the integral

$$\Gamma = \oint \vec{V} \cdot d\vec{s}. \quad (4.9)$$

The result, together with the lifting surface predictions of circulation was used in the lifting line model to predict velocities at the plane of the propeller.

Laser doppler velocimeter measurements were made of the tangential velocity field induced by the stator at the plane of the propeller. A plot of the data at $r/R = 0.75$ is given in figure 4.8. Note the velocity fluctuations associated with the individual stator blades. These are typical of the lifting line predictions. The effective flow inclination



Figure 4.9: Nonaxisymmetric stator operating in the MIT Water Tunnel. Note the flow inclination.

can be deduced from the first harmonic of the tangential velocity and is approximately 4 degrees at this radius. This result is comparable with the lifting line prediction.

A direct impression of the flow inclination can be seen from the photograph in figure 4.9 which shows the cavitating hub vortex generated by the stator.

Chapter 5

Determination of Blade Geometry

The methods of the previous chapters can be used to determine much of the blade geometry. Optimum radial distributions of circulation can be found from the procedures of chapters 2 and 3. Chord and thickness distributions can be estimated from the methods of chapter 4. The radial distributions of rake and skew are also assumed to be known. Skew are usually determined through consideration of unsteady forces [25] [89] and rake through considerations of strength [87] and physical arrangements. The selection of these quantities will not be discussed in the present work. The problem is, therefore, one of finding the blade pitch and camber which produces the prescribed distribution of circulation.

In this chapter the use of existing propeller design methods to determine the geometry of nontraditional propulsors, such as contrarotating propellers, is described.

5.1 Propeller Blade Design

A brief digression to explain the propeller blade geometry is, at this time, appropriate. We here consider a propeller consisting of Z identical, symmetrically arranged blades, attached to a hub that is rotating at constant angular velocity ω about the x -axis. As shown in figure 5.1, the blade is formed starting with a midchord line defined parametrically by the radial distribution of skew angle $\theta_m(r)$ and rake $X_m(r)$. By advancing a distance $\pm \frac{1}{2}c(r)$ along a helix of pitch angle $\phi_p(r)$, one obtains the blade leading and trailing edges. The surface formed by these helical lines at each radius gives a reference surface upon which the actual blade sections are developed. These sections can be defined in standard airfoil terms by a chordwise distribution of camber $f(s)$, and thickness $t(s)$, where s is a curvilinear coordinate along the helix.

Kerwin [57] gives a review of analytical methods for the design of marine propellers. Much of the following discussion is adapted from his presentation.

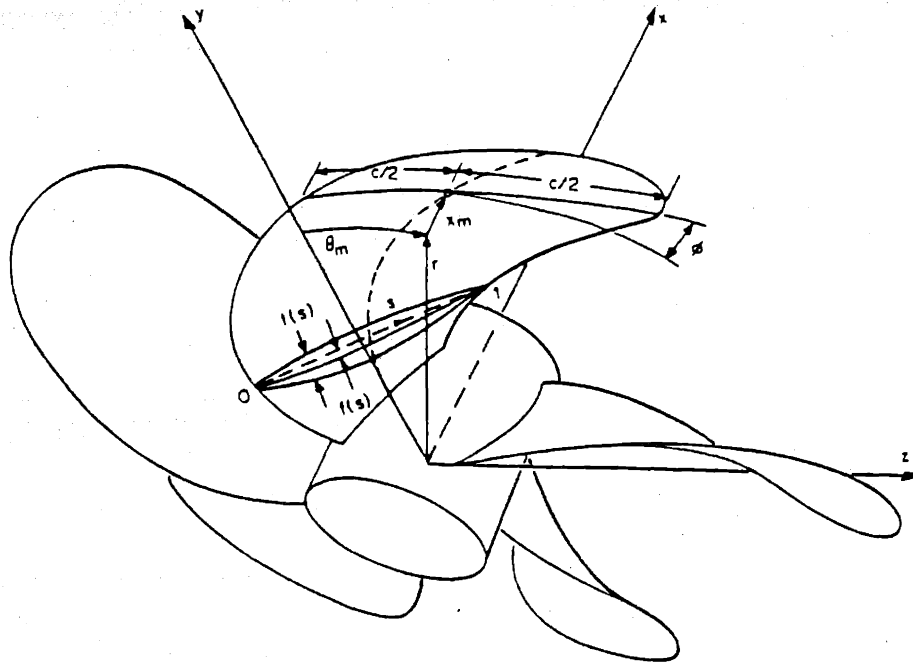


Figure 5.1: Propeller blade geometry.

If the aspect ratio of the blades is high, the lifting line theory originated by Prandtl [91] is appropriate. In this case the three-dimensional flow is considered to be two-dimensional at each radial blade section, with the inflow velocity field there altered with the velocity induced by the vorticity shed from the lifting lines. The blade geometry is then determined by combining the lifting line results with theoretical or experimental, two-dimensional, section data. This approach succeeds for aircraft propellers, which generally have very high aspect ratio blades and operate in relatively uniform inflow.

Marine propeller, however, are usually constrained to have low aspect ratio blades, since they are limited in diameter, and considerations of strength and cavitation limit the lift per unit blade area that they can produce. As a result, marine propeller designs based on lifting line theory have not been found to be satisfactory. For this reason marine propellers were long designed on the basis of systematic series of model experiments.

A number of researchers developed design methods based on combining lifting line theory with lifting surface corrections to section camber and angle of attack. The methods of van Manen [112] and Eckhardt and Morgan [30] are examples of this approach. This was followed by the development of numerical lifting surface methods. Pien [90], Kerwin [58] and van Manen and Bakker [114] made early contributions toward such computer based methods.

Such efforts have continued to the present time. Here, a brief description of one

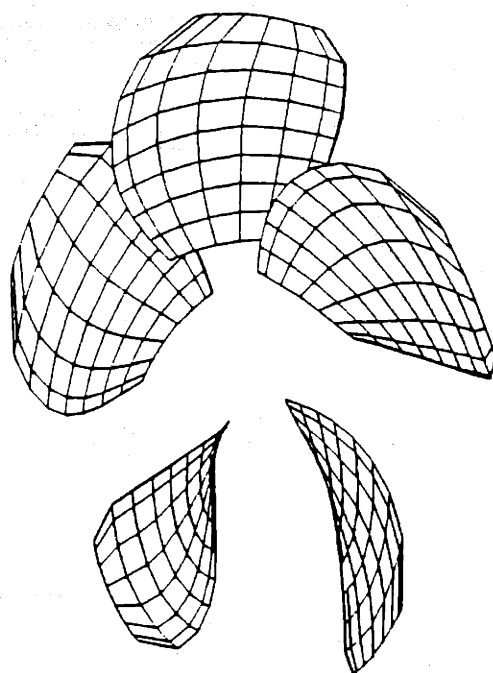


Figure 5.2: Vortex lattice representation of a propeller.

lifting surface design code, PBD-10, is given. PBD-10, developed by Kerwin, along with an analysis procedure developed by Greeley, was published jointly by these two authors [43].

Under lifting surface theory the blades are idealized as sheets of singularities, usually sources and either normal dipoles or vortices. This idealization is a linearization of the governing equations for the velocity potential for an inviscid, incompressible flow about a lifting body in the limit of zero thickness. The source strengths are directly proportional to the streamwise derivative of the thickness function. In a design method such as PBD-10, the vortex strengths are prescribed.

Expressions for the velocity can be found by differentiation of the velocity potential. The resulting singular integrals can be evaluated by direct numerical integration. This is done, for example, in the PROPLS code developed by Brockett [10]. Alternatively, a vortex lattice procedure may be employed, as is done in PBD-10. In PBD-10 the continuous distribution of vortices and sources are replaced by a set of concentrated straight line elements, whose end points lie on the blade surface. Velocities are computed at suitably placed control points between the elements. As for the lifting line problem, care must be taken in setting up the geometrical arrangement of lattice elements and control points in order to ensure proper convergence. An example of such a lattice arrangement is given in figure 5.2. Convergence of a propeller vortex lattice system with

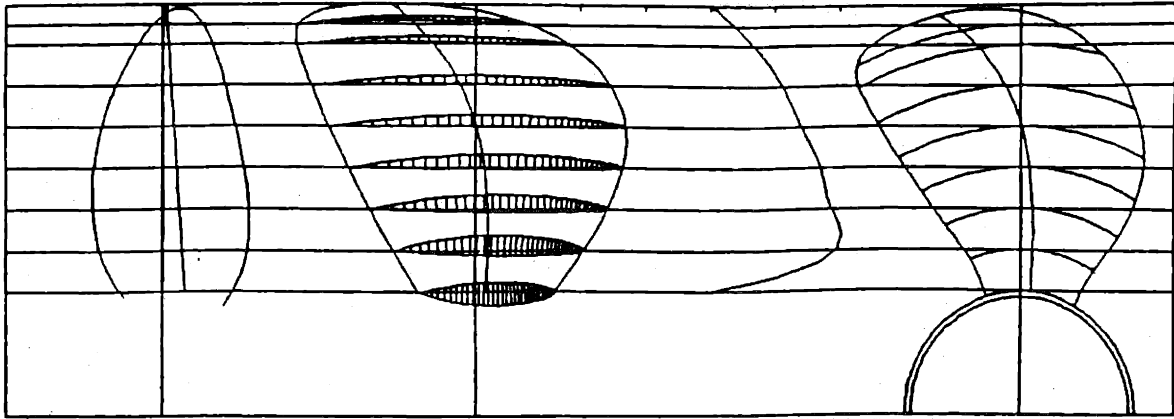


Figure 5.3: Propeller blade geometry as determined by PBD-10.

increased numbers of lattice elements in both the chordwise and spanwise directions is illustrated by Greeley and Kerwin [43]. For such a vortex lattice the computation of the induced velocities is reduced to a geometric problem of finding points on the mean blade surface, and then summing the velocities induced by the source and vortex lines.

In PBD-10 an initial estimate of the blade pitch is used to compute the total fluid velocity at the blade control points. The surface of the blade is then adjusted in such a way that the normal component of velocity is zero at the control points. This process is repeated, using the adjusted surface as the new reference surface, until convergence is obtained. The trailing vortex wake is similarly aligned with the resultant flow. Details of these procedures are given in [43].

Figure 5.3 gives a typical propeller blade geometry as determined by PBD-10. In this case the circulation, chord and thickness distributions were determined from the PLL lifting line model. The distributions of skew and rake used here are somewhat arbitrary. The vortex lattice representation of this propeller is that shown in figure 5.2.

5.1.1 Consideration of the Hub

The presence of the hub as a solid boundary is ignored in the PBD-10 procedure. In chapter 3 we saw that when hub effects were considered the optimum circulation distribution was, in the vicinity of the hub, substantially different from that of the hubless case. Similarly, we expect the circulation distribution of a given blade geometry to be influenced by the presence of the hub.

If the presence of the hub is considered, the result is a mixed design/analysis problem. The hub is considered to be a body of revolution of known shape on which the normal component of total fluid velocity must vanish. However, the shape of the blades which produces the prescribed circulation distribution is still to be determined. Wang [118] modified the PBD-10 procedure to account for the presence of the hub. Wang's procedure is known as PBD-11.

In PBD-11 the hub is represented by a distribution of dipoles. The hub surface is tiled with quadrilateral and triangular panels whose vertices lie on the surface of the hub. Each panel is considered to be a constant dipole sheet with unknown strength. Mathematically such a dipole sheet is equivalent to constant vortex segments along the panel boundary [46]. Therefore the hub, as well as the blades, is represented by a vortex lattice. The mixed nature of the design/analysis problem is, perhaps, now more apparent. The vortex elements representing the hub are of unknown strength, but their geometry is fixed. The vortex and source elements representing the blades have known strength, but their geometry is not determined.

An iterative solution procedure to this problem is employed. The velocity field generated by the initially hubless blades is used as the onset flow for the hub solution. The boundary value problem for the unknown hub vortex strengths which provide for zero velocity normal to the hub in this onset flow is then solved. The velocity field thus generated is added to the onset flow used for the next iteration of the blade solution. This process is continued until a converged result is obtained. Typically three or four iterations are necessary.

In PBD-11 the hub is considered to be a body of revolution, closed both upstream and downstream of the propeller, as illustrated in figure 5.4. The vortex elements representing the hub are positioned so that at the hub/blade junction they are aligned with corresponding elements of the blades. The hub panelling is further arranged so that a similar alignment occurs with the elements of the trailing vortex wake. After each iteration of the blade solution the hub must be repanelled, since the blade shape has changed.

The hub geometry of PBD-11 differs from that of the usual hub in that, typically, the actual hub extends upstream into the hull. In this case the hub is usually modelled as extending infinitely far upstream. In order to cancel the increase in the axial velocity due to PBD-11's artificially closed hub, the inflow to the propeller can be modified with that of an axisymmetric body operating in uniform potential flow.

A comparison of the blade geometries generated by the PBD-10 and PBD-11 procedures is of interest. For this purpose the lifting line code, PLL, was used to generate three circulation distributions, for which blade geometry would be determined. An optimum distribution from the hubless model, an optimum hub-loaded distribution, and an unloaded hub distribution created through use of an "equivalent" propeller were generated. These circulation distributions are shown in figure 5.5. In each case the lifting lines are

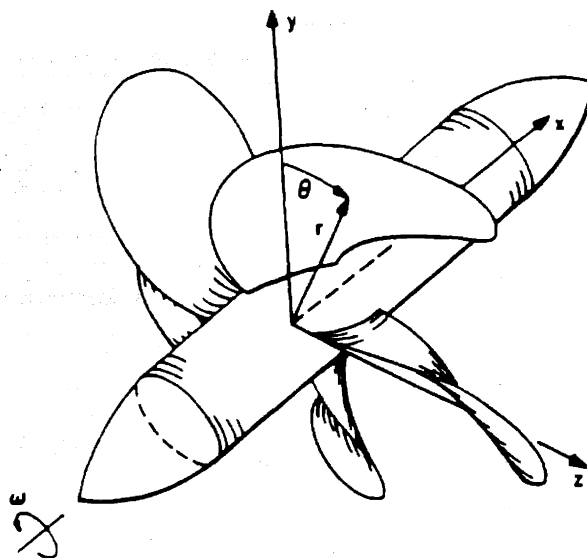


Figure 5.4: PBD-11 hub and blade geometry.

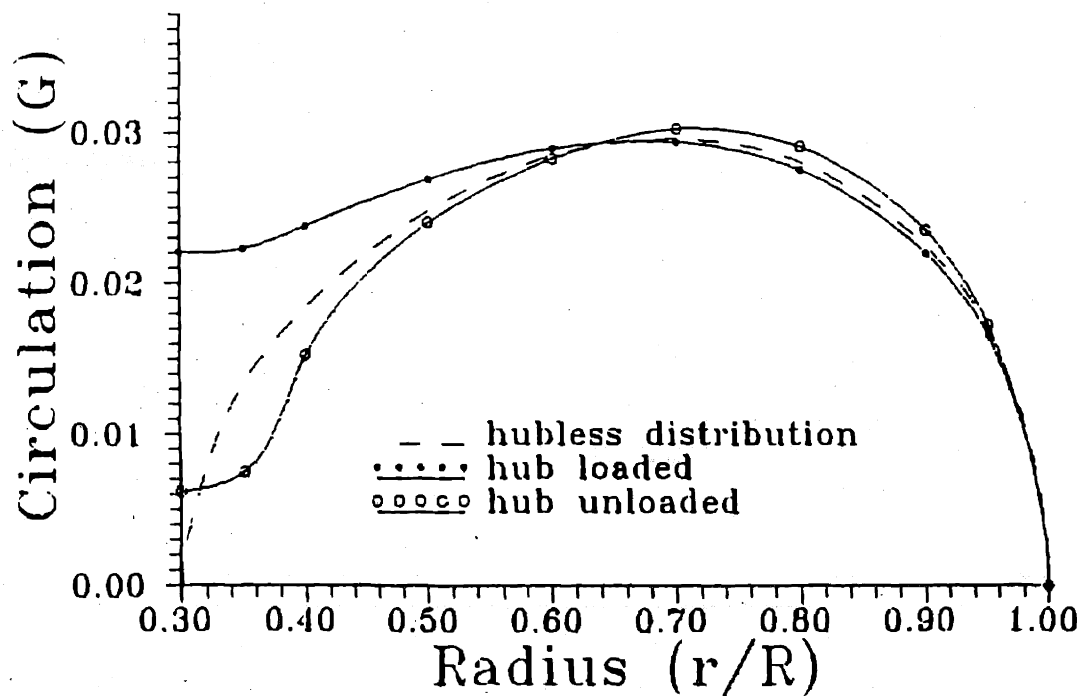


Figure 5.5: Circulation distributions used for the PBD-10/PBD-111 comparisons.

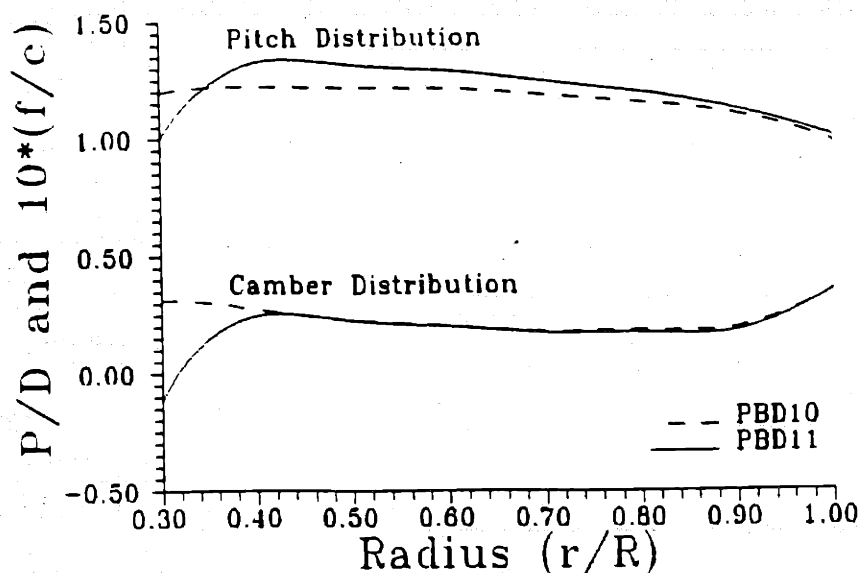


Figure 5.6: Blade geometries determined by PBD-10 and PBD-11 for the “hubless” circulation distribution.

considered to be operating in open water with $J_S = 0.89$. The thrust from the lifting line model corresponds, under moderately loaded theory, to $C_T = 0.69$ for each of these circulation distributions. Viscous forces were included with typical values of the drag coefficient assumed. The chord, rake and skew are the same as those of the propeller shown in figures 5.3 and 5.2.

Figure 5.6 gives radial distributions of pitch and camber as determined by the two codes for the “hubless” circulation distribution. The quantity describing the camber in figure 5.6 is the maximum value of the camber at each blade section divided by the chord length there. The pitch is given as a ratio of pitch to diameter, P/D , where $P = 2\pi r \tan(\phi_p)$. Note that, as expected, the distributions from PBD-10 are quite similar to those of PBD-11 at the outer radii, but differ near the hub. When the presence of the hub is considered, the PBD-11 algorithm, the pitch and camber at the hub must be significantly reduced from that determined by PBD-10 in order to obtain zero circulation at the hub. This implies that a propeller with the roughly constant pitch and camber distribution predicted by PBD-10 would have substantial loading at the hub.

In figure 5.7 a similar comparison is performed for the hub loaded circulation of figure 5.5. Again the blade geometry at the outer radii as determined by the two models is similar. Near the hub, however, the pitch and camber goes up dramatically for the PBD-10 prediction. This is not unexpected, since in the PBD-10 formulation there is

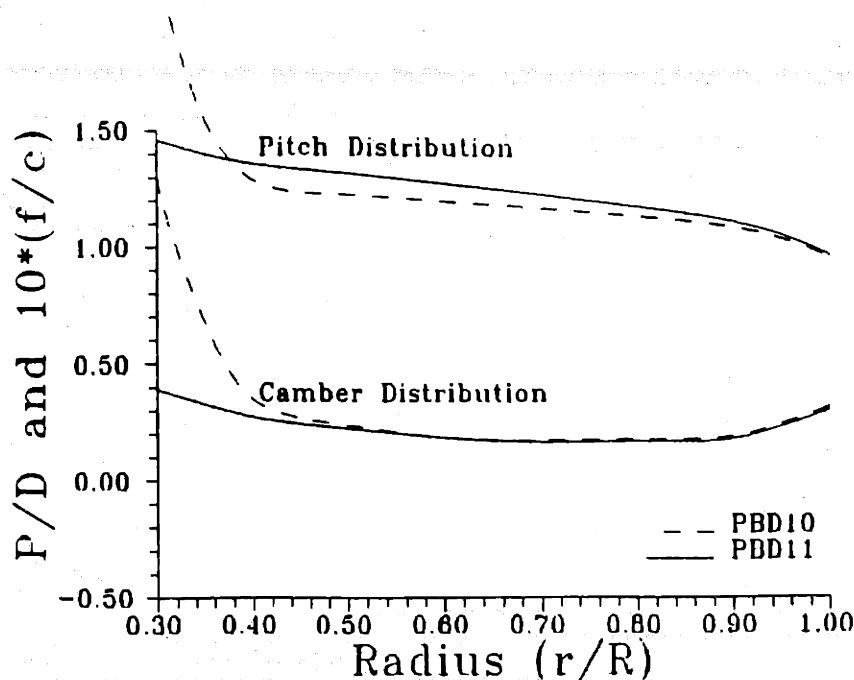


Figure 5.7: Blade geometries determined by PBD-10 and PBD-11 for the hub loaded circulation distribution.

no boundary at the hub and, without such a boundary, the circulation must fall to zero there. In fact, it is somewhat of a surprise that a converged result was achieved for the hubless formulation at all. Note that the PBD-11 geometry which provides this hub loaded circulation distribution is not dissimilar from the PBD-10 prediction for the hubless distribution. This reinforces the idea that if the hub is neglected altogether the resulting blade geometry will produce large loadings at the hub.

Figure 5.8 gives the blade pitch and camber for the hub unloaded circulation distribution. In this case the blade geometry predicted by the two methods is very nearly the same over the entire span of the blade, although PBD-11 predicts slightly higher values of pitch at the inner radii. The geometries for the hub unloaded circulation distribution do not show marked differences between the two models because the hub unloading results in bound vorticity being shed into the wake away from the hub, where it does not produce strong blade/hub interactions.

Figures 5.6-5.8 indicate that if the hub is not included in the design procedure, large, unanticipated hub loadings may result. However, if a hub unloaded circulation distribution is desired, the PBD-10 model may be sufficient. It should be noted that the forces developed by these three circulation distributions under the three models, PLL, PBD-10 and PBD-11, differ only by a few percent.

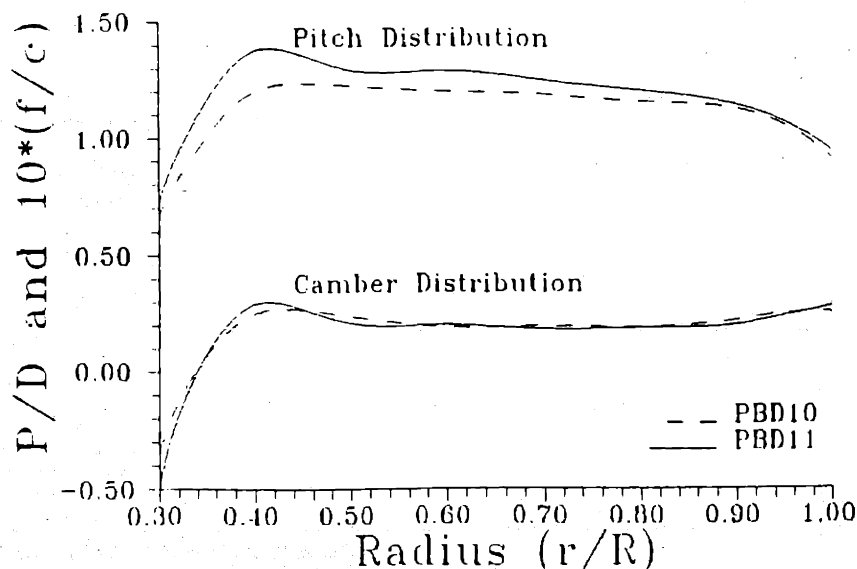


Figure 5.8: Blade geometries determined by PBD-10 and PBD-11 for the hub unloaded circulation distribution.

5.2 Blade Design for Multiple Stage Propulsors

The design of multiple stage propulsors is complicated by the mutual interaction between the propulsor components. Lifting surface methods which account for these interaction velocities have been developed. Nelson [86] used such a procedure to design contrarotating propellers for torpedoes. Nelson's design had the finite circulation at the hub anticipated from the lifting line results of chapter 3.

Chen and Reed [18] adapted the PBD-11 code to the case of contrarotating propellers. In their procedure the single propeller lifting surface model is used in an iterative manner to determine the blade geometries and interaction velocities. Chen and Reed compared the from their lifting surface model with results for propellers designed with PBD-11 for the onset flow predicted by a lifting line model. They concluded that interaction velocities calculated from the lifting line model are sufficiently accurate for design use when the propeller loadings are moderate, and the propellers are not too close to each other.

In the approach adopted here lifting line results are used for the interaction velocities. Circumferential mean interaction velocities from the PLL code are added to the inflow velocity field to form the total onset flow used in the lifting surface model. Since hub loading was found to be of importance for multiple stage propulsors, the PBD-11

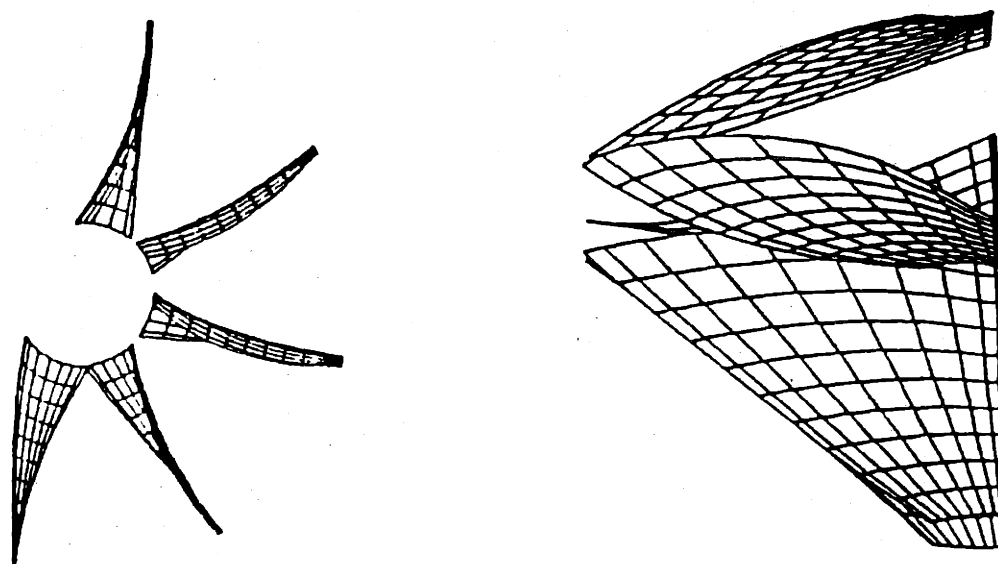


Figure 5.9: A vortex lattice representation of a nonaxisymmetric stator.

procedure, in which the presence of the hub is considered, is used for the lifting surface calculation. Chen and Reed [18] describe the use of such a procedure to design contrarotating propellers. These authors collaborating with Kim [19] also describe the design of a vane-wheel propulsor.

It should be noted that in the described design procedure only steady propulsor forces are considered. Since the velocity field induced on the downstream component is expected to have considerable circumferential variation, an estimate of unsteady forces is necessary for any final propulsor design. The development of reliable methods for the prediction of such unsteady forces for multiple stage propulsors is an area for future research.

5.2.1 Propeller/Stator Design

Lifting surface design methods can also be used for the design of propeller/stator combinations. Nelson's method for the design of contrarotating propellers [86] has been modified to allow for an upstream set of nonrotating blades [76]. In chapter 4 the possibility of nonaxisymmetric stators is discussed. In the present work a vortex lattice, lifting surface code for the design and analysis of nonaxisymmetric stators, SSF-1, is used in conjunction with existing propeller design and analysis codes for the design of propeller/stator combinations.

The SSF-1 code, developed by Hsin [50] [59], makes use of a vortex lattice repre-

sensation of the nonaxisymmetric stator. Figure 5.9 shows the lattice arrangement for such a stator. An image vortex lattice is used to represent the hub in SSF-1. The core routines of Hsin's procedure solve the analysis problem for the stator. In other words these routines find the unknown source and dipole strengths, and thus the circulation, for a given blade geometry operating in a specified onset flow.

The design problem of determining the blade geometry which produces a prescribed distribution of circulation on each blade is attacked through an iterative application of this analysis procedure. In addition to producing the desired circulation distributions, in SSF-1 the stator blade sections are further required to operate at ideal angle of attack. This is equivalent to requiring that the leading edge suction force be zero at all radii of each stator blade.

Two constraints have thus been established: that the local value of the lift coefficient, $C_L = 2\Gamma/V_{sc}$, be equal to a prescribed value and that the leading edge suction force, C_{ls} , be equal to zero. Lan [70] gives the following formula for the leading edge suction force.

$$C_{LS} = \frac{\pi}{2c(r)\Lambda_l(r)} \left(\lim_{s \rightarrow 0} \gamma(r, s) \sqrt{s} \right)^2, \quad (5.1)$$

where $\Lambda_l(r)$ is the leading edge sweep angle at radius r and $\gamma(r, s)$ is the vortex strength per unit area $\gamma = \partial u / \partial s$.

Under the assumption that $C_L(r)$ and $C_{ls}(r)$ are functions of two unknown variables, section angle of attack, $\alpha(r)$, and maximum camber, $f_0(r)$, the nonlinear equations defined by the constraints can be solved iteratively by repeatedly solving the nonlinear system.

$$\delta C_L = \frac{\partial C_L}{\partial \alpha} d\alpha + \frac{\partial C_L}{\partial f_0} df_0, \quad (5.2)$$

$$\delta C_{ls} = \frac{\partial C_{ls}}{\partial \alpha} d\alpha + \frac{\partial C_{ls}}{\partial f_0} df_0. \quad (5.3)$$

Equations 5.2 and 5.3 are solved with a Newton-Raphson method. The chordwise distribution of camber is given by some specified meanline. At each iteration of the overall procedure, $\delta C_L(r)$ is set equal to the difference between the current lift coefficient and the required value. Similarly, $\delta C_{ls}(r)$ is set equal to $-C_{ls}(r)$. In order for this scheme to converge quickly a good first guess at the final solution is necessary. One method to obtain such a guess is to linearly extrapolate or interpolated $\alpha(r)$ and $F_0(r)$ until the prescribed loadings are achieved. The leading edge singularity can then be removed in the solution of equations 5.2 and 5.3.

The circulation distributions and onset flows used in the SSF-1 procedure are obtained from PLL. The lifting line model is also used to generate input quantities for the propeller design code. Propeller/stator geometries from this procedure are presented in chapter 6 and in [22].

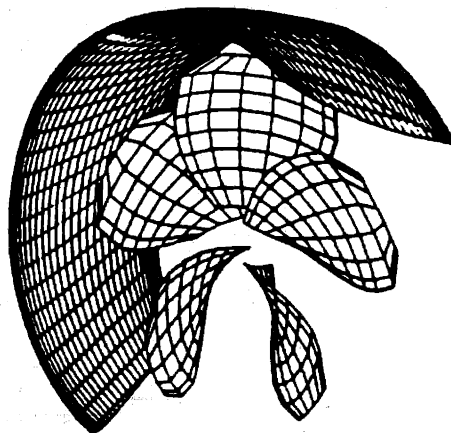


Figure 5.10: Ducted propeller with five percent gap between blade tip and duct.

5.3 Ducted Propeller Design

Several methods have been developed for the analysis of the flow around ducted propellers. Such methods have advanced in parallel with methods for the analysis of conventional propellers.

In the first generation of these methods the propeller was modeled through use of actuator disc, lifting line or lifting surface theories. The duct was represented in linear theory by distributing ring vortices and sources on an approximate mean surface. Representative works in that area have been published by Morgan [81], Caster [13] and Dyne [28].

In the next generation of analysis and design methods the duct was treated in non-linear theory by distributing surface vorticity on the duct and the propeller was treated with actuator disc or lifting line theory. Ryan and Glover [94], Gibson and Lewis [94], and Falcao de Campos [31] have made contributions in that area.

In all the previous methods the interactions between the duct and the propeller were assumed to be axisymmetric. This assumption was relaxed in the next generation of analysis methods where the nonaxisymmetric problem is solved for the duct and propeller. Van Houten [109] and Feng and Dong [32] have published works in that area.

Recently, Kerwin, Kinnas et al. [62] have developed an analysis method where the duct is treated by using a potential based panel method and the propeller by using a lifting surface method. This method provides predictions for the nonaxisymmetric pressure distribution on the duct and the duct thrust. Figure 5.10 gives a panel and

lattice arrangement from their model.

The design methods for ducted propellers have followed the evolution of the analysis methods. They mostly consist of a "trial and error" procedure. For a specified advance coefficient, thrust coefficient and a given thrust division between duct and propeller, a preliminary design is determined. That design is then consequently modified and verified by using any of the previously cited analysis methods, until the design requirements are satisfied.

In the present work a systematic method for determining the appropriate propeller and duct geometries, which will develop the optimum propeller loading and the required propeller and duct thrust is described. The propeller and duct sections are also required to work at near ideal angles of attack so that the occurrence of flow separation and/or cavitation is minimized.

The initially determined duct and propeller geometries are analyzed through use of [62]. The resulting propeller and duct loadings are compared against the initial design objectives. The propeller and duct geometries are then appropriately modified until the design objectives are met within acceptable accuracy.

5.3.1 The Ducted Propeller Design Procedure

The goal of the procedure presented here is to design a ducted propeller which develops a required total propulsor thrust with a specified distribution of thrust between propeller and duct. The propeller is to have an optimum radial distribution of circulation, with the blade sections operating at, or near, their ideal angles of attack. The duct should also be operating at its ideal angle, in some average sense. The propeller's operating condition and many geometric quantities: the propeller's chord, rake, skew and thickness; the duct's chord and thickness; and the meanlines and thickness distributions for the duct and propeller blade sections, are given. The optimum propeller circulation distribution, the blade pitch and camber and the duct angle and camber are to be determined.

First, the propeller lifting-line model is used to find an optimum propeller circulation distribution. The inflow to the lifting-lines is taken to be the velocity field seen at the plane of the propeller created by a duct with zero angle and camber and a specified thickness distribution as analyzed by the method of [62]. This duct is subject only to the incoming flow, without the presence of the propeller. In the lifting-line model the duct, as described in chapter 3, is represented by the combined effects of this inflow from the duct operating at zero angle and without a propeller, the velocities induced by an image system of lifting lines, and the velocities induced by ring vortices representing duct circulation.

The remainder of the design procedure can be broken into two halves. In the first half of the design process a duct/propeller generating the desired propeller thrust is obtained. The duct is further required to have only a small amount of total, circumferentially

averaged circulation. We will refer to this as the design of a *neutral duct*. In the second half of the design procedure the angle of attack of the duct and its camber are modified to achieve the required distribution of thrust between duct and propeller. In both parts of the design procedure the propeller should have the "optimum" circulation distribution.

5.3.2 The Neutral Duct

As well as determining the radial distribution of circulation on the propeller blades, the lifting-line model is used to calculate circumferentially averaged radial velocities induced by the propeller on a cylinder at the duct's nominal radius. These velocities are used to predict approximate streamlines, which are used to provide a first guess at the neutral duct's angle of attack. If these streamlines are also used to provide duct meanlines, the ducts take on "S" shapes similar to those predicted by Morgan [80].

Next, the propeller pitch and camber distributions which produce the desired circulation distribution must be estimated. In the case of a relatively large gap between the duct and propeller, this can be done with an existing, lifting-surface, propeller, design code [43]. The velocity field of the zero angle duct operating without a propeller is taken to be the inflow to the propeller in this case. In the case of small or zero gap between duct and propeller, two-dimensional wing theory applied to the lifting-lines may produce adequate estimates. In either case, the propeller pitch and camber determined at this stage is only a first guess at the final distributions.

This first estimate of propeller/duct geometry is then analyzed using the previously described, duct/propeller, analysis code. This analysis provides us with the forces acting on the current duct and propeller, as well as distributions of circulation and velocity at the propeller plane. At this point the angle of attack of the duct is modified in order to more nearly achieve zero total circulation about the duct. A reasonable estimate of how much to change the current duct angle can come directly from two-dimensional wing theory. The duct circulation can be related to a flat-plate lift coefficient and the lift coefficient can then be related to a change in angle of attack. In the same manner the propeller pitch and camber are also modified in order to obtain the desired circulation distribution as determined by the lifting-line optimization procedure.

The duct/propeller is once again analyzed, now with the updated values of duct angle of attack and propeller blade pitch and camber. This process of analysis and correction can be repeated until the total circulation about the duct is negligible and the propeller achieves the required radial distribution of circulation.

5.3.3 The Thrusting Duct

The propeller/neutral duct is the starting place for a propeller/duct which develops the required distribution of thrust. The current propeller should already develop the desired

propeller thrust. The neutral duct also has a total thrust or drag force operating on it, not necessarily the desired amount. The duct experiences a viscous drag force, which in the current method is simply assumed to be that associated with the duct's velocity of advance and an empirically obtained duct drag coefficient.

The duct also experiences a force associated with the propeller/duct interaction. This force is present, and can be substantial, even when there is zero total circulation about the duct. The propeller/duct analysis code provides us with an estimate of this force.

At this point the total thrust acting on the duct is determined by subtracting the viscous drag from the inviscid duct thrust. This is then compared with the amount of thrust desired from the duct. The difference is the additional required duct thrust. An estimate of camber and additional angle of attack which must be added to the neutral duct can be made from 2-D wing theory as before.

Once again propeller blade pitch and camber distributions are estimated. The analysis code is used to predict velocities and forces acting on the new duct/propeller. The duct angle and camber and the propeller pitch and camber are modified to achieve the desired duct thrust and propeller circulation. This process is repeated until the desired values of thrust and circulation are obtained. Figure 5.11 provides a flowchart for the design procedure.

Examples of propeller/duct geometries determined through use of this procedure are given in the next chapter.

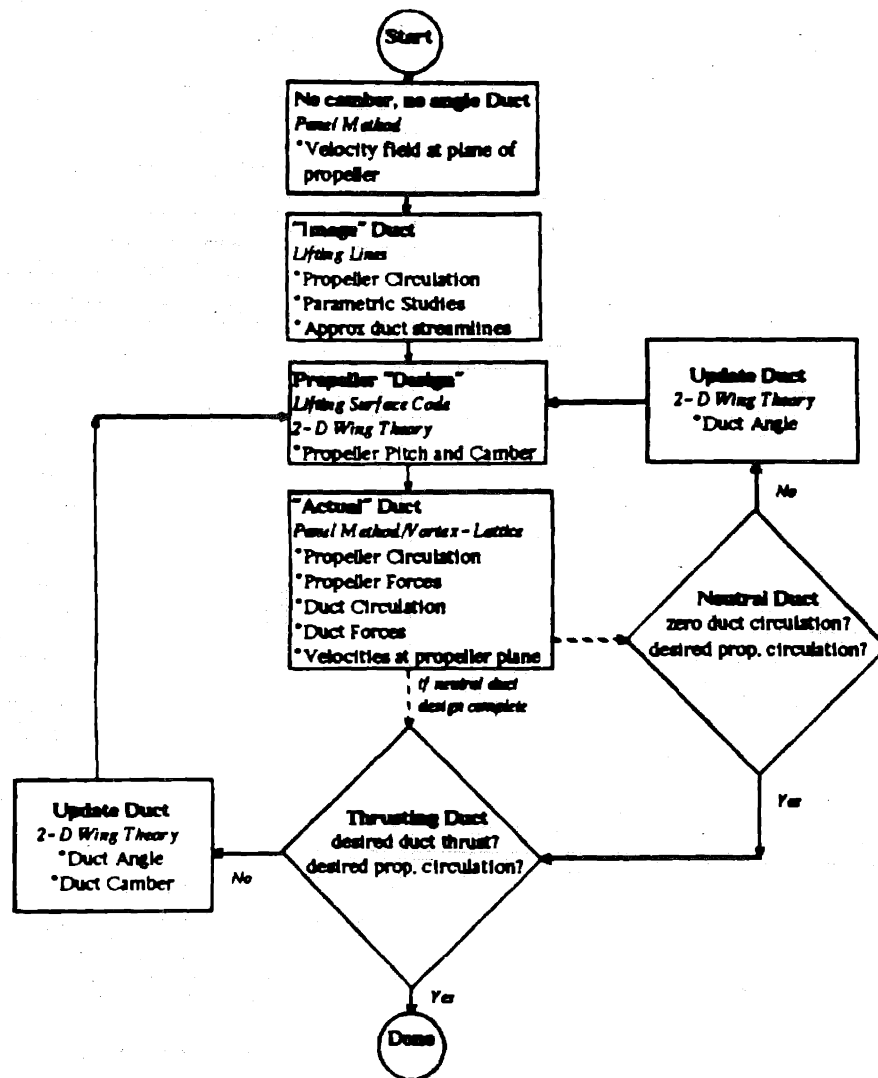


Figure 5.11: Flowchart presenting an overview of the ducted propeller design procedure

Chapter 6

Illustrative Examples

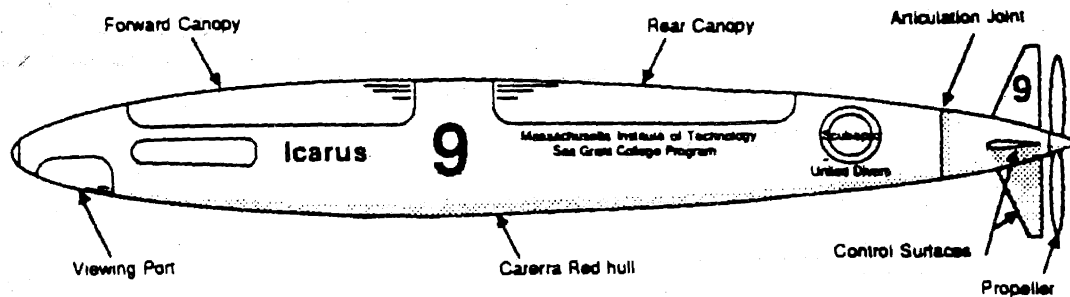
In this chapter several propulsor designs are presented. Each is intended to illustrate specific aspects of the design process, or the design of a certain propulsor type. With the exception of the first example, only selected portions of the overall design procedure are described.

In the first example a propeller is designed for a human powered submarine. In this case the design process is followed from the initial powering estimates through the construction of the actual propeller.

Next a comparative study of various propulsor types is presented. In this study the relative efficiencies of propulsors designed for the same ship operating condition is examined.

In the third example the design of a nonaxisymmetric pre-swirl stator/propeller is presented. Here the ship's power plant is assumed to be fixed and the design must proceed accordingly. Special emphasis is placed on the nonaxisymmetric aspects of the stator design.

Finally several duct/propeller designs are presented. In these examples duct and propeller geometries are determined so that specified distributions of thrust between duct and propeller are achieved.

Figure 6.1: Exterior view of *HPS Icarus*.

6.1 The Design of a Propeller for a Human Powered Submarine

In order to illustrate the overall propulsor design process using the tools and procedures described in this thesis, the design of a propeller for a rather unusual application, a human powered submarine, is presented. The human powered submersible *Icarus*, designed, built and powered by MIT students with the support of the Sea Grant College Program, was the MIT entrant in a race for such submarines sponsored by the H. A. Perry Foundation. Here the design of the propeller for this submarine is followed from the first conceptual design through to the construction of the actual propeller.

6.1.1 The Submarine Hull and Power Train

The submarine was required to be free-flooded and house two SCUBA equipped divers. Two race formats were anticipated: a 100 meter dash and a one-kilometer closed loop course. Submarines were also to be judged on cost effectiveness and innovation. The submarine was additionally required to have a turn radius to both port and starboard of less than 50 feet. Several other requirements dealt with safety concerns but did not significantly impact the overall submarine or propulsor design.

One diver was required to pilot the submarine, the other would serve as its power plant. Early in the submarine design process it was decided that the diver acting as the "engine" would transmit power to a propeller shaft by pedalling on a bicycle gear like apparatus. In order to minimize the diameter of the submarine, and thus its drag, the divers would lie either prone or recumbent.

Hull Shape	Gertler 58-4165
Length Overall	200.0 inches
Diameter	28.5 inches
Length/Diameter	7.0
Location max. diameter	40% of LOA
Prismatic Coefficient	0.60
Displacement	44.5 cu. ft., 1.27 tons
Wetted Surface	90.9 sq. ft.

Table 6.1: Characteristics of the human powered submarine hull.

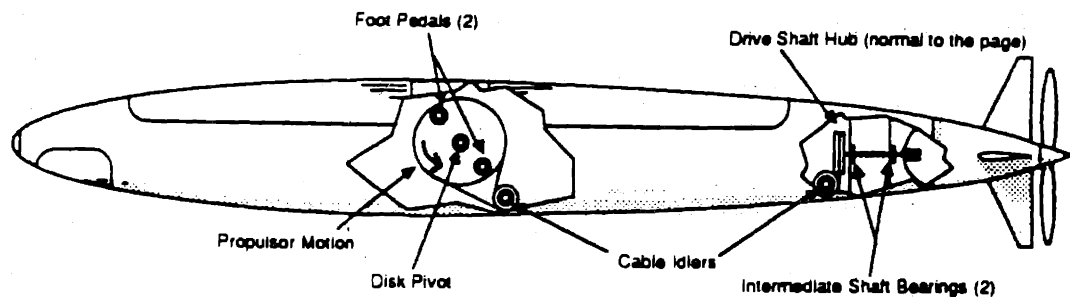


Figure 6.2: The propulsion drive train.

The hull shape of the submarine was selected on the basis of the Gertler/DTMB Series 58 data [36]. The size of the submarine was determined by the volume needed for the two occupants, their life support, and their propulsion and control activity. Table 6.1 gives some characteristics of the selected hull and figure 6.1 a sketch of the submarine exterior.

The design team considered a variety of power transmission schemes ranging from sprocket and chain to shafts and gears. The system which was finally settled upon was unconventional, utilizing a cable and pulley system. Such a system provides a number of advantages including reduced cable drag and bearing losses, low cost, long life and maintenance free operation. Figure 6.2 illustrates the propulsion design train.

The stern of the submarine was articulated in order to provide enhanced maneuverability. Figure 6.3 shows a cutaway view of the articulated tail section. Further details

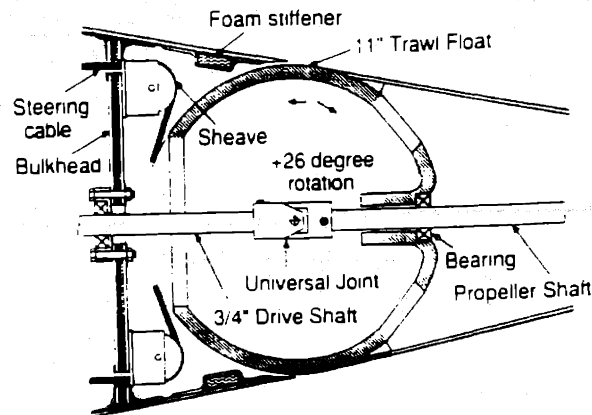


Figure 6.3: Articulated tail section (top view).

Speed	Resistance	Power
5 kts	17.4 lbs	0.27 hp
7 kts	34.1 lbs	0.52 hp

Table 6.2: Preliminary powering estimates.

of the submarine design and fabrication are provided in [41]. A number of other unique design details or special purpose devices, including buoyancy compensators and an underwater ergometer are described in this paper.

6.1.2 Preliminary Propeller Design

Based on the series data, the resistance estimates of table 6.2 were provided for the propeller design. The two speeds were thought of as cruising and sprint conditions. The power figures presented in table 6.2 simply come from the product of resistance and ship speed. The project organizers considered these to be reasonable estimates of the available power for the purposes of preliminary design. Since the actual power levels depended entirely on a diver's ability to pedal underwater while breathing through a regulator, there was more than a little uncertainty in these powering estimates. When reduced to a nondimensional thrust coefficient both conditions reduce to $C_T = 2T/\rho A_0 V_S^2 = 0.0553$.

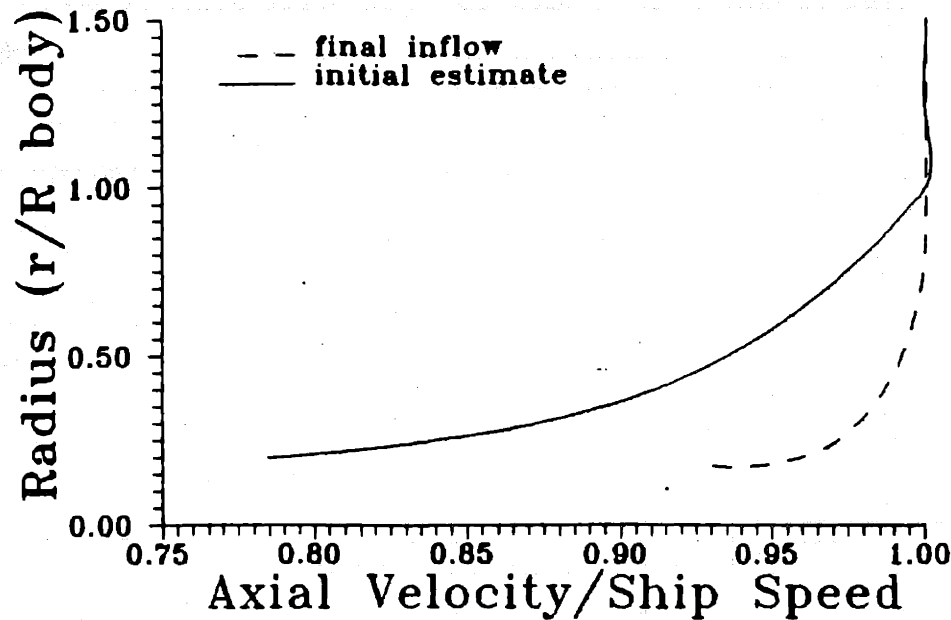


Figure 6.4: Inflow velocities used for the human powered submarine design. Radius is nondimensionalized with that of the submarine.

An almost clean slate was presented to the propeller designer. There were no definite restrictions on the propeller diameter, number of blades or rotation rate. Those constructing the submarine and its drive system were willing to confront the challenge of designing and building a drive system for a multiple stage propulsor if a significant performance enhancement could be obtained.

The PLL lifting line procedures were used to provide initial estimates of propulsor efficiency and operating conditions. Lacking an actual inflow velocity profile at the plane of propeller, that shown in figure 6.4 was assumed. For this preliminary design it was further assumed that the diameter of the hub would be 20% of the body diameter. The blade thickness at the root of the propeller was assumed to be 2% of the propeller diameter.

First single propellers were investigated. The PLL optimization procedures were used to determine spanwise distributions of chord length and circulation. Two and three bladed propellers and propellers of varying diameter were investigated. In each case PLL was used to determine the optimum propeller RPM. A summary of the results of this investigation for the five knot operating condition is shown in table 6.3. Horsepower was used as the figure of merit for this investigation since efficiency, as defined for this thesis, is a function of the wake and would vary with propeller diameter for propellers absorbing identical horsepower.

Diameter <i>feet</i>	RPM	Horsepower
Two bladed propellers		
2.4	150	0.281
3.0	94	0.279
4.0	55	0.280
Three bladed propellers		
2.0	177	0.285
2.4	123	0.282
2.6	102	0.282
3.0	78	0.283

Table 6.3: Preliminary single propeller performance estimates.

The results in table 6.3 are for the five knot operating condition. Over the range of ship speeds considered here the nondimensional thrust coefficient has been assumed constant. Since cavitation is not an issue for this propulsor, due to its relatively small diameter and thus rotational velocity, the propeller geometry for an optimum propeller will be the same for the entire range of ship speeds. The nondimensional forces and the advance coefficient are also the same as long as the thrust coefficient is fixed. The RPM scales with V_S and the horsepower with V_S^3 .

The results of table 6.3 show that a two bladed propeller of approximately three feet in diameter is expected to be the best choice. This propeller is predicted to have an efficiency of over 91%. This high efficiency is not unexpected due to the very light loading allowed by the lack of a constraint on the propeller diameter.

A contrarotating propeller was also investigated under the same set of design assumptions. First, an estimate of the potential efficiency gains for a contrarotating propeller was made. Results presented by Cox and Reed [24] indicate that in the limit of light loading a contrarotating pair of propellers can recover approximately one-half of the induced losses of a single propeller. All of the induced losses are not recovered because some percentage is associated with finite blade effects. For the three foot diameter, two bladed single propeller roughly one-half of the predicted losses were viscous. When viscous forces were neglected the propeller efficiency jumped from 91% to 95%. If viscous forces are assumed to be approximately the same for the contrarotating pair, only a two to three percent increase in efficiency for the contrarotating propellers is indicated.

To confirm this estimate PLL was used to design a contrarotating pair of propellers. The diameter of both propellers was set to three feet. Both propellers were two bladed.

The RPM of the forward propeller was fixed at 90 and the optimum RPM of the aft propeller was determined. The propellers were required to develop equal torque. The efficiency of this contrarotating pair was found to be $\eta = 0.932$ vs 0.912 for the single propeller, a 2.2% gain.

It was felt that when an actual propulsor was constructed such a small efficiency gain could not be realized. Bearing and power transmission losses associated with the more complicated mechanical system necessitated by contrarotating propellers would not be negligible. Since the torque generated by the propulsor is so small any benefit due to a potential torque balance for contrarotating propellers would also be small. It was, therefore, decided not to further investigate the contrarotating alternative. At this time it was also decided to dismiss the consideration of other nontraditional propulsor alternatives such as a propeller/stator combination because of the small potential gains in efficiency. Of course, these decisions would have to be reconsidered if a smaller diameter, more heavily loaded propeller was required for some reason.

6.1.3 Detailed Propeller Design and Fabrication

As the construction of the submarine progressed decisions were made which impacted on the propeller design. The location of the propeller at the stern of the boat was fixed and this resulted in the hub diameter being set to 3 inches in order that the hub be flush with the hull. Data on the inflow to the propeller also became available. The Gertler 58-4165 hull shape is often used as a test case for boundary layer studies (*for example see [15]*), and extensive testing and predictions have been made of the flow about this body. The details of the boundary layer depend strongly on the Reynold's number and surface roughness, however, the boundary layer thickness at the propeller plane could be estimated on the basis of the available literature to be about 1 inch. This is small enough when compared to the propeller diameter to be ignored in the present design. The potential flow solution about the hull was used to estimate the inflow to the propeller and is shown in figure 6.4. Note that this wake is much less severe than that of the original estimate.

The thickness of the propeller blade sections was also examined. Rough estimates of the strength of materials which might be used for the propeller led to a decision that a blade thickness of one-third of an inch at the root would suffice. Since PLL imposes a maximum value on the ratio of thickness to chord when determining the blade chord lengths, the blade thickness distribution had an impact on the chord lengths for such a lightly loaded propeller. These chord lengths in turn influenced the viscous losses. When these new parameters were used to evaluate optimum propeller performance the results shown in table 6.4 were obtained.

A diameter of three feet was no longer found to be optimum. The use of an even larger diameter propeller was indicated. However, there was some concern over a propeller

Diameter <i>feet</i>	RPM	Horsepower
Optimum RPM		
3.0	106	0.285
3.5	83	0.283
4.0	67	0.282
4.5	57	0.282
Fixed RPM		
3.5	90	0.284

Table 6.4: Estimated single propeller performance.

diameter considerably larger than the diameter of the hull. It was estimated that the control surfaces would extend to a diameter of slightly over 3.5 feet and this was chosen as a limiting diameter for the propeller. A slightly higher than optimum propeller rotation rate of 90 RPM was selected in order to better match what was expected to be the “engines’s” most efficient pedalling rate.

Optimum circulation distributions for this operating condition were determined with and without consideration of the presence of the hub. These distributions are shown in figure 6.5. Differences in performance between the two cases were predicted to be negligible. The predicted chord lengths for the propeller were quite small, varying from just under two inches near the root to one-half inch near the tip.

The next step in the propeller design process was to determine the propeller blade geometry. Since the aspect ratio was found to be relatively large, the blade pitch and camber could be estimated on the basis of classical lifting line theory. To do so the velocities acting at the lifting lines are used as inflow to two-dimensional wing sections. The local pitch and camber of these sections is selected so as to produce the desired radial distribution of circulation. PLL provides such pitch and camber distributions under the assumption that the blade sections have an NACA $a = 0.8$ meanline. Figure 6.6 gives the radial distributions pitch and camber for the hubless and hubloaded models. Note that these distributions are very similar.

Pitch and camber distributions which include the three-dimensional, lifting surface effects were also calculated. Included in figure 6.6 is the pitch and camber predicted by the PBD-10 lifting surface design code. Note that these distributions differ only slightly from those predicted by PLL. This is due to the high blade aspect ratio. In many respects this propeller is more like an aircraft propeller than a typical marine propeller. The pitch of all these distributions falls off at the hub due to the lower inflow velocities there. In

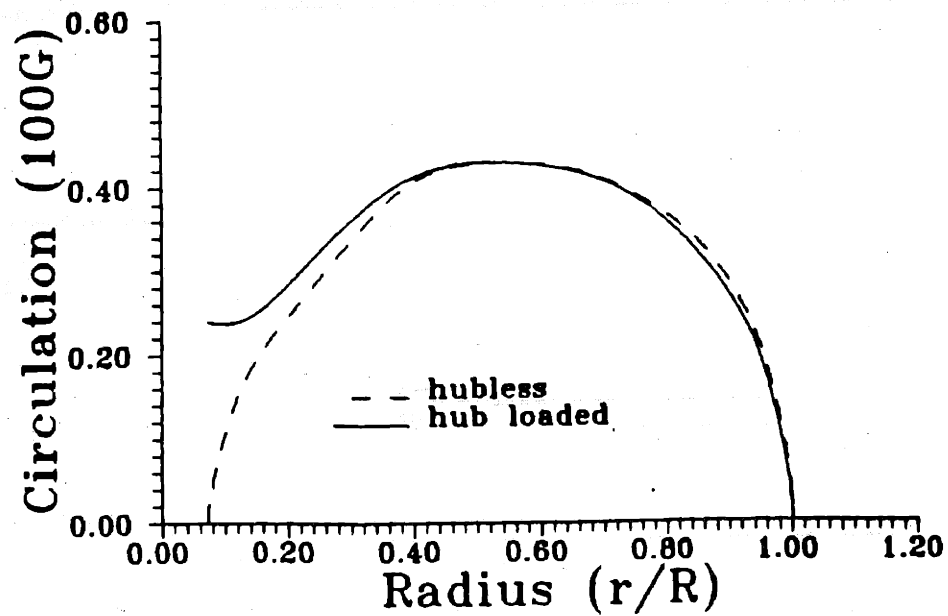


Figure 6.5: Circulation distributions for the human powered submarine propeller.

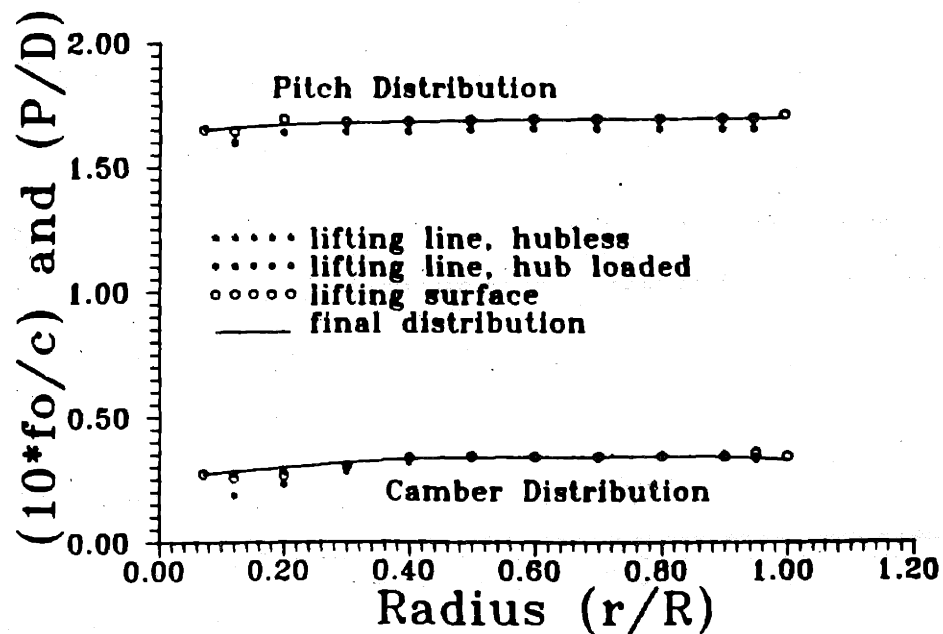


Figure 6.6: Pitch and camber distributions for the human powered submarine.

the case of uniform inflow the pitch would be very nearly constant.

The pitch and camber distributions predicted by PBD-10 were faired in order to obtain smooth distributions. These faired distributions were used for the final propeller and are also shown in figure 6.6. Figure 6.7 is a one-third scale plan view of the final blade design. Figure 6.8 is a computer depiction of the final propeller design.

A table of offsets and full-scale drawing of the propeller blades were produced. Profiles of the two-dimensional blade sections were also generated at a number of radii. These profiles were used to construct gauges, which were, in turn, used to check the dimensions of the actual blade sections.

Two propeller blades were fabricated from .25" by 2" aluminum bar stock, by Derek Moss, an undergraduate student at MIT. The rough planform was cut by a band saw. Next, the suction side was milled until the desired thickness distribution was approximately achieved. The suction surface was then hand filed for smoothness. The half-completed blade was then carefully twisted until the desired pitch distribution was obtained. The nearly flat pressure side was then hand filed to the design overall thickness. This process led to blades which were within one-thousandth of an inch of the design geometry at the measured stations.

Additional blades were made from carbon-fiber. The mold used for this purpose was created from one of the aluminum blades. These carbon-fiber blades proved reliable, and most of the submarine operations have utilized these lighter, more flexible blades.

6.1.4 Postscript

The team racing the submarine seemed quite satisfied with their propeller. Alas, the race itself did not go well. Sea conditions and underwater visibility on the day of the race were not good by the time the MIT submarine was called on to perform. The submarine experienced maneuvering difficulties which those present attributed to the current and poor visibility. The propeller became fouled in an anchor line while rounding a mark and the MIT boat did not complete the course.

However, the race team seemed convinced that they had one of the fastest boats present. Further, the boat was selected the best student design and was awarded the perpetual trophy of the American Society of Engineering Education. In view of the cancellation of most of the in-the-water speed events at the Florida competition, this design award was one of the few prizes awarded by the Perry Foundation not clouded by the weather-induced controversy. At the time of this writing there are tentative plans to perform a time trial. The possibility of another race held in better conditions has also been discussed.

The propeller designed for the human powered submarine is striking in its resemblance to an aircraft propeller. This resemblance should not be surprising since the diameter limitations, which force typical marine propellers to much higher loadings and smaller

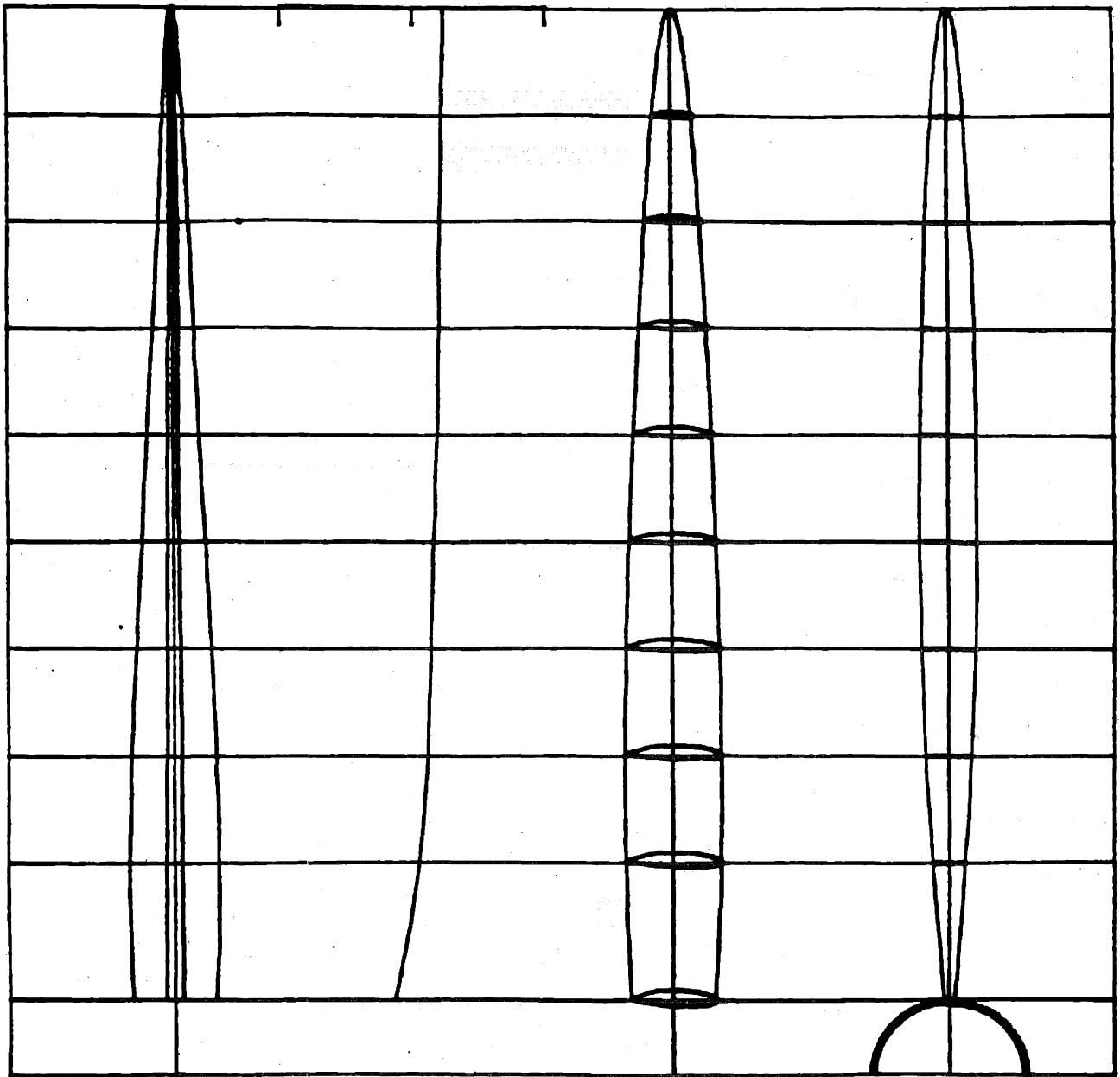


Figure 6.7: One-third scale plan view of propeller blade designed for the human powered submarine.

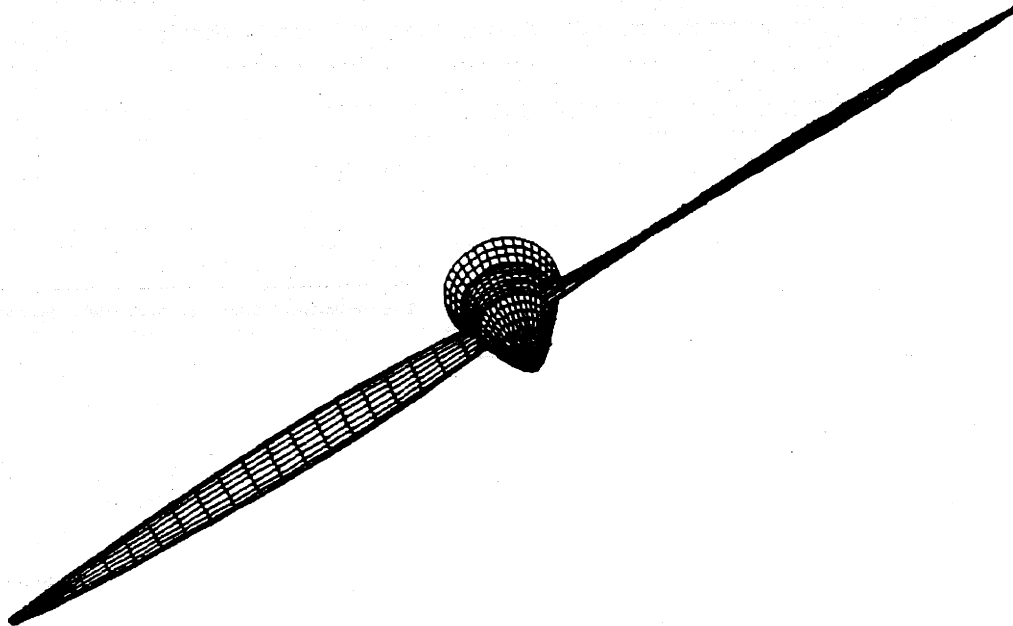


Figure 6.8: Computer depiction of human powered submarine propeller.

blade aspect ratios, were not present in this case. This propeller illustrates the importance of an analytical approach to propeller design. The use of series data would have led to a more traditional marine propeller, of smaller diameter, with a significantly lower predicted efficiency. The fact that the PLL algorithms led to what appears to be the appropriate design for this problem provides increased confidence in the design procedures presented here.

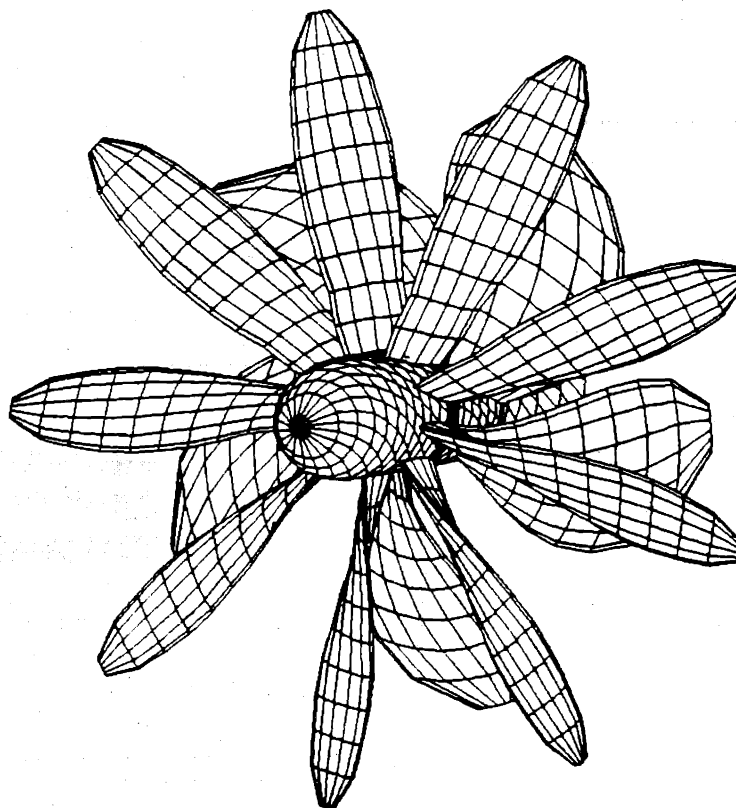


Figure 6.9: Computer depiction of a vane-wheel propulsor.

6.2 A Comparative Study of Marine Propulsors

The comparative study presented here is loosely based on the parameters used for the design of a vane-wheel propulsor described by Chen, Reed and Kim [19]. The design procedure which they employed was generally that described in this thesis. They made use of an early version of the PLL code for their performance estimates and to determine optimum circulation distributions. The lifting surface theory developed by Brockett [10] was used to determine the propeller blade geometries. They found relatively good agreement between the predicted performance of the vane-wheel propulsor and that measured in model tests.

In this study the current PLL code is used to examine the relative efficiencies of various propulsor alternatives for the same ship operating condition. PLL is used to determine optimum distributions of circulation and chord length. Typical values of blade thickness and drag coefficient are assumed. The propulsor is required to generate a thrust of 553,600 lbs. and is to operate in a uniform inflow velocity of 34.81 ft/sec. The centerline of the shaft is assumed to be submerged to a depth of 30 ft.

First a baseline propeller was considered. This propeller was taken to be five bladed

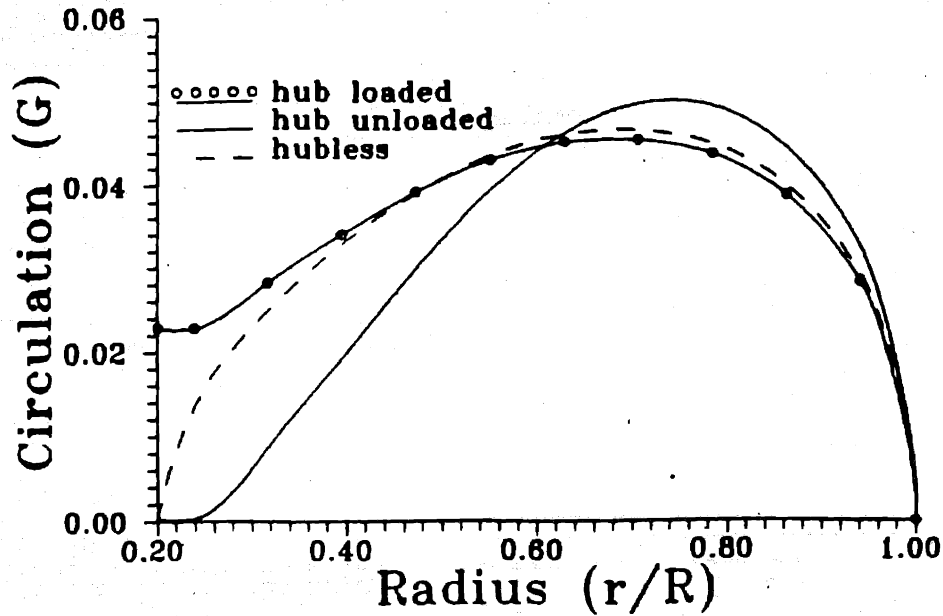


Figure 6.10: Circulation distributions for the baseline propeller.

	J_S	K_T	K_Q	η
hubless	0.762	0.3022	0.0572	0.640
hub loaded	0.747	0.2905	0.0549	0.629
hub unloaded	0.747	0.2904	0.0547	0.632

Table 6.5: Baseline propeller forces.

and have a diameter of 21 ft. The rotor of the vane-wheel propulsor described in [19] is also five bladed and of like diameter. The required thrust corresponds to $C_T = 1.325$. Optimum circulation distributions determined with and without the presence of the hub considered are shown in figure 6.10. In both cases the PLL code was also used to determine the optimum propeller rotation rate. When the presence of the hub was considered a hub unloaded circulation distribution was also examined and is shown in figure 6.10. Table 6.5 gives a summary of the performance results. The efficiency of the baseline propeller will be assumed to be $\eta = 0.632$, that of the hub unloaded distribution. This value for efficiency agrees almost exactly with that given in [19] for the rotor operating alone, $\eta = 0.633$.

The efficiency of vane-wheel propulsor for this operating condition was then examined.

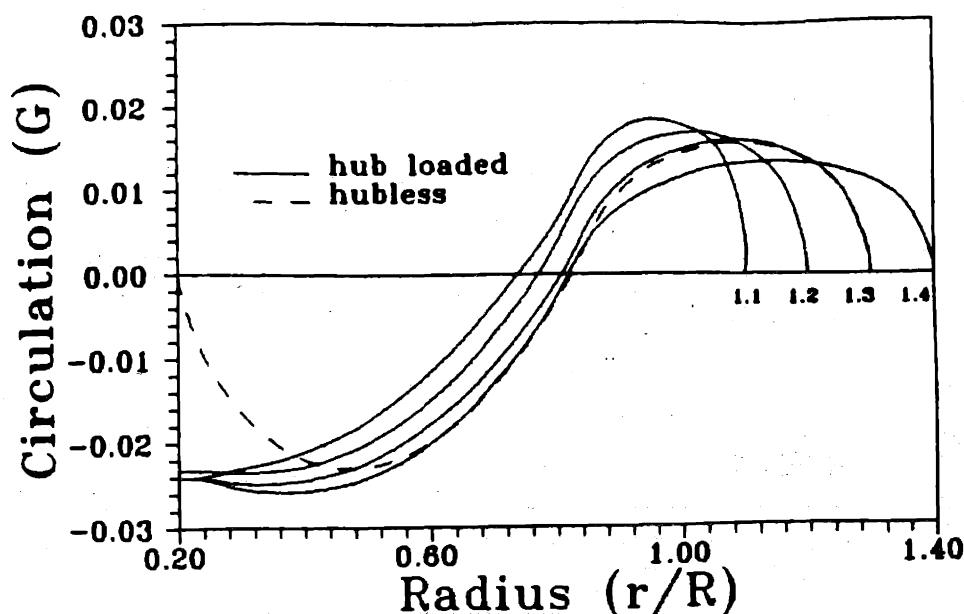


Figure 6.11: Vane-wheel circulation distributions.

The rotor was assumed to be five bladed and have a diameter of 21 ft. The rotor RPM was chosen to correspond to $J_S = 0.75$, very near that of the optimum single propeller. Nine bladed vane wheels with diameters 10, 20, 30 and 40 percent larger than that of the propeller were considered. Optimum circulation distributions for the rotor and vane-wheels were determined. Figure 6.11 gives the vane-wheel circulation distributions. A contraction ratio of 0.83 was assumed for the propeller's slipstream and the vane-wheels were located one-quarter of the rotor's diameter downstream of the rotor.

Table 6.6 gives the forces acting on the vane-wheel propulsors. All forces are nondimensionalized with the diameter and rotation rate of the rotor. While the propeller's RPM was fixed for each propulsor, the optimum vane-wheel rotation was determined and is also given in table 6.6. The overall propulsive efficiency of each propulsor is given in this table along with the percentage increase in efficiency as compared with the baseline propeller. Note that as the diameter of the vane-wheel is increased the efficiency increases.

The vane-wheel designed by Chen et al [19] was 30% larger than the rotor and rotated at 40% of the rotor's rotation rate. Forces for this vane-wheel propulsor are also given in table 6.6. The rotation selected for this propulsor is quite close to the optimum value as determined by PLL. In the design presented in [19] the circulation distribution of the vane-wheel and propeller were unloaded at the hub. Forces from PLL with a similar

	J_s	K_T	K_Q	η	$\% \Delta \eta$
Vane-wheel 10% larger				0.686	8.5
rotor	0.750	0.2688	0.0509		
vane-wheel	1.672	0.0259	0.0000		
Vane-wheel 20% larger				0.700	10.8
rotor	0.750	0.2641	0.0499		
vane-wheel	1.931	0.0288	0.0003		
Vane-wheel 30% larger				0.705	11.6
rotor	0.750	0.2608	0.0494		
vane-wheel	2.010	0.0317	0.0003		
Vane-wheel 40% larger				0.708	12.0
rotor	0.750	0.2619	0.0494		
vane-wheel	1.999	0.0308	-0.0001		
30% larger (hub unloaded)				0.696	10.1
rotor	0.750	0.2697	0.0504		
vane-wheel	2.010	0.0235	-0.0001		
30% larger (DTRC experiment)				0.692	9.5
rotor	0.771	0.2970	0.0557		
vane-wheel	1.928	0.0170	0.0004		

Table 6.6: Vane-wheel propulsor forces. Values are nondimensionalized with the diameter and rotation of the rotor.

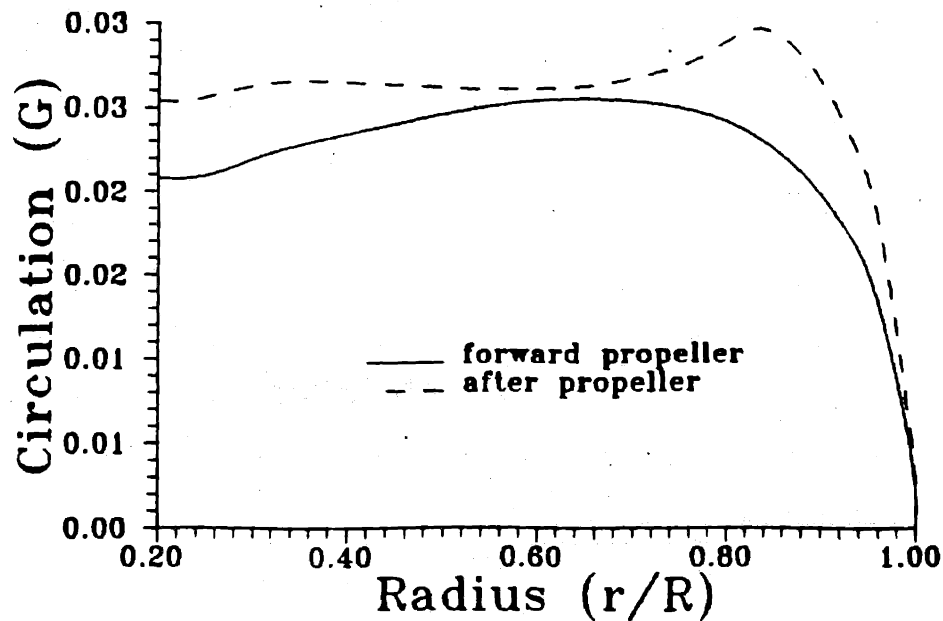


Figure 6.12: Circulation distributions for the contrarotating propellers.

unloading are also presented in table 6.6 for a vane-wheel of the same diameter. The efficiency increase of 10.1% over the baseline propeller predicted by PLL is quite close to the 9.5% measured by Chen et al.

Of course, in order to obtain the efficiency gains from the vane-wheel the physical arrangement of the ship and considerations of unsteady hull excitations must allow for the larger vane-wheel diameter. If a vane-wheel with diameter greater than that of the propeller is acceptable, a larger diameter propeller might also be indicated. PLL was, therefore, used to consider a propeller with diameter 1.3 times that of the baseline propeller. The optimum rotation rate for this propeller was found to be 65% that of the baseline propeller. The efficiency of the large diameter propeller is predicted to be 0.709 a 12% increase over that of the baseline propeller and a slight increase over the vane-wheel propulsor of like diameter. It should be noted that this large diameter, low RPM propeller would incur shaft diameter and weight penalties, including the need for larger reduction gears, etc. The hull excitation from such a propeller might also be increased.

A contrarotating pair of propellers was also considered. They were assumed to have the same diameter as the baseline propeller and be separated by a distance of one-quarter propeller diameter. The forward propeller was five bladed, the aft four. The propellers were required to have equal and opposite rotation and torque. The rotation rate was specified to be $J_S = 0.935$ which corresponds to the optimum rate for a single propeller

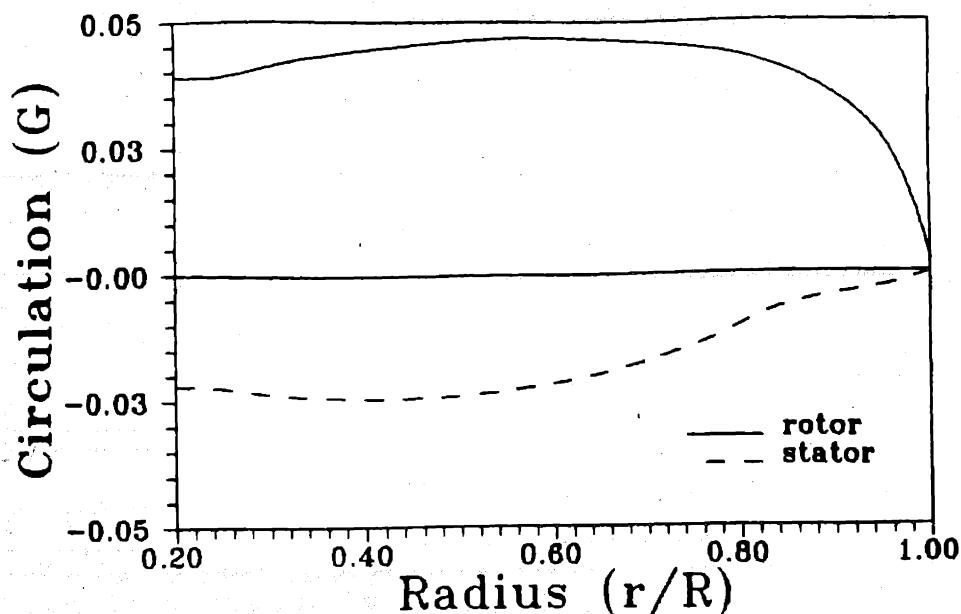


Figure 6.13: Circulation distributions for a propeller/stator.

required to generate one-half the thrust of the contrarotating pair. Figure 6.12 gives the circulation distributions for the contrarotating pair. The propulsor efficiency is $\eta = 0.724$, a 14.5% increase over that of the baseline case.

Similarly a stator operating downstream of the propeller was considered. This post-swirl stator was taken to be nine bladed and have the same diameter as the propeller. PLL was used to determine the optimum circulation distributions on the propeller stator as well as the propeller's rotation rate. Figure 6.13 gives the circulation distributions. The propeller's rotation was found to correspond to $J_S = 0.86$, 86% of the baseline propeller's rotation rate. The efficiency of this combination was found to be $\eta = 0.696$, a 10% increase over that of the baseline propeller. The efficiency is comparable to that of the vane-wheel propulsor without the increased propulsor diameter.

A ducted single propeller was also considered. The propeller diameter was that of the baseline propeller. The gap between the tip of the propeller blades and the inner surface of the duct was taken to be zero. The duct was assumed to develop 15% of the total thrust and to have a chord length of one-half the propeller's diameter. The propeller operating condition was $J_S = 0.75$. The efficiency of this ducted propeller was predicted to be $\eta = 0.679$ a 7.5% increase over that of the baseline propeller.

Finally a ducted propeller/stator was investigated. The stator was taken to have the same design characteristics as the earlier propeller/stator combination. As for the

	$C_T = 0.6625$		$C_T = 1.325$		$C_T = 2.65$	
	η	$\% \Delta \eta$	η	$\% \Delta \eta$	η	$\% \Delta \eta$
Single Propeller	0.733		0.632		0.508	
Vane-Wheel Propulsor	0.779	6.3	0.705	11.6	0.607	19.5
Contrarotating Propellers	0.803	9.6	0.724	14.6	0.614	20.9
Propeller/Stator	0.779	6.3	0.696	10.1	0.591	16.3
Ducted Propeller	0.746	1.8	0.679	7.4	0.576	13.4
Ducted Propeller/Stator	0.797	8.7	0.737	16.6	0.636	25.2
Actuator Disk	0.874	19.2	0.792	25.3	0.687	35.3

Table 6.7: Performance summary for various propulsor alternatives. C_T is based on the diameter of the single propeller.

ducted single propeller, the gap between the propeller blades was assumed to be zero as was the gap between duct and the stator blades. Again the duct was required to develop 15% of the total thrust and to have a chord length of one-half the propeller's diameter. The propeller operating condition was taken to be the same as that of the unducted propeller/stator, $J_S = 0.86$. The efficiency of this ducted propeller/stator was predicted to be $\eta = 0.737$ a 16.6% increase in efficiency over the baseline propeller.

Similar studies were performed for the same conditions, but with required thrusts of one-half and twice that previously described. Efficiencies for the various propulsors for the three required thrusts are given in table 6.7. Percent increases over the baseline propeller for each C_T are also given in this table. The ideal or actuator disk efficiency for each thrust coefficient is also presented.

All of the propulsor alternatives examined show the trend of decreased efficiency with increased thrust coefficient apparent in the actuator disk results. The percent difference in efficiency between that of the single propeller and the ideal efficiency, the actuator disk result, increases with the thrust coefficient. This is an indication that the induced losses increase with the required thrust. If this is the case we would also expect the percent increase in efficiency of the other propulsor alternatives to increase with the thrust coefficient, since the idea behind these propulsors is one of decreasing these losses. This trend is borne out in the results presented in table 6.7. Note that all of the propulsor alternatives show an efficiency gain over the single propeller.

Of the unducted propulsors the contrarotating propellers show the largest efficiency gains for each thrust coefficient. The efficiencies of the vane-wheel propulsor and the propeller/stator combination are comparable for small C_T , however, for larger thrusts the vane wheel shows an efficiency advantage. Since a propeller/stator arrangement is

likely to be mechanically much simpler than a vane-wheel propulsor such an arrangement is probably preferred for small thrust coefficients. While the ducted single propeller shows efficiency gains over the propeller acting alone, these gains are smaller than those predicted for the multiple stage propulsors. At all but the smallest value of C_T the ducted propeller/stator combination showed the largest gain in efficiency. For lightly loaded propellers the viscous drag of the duct is a not insignificant part of the total drag. Since the stator blades could be used to attach the duct to the shaft a ducted propeller/stator is not an unlikely combination.

The results shown in table 6.7 are far from comprehensive. A number of the design parameters used here were chosen arbitrarily. The gains in efficiency predicted in table 6.7 should, however, provide an indication of general trends for various propulsor alternatives. They also give a realistic indication of the magnitude of the efficiency gains which might be expected.

The actual selection of the propulsor type for a given application must also include consideration of many factors in addition to efficiency. Considerations of the ship's physical arrangement, the cost of manufacture and maintenance of the various propulsors and of shafting and reduction gears in the case of contrarotating propellers, considerations of unsteady forces, etc. must all be taken into account. For this reason the efficiency results of this section will be allowed to stand alone, without a discussion of the relative merits of the various propulsor alternatives considered here.

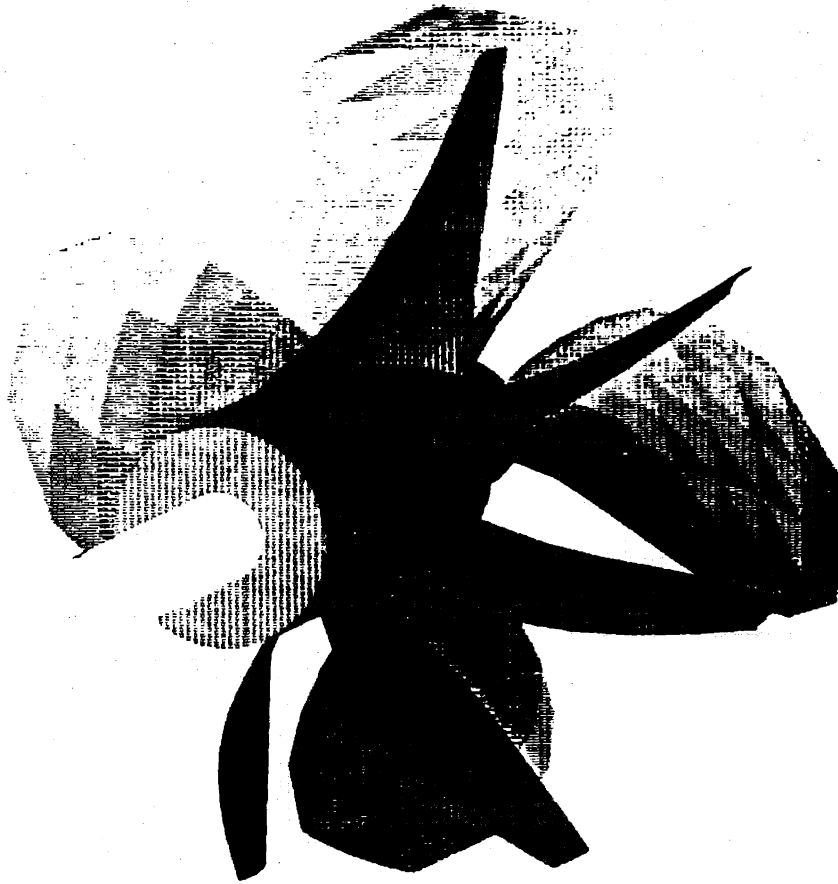


Figure 6.14: Computer generated depiction of a propeller operating behind a nonaxisymmetric, pre-swirl stator.

6.3 Design of a Nonaxisymmetric Pre-swirl Stator

In order to compare the performance of an optimum propeller with an optimum propeller/stator the described procedures are here used to carry out a sample design. The design presented here is for a United States Coast Guard, 41 foot utility boat. Larimer, et al [71] reported on their experience with a propeller/stator on this boat. Further testing and an economic analysis of the results has been presented by Sedat et al [96]. Analysis of their propeller/stator and additional details of the design presented here are provided in [22].

In this example a new propulsor was designed for a given shaft arrangement and powering. The propeller rotation rate was selected to be 1250 RPM at the design ship speed of 23 knots. This operating condition was selected so that the engine would be operating near the optimum point on its fuel map. From a regression of the full-scale

trial data it was determined that the propulsor must generate 2835 lbs. of thrust in order to achieve the design ship speed.

The inflow to the propeller was assumed to be radially uniform. Due to an inclination of the propeller shaft and the trim of the boat, the flow at the propulsor was assumed to be inclined by 13 degrees. This flow inclination results in a once per propeller revolution variation of 22.5% of ship speed in the tangential and radial inflow velocities seen by a propeller operating alone. This fluctuation of the tangential inflow velocity in turn produces unsteady forces and the possibility of unsteady propeller cavitation. The non-axisymmetric stator was to be designed in such a way so as to both increase the overall propulsor efficiency and reduce the variation in tangential inflow velocity at the propeller.

6.3.1 A Propeller Design

A propeller for operation without a stator was designed for comparative purposes before going on to the design of the propeller/stator. The PLL lifting line code was used to investigate the effect of different numbers of propeller blades on propulsive efficiency. Propellers of 3, 4, 5 and 6 blades were investigated. In each case PLL was used to determine the optimum propeller diameter as well as the circulation distributions and chord lengths. The distributions of blade thickness, skew and rake as well as the hub diameter was chosen to be the same as that used for the baseline propeller tests of [71]. These quantities along with the chord, pitch and camber of the new design are given in table 6.8

The optimum propeller diameter, required horsepower and efficiency of the various propellers is given in table 6.9. The design process was continued with the three bladed propeller. The PBD-10 code was used to find the blade pitch and camber needed to generate the load distribution determined from PLL. The geometry of this propeller is given in table 6.8. The geometry of this propeller is further illustrated in figures 6.15 and 6.16.

6.3.2 Propeller/Stator Design

For this example much of the propeller/stator geometry was assumed to be known. The stator was specified to be five bladed with a diameter of 20 inches. Table 6.10 gives other specified stator geometric quantities. The propeller chord, thickness, skew and rake are taken to be that of the baseline propeller tests of [71] and are given in table 6.11. PLL was used to determine the optimum propeller diameter as well as optimum circulation distributions for both the propeller and stator. The stator was here assumed to be axisymmetric and to have the same hub diameter as the propeller.

Since an image system of vorticity was used to represent the hub in PLL, the circulation distributions for both the propeller and stator showed the expected hub load-

radius	pitch	rake	skew	chord	camber	thickness
r/R	P/D	rake/D	degrees	c/D	f_0/c	t/D
0.1255	1.2304	-0.0173	0.00	0.1626	0.0244	0.0346
0.2000	1.1708	-0.0161	-4.48	0.2078	0.0313	0.0321
0.3000	1.1608	-0.0144	-5.38	0.2670	0.0286	0.0288
0.4000	1.1624	-0.0128	-4.65	0.3241	0.0285	0.0255
0.5000	1.1496	-0.0111	-3.56	0.3780	0.0244	0.0222
0.6000	1.1381	-0.0095	-2.24	0.4271	0.0211	0.0189
0.7000	1.1272	-0.0079	-0.20	0.4671	0.0196	0.0157
0.8000	1.1027	-0.0062	2.81	0.4809	0.0173	0.0124
0.9000	1.0534	-0.0046	7.01	0.4385	0.0204	0.0091
0.9500	1.0160	-0.0037	9.63	0.3700	0.0267	0.0074
1.0000	0.9681	-0.0029	12.63	0.0000	0.0336	0.0058

Table 6.8: Geometry of propeller designed for 1250 RPM at 23 knots. This propeller is 25.44 inches in diameter and has 3 blades. It is predicted to develop 2835 lbs. of thrust for 286.3 SHP.

Number of Blades	Diameter <i>feet</i>	SHP	efficiency
3	2.12	286.3	0.710
4	2.03	286.6	0.709
5	1.97	287.8	0.707
6	1.92	289.4	0.703

Table 6.9: Optimum propeller diameter, SHP and efficiency as determined by PLL for propellers with varying number of blades.

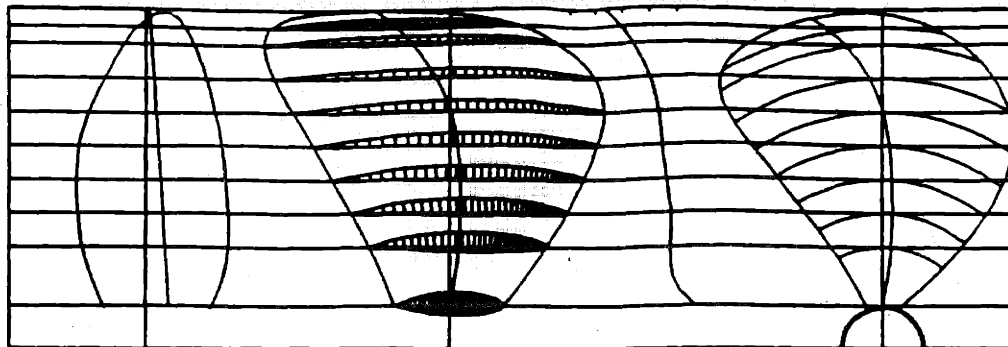


Figure 6.15: Plan view of the 3-bladed propeller geometry as determined by PLL and PBD-10.

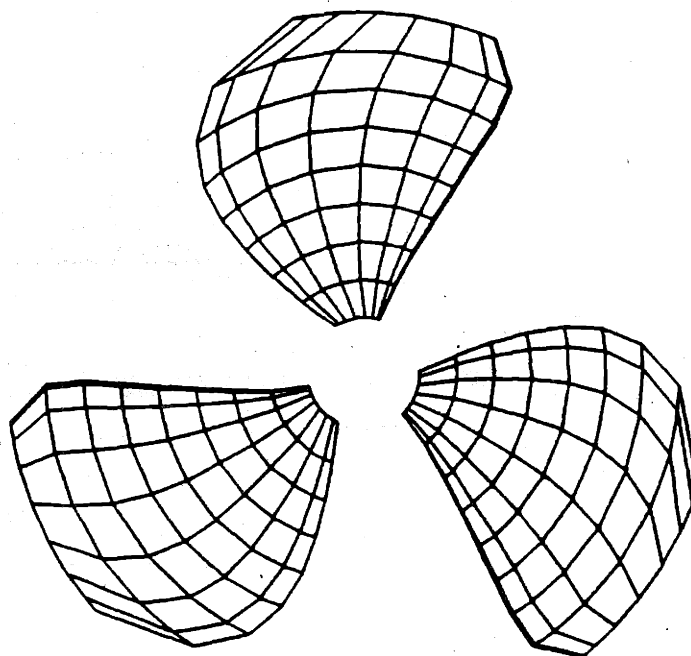


Figure 6.16: A depiction of the PBD-10 vortex lattice for the 3-bladed propeller.

radius r/R	chord c/D	rake rake/D	skew degrees	thickness t/D
0.2375	0.5222	-0.2611	0.00	0.0393
0.3000	0.4862	-0.2431	-0.82	0.0377
0.4000	0.4286	-0.2143	-2.14	0.0352
0.5000	0.3710	-0.1855	-3.45	0.0327
0.6000	0.3134	-0.1567	-4.77	0.0301
0.7000	0.2556	-0.1278	-6.09	0.0270
0.8000	0.1982	-0.0991	-7.42	0.0234
0.9000	0.1406	-0.0703	-8.75	0.0190
0.9500	0.1118	-0.0559	-9.41	0.0165
1.0000	0.0830	-0.0415	-10.00	0.0138

Table 6.10: Stator blade chord, rake, skew and thickness at radii for input to the computer codes.

radius r/R	rake rake/D	skew degrees	chord c/D	camber f_0/c	thickness t/D
0.123	-0.0173	0.00	0.1239	0.0961	0.0346
0.200	-0.0161	-4.48	0.1731	0.0789	0.0321
0.300	-0.0144	-5.38	0.2349	0.0598	0.0288
0.400	-0.0128	-4.65	0.2927	0.0444	0.0255
0.500	-0.0111	-3.56	0.3442	0.0327	0.0222
0.600	-0.0095	-2.24	0.3852	0.0245	0.0189
0.700	-0.0079	-0.20	0.4063	0.0194	0.0157
0.800	-0.0062	2.81	0.3898	0.0162	0.0124
0.900	-0.0046	7.01	0.3128	0.0138	0.0091
0.950	-0.0037	9.63	0.2318	0.0127	0.0074
1.000	-0.0029	12.63	0.0000	0.0113	0.0058

Table 6.11: Nondimensional rake, skew, chord, camber and thickness as a function of radius for propeller of the propeller/stator pair.

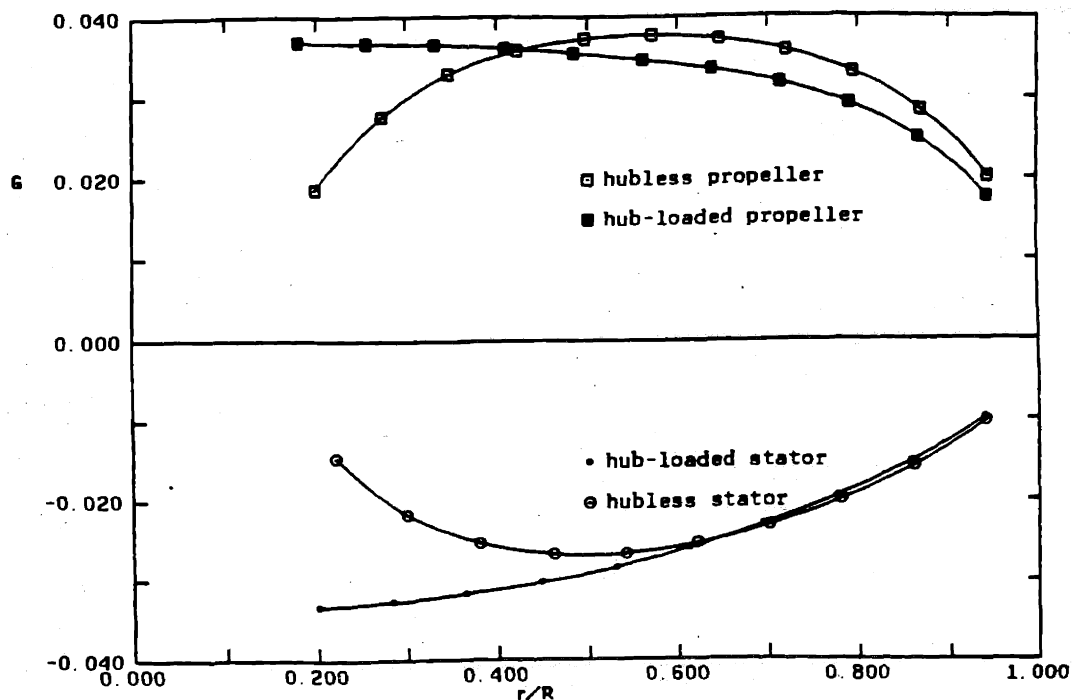


Figure 6.17: Optimum circulation distributions as predicted by PLL for propeller/stator.

ing. Figure 6.17 shows these circulation distributions along with distributions for a propeller/stator pair for which the presence of the hub was ignored. The optimum propeller diameter was found to be 22.5 inches. The propeller was predicted to absorb 270.4 SHP, corresponding to an efficiency of 0.752. This is an increase in efficiency of just under six percent over that of the optimum three bladed propeller.

Next the propeller pitch and camber needed to generate the desired circulation distribution was determined. At the time this design was carried out the PBD-11 code was not available. Therefore, the PBD-10 code was modified so as to include an image system of vorticity in order to represent the hub. This modified version of PBD-10 was used to determine the blade pitch and camber presented in table 6.12. The inflow to the propeller was taken to be the velocity field induced by the stator as determined by PLL. Figure 6.18 gives a plan view of the propeller.

radius	pitch	camber
r/R	P/D	f_0/c
0.1432	0.8674	0.0352
0.2000	0.9518	0.0604
0.3000	1.0609	0.0483
0.4000	1.1328	0.0339
0.5000	1.1709	0.0251
0.6000	1.1918	0.0199
0.7000	1.2028	0.0180
0.8000	1.2035	0.0185
0.9000	1.1956	0.0231
0.9500	1.1911	0.0306
1.0000	1.1489	0.0503

Table 6.12: Pitch and camber distributions as determined by the version of PBD-10 modified to include an image representation of the hub.

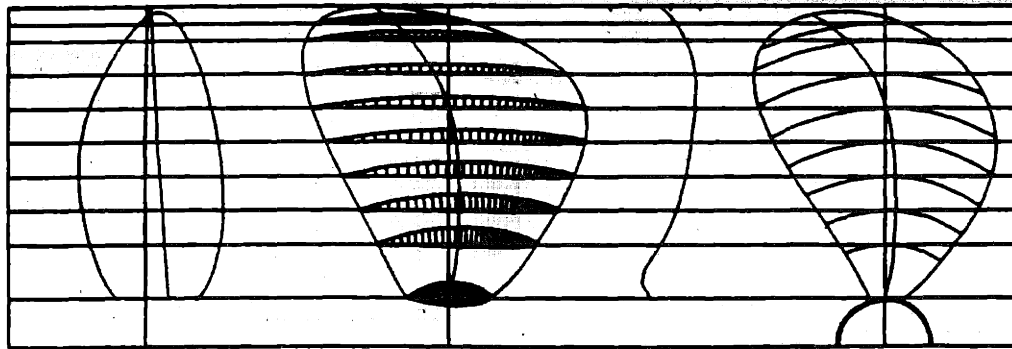


Figure 6.18: Plan view of the propeller designed for operation with the pre-swirl stator.

Next PLL was used to investigate the effects of nonaxisymmetry in the stator design. The stator blades were placed on the side of the propulsor disk which experienced decreased tangential velocity due to the flow inclination. Blades were placed at angular positions of 27 degrees, 72 degrees, 117 degrees, 162 degrees and 207 degrees from top dead center. The circulation on each of the blades was taken to be the mean circulation of the axisymmetric design multiplied by a scale factor. The two outer blades, located at 27 degrees and 207 degrees, were given 90 percent of the mean per blade circulation. The blades at 72 degrees and 162 degrees carried the mean per blade circulation and the central blade 120 percent of the mean. Thus, the overall mean per blade loading was that of the axisymmetric stator as determined by PLL.

PLL was then used to calculate the velocities and forces of the nonaxisymmetric stator. Total stator forces predicted for the nonaxisymmetric stator were found to be in good agreement with those of the equivalent axisymmetric stator. Figure 6.19 gives the mean tangential inflow velocities at the plane of the propeller operating with and without the stator. Note the substantial reduction in the tangential velocity fluctuation at the inner radii.

In an effort to further quantify how much the stator "evened out" the inflow to the propeller, the unsteady variation in the propeller's angle of advance was calculated. This pitch angle includes the inflow velocity, the propeller's rotation and the velocity induced by the stator on the propeller, but does not include the velocity induced by the propeller on the stator.

$$\beta(r, \theta) = \tan^{-1} \left(\frac{V_a(r, \theta) + u_a(r, \theta)_{\text{stator}}}{V_t(r, \theta) + u_t(r, \theta)_{\text{stator}} + \omega r} \right). \quad (6.1)$$

This angle can be thought of as the local blade angle of attack.

Figure 6.20 plots the maximum variation in advance angle vs. radius. One curve is for the propeller operating alone. Note that the magnitude of the variation in pitch angle is much larger at the hub than at the tip. At the outer radii the rotational velocity is dominant. Results for the propeller operating in the mean tangential velocity field of the stator are also presented. Since the tangential velocity field near the hub is increased, the fluctuation of the advance angle is somewhat reduced. Finally results are shown for the propeller operating downstream of the nonaxisymmetric stator. Note the further reduction in the fluctuation of the advance angle, especially in the vicinity of the hub.

The current stator clearly reduces the excursion in tangential velocity near the hub, but has little effect near the tip of the propeller. If a reduction of unsteady cavitation or forces were an overriding concern a larger diameter stator with more blades and increased tip loading could be designed. Such a stator would, however, result in a substantial decrease in the overall propulsor efficiency due to increased viscous losses associated with a necessary increase in blade area.

Finally the actual blade geometry of the nonaxisymmetric stator had to be determined. Before the stator analysis and design code, SSF-1, could be used for this pur-

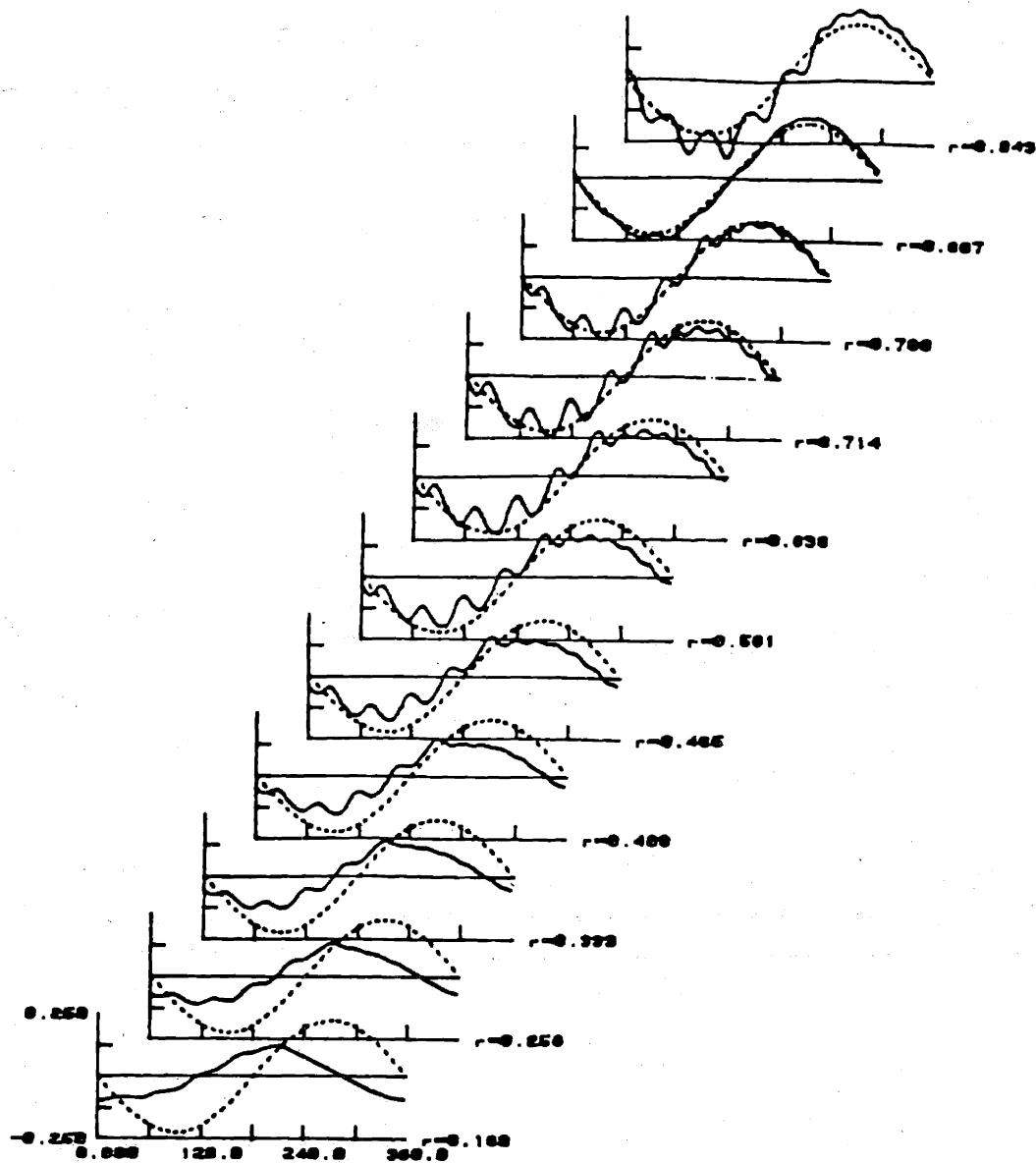


Figure 6.19: Angular variation in tangential velocity at the plane of the propeller presented at a number of radii. The dashed line is the inflow due to the 13 degree flow inclination. The solid line is the same flow as modified by the pre-swirl stator design. The velocities are nondimensionalized with the ship speed and the radii with the propeller radius.

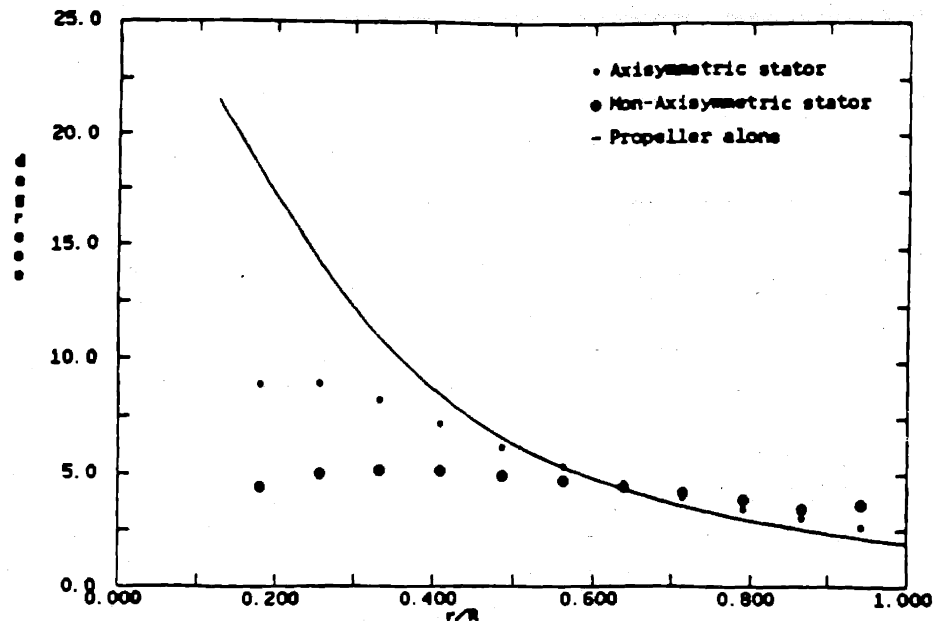


Figure 6.20: Radial distribution of maximum variation in propeller advance angle.

pose, the difference in hub diameter between the stator and the propeller had to be taken into account. The circulation distributions of the stator blades, determined under the assumption of equal hub diameters, was related to the circulation distributions of the actual stator with its larger hub diameter by a application of equation 3.15.

SSF-1 was then used to find the pitch and camber which provided the desired circulation distribution on each the stator blades. Table 6.13 gives these distributions. Figure 6.21 shows a vortex lattice representation of this geometry. A computer generated depiction of the final propeller/stator design is provided in figure 6.14.

radius r/R	Pitch Angle (<i>degrees</i>) for blade at				
	27°	72°	117°	162°	207°
0.237	80.55	83.54	77.57	73.01	68.46
0.300	82.60	85.98	81.00	76.25	70.77
0.400	85.40	89.45	85.92	80.90	74.19
0.500	87.65	92.42	90.18	84.95	77.28
0.600	89.34	94.91	93.80	88.39	80.05
0.700	90.67	96.90	96.76	91.23	82.49
0.800	91.05	98.39	99.08	93.47	84.62
0.900	91.08	99.40	100.74	95.10	86.42
0.950	90.88	99.72	101.33	95.68	87.20
1.000	90.55	99.91	101.76	96.12	87.90
	Camber (f_0/c)				
0.237	0.157	0.160	0.147	0.105	0.087
0.300	0.137	0.140	0.130	0.095	0.079
0.400	0.110	0.113	0.108	0.081	0.068
0.500	0.089	0.092	0.091	0.070	0.057
0.600	0.074	0.077	0.079	0.062	0.051
0.700	0.065	0.068	0.073	0.057	0.050
0.800	0.062	0.065	0.072	0.055	0.052
0.900	0.066	0.068	0.076	0.056	0.054
0.950	0.070	0.072	0.080	0.058	0.056
1.000	0.075	0.077	0.086	0.060	0.050

Table 6.13: Pitch and camber distributions for the nonaxisymmetric stator blades as determined by SSF-1

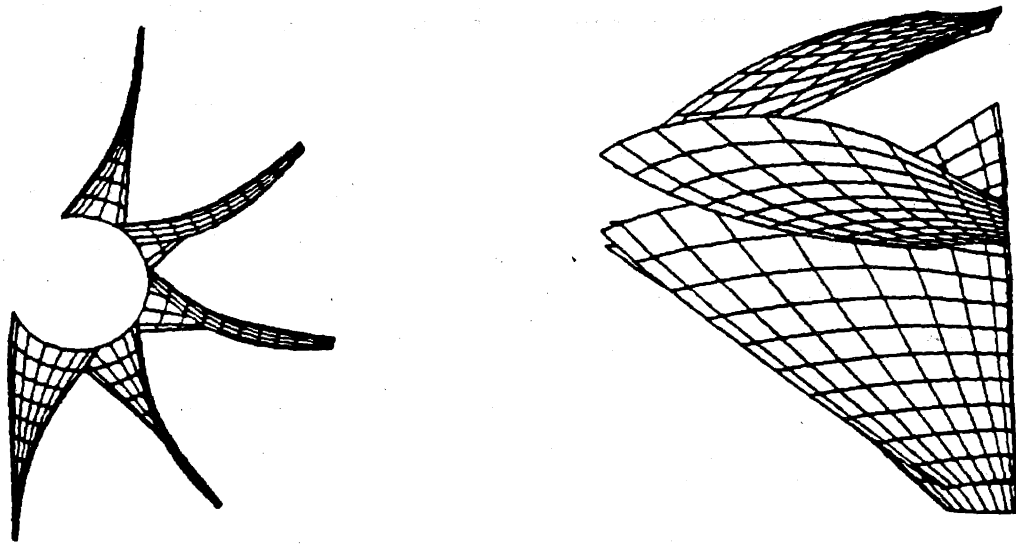


Figure 6.21: Depiction of the nonaxisymmetric stator design. Views of the stator from the front and from above are presented.

6.4 Ducted Propeller Designs

In the two examples which follow the described procedures are used to determine duct and propeller geometries. In each case the required forces and propeller operating conditions are taken as given, as are many of the geometric quantities. The focus of these examples is on finding the optimum propeller load distribution, the propeller's pitch and camber which realizes this distribution, and the duct angle and camber which provide the required division of thrust.

6.4.1 Zero Gap Case

In this example the effective gap between the tip of the propeller blade and the inner surface of the duct will be considered as equal to zero. Here the propeller is to operate at an advance coefficient of $J = V_S/(nD) = 0.6$ and the duct/propeller is to generate a total thrust given by a thrust coefficient of $C_T = T/(\frac{1}{2}\rho V_S^2 A_0) = 2.0$. Five percent of the total thrust is to be generated by the duct, $\tau = T_P/(T_P + T_D) = 0.95$. The inflow to the propulsor is here taken to be uniform and equal to the ship speed, V_S .

We also specify much of the duct and propeller geometry. The distribution of propeller thickness and chord are specified as those employed in the Wageningen KA series [111], and are presented in table 6.14. The skew and rake of the propeller are set equal to zero. The chordwise thickness and camber distributions are given by a modified NACA-66 thickness form [7] and a NACA $a = 0.8$ meanline [1]. This mean line and thickness form are also used for the duct. The chord length of the duct is the same as the radius of the propeller. The maximum thickness of the duct is taken to be fifteen percent of the chord. The center-plane of the propeller is located at the duct mid-chord.

First a duct of the desired thickness and zero angle of attack was run in uniform inflow. The velocities at the plane of the propeller were then used as the inflow in the lifting-line model. The lifting-line code was then run in order to determine the optimum propeller circulation distribution. This circulation distribution is presented in figure 6.23. Note that the circulation at the blade tip does not fall off to zero. The presence to this tip loading implies that the propeller circulation must be transferred to the duct and is not shed into the wake as a tip vortex.

An initial estimate of the propeller blade pitch was made by adding an angle of attack determined from 2-D wing theory to the hydrodynamic pitch angle. The first guess at the blade camber was also determined from 2-D wing theory. Streamlines from the lifting-line model were used to determine a first guess of 10 degrees for the angle of attack of the neutral duct.

The combined lifting-surface/panel method was then used to analyze this propeller-duct geometry. The resulting propeller circulation distribution and the total circulation about the duct were used to adjust the geometry of both the duct and propeller. This

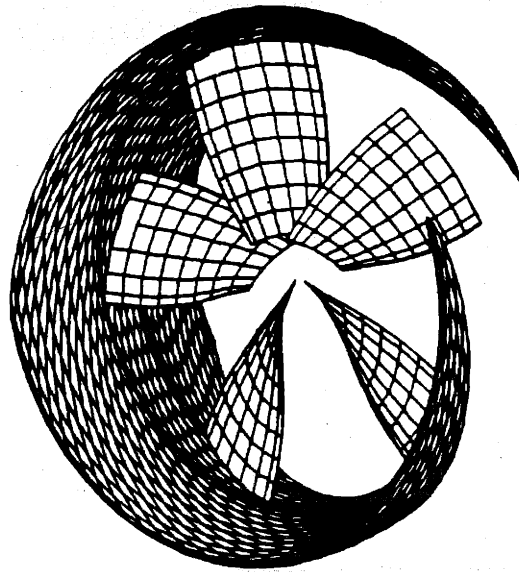


Figure 6.22: Ducted propeller with zero gap between blade tip and duct.

radius	chord	thickness
r/R	c/D	t_0/D
0.182	0.179	0.039
0.300	0.208	0.031
0.400	0.232	0.023
0.500	0.254	0.016
0.600	0.273	0.015
0.700	0.288	0.015
0.800	0.299	0.015
0.900	0.306	0.015
0.950	0.308	0.015
1.000	0.309	0.015

Table 6.14: Radial chord and thickness distributions for the zero-gap propeller.

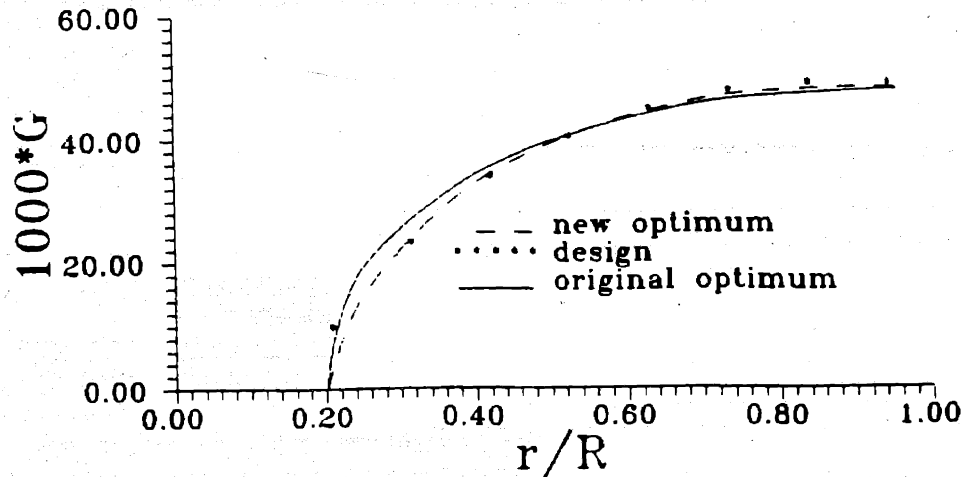


Figure 6.23: Circulation distributions at the plane of the propeller with zero gap between duct and propeller. $G = \Gamma/(\pi D V_S)$.

process was repeated several times until the average circulation about the duct was negligible and the propeller circulation was nearly equal to the optimum distribution. Table 6.15 gives the initial and final propeller pitch and camber distributions. The initial duct angle was 10 degrees. The duct angle which actually achieved zero net duct circulation is 14 degrees. This difference is not unexpected due to the strong propeller/duct interaction when there is no gap between duct and propeller. Figure 6.24 illustrates the final propeller blade geometry and figure 6.22 shows the duct and propeller geometry as discretized for the analysis code.

The forces acting on the propeller and duct are presented in table 6.16. When calculating these forces the viscous drag on both the duct and propeller blade sections was computed with an assumed 2-D airfoil drag coefficient of $C_D = D/(\frac{1}{2}\rho V_S^2 c) = 0.0085$. Forces predicted from the lifting line model and from the analysis of the final blade geometry are shown in table 6.16.

Note that the neutral duct very nearly generates the required five percent of the total thrust. This force is not associated with the total circulation around the duct, but rather with the local duct-propeller interaction. In this zero-gap case the propeller-duct interaction is quite strong and this force relatively large. The character of this interaction can be seen in the pressures on the inner duct surface shown in figure 6.25. The jump in pressure from one side of the propeller blade, $\theta = 0$ degrees, to the other side, $\theta = 72$ degrees, is indicative of this interaction. Note that there is no pronounced suction peak at the duct's leading edge, which indicates that the duct is close to its ideal angle of

radius	pitch P/D		camber f_0/c	
r/R	initial	final	initial	final
0.182	0.6273	0.7860	0.0000	0.0000
0.300	0.9096	0.9820	0.0237	0.0289
0.400	0.9657	0.9987	0.0255	0.0310
0.500	0.9804	0.9954	0.0232	0.0272
0.600	0.9919	0.9945	0.0204	0.0252
0.700	1.0025	0.9910	0.0178	0.0220
0.800	1.0154	1.0065	0.0156	0.0194
0.900	1.0351	1.0350	0.0137	0.0172
0.950	1.0469	1.0380	0.0129	0.0165
1.000	1.0608	1.0220	0.0129	0.0165

Table 6.15: Radial pitch and camber distributions zero-gap propeller.

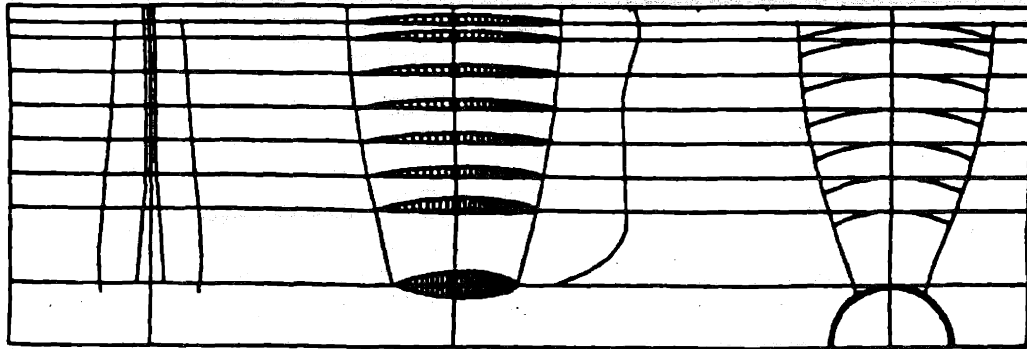


Figure 6.24: Propeller blade geometry for the zero-gap design.

	K_T	K_Q	C_T duct	C_T total	τ
lifting-line	0.283	0.0514	0.1051	2.105	0.950
final analysis	0.286	0.0509	0.1027	2.126	0.952

Table 6.16: Total forces acting on the zero-gap propeller/duct.

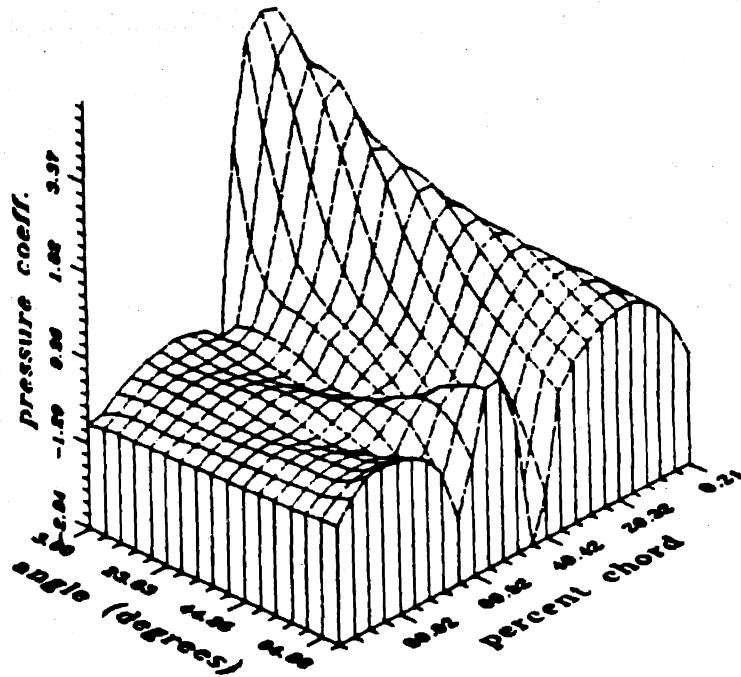


Figure 6.25: Pressure coefficients on the inner surface of the zero-gap duct. The circumferential coordinate is given in degrees and runs from the suction side of one propeller blade to the pressure side of the next. The chordwise coordinate varies along helical strips aligned with the blade tips. The duct pressure coefficient is defined as $C_P = (p - p_\infty) / (\frac{1}{2} \rho V_S^2)$.

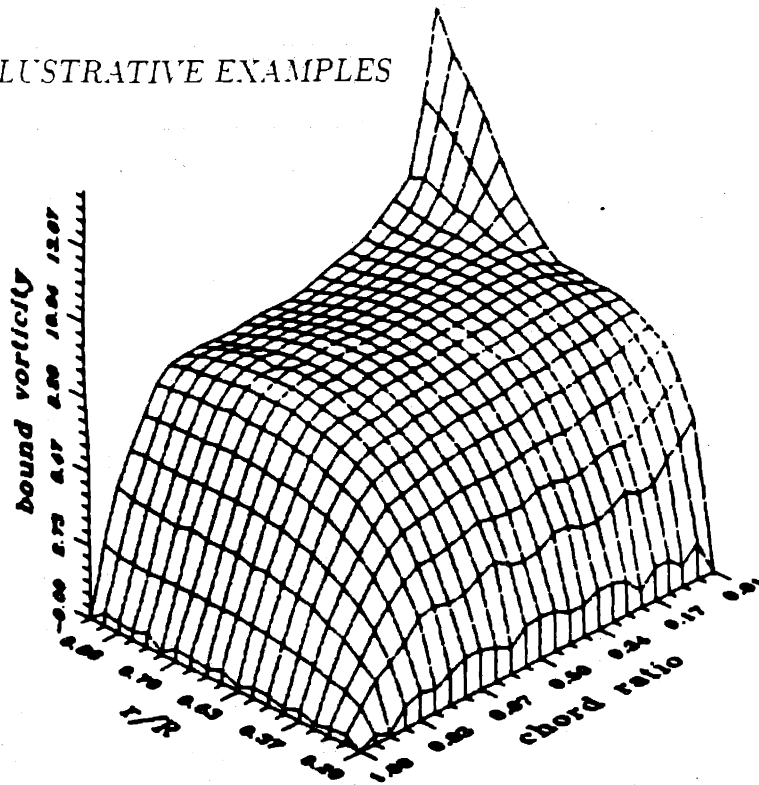


Figure 6.26: Chordwise circulation distributions on the propeller blade for the zero gap design.

attack.

The propeller circulation distribution from final analysis is plotted in figure 6.23 along with the optimum circulation distribution. If the velocities at the plane of the propeller lifting lines are input back into the circulation optimization algorithm a new optimum distribution can be obtained. This distribution is also shown in figure 6.23. Note that the three circulation distributions are very nearly the same. Figure 6.26 shows the distribution of bound vorticity on the propeller blade. Note that, with the exception of the tip section, the blade appears to be operating at its ideal angle of attack.

The thrust generated by the duct/propeller interaction very nearly equals the desired duct thrust. For this reason no additional camber or angle of attack was added to the duct.

6.4.2 Finite Gap Case

In this example the gap between the tip of the propeller and the duct is five percent of the propeller radius. The propeller is to operate at an advance coefficient of $J = 0.89$ and the duct/propeller is to generate a total thrust given by $C_T = 0.69$. Ten percent of this thrust is to be generated on the duct, i.e., $\tau = 0.90$. The inflow to the propulsor is again taken to be uniform and equal to the ship speed, V_S .

radius	chord	thickness
r/R	c/D	t_0/D
0.182	0.2022	0.0433
0.300	0.2846	0.0376
0.400	0.3456	0.0328
0.500	0.3959	0.0280
0.600	0.4323	0.0232
0.700	0.4487	0.0184
0.800	0.4417	0.0136
0.900	0.4020	0.0088
0.950	0.3423	0.0064
1.000	0.1500	0.0040

Table 6.17: Radial chord and thickness distributions for the five percent gap propeller.

The skew and rake of the propeller are set equal to zero. The propeller chord and thickness distributions are given in table 6.17. The chordwise thickness and camber distributions are given by a modified NACA-66 thickness form [7] and a NACA $a = 0.8$ meanline [1]. This mean line and thickness form are also used for the duct. Again the propeller is to be located at the duct midchord and the duct chord is taken to be equal to the propeller radius.

For this design the same general procedure was followed as for the zero-gap case. Figure 6.27 presents the optimum propeller circulation distribution predicted by the lifting-line code. Note that the circulation falls off to zero at the propeller tip when there is a nonzero gap between duct and propeller. Again the pitch and camber distributions which provide the required circulation distribution inside of the neutral duct are estimated, as is the duct angle. After five iterations of analysis and modifications to the propeller and duct a neutral duct design was arrived at. Figure 6.28 gives the propeller geometry. The neutral duct angle is 4.5 degrees, compared with an initial estimate from the lifting line streamlines of 2.25 degrees.

The forces from analysis of the neutral duct/propeller and from the lifting-line method are presented in table 6.18. Notice that the force acting on the neutral duct is quite small compared to that generated in the case of zero-gap between duct and propeller. This time camber and angle will have to be added to the duct to produce the desired division of thrust.

After nine iterations of modifying duct angle and camber in order to achieve the desired duct thrust, and of changing the propeller blades' pitch and camber to achieve the

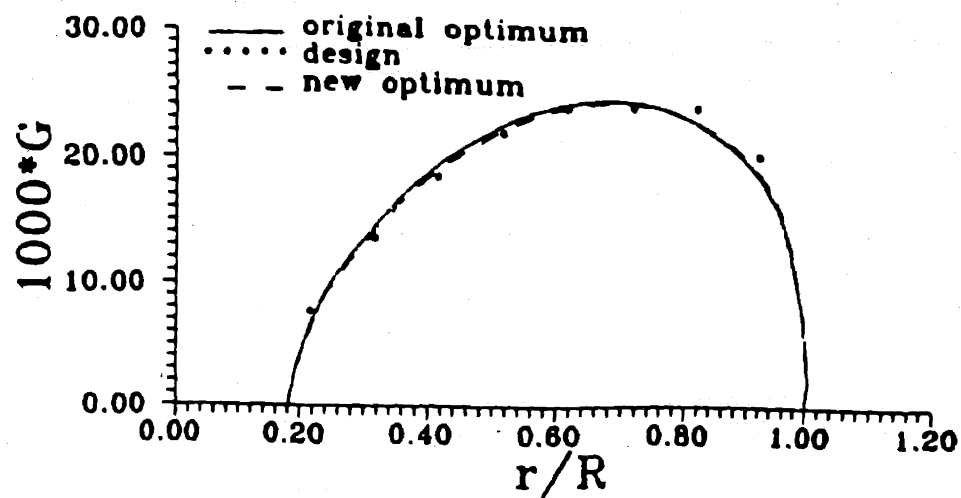


Figure 6.27: Propeller circulation for the five percent gap design.

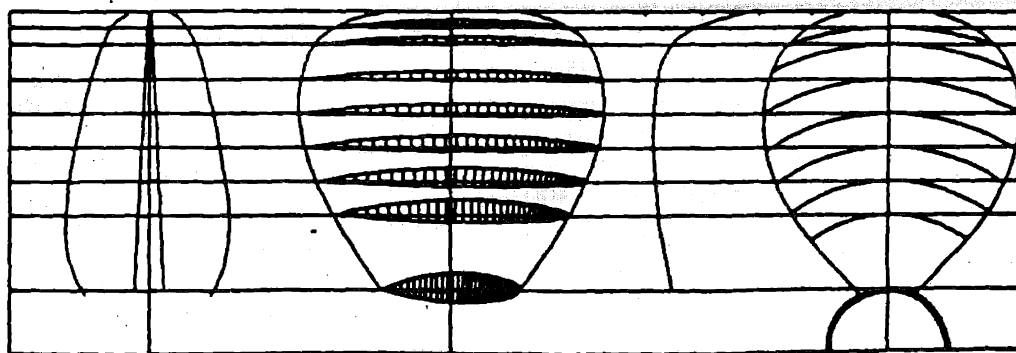


Figure 6.28: Geometry of five-percent gap propeller inside of the neutral duct.

	K_T	K_Q	C_T duct	C_T total	τ
lifting-line, <i>no rings</i>	0.193	0.0442	0.0000	0.621	1.000
neutral duct analysis	0.196	0.0466	0.0099	0.641	0.985
lifting-line	0.193	0.0515	0.0690	0.690	0.900
final duct analysis	0.191	0.0515	0.0743	0.690	0.892

Table 6.18: Total forces acting on the five percent gap propeller/duct.

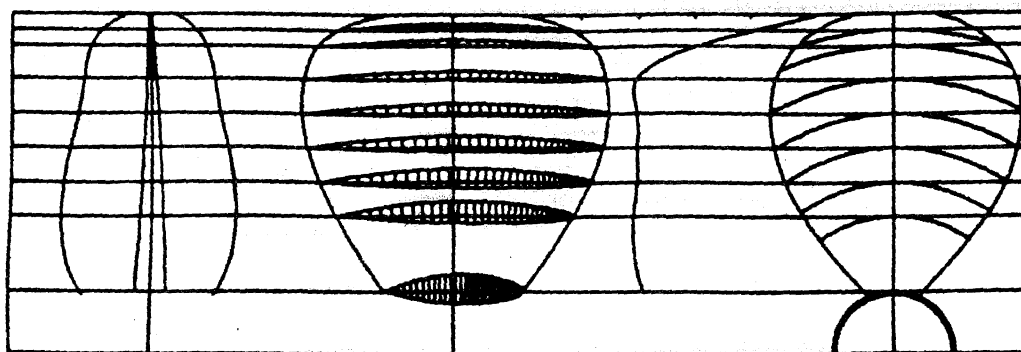


Figure 6.29: Geometry of five-percent gap propeller inside of the thrusting duct.

desired propeller circulation, a final design was obtained. Figure 6.29 gives the propeller geometry and figure 5.10 shows the geometry used in the propeller/duct analysis code. The final duct angle was 3.85 degrees with the maximum duct camber 2.9 percent of the duct chord.

The forces acting on this final duct design are given in table 6.18 along with those for the neutral duct. Forces predicted by the lifting line model are also presented. Note the close agreement between the lifting line prediction and the analysis of the final design. The propeller circulation distribution from final analysis is plotted in figure 6.27 along with the optimum circulation distribution. The circulation distribution obtained by using the velocities from the final analysis in the optimization procedure is also presented in figure 6.27. As was the case for the zero gap design the three distributions are very nearly the same.

Chapter 7

Concluding Remarks

Much of the work presented here is a synthesis of the efforts of earlier researchers. Following is a list of what the author considers to be some of the key new developments of this effort.

- The development of circulation optimization algorithms for multiple stage propulsors and the inclusion of hub and duct effects in these algorithms.
- The development and synthesis of a lifting line code which can treat a wide range of propulsor types in a consistent manner.
- The development of a relatively simple model for the ducted propeller which takes into account both the “end-plate” and “accelerating” effects of ducted propellers.
- The demonstration of a design procedure for ducted propellers in which the blade and duct geometry is determined so as to produce a specified blade circulation distribution and distribution of thrust between duct and propeller.
- The description of the propeller design process using modern methods with and emphasis on the design of nontraditional propulsors.

7.1 Future Considerations

The circulation optimization procedure presented here makes use of a classical variational approach to the constrained optimization problem. This problem can also be attacked by numerical methods for nonlinear programming. The literature on such methods is vast. Many methods allow for the possibility of inequality constraints. These are of particular interest. A constraint, by way of example, on tip vortex cavitation could be formulated in terms of some function of circulation being less than a specified value. The circulation

optimization procedure could then be made to consider cavitation inception as well as efficiency.

The important concept to be carried over from this thesis to a new optimization algorithm is the idea of entering the method with a discretized version of the constrained optimization problem. A discrete formulation of the problem allows for the consideration of propulsor geometries of theoretically unlimited complexity. Propulsors of more than two stages, or more unusual propulsor configurations such as vertical axis propellers or sculling oars could be investigated. The discrete formulation of the problem also makes it a relatively simple matter to change details of the model which is used to represent the propulsor. The importance of this capability can be seen in the use in this thesis of panel method representations for the duct and hub to confirm the results of simpler procedures.

An optimization procedure which incorporates a more complete representation of the propeller and its trailing vortex wake might be of interest. In such a procedure the shape of the chordwise distribution of circulation could be specified with its magnitude varying radially in some unknown manner. The blade geometry would be linearized about some reference geometry much as is done in current lifting surface design procedures. Such an optimization procedure would provide the complete propeller blade geometry and could more accurately model the propeller's wake geometry.

The current lifting surface blade design procedures are somewhat inflexible. This does not appear to be due to any limitation imposed by the underlying theory, but rather to the structure of the computer codes, which—from the perspective of advances in computing capability—were written quite long ago. A more modular, lifting surface, design and analysis code which could handle a wide variety of propulsor types would complement the PLL lifting line procedures.

PLL does not automatically allow for hub diameters which differ between propulsor components. Modifications to the code in order to allow for this possibility would enhance its usefulness.

In the current work unsteady propulsor forces and cavitation were only briefly touched upon. Since they play a crucial role in many design applications this is done with some regret. Unsteady analysis procedures for a single propeller operation in nonuniform inflow have been developed [61] [55]. The use of such procedures for the analysis of the unsteady interaction between components of multiple stage propulsors should be investigated and new procedures developed if necessary.

7.2 Some Final Remarks on Propulsor Design

There are frequently examples of propulsor geometry for which dramatic increases in efficiency are cited. Such claims are usually true, but only in some limited sense. For

example substantial efficiency increases were measured for a propeller/pre-swirl stator combination tested on a USCG 41 foot utility boat [71]. These large gains were relative to the propeller in current service. A significant fraction of these gains was also achieved simply by use of a better propeller. A subsequent investigation showed that under current economic conditions the best option for this boat is a new propeller, but no stator vanes [96].

The general design procedures described in this thesis provide tools for examining such claims. The PLL code is particularly well suited for the realistic evaluation of many propulsor geometries. In the case of the utility boat mentioned above the PLL procedures confirm that only relatively small efficiency gains are possible for a propeller/stator combination over an optimum single propeller [22].

In section 6.2 a number of propulsors designed for several operating conditions were examined. The results presented in table 6.7 show that dramatic gains in efficiency over an optimum single propeller are only possible when the induced losses, and therefore the blade loadings, are large. If the design constraints allow the propeller to be lightly loaded, the potential gains in efficiency for novel propulsor geometries are small.

In chapter 3 it was shown that drag associated with loading at the hub of a single propeller can significantly reduce the overall propulsive efficiency. For this reason the propeller should be unloaded at the hub. Traditional constant pitch propellers often have significant hub loading, as do many propellers designed with computer methods which do not account for the presence of the hub. Hub boss fins have been proposed as a means of increasing propulsive efficiency [34]. These are small radius blades which rotate with the propeller and are placed between the propeller blades. A lifting line analysis of such a configuration showed no efficiency increase. They could be used, however, to unload the hub. Of course, a propeller designed so that the hub was properly unloaded would not benefit from the use of such hub boss fins.

With the exception of hub unloading the procedures presented in this thesis recover traditional results for circulation and blade geometry of single propellers. However, these procedures can also be used for the design and evaluation of less traditional propulsor alternatives such as contrarotating and ducted propellers. They can also be used to design propellers for unusual operating conditions, such the propeller for a human powered submarine described in section 6.1. A design method which is systematic and provides consistent results over a wide range of propulsor types is essential for the evaluation of the use of nontraditional propulsors. The method presented in this thesis is intended to fulfill this role.

Bibliography

- [1] I. H. Abbott and A. E. von Doenhoff. *Theory of Wing Sections*. Dover, New York, 1959.
- [2] A. S. Achkinadze. Generalization of the Betz theorem for the case of arbitrary induced velocities accounting for the profile losses at a given shape of free vortices. In *Proceedings of the 5th National Congress on Theoretical and Applied Mechanics*. Varna. Bulgaria, 1985.
- [3] B. Andrews and D. E. Cummings. Design procedure for large hub propellers. *Journal of Ship Research*. September 1972.
- [4] A. Betz. Schraubenpropeller mit geringstem energieverlust. *Nachrichten der K. Gesellschaft der Wissenschaften zu Gottingen Math-Phys Klas*, 1919.
- [5] A. Betz. *The Theory of Contra-Vanes Applied to the Propeller*. Technical Report TM-909, NACA. 1939. Translation by J. Vanier.
- [6] L. J. Bowling. *Design of a Non-axisymmetric Stator for Improved Propeller Performance*. Master's thesis, Massachusetts Institute of Technology, Department of Ocean Engineering, 1987.
- [7] T. Brockett. *Minimum Pressure Envelopes for Modified NACA-66 Sections with NACA $a=0.8$ Camber and Buships Type I and Type II Sections*. Report 1780, DTNSRDC, Teddington, England, Feb 1966.
- [8] T. Brockett and R. Korpus. Marine propellers for minimum shaft-horsepower. In *Proceedings of the American Towing Tank Conference*, Washington D. C., 1986.
- [9] T. Brockett and R. Korpus. Parametric evaluation of the lifting-line model for conventional and preswirl propulsors. In *Proceedings of the International Symposium on Propellers and Cavitation*. Wuxi. China, 1986.
- [10] T. E. Brockett. Lifting surface hydrodynamics for design of rotating blades. In *Proceedings of the Propellers '81 Symposium*, Virginia Beach, Virginia, 1981.

- [11] L. C. Burrill. The optimum diameter of marine propellers. a new design approach. In *Transactions, NECIES*, 1955.
- [12] A. S. Caja. *On the Optimum Propeller Loading with Inclusion of Duct and Hub*. Master's thesis. Massachusetts Institute of Technology, Department of Ocean Engineering, 1988.
- [13] E. B. Caster. *A Computer Program for Use in Designing Ducted Propellers*. Technical Report 2507, NSRDC, 1967.
- [14] E. B. Caster and T. A. LaFone. *A Computer Program for the Preliminary Design of Contra Rotating Propellers*. Technical Report SPD-596-01, DTNSRDC, 1975.
- [15] T. Cebeci and A. M. O. Smith. *Analysis of Turbulent Boundary Layers*. Academic Press, New York, 1974.
- [16] L. K. Chang and G. L. Stefko. Application of an optimization method to high performance propulsor designs. In *20th Joint Propulsion Conference*, AIAA/SAE/ASME, 1984. AIAA Paper 84-1203.
- [17] L. K. Chang and J. P. Sullivan. Optimization of propeller blade shape by an analytical method. In *18th Joint Propulsion Conference*, AIAA/SAE/ASME, 1982. AIAA Paper 82-1125.
- [18] B. Y.-H. Chen and A. M. Reed. A lifting-surface program of contrarotating propellers. In *Proceedings of the Symposium on Hydrodynamic Performance Enhancement for Marine Applications*. Naval Underwater Systems Center and the University of Rhode Island, Newport, RI, 1988.
- [19] B. Y.-H. Chen, A. M. Reed, and K.-H. Kim. A vane-wheel propulsor for a naval auxiliary. In *Proceedings of the Symposium on Hydrodynamic Performance Enhancement for Marine Applications*, Naval Underwater Systems Center and the University of Rhode Island, Newport, RI, 1988.
- [20] J. P. Comstock, editor. *Principles of Naval Architecture*, pages 401-402. Society of Naval Architects and Marine Engineers, 1967.
- [21] J. P. Comstock, editor. *Principles of Naval Architecture*, pages 374-376. Society of Naval Architects and Marine Engineers, 1967.
- [22] W. B. Coney. *Analysis and Design of Non-Axisymmetric Pre-Swirl Stator/Propeller Systems*. Technical Report 89-2, Massachusetts Institute of Technology, Department of Ocean Engineering, 1989.

- [23] W. B. Coney. *MIT-PLL: Propulsor Lifting Line Code, A Users Manual*. Massachusetts Institute of Technology. Department of Ocean Engineering, 1989.
- [24] B. D. Cox and A. M. Reed. Contrarotating propellers — design theory and application. In *Proceedings. Propellers '88 Symposium*. Virginia Beach, VA, 1988.
- [25] R. A. Cumming, W. B. Morgan, and R. J. Boswell. Highly skewed propellers. In *Transactions, Society of Naval Architects and Marine Engineers*, 1972.
- [26] R. E. Davidson. *Optimization and Performance Calculation of Dual-Rotation Propellers*. Technical Report, NASA, 1981. 1948.
- [27] S. B. Denny, L. T. Puckette, E. D. Hubble, S. K. Smith, and R. F. Najarian. A new usable propeller series. *Marine Technology*, 26(3), July 1989.
- [28] G. Dyne. *A Method for the Design of Ducted Propellers in a Uniform Flow*. Technical Report 62, Swedish State Shipbuilding Tank, Goteberg, Sweden, 1967.
- [29] G. Dyne. Systematic studies of accelerating ducted propellers in axial and inclined flows. In *Transactions of the Symposium on Ducted Propellers*, Royal Institution of Naval Architects. London, England, 1973.
- [30] M. K. Eckhardt and W. B. Morgan. A propeller design method. In *Transactions, Society of Naval Architects and Marine Engineers*, 1955.
- [31] J. A. C. Falcão de Campos. *On the Calculation of Ducted Propeller Performance in Axisymmetric Flows*. Technical Report 696, Netherlands Ship Model Basin, Wageningen, The Netherlands, 1983.
- [32] Jinzhang Feng and Shitang Dong. *A Method for the Prediction of Unsteady Hydrodynamic Performance of the Ducted Propeller With a Finite Number of Blades*. Technical Report 85006, China Ship Scientific Research Center, Wuxi, China, August 1985.
- [33] W. S. Gearheart and R. C. Marboe. Asymmetric reaction fin application. In *Proceedings of the Symposium on Hydrodynamic Performance Enhancement for Marine Applications*, Naval Underwater Systems Center and the University of Rhode Island, Newport, RI, 1988.
- [34] W. S. Gearheart and McBride M. W. Performance assessment of propeller boss cap fin type device. In *Proceedings of the American Towing Tank Conference*, Halifax, Nova Scotia, 1989.

- [35] M. F. George. A model of an axisymmetrical ducted propeller with zero tip clearance. *Journal of Ship Research*, December 1979.
- [36] M. Gertler. *Resistance Experiments on a Systematic Series of Stream-lined Bodies of Revolution. for Application to the Design of High-Speed Submarines*. Technical Report C-297, TMB, 1950.
- [37] H. Glauert. Airplane propellers. In W. Durand, editor, *Aerodynamic Theory*, chapter 3, California Institute of Technology, 1943.
- [38] E. J. Glover. Contrarotating propellers for high speed cargo vessels. In *Transactions*, NECIES, 1967.
- [39] E. J. Glover and P. G. Ryan. A comparison of the theoretical and experimental performance of a ducted propeller system. In *Proceedings of the Symposium on Ducted Propellers*, The Royal Institution of Naval Architects, Teddington, England, May 1973.
- [40] S. Goldstein. On the vortex theory of screw propellers. In *Proceedings of the Royal Society of London*, London, 1929.
- [41] C. A. Goudey, L. A. Cangahuala, and E. H. Mead. Icarus: design and testing of a human-powered submersible. In *Oceans '89*, IEEE, Seattle, Washington, September 1989.
- [42] D. S. Greeley and J. H. Cross-Whiter. Design and hydrodynamic performance of sailboat keels. March 1989. Presented at a meeting of the New England Section of The Society of Naval Architect and Marine Engineers.
- [43] D. S. Greeley and J. E. Kerwin. Numerical methods for propeller design and analysis in steady flow. In *Transactions*, The Society of Naval Architects and Marine Engineers, 1982. Volume 90.
- [44] O. Grim. Propeller and vane wheel. *Journal of Ship Research*, Volume 24, 1980.
- [45] O. Grim. Propeller und leitrads. *Jarbuch der Schiffbautechnischen Gesellschaft*, 1966. Band 60.
- [46] J. L. Hess. *Calculation of Potential flow About Arbitrary Three-Dimensional Lifting Bodies*. Technical Report MDC J5679-01, McDonnell Douglas, October 1972.
- [47] F. B. Hildebrand. *Advanced Calculus for Applications*, pages 357-359. Prentice-Hall, 1976.

- [48] M. G. Honkanen. On the design and use of contra-rotating propellers in high-speed craft. In *Proceedings of the Propellers '78 Symposium*. Virginia Beach, Virginia. 1978.
- [49] G. R. Hough and D. E. Ordway. *The Generalized Actuator Disk*. Technical Report TAR-TR 6401. Therm Advance Research. January 1964.
- [50] C.-Y. Hsin. *Analysis of the Performance of a Non-Axisymmetric Stator by Lifting Surface Theory*. Massachusetts Institute of Technology, Department of Ocean Engineering, 1987.
- [51] C.-Y. Hsin. *Efficient Computational Methods for Multi-Component Lifting Line Calculations*. Master's thesis, Massachusetts Institute of Technology, Department of Ocean Engineering, 1986.
- [52] T. T. Huang and N. C. Groves. Effective wake: theory and experiment. In *13th Symposium on Naval Hydrodynamics*, Tokyo. October 1980.
- [53] R. M. James. On the remarkable accuracy of the vortex lattice method. *Computational Methods for Applied Mechanical Engineering*, Volume 1, 1972.
- [54] S. Kawada. Induced velocity by helical vortices. *Journal of the Aeronautical Sciences*, 1936.
- [55] D. P. Keenan. *Marine Propellers in Unsteady Flow*. PhD thesis, Massachusetts Institute of Technology, Department of Ocean Engineering, June 1989.
- [56] J. E. Kerwin. Hydrofoils and propellers. 1989. Lecture Notes. Massachusetts Institute of Technology, Department of Ocean Engineering.
- [57] J. E. Kerwin. Marine propellers. In *Annual Review of Fluid Mechanics*, pages 367-403, Annual Reviews Inc., 1986.
- [58] J. E. Kerwin. *The Solution of Propeller Lifting Surface Problems by Vortex Lattice Methods*. Technical Report. Massachusetts Institute of Technology, Department of Ocean Engineering, 1961.
- [59] J. E. Kerwin, W. B. Coney, and C.-Y. Hsin. Hydrodynamic aspects of propeller/stator design. In *Proceedings, Propellers '88 Symposium*, Virginia Beach, VA, 1988.
- [60] J. E. Kerwin, W. B. Coney, and C.-Y. Hsin. Optimum circulation distributions for single and multi-component propulsors. In *Proceedings of the American Towing Tank Conference*, Washington, D. C., 1986.

- [61] J. E. Kerwin, S. A. Kinnas, Wilson M. B., and J. McHugh. Experimental and analytical techniques for the study of unsteady propeller sheet cavitation. In *Proceedings of the Sixteenth Symposium on Naval Hydrodynamics*, Berkeley, California, 1986.
- [62] J. E. Kerwin, S. A. Kinnas, J.-T. Lee, and W.-Z. Shih. A surface panel method for the hydrodynamic analysis of ducted propellers. In *Transactions*, Society of Naval Architects and Marine Engineers, 1987.
- [63] J. E. Kerwin and C.-S. Lee. Prediction of steady and unsteady marine propeller performance by numerical lifting-surface theory. In *Transactions*, Society of Naval Architects and Marine Engineers, 1978. Volume 86.
- [64] J. E. Kerwin and R. Leopold. A design theory for subcavitating propellers. In *Transactions*, Society of Naval Architects and Marine Engineers, 1964.
- [65] S. A. Kinnas. A reciprocity relationship for the cosine spaced vortex lattice. 1989. Private communication.
- [66] S. A. Kinnas and W. B. Coney. On the optimum ducted propeller loading. In *Proceedings, Propellers '88 Symposium*, Virginia Beach, VA, 1988.
- [67] L. Kort. Der neue düsenchrauben-antrieb. *Wert-Reederer-Hafen*, Jahrgang 15(Heft 4), 1934.
- [68] N. B. Kroeger. *Optimization of Propulsion Speeds*. Master's thesis, Massachusetts Institute of Technology, Department of Ocean Engineering, June 1972.
- [69] D. Küchemann and J. Weber. *Aerodynamics of Propulsion*. McGraw-Hill, New York, 1953.
- [70] C. E. Lan. A quasi-vortex-lattice method in thin wing theory. *Journal of Aircraft*, September 1974.
- [71] G. Larimer, W. Gearheart, D. Van Liew, and C. Shields. Reaction fin applications in marine propulsion. March 1987. Presented at a meeting of the Hampton Roads Section of The Society of Naval Architect and Marine Engineers.
- [72] H. W. Lerbs. *Contra-Rotating Optimum Propellers Operating in a Radially Non-Uniform Wake*. Technical Report 941, DTMB, 1955.
- [73] H. W. Lerbs. Moderately loaded propellers with a finite number of blades and an arbitrary distribution of circulation. In *Transactions*, Society of Naval Architects and Marine Engineers, 1952.

- [74] D. J. Lesieutre. *The Theoretical Performance of Counter-Rotating Propeller Systems*. Master's thesis, Purdue University, 1985.
- [75] T. A. Loukakis. *A New Theory for the Wake of Marine Propellers*. Technical Report 71-7, Massachusetts Institute of Technology, Department of Ocean Engineering, 1971.
- [76] T. S. Mautnert, D. M. Nelson, and M. C. Gillcrist. Investigation of the SISUP (swirl inducing stator upstream of propeller) concept for marine propulsion. In *Proceedings of the Propellers '88 Symposium*, Virginia Beach, Virginia, 1988.
- [77] B. W. McCormick. The effect of a finite hub on the optimum propeller. *Journal of the Aeronautical Sciences*, 1955.
- [78] K.-S. Min. *Numerical and Experimental Methods for the Prediction of Field Point Velocities Around Propeller Blades*. Technical Report 78-12, Massachusetts Institute of Technology, Department of Ocean Engineering, 1978.
- [79] W. B. Morgan. The design of counterrotating propeller using Lerbs' theory. In *Transactions, Society of Naval Architects and Marine Engineers*, 1960.
- [80] W. B. Morgan. Some results from the inverse problem of the annular airfoil and ducted propeller. *Journal of Ship Research*, March 1969.
- [81] W. B. Morgan. Theory of the annular airfoil and ducted propeller. In *Fourth Symposium on Naval Hydrodynamics*, pages pp 151-197, 1962.
- [82] W. B. Morgan and E. B. Caster. Comparison of theory and experiment on ducted propellers. In *Proceedings of the Seventh Symposium on Naval Hydrodynamics*, Rome, Italy, 1968.
- [83] W. B. Morgan and J. W. Wrench. Some computational aspects of propeller design. In *Methods in Computational Physics*, Academic Press, 1965.
- [84] L. Morino and B. Bharadua. *Two Methods for Viscous and Inviscid Free-Wake Analysis of Helicopter Rotors*. Technical Report CCAD-TR-85-02, Boston University, 1985.
- [85] W. B. Murman and P. M. Stremiel. A vortex wake capturing method for potential flow calculations. In *3rd Joint Conference, AIAA/ASME*, 1982. AIAA Paper 82-0947.
- [86] D. M. Nelson. *Development and Application of a Lifting Surface Design Method for Counterrotating Propellers*. Technical Report TP 326, Naval Undersea Systems Center, 1972.

- [87] J. A. Norton and J. W. Elliot. Current practices and future trends in marine propeller design and manufacturing. *Marine Technology*. April 1988.
- [88] M. W. C. Oosterveld. *Wake Adapted Ducted Propellers*. Technical Report 345, Netherlands Ship Model Basin. 1970.
- [89] M. G. Parsons and J. E. Greenblatt. *Optimization of Propeller Skew Distribution to Minimize the Vibratory Forces and Moments Acting on the Propeller Hub*. Technical Report 206, The University of Michigan, Department of Naval Architecture and Marine Engineering, 1978.
- [90] P. C. Pien. The calculation of marine propeller based on lifting surface theory. *Journal of Ship Research*, 1961.
- [91] L. Prandtl. *Applications of Modern Hydrodynamics to Aeronautics*. Technical Report 116, NACA, 1921.
- [92] L. Prandtl. *Nachrichten der K. Gesellschaft der Wissenschaften zu Gottingen Math-Phys Klas*, 1918.
- [93] D. F. Rogers and J. A. Adams. *Mathematical Elements for Computer Graphics*. McGraw-Hill, 1976.
- [94] P. G. Ryan and E. Glover. A ducted propeller design method: a new approach using surface vorticity distribution techniques and lifting line theory. In *Transactions*, The Royal Institution of Naval Architects, 1972.
- [95] A. H. Sacks and J. A. Burnell. Ducted propellers—a critical review of the state-of-the-art. In *Progress in Aeronautical Sciences*, Pergamon Press, 1962.
- [96] R. D. Sedat, E. S. Purcell, and C. L. Hervey. Full-scale trials of pre-swirl vanes and modified propellers. *Naval Engineers Journal*, May 1989.
- [97] J. A. Sparenberg. On optimum propellers with a duct of finite length. *Journal of Ship Research*, Volume 13(Number 2), 1969.
- [98] J. A. Sparenberg. On optimum propellers with a duct of finite length II. *Journal of Ship Research*, Volume 14(Number 4), 1970.
- [99] J. A. Sparenberg. On the efficiency of a class of nonstationary ship's propulsors. *Journal of Ship Research*, Volume 11(Number 4), 1968.
- [100] J. A. Sparenberg. An upper bound for the efficiency of lightly loaded ship propellers. In *Transactions*, The Royal Institution of Naval Architects, 1968.

- [101] L. Stipa. *Experiments with Intubed Propellers*. Technical Report TM655. NACA, 1932.
- [102] A. J. Tachmindji. The potential problem of the optimum propeller with finite hub. *International Shipbuilding Progress*, November 1956.
- [103] A. J. Tachmindji. Potential problem of the optimum propeller with finite number of blades operating in a cylindrical duct. *Journal of Ship Research*, Volume 2(Number 3), 1958.
- [104] K. Takekuma. Evaluation of various type of nozzle propellers and reaction fin as the device for the improvement of propulsive performance of high block coefficient ships. In *Proceedings of the Shipboard Energy Conservation Symposium*, The Society of Naval Architects and Marine Engineers, New York, September 1980.
- [105] T. Theodorsen. *The Theory of Propellers: I — Determination of the Circulation Function and the Mass Coefficient for Dual Rotating Propellers*. Technical Report 775, NACA, 1944.
- [106] T. Theodorsen. *The Theory of Propellers: IV — Thrust, Energy, and Efficiency Formulas for Single- and Dual-Rotating Propellers with Ideal Circulation Distribution*. Technical Report 778, NACA, 1944.
- [107] S. Tsakonas and W. R. Jacobs. Propeller-duct interactions due to loading and thickness effects. In *Proceedings of the Propellers '78 Symposium*, Virginia Beach, Virginia, 1978.
- [108] L. A. van Gunsteren. Application of momentum theory in counterrotating propeller design. *International Shipbuilding Progress*, 1971.
- [109] R. J. van Houten. *Analysis of Ducted Propellers in Steady Flow*. Technical Report 4.76-1, Airflow Research and Manufacturing Corp., Watertown, MA., February 1986.
- [110] R. J. van Houten and H. B. Wilson. *A Program for Interpolation, Smoothing, Fourier Analysis and Effective Wake Estimation of Propeller Inflow Fields: MIT-WKPROC, User's Manual*. Massachusetts Institute of Technology, Department of Ocean Engineering, 1983. Report 83-8.
- [111] J. D. Van Manen. Effects of radial load distribution on the performance of shrouded propellers. In *Transactions*, The Royal Institution of Naval Architects, 1962.
- [112] J. D. van Manen. *Fundamentals of Ship Resistance and Propulsion; Part B: Propulsion*. Technical Report 132a, Netherlands Ship Model Basin, 1955.

- [113] J. D. van Manen. Recent research on propellers in nozzles. *Journal of Ship Research*, 1957.
- [114] J. D. van Manen and A. R. Bakker. Numerical results of Sparenberg's lifting surface theory for ship screws. In *Proceedings of the Fourth Symposium on Naval Hydrodynamics*, Washington, D. C., 1962.
- [115] J. D. van Manen and M. W. C. Oosterveld. Analysis of ducted-propeller design. In *Transactions*, Society of Naval Architects and Marine Engineers, 1966.
- [116] J. D. van Manen and J. Sentic. Contra-rotating propellers. In *Transactions*. Institution of Naval Architects, 1956.
- [117] Q. R. Wald. The distribution of circulation on propellers with finite hubs. ASME paper 64-WA/UNT-4, November 1964.
- [118] M.-H. Wang. *Hub Effects in Propeller Design and Analysis*. Technical Report 85-12. Massachusetts Institute of Technology, Department of Ocean Engineering, May 1985.
- [119] J. V. Wehausen. Lecture notes on propeller theory. 1964. College of Engineering, University of California, Berkeley.
- [120] J. Weissinger and D. Maas. Theory of the ducted propeller—a review. In *Proceedings of the Seventh Symposium on Naval Hydrodynamics*, Rome, Italy, 1968.
- [121] S. L. Wilhelm. *Propeller Protection in Ice Using Pre-Swirl Stator Vanes*. Master's thesis, Massachusetts Institute of Technology, Department of Ocean Engineering, 1984.
- [122] J. W. Wrench. *The Calculation of Propeller Induction Factors*. Technical Report 1116, DTMB, 1957.
- [123] B. Yim. Optimum propellers with cavity-drag and frictional drag effects. *Journal of Ship Research*, Volume 20, June 1976.

Appendix A

Velocity Calculation Algorithms

A.1 Self-Induced Velocities

Hsin [51] compared several methods for the calculation of the self-induced velocity. He found the Lerbs-Wrench asymptotic formulas to be both the fastest and most accurate of the methods.

If the vortex system is assumed to be purely helical and to extend infinitely far in both the upstream and downstream directions, then the flow is independent of the helical coordinate. Thus, the flow is two-dimensional in terms of r and θ .

The potential problem for this type of flow was posed by Goldstein [40] and solved independently by Kawada [54] and Lerbs[73]. A derivation may be found in Appendix I of Lerbs' paper.

The resulting potential can be expressed in terms of infinite sums of modified Bessel functions. For internal flow ($r_c \leq r_v$):

$$\begin{aligned}\Phi_i &= \frac{\mathcal{Z}}{2}\gamma \\ &+ \frac{\mathcal{Z}}{2\pi}\gamma \left\{ \frac{x}{h} + 2\frac{r_v}{h} \sum_{m=1}^{\infty} \mathbf{I}_{m\mathcal{Z}}\left(\frac{m\mathcal{Z}}{h}r_c\right) \mathbf{K}'_{m\mathcal{Z}}\left(\frac{m\mathcal{Z}}{h}r_v\right) \times \sin(m\mathcal{Z}\vartheta) \right\},\end{aligned}\quad (\text{A.1})$$

and for external flow ($r_c > r_v$):

$$\begin{aligned}\Phi_e &= \frac{\gamma}{2\pi} \left\{ \mathcal{Z}\varphi \right. \\ &\quad \left. - 2\pi \sum_{k=1}^{\mathcal{Z}} \frac{k-1}{\mathcal{Z}} \right. \\ &\quad \left. + 2\mathcal{Z}\frac{r_v}{h} \sum_{m=1}^{\infty} \mathbf{K}_{m\mathcal{Z}}\left(\frac{m\mathcal{Z}}{h}r_c\right) \mathbf{I}'_{m\mathcal{Z}}\left(\frac{m\mathcal{Z}}{h}r_v\right) \times \sin(m\mathcal{Z}\vartheta) \right\},\end{aligned}\quad (\text{A.2})$$

where $h = r_v \tan \beta$, and $\vartheta = \varphi - x/h$ and \mathbf{I} is the modified Bessel function of the first kind, \mathbf{K} is the modified Bessel function of the second kind. Here γ is the strength of the trailing vorticity, r_v is the radius of the vortex and r_c is the radius of the control point.

For axial and tangential components of induced velocities, the effect of the vortex system between $x = -\infty$ and $x = 0$, the plane of the lifting line, is equal to the effect of the vortex system between $x = 0$ and $x = \infty$, therefore:

$$u_a = \frac{1}{2} \frac{\partial \Phi}{\partial x} \quad u_t = \frac{1}{2r} \frac{\partial \Phi}{\partial \varphi} \quad (\text{A.3})$$

Thus, the axial and tangential velocities induced by \mathcal{Z} helical vortex lines of unit strength can be expressed as follows:

for $r_c \leq r_v$;

$$\bar{u}_a = \frac{\mathcal{Z}}{4\pi\lambda} (1 - 2\mathcal{Z} \frac{r_v}{\lambda} F_1), \quad \bar{u}_t = \frac{\mathcal{Z}^2}{2\pi r_c} \frac{r_v}{\lambda} F_1; \quad (\text{A.4})$$

for $r_c > r_v$;

$$\bar{u}_a = -\frac{\mathcal{Z}^2}{2\pi} \frac{r_v}{\lambda^2} F_2, \quad \bar{u}_t = \frac{\mathcal{Z}}{4\pi r_c} (1 + 2\mathcal{Z} \frac{r_v}{\lambda} F_2); \quad (\text{A.5})$$

where

$$\begin{aligned} F_1 &= \sum_{n=1}^{\infty} n \mathbf{I}_{n\mathcal{Z}} \left(\frac{n\mathcal{Z}}{\lambda} r_c \right) \mathbf{K}'_{n\mathcal{Z}} \left(\frac{n\mathcal{Z}}{\lambda} r_v \right); \\ F_2 &= \sum_{n=1}^{\infty} n \mathbf{K}_{n\mathcal{Z}} \left(\frac{n\mathcal{Z}}{\lambda} r_c \right) \mathbf{I}'_{n\mathcal{Z}} \left(\frac{n\mathcal{Z}}{\lambda} r_v \right). \end{aligned} \quad (\text{A.6})$$

Note that these are the influence functions for a single helical element of trailing vorticity. These influence functions can be combined to form velocities induced by the complete vortex horseshoe, since the bound vorticity induces no velocities on the lifting lines.

$$\bar{u}_a^*(m, p) = \bar{u}_a(m, p) - \bar{u}_a(m, p+1), \quad (\text{A.7})$$

$$\bar{u}_t^*(m, p) = \bar{u}_t(m, p) - \bar{u}_t(m, p+1). \quad (\text{A.8})$$

The numerical results obtained by Lerbs [73] and Wrench [122] [83] were derived through the use of asymptotic formulas for the modified Bessel functions of the first and second kind \mathbf{I} and \mathbf{K} . Wrench's approach gives better accuracy and has been used in the subroutine LERBS of the propeller lifting line programs LLL2 and PLL:

$$\begin{aligned} F_1 \approx & -\frac{1}{2\mathcal{Z}y_0} \left(\frac{1+y_0^2}{1+y^2} \right)^{0.25} \left\{ \frac{1}{U^{-1}-1} \right. \\ & \left. + \frac{1}{24\mathcal{Z}} \left[\frac{9y_0^2+2}{(1+y_0^2)^{1.5}} + \frac{3y^2-2}{(1+y^2)^{1.5}} \right] \ln \left(1 + \frac{1}{U^{-1}-1} \right) \right\}, \end{aligned}$$

$$F_2 \approx -\frac{1}{2Zy_0} \left(\frac{1+y_0^2}{1+y^2} \right)^{0.25} \left\{ \frac{1}{U-1} - \frac{1}{24Z} \left[\frac{9y_0^2+2}{(1+y_0^2)^{1.5}} + \frac{3y^2-2}{(1+y^2)^{1.5}} \right] \ln \left(1 + \frac{1}{U-1} \right) \right\}, \quad (\text{A.9})$$

where

$$U = \left\{ \frac{y_0(\sqrt{1+y^2}-1)}{y(\sqrt{1+y_0^2}-1)} \exp(\sqrt{1+y^2}-\sqrt{1+y_0^2}) \right\}^Z, \quad (\text{A.10})$$

and

$$y = \frac{r_c}{r_v \tan \beta}, \quad y_0 = \frac{1}{\tan \beta} \quad (\text{A.11})$$

Hsin also showed that the calculation of propeller induction factors with this procedure should be performed with double precision numerics.

A.2 Circumferential Mean Velocities

The time-averaged velocities induced by one propulsor component on the other are equal to the circumferential mean velocities calculated in the rotating reference frame of that component.

A horseshoe vortex of strength Γ with lattice points at radii $r_{v_i}(p-1)$ and $r_{v_i}(p)$ will, by Kelvin's theorem, induce a tangential circumferential mean velocity on a control point, at radius $r_{c_j}(m)$ of the other component, of:

$$\bar{u}_{i,j}^*(m,n) = \begin{cases} 0, & S > 0, \quad -\infty \leq x_f \leq \infty \\ 0, & S \leq 0, \quad x_f < 0; \\ \frac{-Z\Gamma}{2\pi r_{c_j}(m)}, & S < 0, \quad x_f > 0; \end{cases} \quad (\text{A.12})$$

where

$$S = (r_{v_j}(p-1) - r_{c_j}(m))(r_{v_j}(p) - r_{c_j}(m)). \quad (\text{A.13})$$

That is, the tangential velocity vanishes everywhere outside of the slipstream of the horseshoe vortex, and is proportional to $\Gamma(p)/r_{c_j}(m)$ inside the slipstream. The tangential circumferential mean velocity induced by both the bound and trailing vorticity can be found from equations A.12 and A.13.

Since the circumferential mean velocities induced on the other component by the bound vortices are only tangential, the problem now is to solve for the circumferential mean axial and radial velocities induced by the trailing vortices. By comparing a variety of computation methods with respect to accuracy and computation time, Hsin [51] concluded that Hough and Ordway's formulas should be used for this application.

Through Fourier analysis of the velocity field, Hough and Ordway [49] derived formulas for the induced velocities of an actuator disk in terms of elliptical integrals. These can be thought of as the velocities induced by a propeller with an infinite number of blades. Since the circumferential mean velocities are the average of the sum of local induced velocities along a circle (with an infinite number of points), we can apply the following formulas to calculate the circumferential mean velocities.

$$\bar{u}_{a,j,l}(m,p) = \frac{Z_l}{\pi r_{v_l}(p) \tan(\beta_l(p))} C_1, \quad (\text{A.14})$$

$$\bar{u}_{t,j,l}(m,p) = \frac{Z_l}{\pi r_{c_j}(m)} C_2 \quad (\text{A.15})$$

$$\bar{u}_{r,j,l}(m,p) = \frac{Z_l}{\pi \sqrt{r_{c_j}(m) r_{v_l}(p)} \tan(\beta_l(p))} Q_{\frac{1}{2}}. \quad (\text{A.16})$$

Here

$$C_1 = \begin{cases} \pi + \frac{x_f}{2\sqrt{r_{c_j}(m)r_{v_l}(p)}} Q_{-\frac{1}{2}}(q) + \frac{\pi}{2} \Lambda_0(s,t), & r_{c_j}(m) \leq r_{v_l}(p) \\ \frac{x_f}{2\sqrt{r_{c_j}(m)r_{v_l}(p)}} Q_{-\frac{1}{2}}(q) - \frac{\pi}{2} \Lambda_0(s,t), & r_{c_j}(m) > r_{v_l}(p) \end{cases} \quad (\text{A.17})$$

where

$$\begin{aligned} q &= 1 + \frac{x_f^2 + (r_{c_j}(m) - r_{v_l}(p))^2}{2r_{c_j}(m)r_{v_l}(p)}, \\ s &= \sin^{-1} \left[\frac{x_f}{\sqrt{x_f^2 + (r_{c_j}(m) - r_{v_l}(p))^2}} \right], \\ t &= \sqrt{\frac{4r_{c_j}(m)r_{v_l}(p)}{x_f^2 + (r_{c_j}(m) + r_{v_l}(p))^2}}, \end{aligned} \quad (\text{A.18})$$

and

$Q_{-\frac{1}{2}}$ is the Legendre function of the second kind and half integer order.

Λ_0 is the Heumann's Lambda function.

C_2 is the same as C_1 except the r_c , r_v inequalities are reversed.

The tangential velocity due to a vortex horseshoe is obtained directly from equation A.12. The axial and radial velocities are found by combining the results of equations A.14 and A.16, since there is no contribution from the bound vorticity to these

velocities.

$$\bar{u}_{a,j,l}^*(m,p) = \bar{u}_{a,j,l}(m,p) - \bar{u}_{a,j,l}(m,p+1). \quad (\text{A.19})$$

$$\bar{u}_{r,j,l}^*(m,p) = \bar{u}_{r,j,l}(m,p) - \bar{u}_{r,j,l}(m,p+1). \quad (\text{A.20})$$

A.3 Asymmetric Stator Velocities

For asymmetric stators, the trailing vortices are assumed to be straight lines, and the wake geometry is assumed to be fixed.

If we have the coordinate, $(0, -r_{v_j}(m) \sin \delta, r_{v_j}(m) \cos \delta)$ of a lattice point m , which sheds a trailing vortex of unit strength, from a stator denoted component j , and the coordinate, $(x_f, -r_c \sin \theta, r_c \cos \theta)$, of a field point which the velocity is induced upon, then the x , y and z components of the induced velocity can be obtained by a direct application of the law of Biot and Savart.

$$\begin{aligned} u_x &= 0 \\ u_y &= \frac{1}{4\pi} \int_0^\infty \frac{(-r_c \cos \theta + r_{v_j}(m) \cos \delta)}{S^3} dx \\ u_z &= \frac{1}{4\pi} \int_0^\infty \frac{(-r_c \sin \theta + r_{v_j}(m) \sin \delta)}{S^3} dx \end{aligned} \quad (\text{A.21})$$

where δ, θ are positive for counterclockwise, and:

$$S = \sqrt{(x - x_f)^2 + (-r_{v_j}(m) \sin \delta + r_c \sin \theta)^2 + (r_{v_j}(m) \cos \delta - r_c \cos \theta)^2} \quad (\text{A.22})$$

The axial, tangential and radial components of the induced velocity $\bar{u}_a^{(t)}$, $\bar{u}_t^{(t)}$, $\bar{u}_r^{(t)}$ due to the trailing vorticity are therefore:

$$\begin{aligned} \bar{u}_a^{(t)} &= u_x = 0, \\ \bar{u}_t^{(t)} &= -u_y \cos \theta - u_z \sin \theta = \frac{1}{4\pi} \int_0^\infty \frac{r_c - r_{v_j}(m) \cos(\theta - \delta)}{S^3} dx, \\ \bar{u}_r^{(t)} &= -u_y \sin \theta + u_z \cos \theta = -\frac{1}{4\pi} \int_0^\infty \frac{r_{v_j}(m) \sin(\theta - \delta)}{S^3} dx. \end{aligned} \quad (\text{A.23})$$

These velocities can be integrated analytically:

$$\begin{aligned} \bar{u}_a^{(t)} &= 0 \\ \bar{u}_t^{(t)} &= \frac{1}{4\pi} \frac{r_c - r_{v_j}(m) \cos(\theta - \delta)}{G - x_f \sqrt{G}} \\ \bar{u}_r^{(t)} &= -\frac{1}{4\pi} \frac{r_{v_j}(m) \sin(\theta - \delta)}{G - x_f \sqrt{G}}, \end{aligned} \quad (\text{A.24})$$

where $G = x_f^2 + r_{v_j}(m)^2 + r_c^2 - 2r_c r_{v_j}(m) \cos(\theta - \delta)$.

Similarly, the velocities induced by the bound vorticity can be obtained. If the m^{th} element of component j is surrounded by lattice points with radii $r_{v_j}(m)$, $r_{v_j}(m+1)$, then this element is just one bound vortex segment in the presented lifting line model. Let this bound vortex have unit strength, then the axial, tangential and radial components of velocity induced by this bound vortex are:

$$\begin{aligned}\bar{u}_a^{(b)} &= \frac{1}{4\pi} r_c \sin(\theta - \delta) H \\ \bar{u}_t^{(b)} &= -\frac{1}{4\pi} x_f \cos(\theta - \delta) H \\ \bar{u}_r^{(b)} &= -\frac{1}{4\pi} x_f \sin(\theta - \delta) H,\end{aligned}\tag{A.25}$$

where

$$\begin{aligned}H &= \int_{r_{v_j}(m)}^{r_{v_j}(m+1)} \frac{1}{[x_f^2 + r_c^2 \sin^2(\theta - \delta) + (r_c \cos(\theta - \delta) - z)^2]^{1.5}} dz \\ &= \frac{1}{r_c^2 \sin^2(\theta - \delta) + x_f^2} \left[\frac{r_{v_j}(m+1) - r_c \cos(\theta - \delta)}{\sqrt{r_{v_j}(m+1)^2 - 2r_c r_{v_j}(m+1) \cos(\theta - \delta) + r_c^2 + x_f^2}} \right. \\ &\quad \left. - \frac{r_{v_j}(m) - r_c \cos(\theta - \delta)}{\sqrt{r_{v_j}(m)^2 - 2r_c r_{v_j}(m) \cos(\theta - \delta) + r_c^2 + x_f^2}} \right]\end{aligned}\tag{A.26}$$

A.4 Vortex Ring Velocities

Formulas in terms of elliptic integrals are given by Kücheman and Weber [69] for the velocities induced by a ring vortex. These formulas are implemented in the PLL code.

A vortex filament which forms a circle of radius r_v is called a vortex ring. We use the coordinate systems (x, r, θ) and (x, y, z) , with x in the direction of the axis of the ring. The ring is here assumed to be located at $x = 0$. The Biot-Savart law in vector notation is

$$d\mathbf{V} = \frac{\Gamma}{4\pi} \frac{\mathbf{R} \times d\mathbf{s}}{R^3}\tag{A.27}$$

giving the velocity vector $d\mathbf{V}$ induced by an element of length $ds = r_v d\theta_v$ of the vortex ring at the point (x, r, θ) or (x, y, z) . ds/ds is the unit vector tangential to the vortex ring at the position of the vortex element. With the unit vectors $\mathbf{i}, \mathbf{j}, \mathbf{k}$ in the directions of the x, y, z axes, ds/ds can be written as

$$\frac{ds}{ds} = 0\mathbf{i} + \cos \theta_v \mathbf{j} - \sin \theta_v \mathbf{k}.\tag{A.28}$$

\mathbf{R} is the radius vector from the vortex element to the control point:

$$\mathbf{R} = x_c \mathbf{i} + (r_c \sin \theta_c - r_v \sin \theta_v) \mathbf{j} + (r_c \cos \theta_c - r_v \cos \theta_v) \mathbf{k} \quad (\text{A.29})$$

with

$$R = \sqrt{x_c^2 + r_c^2 + r_v^2 - 2r_c r_v \cos(\theta_c - \theta_v)}. \quad (\text{A.30})$$

Hence,

$$\begin{aligned} \mathbf{R} \times \frac{d\mathbf{s}}{ds} &= -[\cos \theta_v (r_c \cos \theta_c - r_v \cos \theta_v) + \sin \theta_v (r_c \sin \theta_c - r_v \sin \theta_v)] \mathbf{i} \\ &\quad + x_c \sin \theta_v \mathbf{j} + x_c \cos \theta_v \mathbf{k} \\ &= -[r_c \cos(\theta_c - \theta_v) - r_v] \mathbf{i} + x_c \sin \theta_v \mathbf{j} + x_c \cos \theta_v \mathbf{k}. \end{aligned} \quad (\text{A.31})$$

The x component of the velocity induced by the whole vortex ring is obtained from an integration round the circumference:

$$\bar{u}_a(x, r) = -\frac{\Gamma}{4\pi r_v} \int_0^{2\pi} \frac{r \cos(\theta_c - \theta_v) - 1}{\sqrt{x^2 + r^2 + 1 - 2r \cos(\theta_c - \theta_v)}} d\theta_v \quad (\text{A.32})$$

(x_c/r_v and r_c/r_v have been replaced by x and r for simplicity). The integral can be expressed conveniently by writing

$$\bar{u}_a(x, r) = -\frac{\Gamma}{4\pi r_v} \frac{1}{\sqrt{x^2 + (r+1)^2[x^2 + (r-1)^2]}} I_1 \quad (\text{A.33})$$

where

$$I_1 = 2r4(\mathbf{K} - \mathbf{D}) - r(r+1)\mathbf{E}. \quad (\text{A.34})$$

\mathbf{K} , \mathbf{E} and \mathbf{D} are complete elliptic integrals as functions of k .

$$\begin{aligned} \mathbf{K}(k) &= \int_0^{\pi/2} \frac{1}{\sqrt{1 - k^2 \sin^2 \alpha}} d\alpha \\ \mathbf{E}(k) &= \int_0^{\pi/2} \sqrt{1 - k^2 \sin^2 \alpha} d\alpha \\ \mathbf{D} &= \int_0^{\pi/2} \frac{\sin^2 \alpha}{\sqrt{1 - k^2 \sin^2 \alpha}} d\alpha = \frac{\mathbf{K} - \mathbf{E}}{k^2} \end{aligned} \quad (\text{A.35})$$

with

$$k^2 = \frac{4r}{z^2 + (r+1)^2}. \quad (\text{A.36})$$

The radial velocity component can be found in a similar manner from equations A.27 and A.31:

$$\bar{u}_a = \frac{\Gamma}{2\pi r'} \frac{2x(2\mathbf{K} - 2\mathbf{D} - \mathbf{E})}{\sqrt{x^2 + (r+1)^2[x^2 + (r-1)^2]}}. \quad (\text{A.37})$$

Appendix B

On the Tip Loaded Optimum

The discussion presented here is due to Kerwin and is essentially the same as that given in [60].

The classical solution for the optimum radial circulation distribution follows from the original work of Betz [4], who treated the case of uniform inflow, and Lerbs [73], who considered the influence of radial variations of the circumferential mean wake. More formal treatments of the problem were given subsequently by Wehausen [119] and Yim [123], who confirmed the earlier results. The solution can be stated very simply by the kinematic relationship,

$$\frac{\tan \beta_i(r)}{\tan \beta(r)} = \frac{H}{\sqrt{V_a(r)/V_s}}, \quad (\text{B.1})$$

where the constant H sets the desired level of thrust or torque.

This result is correct in the limit of vanishing loading, where the propeller induced velocities are small compared to the relative onset flow, and where the path of the trailing vortex sheets can be assumed to follow the streamlines of the undisturbed flow. However, this result is generally applied within the framework of the theory of the "moderately loaded propeller", in which the pitch of the trailing vortex wake is adjusted to match the induced flow at the lifting line.

Clearly one can satisfy equation B.1 in this case, but will the result be optimum? Loukakis [75] found efficiencies higher than that given by equation B.1 by applying a systematic search procedure to the determination of the eleven term sine series approximation to the circulation. The resulting circulation distributions found by Loukakis were characterized by a high concentration of loading at the tip.

Being somewhat puzzled by Loukakis' findings, one of the present authors (Kerwin) recomputed the efficiencies of the tip loaded circulation distributions with the same lifting line code, modified to keep the trailing vortex wake at the pitch of the undisturbed flow, and found that the results were always lower than for the circulation distribution obtained

	η	C_T
10 panel solution	0.80636	0.68467
20 panel solution	0.80681	0.68636
40 panel solution	0.80697	0.68679
80 panel solution	0.80704	0.68690
160 panel solution	0.80706	0.68693
Ind. Fact: B-K Opt.	0.81011	0.68693
Ind. Fact: Lerbs Opt.	0.79368	0.68693

Table B.1: Convergence test

by applying equation B.1. The anomaly was therefore a direct consequence of the radial variation in trailing vortex pitch introduced by moderately loaded theory. This, of course, did not answer the question of whether Loukakis' findings were physically correct or not, and it is perhaps sufficient to say that this issue is still controversial.

This question has come up again for two reasons. First of all, we were concerned with the question of how to optimize multiple component propulsors, where it would seem desirable to use moderately loaded lifting line theory. But in addition, Brockett and Korpus [9] [8] have recently presented lifting line results which again show that increased loading at the tip increases efficiency. They show results for a five term sine series representation of the distribution of circulation which produces an efficiency which is higher than that obtained by applying equation B.1.

It seemed that one possible explanation for both Loukakis' and Brockett and Korpus' results was associated with the Lerbs lifting line procedure which both employed (although in somewhat different forms). The efficiency resulting from the five term circulation distribution found by Brockett and Korpus was therefore computed using the present vortex lattice method with increasing numbers of panels. Calculations were also made using Lerb's induction factor method for the same set of circulation coefficients and for the Lerbs optimum distribution obtained from equation B.1. To make the comparison as pure as possible, no viscous drag was included in this exercise. For both runs with the Lerbs induction factor program, the thrust coefficient was set equal to the value obtained with the present vortex lattice program using 160 panels. The results shown in table B.1 confirm the results obtained by Brockett and Korpus, and lay to rest any doubts about the role of numerics in this issue. The efficiency obtained from the vortex lattice procedure has converged to five significant digits (a challenge for the experimenter) and differs from the Lerbs result by four tenths of a percent.

Another question is whether the variational approach somehow produces a local op-

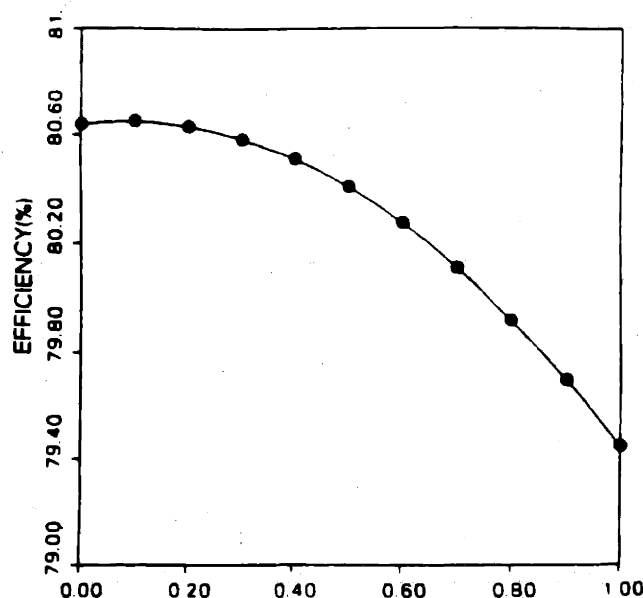


Figure B.1: Efficiency as a function of circulation distribution derived from a linear combination of the present results and those of Brockett and Korpus. (0.0 = Brockett and Korpus, 1.0 = all present theory) The wake is aligned using moderately loaded theory.

timum. To check this, an optimum circulation distribution for Brockett and Korpus' example was first computed using the vortex lattice optimization procedure of chapter 2. For present purposes, it is sufficient to say that it is essentially equivalent to results obtained from equation B.1. The resulting efficiency is 0.794, which agrees to three significant digits with that obtained from the Lerbs induction factor code. A set of calculations were then made with circulation distributions consisting of linear combinations of the two differently obtained optima. The result is shown in figure B.1, which shows that no local optimum exists, and that the Brockett and Korpus distribution yields the highest efficiency obtainable with such a linear combination. The same exercise was repeated with the pitch of the trailing vortex wake forced to remain at the undisturbed flow angle, and these results are shown in figure B.2. Now the conclusion is opposite, with the circulation distribution derived from the present vortex lattice procedure being optimum. This confirms the earlier finding that the circulation from equation B.1 obtained from Lerbs procedure produced higher efficiencies than those obtained by Loukakis when the trailing vortex wake was fixed.

The results given by Brockett and Korpus are therefore confirmed as the true five term optimum circulation distribution in accordance with moderately loaded lifting line theory. But what is the optimum if the circulation is allowed to be an arbitrary function of radius? This can be approached either by progressively increasing the number of terms in the sine

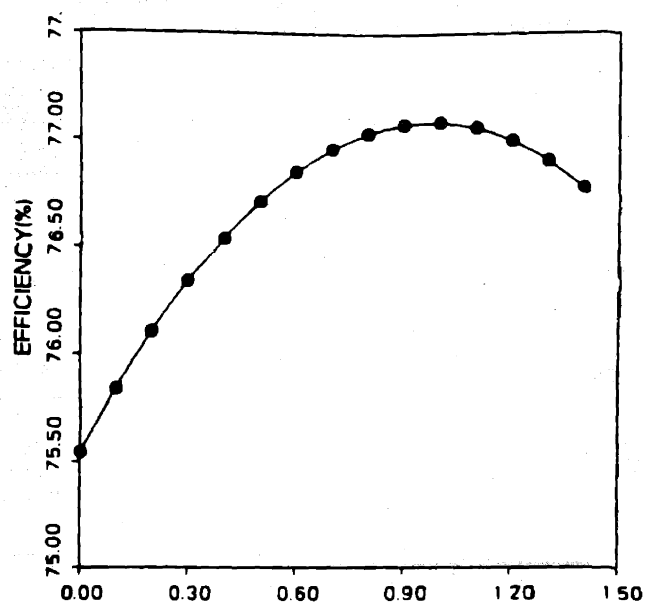


Figure B.2: Efficiency as a function of the circulation distribution as in the previous figure, except that the wake is here constrained to follow the undisturbed inflow.

series, or in the case of the vortex lattice method, by increasing the number of panels. To implement the latter, a crude systematic search technique was incorporated in the vortex lattice program, whereby the circulation of one panel was incremented by a small amount and the entire circulation scaled to yield constant thrust. If the efficiency increased, the circulation increment was kept, otherwise it was discarded. The procedure was repeated, systematically moving back and forth along the radius, running overnight on a personal computer. The authors should emphasize that this unsophisticated optimizer (which only involved a dozen extra lines of code) was only intended to be run once.

The results were spectacular. By morning, the ideal efficiency was up to about 97%, and the induced velocity at the tip was almost three times the speed of advance! In addition to demonstrating that there is no limit to the absurdity of the optimum circulation distribution for a moderately loaded lifting line, the exercise showed clearly how the model defeats itself. A sharp increase in loading at the tip increases the pitch of the tip vortex (in this case the wake pitch increased from 35 degrees to 69 degrees in the last two percent of the radius) which then decreases the induced velocity everywhere inside the tip. The tip panel has high induced drag, but all the panels inside have essentially zero drag, or possibly even propulsion.

There is clearly something wrong with this physically, and the answer can be found, at least qualitatively, in the way a "real" vortex sheet deforms behind a wing or propeller blade tip. Perhaps it is easiest to consider the simple case of an elliptically loaded wing, where lifting line theory predicts constant downwash over the span. The equivalent of

moderately loaded propeller theory would place the trailing vortex sheet on a plane inclined at a constant angle equal to the induced angle at the lifting line. Both observations and computations by a variety of "vortex chasing" methods show, on the contrary, that the middle of the vortex sheet moves down at a rate faster than that given by the flow angle at the lifting line, and that the tip region moves up relative to this same reference plane. The upward movement of the tip vortices is a result of the rolling up and diffusion of the viscous region in the interior of the vortex sheets. Moreover, as the wing loading is increased, the rolling up process, and hence the upward movement of the tip vortices, takes place more rapidly.

Laser-doppler anemometer measurements in the MIT water tunnel by Min [78] and subsequent experimenters have shown the same behavior for marine propellers. Similar numerical results have been presented recently by Keenan [55] and by numerous investigators in the area of helicopter wake trajectories, for example Murman and Stremel [85] and Morino and Bharadua [84].

A relatively simple propeller wake alignment scheme was devised by Greeley and Kerwin [43] and found to agree well with existing water tunnel observations. This procedure was therefore used to determine the initial wake geometry for the Brockett and Korpus example, both for the classical optimum and for their five term, tip loaded, circulation distribution. This was done by running the MIT-PBD-10 lifting surface design program, which incorporates this wake model, for both circulation distributions. The axial induced velocity at the tip obtained from the wake alignment procedure was $0.185V_S$ compared with a value of $0.562V_S$ obtained from moderately loaded theory. Clearly the high axial induced velocities at the tip predicted from moderately loaded lifting line theory do not materialize with this wake model. Furthermore, the efficiency of the tip loaded propeller according to the lifting surface calculations, was slightly less than for the classical optimum load distribution.

This is not considered to be conclusive evidence that the classical optimum cannot be improved upon, since the wake alignment scheme is not necessarily accurate for such an extreme load distribution. In fact, we were pleasantly surprised that it converged at all. Nevertheless, the trend is expected.

To conclude this discussion, it is our opinion that the trailing vortex wake geometry associated with moderately loaded lifting line theory can only be regarded as correct in a gross sense, and cannot be relied upon as regards to the change in radial distribution of pitch of the trailing vortex sheets brought about by a change in radial load distribution. The tip loaded optimum solution succeeds only as a result of a predicted local increase in pitch of the trailing vortex sheet at the tip, which probably cannot be achieved in a real fluid. Therefore, until such time as an accurate, complete, viscous solution of the vortex wake region becomes practical, the optimization problem should best be solved within the framework of linear theory.

It should be emphasized that the question of whether or not high tip loading can

increase efficiency should not be confused with the evaluation of the merits of adding physical boundaries such as ducts, bands or tip fins. In these cases linear theory will show that increased loading at the tip will be optimum.

Appendix C

The Effective Wake Calculation

The effective wake procedure described here is a modified version of that developed by Van Houten and used in WKPROC [110], which in turn is based on a method developed by Huang and Groves [52].

The two governing equations of the flow into the propeller given below follow from assuming that the flux in a streamtube is constant.

$$u_x r dr = u_p r_p dr_p \quad (C.1)$$

and

$$u_p (du_p - du_a) = u_x du_x, \quad (C.2)$$

where u_x is the mean nominal axial velocity, u_p is the mean axial velocity into the propeller plane, r is the flow radius in the nominal wake and r_p is the flow radius as it enters the propeller plane.

Integration of the first governing equation over a stream tube annulus gives the finite difference form of the equation. This provides a numerical method of solving for the contracted flow radii in the propeller plane.

$$r_{p_{i+1}} = \frac{-c + \sqrt{c^2 - 4BD}}{2B} \quad (C.3)$$

where i is the index of the radius and

$$\begin{aligned} B &= 2u_{p_{i+1}} + u_{p_i} \\ C &= -r_{p_i}(u_{p_{i+1}} - u_{p_i}) \\ D &= -r_{p_i}^2(u_{p_{i+1}} + 2u_{p_i}) - F \\ F &= (r_{i+1}^2 - r_i^2)(2u_{x_{i+1}} + u_{x_i}) \\ &\quad - r_i(u_{x_{i+1}} - u_{x_i})(r_{i+1} - r_i). \end{aligned}$$

The definition of the effective wake, u_e , is used to modify the second governing equation given by equation C.4 below:

$$u_e \equiv u_p - u_a$$

$$u_x dx = (u_e + u_a) du_e \quad (C.4)$$

The finite difference form of equation C.4 is used to solve for the effective velocity.

$$u_{e_i} = \frac{\sqrt{(u_{e_{i+1}} + \frac{u_{a_{i+1}} + u_{a_i}}{2})^2 + (u_{x_i}^2 - u_{x_{i+1}}^2)} - \frac{u_{a_{i+1}} + u_{a_i}}{2}}{1} \quad (C.5)$$

The axial induced velocity, $u_a(r)$, is obtained by using actuator disk theory to calculate the integrated induced velocity.

$$Q_a = 2\pi \int_{r_H}^1 u_a(r) r dr. \quad (C.6)$$

For a propeller in uniform flow of velocity V , actuator disk theory gives:

$$Q_a = \pi V \frac{\sqrt{C_T + 1} - 1}{2}, \quad (C.7)$$

where $C_T = 2T/(\rho V^2 \pi)$ and T = the propeller thrust. For a propeller in a shear flow the present program assumes that this equation still holds. If V is taken to be the volumetric mean effective wake velocity:

$$Q_a = 2\pi \int_{r_H}^1 u_e(r) r dr \frac{\sqrt{C_T + 1} - 1}{2}. \quad (C.8)$$

The distribution of induced velocity is arbitrarily taken to be the following:

$$\frac{u_a(r)}{u_{a_{\max}}} = 1 - \left(2 \left(\frac{r - r_H}{1 - r_H} \right) - 1 \right)^4 \quad (C.9)$$

where $u_{a_{\max}}$ is obtained by integrating $u_a(r)$ over the propeller disk and applying equation C.8.

Initially assuming that $u_e(r) = u_x(r)$ in equation C.8, the effective velocity is now determined using equation C.5. This is done by starting at a radius where the effective velocity is known. Beyond the propeller tip, the induced velocities are assumed to be zero. If the propeller is not in a tunnel, the nominal and effective velocities will be identical here. Successive applications of equation C.5 inward gives the effective velocity on each successive streamline.

The contracted position of the streamlines is then solved for using equation C.3. Again the application begins at a known final radius position, namely the hub radius, whose streamline remains unchanged. Successive applications of equation C.3 outward gives the flow contraction.

Since the induced velocity field is a function of radius, the contracted streamlines will encounter a different value of u_a than did the uncontracted streamlines. The process is therefore iterated with the revised values of u_a . At this time the induced velocities are also modified by using an updated effective wake $u_e(r)$ in equation C.8. The entire iteration process is repeated until convergence.

In the case of a propeller in a tunnel, the effective velocity outside the propeller tip need not be the same as the nominal velocity, due to tunnel blockage. The starting point for the application of equation C.5 is taken to be the tunnel wall, at which point the effective velocity is assumed to be equal to the nominal velocity, as a first approximation only. After finding the streamline velocities from equation C.5 and the streamline radii from equation C.3, the radius of the outermost streamline is compared to the tunnel radius. Since physically these radii must be equal, the assumed value of the effective wake velocity at the tunnel wall is adjusted iteratively by Newton's method until agreement is reached. At that point $u_a(r)$ is modified as in the case of a propeller in an unbounded flow, and the entire process is repeated.

Thus far, only the mean effective wake has been determined under the assumption of axisymmetric flow. The more common V-wake has higher harmonics to be modified. Experiments have confirmed that the contraction and acceleration of the V-wake can be predicted from the mean wake results. The derivation of the method used for higher harmonics is based on the following two assumptions.

- The circumferential gradient in the wake is due to radial vortex lines convecting downstream with the mean velocity field.
- The radial vortex lines change only in length and move inward as the flow contracts. their circumferential positions remain steady.

The vorticity equation states that as the vortex lines contract, the vorticity reduces proportionately. The nominal and effective vorticities are related below:

$$\frac{\omega_{r_{\text{eff}}}}{\omega_{r_{\text{nom}}}} = \frac{\frac{1}{r_p} \frac{\partial u_e}{\partial \theta}}{\frac{1}{r} \frac{\partial u_x}{\partial \theta}} = \frac{\Delta r_p}{\Delta r} \quad (\text{C.10})$$

where $\omega_{r_{\text{eff}}}$ and $\omega_{r_{\text{nom}}}$ are the radial vorticity components of the effective and nominal wakes, u_e is the axial effective velocity, u_x is the axial nominal velocity, and Δr , Δr_p are the lengths of vortex filaments in the nominal and effective wakes.

The ratio of vortex filament lengths in equation C.10 can be expressed in differential form by replacing Δr with dr . Equation C.1 can then be used to provide an alternate

form of the ratio. by substituting Fourier series terms for the velocities, the Fourier coefficients are related as shown below:

$$\frac{A_{n_{\text{eff}}}(r)}{A_{n_{\text{nom}}}(r)} = \frac{u_x(r)}{u_e(r) + u_a(r)}, \quad \text{for } n \geq 1 \quad (\text{C.11})$$

where $A_{n_{\text{eff}}}(r)$ and $A_{n_{\text{nom}}}(r)$ are the n th degree Fourier coefficients for a given radius r in the effective and nominal wakes. Sine and cosine coefficients are treated identically.

Appendix D

Reciprocity for Cosine Spacing

The goal here is to show that the reciprocity relationship,

$$w_{i,n}\Delta y(i) = w_{n,i}\Delta y(n), \quad (\text{D.1})$$

holds for the cosine spaced vortex lattice representation of the planar lifting line.

If the postulated relationship is expanded with the expression for the velocity induced by the trailing vortices, equation 2.2, it can be rewritten as

$$\begin{aligned} & \frac{y_v(i+1) - y_v(i)}{4\pi} \left\{ \frac{1}{y_v(n) - y_v(i)} - \frac{1}{y_v(n+1) - y_v(i)} \right\} \\ = & \frac{y_v(n+1) - y_v(n)}{4\pi} \left\{ \frac{1}{y_v(i) - y_v(n)} - \frac{1}{y_v(i+1) - y_v(n)} \right\}. \end{aligned} \quad (\text{D.2})$$

This expression can be reduced to

$$\frac{[y_v(i+1) - y_v(i)][y_v(n+1) - y_v(n)]}{4\pi [y_v(n) - y_c(i)][y_v(n+1) - y_c(i)]} = \frac{[y_v(n+1) - y_v(n)][y_v(i+1) - y_v(i)]}{4\pi [y_v(i) - y_c(n)][y_v(i+1) - y_c(n)]}. \quad (\text{D.3})$$

Noting that the numerator on both sides of the equality is simply $\Delta y(n)\Delta y(i)$ the proof is reduced to showing that the denominators are equal. In other words it must be shown that

$$\begin{aligned} & y_v(n)y_v(n+1) - y_v(n)y_c(i) - y_v(n+1)y_c(i) + y_c^2(i) \\ = & y_v(i)y_v(i+1) - y_v(i)y_c(n) - y_v(i+1)y_c(n) + y_c^2(n) \end{aligned} \quad (\text{D.4})$$

In the case of unit span, the cosine spacing algorithm may be written out as

$$y_v(n) = \cos((n-1)\Delta\theta), \quad (\text{D.5})$$

$$y_v(n+1) = \cos(n\Delta\theta), \quad (\text{D.6})$$

$$y_c(n) = \cos\left(\left(n - \frac{1}{2}\right)\Delta\theta\right). \quad (\text{D.7})$$

An expansion of equation D.4 with equations D.5-D.7 yields the following.

$$\begin{aligned}
& \cos(n\Delta\theta - \Delta\theta) \cos(n\Delta\theta) - \cos(n\Delta\theta - \Delta\theta) \cos(i\Delta\theta - \frac{\Delta\theta}{2}) \\
& - \cos(n\Delta\theta) \cos(i\Delta\theta - \frac{\Delta\theta}{2}) + \cos^2(i\Delta\theta - \frac{\Delta\theta}{2}) \\
& = \cos(i\Delta\theta - \Delta\theta) \cos(i\Delta\theta) - \cos(i\Delta\theta - \Delta\theta) \cos(n\Delta\theta - \frac{\Delta\theta}{2}) \\
& - \cos(i\Delta\theta) \cos(n\Delta\theta - \frac{\Delta\theta}{2}) + \cos^2(n\Delta\theta - \frac{\Delta\theta}{2}). \tag{D.8}
\end{aligned}$$

Making use of several trigonometric identities the first and last terms of each side of equation D.8 can be rewritten, resulting in

$$\begin{aligned}
& \cos^2(n\Delta\theta) \cos(\Delta\theta) + \sin(n\Delta\theta) \cos(n\Delta\theta) \cos(\Delta\theta) \\
& - \cos(n\Delta\theta - \Delta\theta) \cos(i\Delta\theta - \frac{\Delta\theta}{2}) - \cos(n\Delta\theta) \cos(i\Delta\theta - \frac{\Delta\theta}{2}) \\
& + \frac{1}{2} + \cos^2(i\Delta\theta) \cos(\Delta\theta) - \cos(\frac{\Delta\theta}{2}) + \sin(i\Delta\theta) \cos(i\Delta\theta) \cos(\Delta\theta) \\
& = \cos^2(i\Delta\theta) \cos(\Delta\theta) + \sin(i\Delta\theta) \cos(i\Delta\theta) \cos(\Delta\theta) \\
& - \cos(i\Delta\theta - \Delta\theta) \cos(n\Delta\theta - \frac{\Delta\theta}{2}) - \cos(i\Delta\theta) \cos(n\Delta\theta - \frac{\Delta\theta}{2}) \\
& + \frac{1}{2} + \cos^2(n\Delta\theta) \cos(\Delta\theta) - \cos(\frac{\Delta\theta}{2}) + \sin(n\Delta\theta) \cos(n\Delta\theta) \cos(\Delta\theta). \tag{D.9}
\end{aligned}$$

Cancelling terms that appear on both sides of equation D.9 it must still be shown that

$$\begin{aligned}
& \cos(n\Delta\theta - \Delta\theta) \cos(i\Delta\theta - \frac{\Delta\theta}{2}) + \cos(n\Delta\theta) \cos(i\Delta\theta - \frac{\Delta\theta}{2}) \\
& = \cos(i\Delta\theta - \Delta\theta) \cos(n\Delta\theta - \frac{\Delta\theta}{2}) + \cos(i\Delta\theta) \cos(n\Delta\theta - \frac{\Delta\theta}{2}). \tag{D.10}
\end{aligned}$$

If equation D.10 is expanded with a trigonometric identity the following is obtained.

$$\begin{aligned}
& \cos(n\Delta\theta) \cos(i\Delta\theta) \cos(\Delta\theta) \cos(\frac{\Delta\theta}{2}) + \sin(n\Delta\theta) \cos(i\Delta\theta) \sin(\Delta\theta) \cos(\frac{\Delta\theta}{2}) \\
& + \cos(n\Delta\theta) \sin(i\Delta\theta) \cos(\Delta\theta) \sin(\frac{\Delta\theta}{2}) + \sin(n\Delta\theta) \sin(i\Delta\theta) \sin(\Delta\theta) \sin(\frac{\Delta\theta}{2}) \\
& + \cos(n\Delta\theta) \cos(i\Delta\theta) \cos(\frac{\Delta\theta}{2}) + \cos(n\Delta\theta) \sin(i\Delta\theta) \sin(\frac{\Delta\theta}{2}) \\
& = \cos(i\Delta\theta) \cos(n\Delta\theta) \cos(\Delta\theta) \cos(\frac{\Delta\theta}{2}) + \sin(i\Delta\theta) \cos(n\Delta\theta) \sin(\Delta\theta) \cos(\frac{\Delta\theta}{2})
\end{aligned}$$

$$\begin{aligned}
& + \cos(i\Delta\theta) \sin(n\Delta\theta) \cos(\Delta\theta) \sin\left(\frac{\Delta\theta}{2}\right) + \sin(i\Delta\theta) \sin(n\Delta\theta) \sin(\Delta\theta) \sin\left(\frac{\Delta\theta}{2}\right) \\
& + \cos(i\Delta\theta) \cos(n\Delta\theta) \cos\left(\frac{\Delta\theta}{2}\right) + \cos(i\Delta\theta) \sin(n\Delta\theta) \sin\left(\frac{\Delta\theta}{2}\right). \quad (D.11)
\end{aligned}$$

Removing terms which appear on both sides of equation D.11 leaves

$$\begin{aligned}
& \sin(n\Delta\theta) \cos(i\Delta\theta) \sin(\Delta\theta) \cos\left(\frac{\Delta\theta}{2}\right) + \cos(n\Delta\theta) \sin(i\Delta\theta) \cos(\Delta\theta) \sin\left(\frac{\Delta\theta}{2}\right) \\
& + \cos(n\Delta\theta) \sin(i\Delta\theta) \sin\left(\frac{\Delta\theta}{2}\right) \\
= & \sin(i\Delta\theta) \cos(n\Delta\theta) \sin(\Delta\theta) \cos\left(\frac{\Delta\theta}{2}\right) + \cos(i\Delta\theta) \sin(n\Delta\theta) \cos(\Delta\theta) \sin\left(\frac{\Delta\theta}{2}\right) \\
& + \cos(i\Delta\theta) \sin(n\Delta\theta) \sin\left(\frac{\Delta\theta}{2}\right). \quad (D.12)
\end{aligned}$$

Through use of further trigonometric identities and some rearrangement, D.12 can be shown to be equal to

$$\begin{aligned}
& \cos(n\Delta\theta) \sin(i\Delta\theta) \sin(\Delta\theta) \cos\left(\frac{\Delta\theta}{2}\right) + \cos(i\Delta\theta) \sin(n\Delta\theta) \sin(\Delta\theta) \cos\left(\frac{\Delta\theta}{2}\right) \\
= & \cos(i\Delta\theta) \sin(n\Delta\theta) \sin(\Delta\theta) \cos\left(\frac{\Delta\theta}{2}\right) + \cos(n\Delta\theta) \sin(i\Delta\theta) \sin(\Delta\theta) \cos\left(\frac{\Delta\theta}{2}\right). \quad (D.13)
\end{aligned}$$

The equivalence of the two sides of equation D.13 is apparent. Thus, the reciprocity relationship of equation D.1 is confirmed.